

Multivariable System Identification, Enhanced Disturbance Rejection, and Precision Motion Control for CNC Machine Tool Feed Drives

by

Hessam Kalbasi Shirvani

A thesis

presented to the University of Waterloo

in fulfillment of the

thesis requirement for the degree of

Doctor of Philosophy

in

Mechanical and Mechatronics Engineering

Waterloo, Ontario, Canada, 2021

©Hessam Kalbasi Shirvani 2021

Examining Committee Membership

The following served on the Examining Committee for this thesis. The decision of the Examining Committee is by majority vote.

External Examiner	Yasuhiro Kakinuma Professor, System Design Engineering Keio University
Supervisor	Kaan Erkorkmaz Professor, Mechanical and Mechatronics Engineering University of Waterloo
Internal Member	Soo Jeon Associate Professor, Mechanical and Mechatronics Engineering University of Waterloo
Internal-external Member	Sriram Narasimhan Adjunct Professor, Civil and Environmental Engineering, and Mechanical and Mechatronics Engineering (cross-appointed) University of Waterloo Professor, Civil and Environmental Engineering University of California, Los Angeles
Internal-external Member	Daniel Davison Associate Professor, Electrical and Computer Engineering University of Waterloo

Author's Declaration

This thesis consists of material all of which I authored or co-authored: see Statement of Contribution included in the thesis. This is a true copy of the thesis, including any required final revisions, as accepted by my examiners.

I understand that my thesis may be made electronically available to the public.

Statement of Contribution

This thesis develops new methodologies to address the problem of modeling and control of machine tool feed drives to improve tracking accuracy and disturbance rejection capabilities. The result of this thesis have been published or submitted as follows:

[J1] H. K. Shirvani, Y. Hosseinkhani, K. Erkorkmaz, “Suppression of Harmonic Positioning Errors in Ball-Screw Drives using Adaptive Feedforward Cancellation,” *Precision Engineering*, vol. 68, pp. 235-255, 2021.

This paper presents:

- Analysis and design of adaptive feedforward cancellation (AFC) within the dual (i.e., rotational and translational) position feedback structure used in ball-screw drives.
- Definition of a new frequency-dependent parameter, named here as the *response modification factor* α . This parameter allows for the impact of AFC on the response to different input channels to be gauged in a unified manner.
- Development of a design strategy to adjust the resonator gains (g_n) using the *response modification factor*, which allows the consideration of both robust stability and performance retention requirements, particularly at frequencies outside those targeted by the resonators.
- Validation of the effectiveness of the proposed design in counteracting harmonic positioning errors of temporal (time-dependent) or spatial (position-dependent) nature, caused by machining (i.e., milling) forces or ball-screw mechanical (e.g., lead) errors.

The author, conducting research with Prof. Erkorkmaz, developed the theory behind this approach and performed tracking experiments. Dr. Hosseinkhani, who was an earlier Ph.D. student, is given the credit for having initiated the earlier research on AFC during his Ph.D. thesis. He had also conducted machining tests to demonstrate the rejection of cutting force disturbances and had initially used AFC in combination with a ball-screw system.

The more advanced formal frequency-domain modeling and analysis applicable to the dual-feedback structure of a ball-screw drive, which is critical for guaranteeing stability, was developed in the scope of the author’s Ph.D. research, and is reported in this publication and in Chapter 6 of this thesis. This development also includes the definition of the response modification factor α , and the connection to robust stability analysis and guarantee in designing multiple resonators. The author also performed all of the tracking experiments and simulations reported in this paper and thesis.

[J2] H. K. Shirvani, J. Q. C. Zeng, P. Bevers, T. Oomen, K. Erkorkmaz, “Linear Time-Invariant (LTI) Model Identification Algorithm for Mechatronic Systems based on Multi-Input Multi-Output (MIMO) Frequency Response Data ” (under preparation for submission).

This paper presents:

- Development of a MIMO model estimation method from frequency-domain data for servo systems that can capture the effects of time-delay, structural resonances, highly damped modes (originating from the excessive friction and potential filtering effects), real poles and any direct / derivate-like terms.
- Validation of the effectiveness of the proposed identification algorithm through model fitting to different sets of frequency responses from a ball-screw, gantry type, and direct linear drive systems.
- Comparison of the new identification method with general transfer function estimation and modal parameter estimation tools as benchmarks.

The author has realized the majority of the development, integration, formulation, iterations of programming, and extensive testing of the algorithm, as well as the writing of the manuscript. An earlier SISO version of the algorithm was developed and tested by MASc student, Mr. Jason Zeng. The initial prototype in extending the SISO algorithm to the MIMO case and developing the first software implementation was accomplished with the assistance of Mr. Patrick Bevers, who was a visiting MASc student from TU Eindhoven and had participated in the research under the oversight of Prof. Erkorkmaz and the author. Prof. Tom Oomen is Mr. Bevers’ supervisor from his home institution. Some of the frequency domain data from a precision T-Type gantry, which is used in the validation of the algorithm, had been collected by Mr. Daniel Gordon during his MASc thesis back in 2010, which is also to be acknowledged in the manuscript. The valuable additions made by all of the co-authors and contributors are gratefully acknowledged.

[J3] H. K. Shirvani, J. Q. C. Zeng, K. Erkorkmaz, “Robust Tracking and Active Vibration Damping Control of Feed Drive Systems,” (under preparation for submission).

This paper presents:

- Development of a new model-based tracking and vibration damping control technique for multiple-mode vibration suppression of feed drive systems using a vibration-damping controller based on mixed-sensitivity \mathcal{H}_2 and \mathcal{H}_∞ and a lead-lag compensator as the tracking controller.
- Comparison of the new control synthesis methods against the conventional parameterization of the weighting functions for mixed-sensitivity \mathcal{H}_2 and \mathcal{H}_∞ controllers.
- Validation of the effectiveness of the proposed control strategy through high-speed tracking experiments and closed-loop disturbance rejection measurements.
- Comparison of the newly proposed method with the industry-standard P-PI position-velocity cascade controller and a vibration-damping pole-placement controller.

The author developed and implemented the complete methodology for ball-screw drives in this paper. The application of $\mathcal{H}_2/\mathcal{H}_\infty$ to fixed structures, such as stationary columns, rams, etc., had been earlier studied and experimentally investigated by Mr. Jason Zeng (MA Sc student), which provided some of the foundation in active damping controller design. The application of $\mathcal{H}_2/\mathcal{H}_\infty$ active damping to moving (servo) systems was initiated by the author, integrated into a more elaborate control scheme suitable for ball-screw drives, and validated experimentally both for disturbance rejection and position tracking.

[C1] H. K. Shirvani, P. Bevers, K. Erkorkmaz, “Harmonic Positioning Error Correction and MIMO Based Identification of Ball-Screw Drives,” *VMPT 2018 7th International Conference on Virtual Machining Process Technology – Implementing Industry 4.0*, Hamilton, Canada, May (2018).

This paper presents the early results of the [J1] and [J2].

In all publications, Prof. Kaan Erkorkmaz supervised this research and helped with the development of the theories. He also provided feedback for the paper manuscripts and chapters of this thesis.

Abstract

In this thesis, precision modeling, multivariable system identification, and advanced motion control techniques are developed in order to improve the positioning accuracy and disturbance rejection of machine tool servo systems. Improving the positioning accuracy and disturbance rejection in machine tools enables the increase of manufacturing productivity, energy efficiency, and part quality of products produced on such industrial equipment. The implementation results in this thesis were developed on a ball-screw drive, which is the principal motion delivery mechanism used in a vast majority of machine tools. However, the proposed modeling, model estimation, and controller design methodologies are also applicable to other kinds of mechatronic systems, which possess multi-input multi-output linear time-invariant dynamics.

In enabling the realization of better productivity, process throughput, and part quality, accurate generation of the relative motion between the workpiece and the tool is critical in multi-axis machining operations. The higher the closed-loop bandwidth (i.e., responsive frequency range) that can be achieved for the servo control system, the more accurately the corresponding feed drives replicate the desired multi-axis tool movements in producing the manufactured parts. Furthermore, the dynamic stiffness (i.e., inverse of mechanical compliance) achieved between the tool and workpiece is critical to absorbing the relatively large machining forces, which are also typically rich in frequency content. Servo bandwidth increase also enables equivalent dynamic stiffness increase, especially in the frequency ranges that overlap with the most significant structural vibration modes of a feed drive assembly. However, the achievable servo bandwidth is typically limited by the mechanical vibrations, which can lead to feedback loop stability problems, if they are not explicitly considered in the control law design.

The research in this thesis aims at overcoming the limitations posed by a feed drive's structural vibrations, through detailed modeling, dynamic model estimation, and advanced motion controller design with active vibration damping capability, in order to achieve improved disturbance rejection near the cutting force application point (i.e., load side), as well as high accuracy motion tracking. Thus, the achieved contributions and results can be summarized as follows:

1. A new frequency-domain Multi-Input Multi-Output (MIMO) system identification algorithm has been developed and validated, which is suitable for mechatronic motion delivery systems with LTI dynamics.

The new algorithm can capture both the effects of lightly damped modes (coming from the mechanical structure) as well as other highly damped dynamics. The proposed algorithm is able to achieve pole commonality across multiple output-input channels. In benchmarks conducted with experimental MIMO

frequency response data, the proposed algorithm has been able to demonstrate 1-2 orders of improvement over other MIMO model fitting algorithms, such as `modalfit` and `tfest` available in MATLAB.

2. The disturbance rejection capability of a ball-screw drive has been enhanced through active damping of multiple vibration modes.

In the best of the author's knowledge, this thesis is the first time that successful active damping of multiple vibration modes has been demonstrated experimentally for a ball-screw drive. The proposed methodology is based on applying $\mathcal{H}_2/\mathcal{H}_\infty$ synthesis to damp vibrations and further improve the position tracking using loop-shaping, in conjunction with suitable feedforward terms. In experimental benchmarks, the new designs have demonstrated, for wide frequency ranges, 2...3 \times better disturbance rejection compared to other control techniques, such as P-PI position-velocity cascade (used extensively in industry) and pole-placement control (PPC, proposed earlier in research). The proposed designs have also achieved 2.5 \times better damping of the most significant axial vibration mode, which is the common weak point in ball-screw mechanisms. The achieved tracking performance is comparable to that of PPC, and better than that of P-PI, maintaining <10 microns of dynamic accuracy under 420 mm/s velocity and 0.12 g acceleration conditions. However, proposed controller design requires expert knowledge and interaction. Thus, further development is needed before it can be used safely and effectively in industry.

3. A robust Adaptive Feedforward Cancellation (AFC) framework has been proposed for the mitigating harmonic (oscillatory) positioning errors which occur in ball-screw drives, due to mechanism and sensor imperfections, misalignment, and repetitive disturbances (e.g., cutting forces).

In this contribution, a new methodology has been developed for adopting the multi-resonator AFC design to the dual-feedback structure of ball-screw drives. The methodology allows for the performance degradation outside the target compensation frequencies of the resonators to be quantified and capped, while guaranteeing the robust stability requirements from the point of view of the vector (i.e., inverse closed-loop sensitivity) margin.

To achieve the above listed contributions, detailed modeling, experimental identification, controller design, and testing were also undertaken extensively, and documented in detail throughout the relevant chapters of this thesis, to facilitate the reproducibility of the results as much as possible.

Acknowledgements

First and foremost, I would like to express my deep gratitude to my supervisor Prof. Kaan Erkorkmaz for all the support and encouragement he gave me. This journey would not have been possible without his guidance and constant feedback.

I would like to thank my committee members: Prof. Soo Jeon, Prof. Sriram Narasimhan, Prof. Daniel Davison, and Prof. Yasuhiro Kakinuma for their constructive feedback and helpful advice.

My sincere thanks go to the University of Waterloo technical staff: Mr. Neil Griffett, Mr. Robert Wagner, Mr. Jason Benninger, Mr. Karl Janzen, Mr. Andy Barber, and Mr. James Merli.

I would like to thank my colleagues at Precision Controls Laboratory. Especially, I would like to recognize the assistance that I received from Dr. Yasin Hosseinkhani in the early stages of my Ph.D. I also express my gratitude to Dr. Ahmet Okyay, Dr. Hakan Turhan, Jason Zeng, Milad Azvar, Chia-Pei Wang, Oier Franco, Andrew Katz, and Pierce McCloskey from whom I had the privilege of learning something in one way or another.

This research was supported by Natural Sciences and Engineering Research Council of Canada (NSERC) through the Discovery Grant RGPIN-03879 and the NSERC - Canadian Network for Research and Innovation in Machining Technology (CANRIMT2) grant: NETGP 479639-15.

Many thanks to all my friends for providing support and encouragement.

Finally, I would like to thank my parents for their unconditional love and support throughout my life and my beloved wife, Atefeh, whose love, and endless support made it possible to finish this research work.

Dedication

To my dear wife Atefeh and my parents.

Table of Contents

Author's Declaration	iii
Statement of Contribution	iv
Abstract.....	vii
Acknowledgements	ix
Dedication	x
List of Figures.....	xiv
List of Tables	xx
Chapter 1 Introduction.....	1
1.1. Background	1
1.2. Thesis Overview and Contributions.....	3
Chapter 2 Literature Review	7
2.1. Introduction.....	7
2.2. Modeling and Identification of Ball-Screw Drives.....	8
2.2.1. Rigid Body Dynamics	8
2.2.2. Lumped Mass-Spring-Damper, Hybrid, and Finite Element Models	9
2.2.3. Modal Analysis	11
2.2.4. Multivariable System Identification.....	12
2.3. Friction Identification and Compensation.....	15
2.4. Control for Precision Motion and Active Vibration Damping.....	18
2.4.1. Sliding Mode Control (SMC)	19
2.4.2. Pole-Placement Control	20
2.4.3. Linear Quadratic Gaussian (LQG) Control.....	22
2.4.4. $\mathcal{H}2/\mathcal{H}\infty$ Control.....	23
2.5. Suppression of Harmonic Positioning Errors using Adaptive Feedforward Cancelation (AFC) 24	
2.5.1. Brief Review of AFC	26
2.6. Conclusions.....	29
Chapter 3 Modeling and Identification of Ball-Screw Driven Feed Drives	31
3.1. Introduction.....	31
3.2. Experimental Setup.....	31
3.3. Frequency Response Measurements using a PWM Driver.....	32
3.4. Modeling and Identification of the Current Loop Dynamics upon Retrofitting the Setup with a Linear Amplifier	34
3.5. Identification of Rigid Body Dynamics	45
3.6. Frequency Response Measurement using Linear Amplifier	47

3.7.	Modeling and Identification of a Lumped Two-Inertia System Model	48
3.8.	Identification of a Stribeck-Type Friction Model using a Kalman Filter	50
3.9.	Identification of Friction Considering the Generalized Maxwell-Slip (GMS) Model	53
3.10.	Friction Compensation using Stribeck-Type Model vs. GMS Model	56
3.11.	Vibration Modal Analysis	57
3.12.	Conclusions	64
Chapter 4 Linear Time-Invariant (LTI) Model Identification Algorithm for Mechatronics Systems based on Multi-Input Multi-Output (MIMO) Frequency Response Data		65
4.1.	Introduction	65
4.2.	MIMO LTI Model Identification Algorithm	65
4.2.1.	Formulation of the MIMO model and overview of the identification algorithm	65
4.2.2.	Details of the algorithm considering an LTI model	70
4.3.	Experimental Validation on a Precision T-Type Gantry Machine	88
4.3.1.	MIMO Identification of Y-Axis	89
4.3.2.	SISO Identification of the X-Axis	95
4.4.	Experimental Validation on a Single-Axis Ball Screw Drive	96
4.5.	Experimental Validation on a 3-Axis H-Type Gantry Machine	98
4.6.	Comparison of Proposed MIMO Algorithm with MATLAB's <code>tfest</code> and <code>modalfit</code> Functions	104
4.7.	Conclusions	109
Chapter 5 Control for Precision Motion and Active Vibration Damping		110
5.1.	Introduction	110
5.2.	Case Study Demonstrating Limiting Influence of Vibration Modes	112
5.3.	Benchmark #1 Industry-Standard P-PI Position-Velocity Cascade Controller	115
5.4.	Benchmark #2 PPC Vibration Damping Controller	116
5.5.	Mixed-Sensitivity $\mathcal{H}2$ and $\mathcal{H}\infty$ Optimization Problem	118
5.6.	Proposed Control Design for Multiple-Mode Vibration Damping and Tracking Control of Feed Drive Systems	122
5.6.1.	Feed Drive Model	123
5.6.2.	Mixed-Sensitivity $\mathcal{H}2$ and $\mathcal{H}\infty$ Control for Multiple-Mode Vibration Suppression	128
5.6.3.	Tracking Controller Design	132
5.7.	Proposed versus Conventional Design for the Sensitivity Weighting Function	134
5.8.	Experimental Evaluation of the Developed Control Laws	136
5.8.1.	Frequency-Domain Loop Gain, Stability, and Sensitivity Comparison	138
5.8.2.	Load Side Mechanical Disturbance Rejection	142

5.8.3.	Tracking Performance Evaluation.....	145
5.9.	Conclusions.....	148
Chapter 6	Suppression of Harmonic Positioning Errors in Ball-Screw Drives using AFC	150
6.1.	Introduction.....	150
6.2.	AFC Design for Dual-Feedback Ball-Screw Drive Control System.....	150
6.2.1.	Basic Structure	150
6.3.	Influence of AFC on Rejecting Harmonic Disturbances	152
6.4.	Influence of AFC on Positioning Errors Due to Command Following.....	158
6.5.	AFC in Conjunction with Different Motion Control Laws for Ball-Screw Drives	159
6.6.	Experimental Implementation: AFC for Rejecting Position Dependent Harmonic Errors.....	160
6.7.	Simulation Results #1: Comparison of the New Tuning Strategy with the Conventional Method 167	
6.8.	Simulation Results #2: Rejection of Position Dependent Harmonic Errors During Variable Velocity Motion.....	169
6.9.	Conclusions.....	172
Chapter 7	Conclusions and Future Work.....	174
7.1.	Conclusions.....	174
7.2.	Future Research Directions.....	175
Bibliography		177
Appendices		187
Appendix A.1		187
Appendix A.2		189
Appendix A.3		190
Appendix A.4		191
Appendix A.5		194
Appendix A.6		196
Appendix A.7		199

List of Figures

Figure 1.1: Thesis overview.....	6
Figure 2.1: Two-inertia model.....	9
Figure 2.2: Schematic of the axial (a) and rotational (b) decoupled models [15].....	11
Figure 2.3: Drive system with linear direct drive and mode shape for natural frequency at 300 Hz [23]..	12
Figure 2.4: Schematic of the Maxwell-slip model with N-elementary blocks.....	16
Figure 2.5: Input-amplitude-dependent frequency responses of the open-loop servo system with Dahl resonances [44].	17
Figure 2.6: Excitation of the counter-phase mode in a vertical ram-type machining center [62].....	19
Figure 2.7: PPC versus P-PI [71]. Top left: Concept of damping via pole shifting. Top right: Loop transfer function gain comparison between mode-compensating PPC and P-PI. Bottom left: Optimization of table side cutting force response in PPC. Bottom right: Improvement in disturbance rejection during machining tests.	21
Figure 2.8: Multi-mode Pole Placement Controller (PPC) with a Kalman Filter observer [73].....	22
Figure 2.9: Brief review of AFC.....	27
Figure 2.10: Frequency response of an AFC resonator with a pair of complex conjugate poles at 100 Hz for different values of the phase advance parameter.	28
Figure 3.1: Single-axis ball-screw setup.....	32
Figure 3.2: Current loop frequency response measurement using the PWM driver in logarithmic (left) and linear scale (right).	34
Figure 3.3: Rotary (left) and linear encoder (right) position frequency responses.	34
Figure 3.4: Illustration of space vector (abc), stationary ($\alpha - \beta$) and synchronous ($d - q$) reference frames.	36
Figure 3.5: Simplified electrical dynamics with PI controller.	38
Figure 3.6: Schematic of the current-loop implementation.	40
Figure 3.7: Block diagram of the current-loop controller and PMSM dynamics.	41
Figure 3.8: Measured and estimated FRF of the current loop dynamics (left), coherence of the FRF (right).	42
Figure 3.9: Measured and simulated current loop responses using a chirp excitation signal.	44
Figure 3.10: Measured frequency response of the linear amplifier current loop dynamics at different output voltages.	44
Figure 3.11: Measured linear amplifier vs measured PWM current loop frequency responses.	45
Figure 3.12: Predicted and actual velocity responses, perdition error, and the input signal.	47

Figure 3.13: Rotary and linear encoder position (upper-hand panels) and acceleration (lower-hand panels) frequency responses.	48
Figure 3.14: Measured (dashed line) and modeled (solid line) open-loop FRFs.	49
Figure 3.15: Measured motor torque command and estimated disturbance with Kalman filtering at 15 mm/s and 100 mm/s.	52
Figure 3.16: Stribeck curve.	52
Figure 3.17: Experimental friction torque vs. load side displacement at different amplitudes of excitation (frequency of excitation: 0.1 Hz).	54
Figure 3.18: Virgin curve with selected knots for identification of stiffness in pre-sliding regime (left), and the measured and estimated virgin curves (right).	55
Figure 3.19: The Stribeck curve used in GMS model.	55
Figure 3.20: Tracking error profile without compensation, with Stribeck model-based compensation, and with GMS model-based compensation.	56
Figure 3.21: Impact locations for peak-picking method (a) Impact in x and y-direction and measuring in the x-direction (axial), (b) Impact and measurement in the y-direction (lateral) (c) Impact and measurement in the z-direction.	58
Figure 3.22: Second-order accelerance plot.	59
Figure 3.23: Experimental and synthesized FRF for impact point $F1$ in the x- (left), and y-direction (right).	59
Figure 3.24: Accelerometer roving and impact location for PolyMAX method.	60
Figure 3.25: Experimental and synthesized FRF for impact point $P1$ in the x- (left), y- (middle), and z-directions (right).	60
Figure 3.26: Mode shapes of the ball-screw drive, estimated by manual (left) and automated (right) modal analysis methods.	63
Figure 4.1. Flow chart for the proposed identification algorithm.	69
Figure 4.2: Use of the CMIF in identifying resonant frequencies and selecting frequency ranges to fit individual modes: (a) acceleration response to torque command for single-axis linear motor drive. (b) position response to torque command due a dual linear motor driven gantry axis.	72
Figure 4.3: Use of the SISO MIF in identifying resonant frequencies and selecting frequency ranges to fit individual modes: position response to torque command for a dual linear motor-driven gantry axis.	73
Figure 4.4: Linear motor driven T-type gantry and worktable (left) and the schematic of the setup (right) [130].	89
Figure 4.5: Raw FRFs, also containing the system's pure delay in the measurement.	90
Figure 4.6: Frequency response data before and after the removal of pure delay (Step 1).	90

Figure 4.7: Fitting of vibration modes and residual FRFs (left) and zoomed view (right) (Steps 2 and 3).	91
Figure 4.8: Subtraction of fitted modes to reveal remainder frequency response contributions (start of Step 4), shown from 50 Hz onwards.	91
Figure 4.9: Fitting of the remainder dynamics <i>Tkoki</i> (Step 4).	92
Figure 4.10: Measured and fitted model before (shown in left hand panels) and after (shown in right hand panels) pole consolidation and simultaneous fitting of all participation factors (Step 5).	93
Figure 4.11: Topologies of RMS values for the MIMO fitting error, obtained by iterating different values for the assumed pure delay (<i>Td</i>) and denominator / numerator model orders for the remainder dynamics (Steps 1-5).	94
Figure 4.12: Experimental FRF (including delay) and fitted model before and after the nonlinear optimization of the pole locations. (left), and the corresponding real and imaginary response fitting errors (right) (Step 6).	94
Figure 4.13: Experimental FRF (including delay) and fitted model before (RMS (E) = 94.57) & after the optimization (RMS(E) = 28.13).	96
Figure 4.14: Nyquist diagram for experimental FRF and fitted model at Step 6.	96
Figure 4.15: Schematic of the Single-axis ball-screw drive and worktable.	97
Figure 4.16: Measured MIMO FRF and fitted model (after Step 6) for the single-axis ball screw drive.	98
Figure 4.17: 3-axis H-type CNC router (left) and schematic view of actuation and measurement points (right).	98
Figure 4.18: Raw FRF data and fitted model for the x-axis of the CNC router.	102
Figure 4.19: Nyquist plots of the experimental FRF including delay and fitted model.	103
Figure 4.20: Mode shape visualization for the gantry x-axis.	104
Figure 4.21: FRF (left), Nyquist plots (right) of the raw data including delay and fitted model for the y-axis of the CNC gantry machine.	104
Figure 4.22: Raw FRF data and fitted models using <i>tfest</i> (left) <i>modalfit</i> (right) vs. the proposed algorithm.	106
Figure 4.23: Raw FRF data and fitted models using the proposed algorithm vs. <i>tfest</i> .	107
Figure 4.24: Raw FRF data and fitted models using the proposed algorithm vs. <i>modalfit</i> .	107
Figure 5.1: Frequency-domain analysis of y-axis PID control feedback loop closed using different measurement signals.	112
Figure 5.2: Block diagram of the dual-feedback loop-shaping PID controller.	113
Figure 5.3: Tracking error profiles and control signals using different feedback structure.	114
Figure 5.4: Dual-feedback P-PI position-velocity cascade control structure.	116
Figure 5.5: Vibration-damping pole-placement control structure [72].	118

Figure 5.6: Structure of a feedback control system.....	118
Figure 5.7: General control configuration.....	120
Figure 5.8: Standard mixed-sensitivity $\mathcal{H}2$ and $\mathcal{H}\infty$ control configuration.....	121
Figure 5.9: Conventional sensitivity shaping function.	122
Figure 5.10: Vibration damping and tracking controller design.	123
Figure 5.11: Worktable disturbance FRF obtained by impact hammer test, the mode shapes, and their corresponding frequencies.	124
Figure 5.12: $G\infty$ of the system modes.	126
Figure 5.13: Model order reduction through truncation.....	127
Figure 5.14: Model reduction error for output-input channel terms $ Hkoki\omega - Gkoki\omega $	127
Figure 5.15: Block diagram manipulation for closed-loop analysis [72].....	128
Figure 5.16: Augmented plant with the sensitivity weighting function W_e , control input weighting function W_u , and measurement noise weighting functions W_{n1} , W_{n2}	129
Figure 5.17: Frequency responses of the originally synthesized and reduced-order mixed-sensitivity $\mathcal{H}2$ and $\mathcal{H}\infty$ vibration damping controllers.	131
Figure 5.18: Frequency responses of the synthesized mixed-sensitivity $\mathcal{H}2$ and $\mathcal{H}\infty$ damping controllers with the addition of filter package (Gfp) in continuous and discrete forms.....	132
Figure 5.19: Magnitude plots of the proposed and conventional sensitivity shaping function for mixed-sensitivity $\mathcal{H}2$ (left) and $\mathcal{H}\infty$ (right) damping controllers.	135
Figure 5.20: Open loop and closed loop load-side disturbance response measurements for the proposed $\mathcal{H}2$ (left) and conventional $\mathcal{H}2$ (right) mixed-sensitivity vibration damping controllers, measured via impact hammer tests.	135
Figure 5.21: Open loop and closed loop load-side disturbance response measurements for the proposed $\mathcal{H}\infty$ (left) and conventional $\mathcal{H}\infty$ (right) mixed-sensitivity vibration damping controllers, measured via impact hammer tests.	135
Figure 5.22: Schematic of the feed drive system.	136
Figure 5.23: Axial vibration mode FRFs at different table locations. Rotary (left) and linear encoder (right) frequency response measurements at motor end (A), middle point (B) and free end (C).....	137
Figure 5.24: Rotary (left) and linear encoder (right) frequency response measurements at motor end (A), middle point (B) and free end (C).....	138
Figure 5.25: Loop transfer function magnitudes for: (a) proposed $\mathcal{H}2$ + LS, (b) P-PI Cascade Structure, (c) proposed $\mathcal{H}\infty$ + LS, and (d) the vibration-damping PPC.....	139
Figure 5.26: Nyquist plots for: (a) proposed $\mathcal{H}2$ + LS control, (b) P-PI cascade structure, (c) proposed $\mathcal{H}\infty$ + LS, (d) vibration-damping PPC.	140

Figure 5.27: Equivalent SISO analysis based sensitivity function gain plots for: (a) proposed $\mathcal{H}2+LS$ (a), (b) P-PI cascade structure, (c) proposed $\mathcal{H}^\infty+LS$, (d) vibration-damping PPC.	142
Figure 5.28: Open-loop and closed-loop load-side disturbance response predictions and impact hammer based measurements for: (top-left) proposed $\mathcal{H}2 + LS$ control, (top-right) P-PI cascade control, (bottom-left) proposed $\mathcal{H}^\infty + LS$ control, and (bottom-right) vibration damping PPC (right).....	143
Figure 5.29: Comparison of experimental dynamic compliance characteristics achieved with the proposed controllers versus the other two benchmarks: (top row) $\mathcal{H}2 + LS$ versus P-PI and PPC, (bottom row) $\mathcal{H}^\infty + LS$ versus P-PI and PPC.	144
Figure 5.30: Reference trajectory used in the tracking experiments (displacement 300 mm).	145
Figure 5.31: Experimentally measured tracking errors and control signals for the proposed $\mathcal{H}2 + LS$ controller without (left) and with (right) velocity and acceleration feedforward terms.	146
Figure 5.32: Experimentally measured tracking errors and control signals for the proposed $\mathcal{H}^\infty + LS$ controller design without (left) and with (right) velocity and acceleration feedforward terms.	146
Figure 5.33: Experimentally measured tracking errors and control signals for: (a) proposed $\mathcal{H}2 + LS$, (b) cascade P-PI, (c) proposed $\mathcal{H}^\infty + LS$, (d) the vibration-damping pole-placement controllers.	148
Figure 6.1: AFC integrated inside the dual feedback ball-screw drive control structure.	151
Figure 6.2: Equivalent dynamics in translational position feedback channel, due to inclusion of AFC. .	152
Figure 6.3: Expected harmonic disturbance sources in closed-loop control of a ball-screw drive.	153
Figure 6.4: Closed-loop response of table position to lead error disturbance, without (w/o) and with (w/) AFC in the translational feedback loop.	154
Figure 6.5: Integration of AFC with: (a) P-PI position velocity cascade and, (b) pole-placement control schemes.	154
Figure 6.6: Loop sensitivity without and with AFC.	157
Figure 6.7: Design of AFC through inspection of the response modification factor (α).	157
Figure 6.8: Loop transfer function for P-PI controller without and with AFC resonators (target frequencies: 15 Hz, and 30 Hz).	158
Figure 6.9: Nyquist plot of the loop transfer function for P-PI controller without and with AFC resonators (target frequencies: 15 Hz, and 30 Hz).	158
Figure 6.10: Measured and modeled lead error.	161
Figure 6.11: Loop sensitivity without and with AFC (target frequencies: 10 Hz & 20 Hz, 15 Hz & 30 Hz, 20 Hz & 40 Hz.	164
Figure 6.12: Robust design of AFC for 200 mm/s (10 Hz, 20 Hz), 300 mm/s (15 Hz, 30 Hz), 400 mm/s (20 Hz, 40 Hz) through inspection α	164
Figure 6.13: Commanded trajectory (displacement: 300 mm).	165

Figure 6.14: Tracking errors at different table speeds in time (left) and frequency-domain components (right).	165
Figure 6.15: RMS value of tracking error without and with AFC, observed over five tests.	166
Figure 6.16: Loop sensitivity ((a), (c)), response modification factor ((b), (d)) and Nyquist ((c) and (f)) plots, comparing the proposed AFC tuning method ((a), (b), (c)) with the conventional design ((d), (e), (f)). Target frequencies: 10, 20 Hz.	168
Figure 6.17: Simulated tracking errors at 200 mm/s feed rate using the proposed tuning procedure (top) vs. the conventional tuning procedure (bottom).	169
Figure 6.18: Airfoil profile and commanded trajectories for the x- and y-axes.....	171
Figure 6.19: Tracking error without (w/o) and with (w/) AFC compensation.....	172

List of Tables

Table 3.1: 3-phase PMSM motor specification.	35
Table 3.2: Summary of the identified current loop dynamics.....	43
Table 3.3: Current loop dynamics linear amplifier vs. PWM driver.	45
Table 3.4: Estimated inertia and viscous coefficients of the servo motor.....	46
Table 3.5: Estimated rigid body parameters of the ball-screw drive.	47
Table 3.6: Identified Stribeck friction parameters.	53
Table 3.7: Identified pre-sliding GMS model parameters.	54
Table 3.8: Identified sliding GMS model parameters.....	55
Table 3.9: Friction compensation using Stribeck-type model vs GMS model.	57
Table 4.1: Comparison between the proposed algorithm, <code>tfest</code> and <code>modalfit</code> (SISO case).....	106
Table 4.2: Comparison between the proposed algorithm, <code>tfest</code> and <code>modalfit</code> (MIMO case).....	108
Table 5.1: Lead-lag compensator parameters.	133
Table 5.2: Proposed controller design parameters.	134
Table 5.3: Conventional controller design parameters.	134
Table 6.1: Sweep of expected traversal speeds and corresponding 1st and 2nd harmonic frequencies....	163
Table 6.2: AFC resonator gains and phase values for different traversal speeds.....	163
Table 6.3: Summary of the tracking experiments.	166
Table 6.4: Summary of the tracking simulations.	169
Table 6.5: Summary of the tracking simulation y-axis.....	172

Chapter 1

Introduction

1.1. Background

In recent decades, significant amount of research in the field of manufacturing has focused on high-speed machining and ways to shorten machining times, while continuing to produce high-quality finished parts. Examples of such parts include: intricate and critical aircraft engine components produced from aerospace alloys (e.g., fans, blades, turbine disks), automotive components (for engines and powertrains), consumer electronics parts (e.g., cases for high-end cell phones and computers), green energy installation equipment (e.g., wind-turbine gearboxes), and biomedical devices (e.g., implants, surgical markers, etc.). To enable the realization of better productivity and part quality in machining, the accurate generation of the relative motion between the workpiece and the tool is critical, which is realized by a machine tool's feed drive (i.e., servo positioning) system. Furthermore, a minimal degree of dynamic stiffness (i.e., inverse of mechanical compliance) needs to be achieved between the tool and workpiece, in order to absorb the relatively large machining forces, which are typically rich in frequency content. Dynamic stiffness also helps prevent excessive susceptibility to part errors due to elastic deformations, as well as machining vibrations, which are detrimental to the part quality, the tooling, and machine life.

Thus, the control design of the feed drive system plays a central role, affecting all of the above outcomes. Ball-screw drives are widely used in machine tools as the principal motion delivery mechanism, due to their low cost and high efficiency. They can meet the precise positioning and stiffness requirements between the tool and workpiece, typically described in microns for tolerances, and tens-to-hundreds of Newtons per microns for stiffness values.

Whether using ball-screws or other means of motion delivery, such as rack and double-pinion mechanisms or direct drives, the control of feed drives is critical to meeting the growing demands for higher productivity, accuracy, and part quality. Consequently, research related to motion control systems for multi-axis production machines has constantly been evolving over the past decades, especially in the following three categories:

- i) Trajectory generation for multi-axis machines, to enhance the motion smoothness, accuracy, and production throughput enabled by machine tool feed drives.

- ii) Detailed modeling of feed drive systems, ball-screw, gantry type, and direct linear drives, and more recently rack-and-pinion mechanisms, for simulation, monitoring, machine design, and controls purposes.
- iii) Design of the model-based controllers to achieve high-accuracy tracking and improved rejection of external disturbance forces, typically through active vibration damping.

Regarding the first category, smooth trajectory generation and optimization of the feedrate (i.e., the traverse rate between the tool and workpiece along a given toolpath) enables the reduction of machining cycle time while adhering to cutting force limitations, as well as velocity, acceleration, and jerk limits of the drive system. This indirectly helps to preserve the high-speed positioning accuracy and linear (stable and safe) operation of the actuation system [1][2]. Generating a smooth trajectory prevents the feed drive from rapidly accelerating and decelerating, which consequently reduces the excitation of the resonant vibration modes that can trigger residual vibrations and reduce part quality. On the other hand, high-speed positioning requires a controller with high positioning bandwidth as well.

As with all mechanical systems, ball-screw drives have resonant frequencies corresponding to the natural modes of vibration. Transmission components like couplings, as well as bearings, gears, and the machine frame can also influence the resonant frequencies. Excitation of the natural modes, via the servo system or cutting process, can lead to excessive vibration, which can result in long-term wear and ultimately failure of the components in a machine tool. Furthermore, the vibration modes constitute a major bottleneck in the way of achieving high positioning and disturbance rejection in feed drive structures.

The mechanical resonances in a feed drive system can broadly be categorized into low- and high-frequency types. Low-frequency resonances occur more often due to large and heavy structural components that are connected to, or driven by, the feed drives, such as gantry or column structures. They can also originate from the machine base structural response. High-frequency resonances, on the other hand, typically originate from the light-weight and stiffer components, such as torsional vibration modes of a ball-screw itself, from tool/workpiece fixturing, or from a sensor (e.g., encoder) or actuator mounting assemblies. There are several methods available for addressing low-frequency vibrations, such as using various filtering approaches (high-pass or low-pass) and using acceleration feedback for active vibration suppression [3]. High-frequency resonances normally occur at frequencies beyond the position closed-loop bandwidth (typically above 100-200 Hz). However, they can have a detrimental influence on the stability margins of the servo system. Overall, both low- and high-frequency resonances can lead to reduction of the

stability margins and the responsive frequency range (i.e., bandwidth). Their detrimental effect can only be avoided or overcome by developing more advanced, and also robust, motion control algorithms.

The research proposed in this thesis addresses the problem of modeling and control of CNC feed drives to achieve better disturbance rejection near the cutting force application point (i.e., load side) as well as better positioning accuracy. This has to be realized in the presence of control challenges posed by the mechanical vibration modes. Realizing better disturbance rejection and higher control bandwidth translates directly into better quality and accuracy for parts produced on CNC machine tools. Higher control bandwidth also means that similar or better tool positioning accuracy can be maintained, in a dynamic sense, during elevated speeds and accelerations of the feed drives. This contributes to enhanced productivity in machining parts at higher speeds. The results of such a solution would be applicable, also, to other types of manufacturing operations, like additive manufacturing (3D printing) or laser-based processing (e.g., cutting or drilling). This is particularly relevant, because advances in high-speed machining spindle and laser processing technologies are now enabling over 10-fold increase in the achievable process rates, thus requiring motion control systems that can also keep up, by executing high speed trajectories at correspondingly accelerated rates while retaining (or possibly improving) the dynamic positioning accuracy.

1.2. Thesis Overview and Contributions

As ball-screw drives are among the most widely used feed drive mechanism, the target implementation platform in this thesis has also been selected as a ball-screw drive. However, the modeling, model estimation, and controller design methodologies developed and applied in this thesis are also applicable to other kinds of mechatronic systems for motion control, which possess multi-input multi-output linear time-invariant dynamics.

Henceforth in this thesis, Chapter 2 presents a literature review and background information related to the modeling and control of ball-screw drives. Chapter 3 presents the initial modeling and identification of a single-axis ball-screw. This includes the modeling and identification of the current loop dynamics for a PWM (pulse-width modulated) driver and a high-bandwidth linear amplifier. The estimation of rigid-body parameters, a discrete two-inertia dynamic model (to capture a single vibration mode), and friction modeling are also included. The friction modeling and identification consist of Stribeck-type friction, as well as the generalized Maxwell-slip model, which is particularly successful in modeling stick-slip behavior. At the end of the chapter, experimental modal analysis of the feed drive setup is presented, in order to establish deeper insight into the vibratory behavior of the ball-screw setup.

Chapter 4 introduces a new MIMO frequency-domain model estimation algorithm for the system identification of servo drives. The model can capture the effect of lightly damped structural vibrations as well as highly damped complex or real poles. The effectiveness of the algorithm is evaluated by model fitting to different sets of experimental MIMO frequency response measurements. The measurements were obtained from single- and multiple (coupled gantry type axes) of ball-screw and linear motor-driven machines.

Chapter 5 describes a new model-based damping and tracking controller for the suppression of multiple vibration modes in ball-screw drives using mixed-sensitivity $\mathcal{H}_2/\mathcal{H}_\infty$ control synthesis, in conjunction with loop shaping and feed forward controllers. The performance of the controller in counteracting the disturbances and in tracking trajectories is validated with experiments. The proposed \mathcal{H}_2 and \mathcal{H}_∞ versions of the control law have been compared to the industry-standard P-PI position-velocity cascade controller, and a pole-placement controller (PPC) with vibration damping and precision motion tracking, which have been chosen as benchmarks.

In Chapter 6, the suppression of harmonic positioning errors in ball-screw drives using the adaptive feedforward cancelation (AFC) is studied. For the first time, AFC is adapted to the dual (rotational and translational) feedback structure of ball screw drives, and new analysis and tuning guidelines are established. Finally, the conclusions and future research directions are presented in Chapter 7.

The main contributions of this thesis can be listed as follows:

C.1 Development of a new frequency-domain MIMO system identification algorithm suitable for mechatronic motion control systems with LTI dynamics. The new algorithm, presented in Chapter 4, can capture both the effects of lightly damped modes (coming from the mechanical structure) as well as other highly damped dynamics, originating from the existence of friction and any potential filtering effects due to the sensing and actuation components. The proposed algorithm is also able to achieve pole commonality across multiple output-input channels. Thus, in situations where the experimental frequency response data contains several input and output channels, and response components originating from lightly damped structural modes as well as well-damped dynamics (e.g., rigid body interactions with friction), the proposed algorithm has been able to achieve 1-2 orders of improvement over other MIMO model-fitting algorithms, such as `modalfit` and `tfest` available in MATLAB.

C.2 Enhancement of the disturbance rejection capability of ball-screw drives through active damping of multiple vibration modes. To the best of the author's knowledge, this thesis is the first time that successful active damping of multiple vibration modes has been demonstrated experimentally for a ball-

screw drive. The proposed methodology is based on applying $\mathcal{H}_2/\mathcal{H}_\infty$ synthesis to damp vibrations and further improve the position tracking using loop-shaping, in conjunction with suitable feedforward terms. The new design, in experimental benchmarks, has demonstrated in wide frequency ranges typically 2...3× better disturbance rejection compared to P-PI and PPC designs, and has also achieved 2.5× better damping of the most significant axial vibration mode, which is the common weak point in ball-screw mechanisms. The tracking performance is also as good (for PPC) or typically better (for P-PI), maintaining $<10 \mu\text{m}$ of dynamic accuracy under 420 mm/s velocity and 0.12 g acceleration conditions. However, design of the proposed controller requires expert knowledge and interaction. Thus, some more development is needed before it can be safely and effectively used in industry.

C.3 A robust AFC framework for the mitigating harmonic positioning errors which occur in ball-screw drives, due mechanism and sensor imperfections, misalignment, as well as repetitive disturbances.

In this thesis, a new methodology is developed for adopting the multi-resonator AFC design to the dual-feedback structure of ball-screw drives. The methodology allows for the performance degradation outside the target compensation frequencies of the resonators to be quantified and capped, while guaranteeing the robust stability requirements from the point of view of the vector (i.e., inverse closed-loop sensitivity) margin.

To achieve these three main contributions (see Figure 1.1), detailed modeling, experimental identification, controller design, and testing were also undertaken extensively, and documented in detail throughout the relevant chapters of this thesis, to facilitate reproducibility of the results as much as possible.

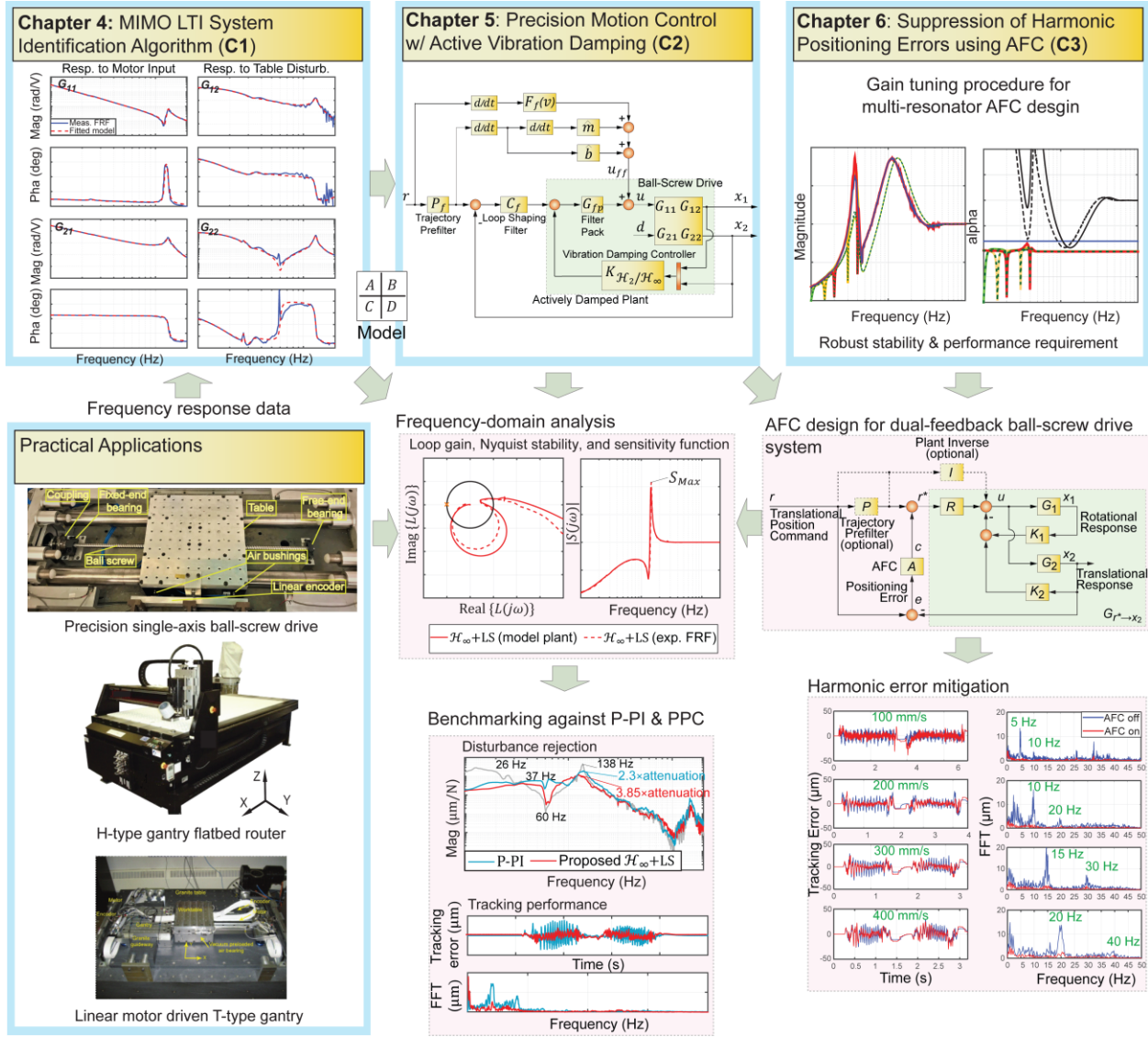


Figure 1.1: Thesis overview.

Chapter 2

Literature Review

2.1. Introduction

CNC feed drives are a vital component of high-speed machine tools that have been the focus of many studies. In the past few decades, there have been many significant developments in high-speed machine tools, corresponding, in more advanced trajectory planning, dynamic modeling, and control for feed drives. The successful application of modeling and control techniques will undoubtedly improve the high-speed machining operations in terms of part quality and cycle time reduction. The modeling and identification techniques for feed drive systems involve efforts to capture the current loop dynamics of the actuators, the vibratory and rigid body dynamics, as well as disturbance effects such as friction. High-bandwidth control design for a feed drive system also requires suitable analysis methods to guarantee stability in the presence of structural vibration modes and disturbances, while preventing significant tracking errors at high accelerations.

In the following, Section 2.2 reviews the literature related to modeling and identification of feed drives, including a discussion of several approaches with varying levels of complexity and detail related to ball-screw drives (Sections 2.2.1 and 2.2.2). The significance of modal testing in the study of the structural behavior of machine tools is also highlighted in Section 2.2.3. Section 2.2.4 covers the literature related to the multivariable system identification of machine tool feed drives. Section 2.3 addresses the friction force as being one of the main sources of disturbances, which negatively affect the tracking accuracy in feed drives. This section discusses various friction models, which have been developed for motion control systems.

Section 2.4 presents various precision motion and vibration control methods that have been proposed for servo systems, including techniques like sliding mode (2.4.1), pole-placement (2.4.2), linear quadratic Gaussian (LQG) (2.4.3), and mixed-sensitivity \mathcal{H}_∞ control synthesis (2.4.4). Section 2.5 introduces the concept of adaptive feedforward cancellation (AFC) for eliminating harmonic positioning error in feedback control systems. This approach is proposed for ball-screw drives in this thesis, for dealing with harmonic servo errors originating from the ball-screw lead or repetitive machining force profiles.

2.2. Modeling and Identification of Ball-Screw Drives

Before a high-bandwidth controller can be designed, it is essential to accurately model and identify the dynamics of feed drives. This section examines the literature related to modeling and identifying ball-screw drives with different levels of complexity.

2.2.1. Rigid Body Dynamics

The rigid body model simplifies the dynamic analysis by reducing the parameters to describe only rigid mass behavior is only capable of capturing the low-frequency dynamics of the system. Erkorkmaz and Altintas [4] introduced an open-loop identification method for least-squares estimation of the axis inertia, viscous friction, and Coulomb friction parameters. In another study, a technique for quickly identifying the closed-loop response of a machine tool's feed drive was presented by Erkorkmaz and Wong [5]. In this study, the whole system is considered, including the feed drive mechanism, motor amplifier, and control law. The pole locations were constrained by limiting the frequency and damping ratio values, which also guarantees the stability of the identified model. They cast the identification problem as a Lagrange Multipliers based constrained optimization, which was later also solved using a genetic algorithm (GA) [5][6]. Altintas and Sencer [7] proposed a similar closed-loop identification method for 5-axis CNC machine tools, and used the particle swarm optimization (PSO) to solve the nonlinear estimation problem. Considering only rigid-body dynamics, a drive's velocity response in the s - (i.e., Laplace) domain can be expressed using the following equation, where J is the inertia, and B is the viscous damping, as scaled in terms of the actuator's rotational displacement (θ) and velocity (ω). When machining is not taking place, the external disturbance is considered to be a constant Coulomb friction term T_d , which applies in the opposite direction of the feed drive's velocity. Thus,

$$\omega(s) = \frac{1}{Js + B}(\tau - T_d) \quad (2.1)$$

The motor torque can be expressed as $\tau = K_a K_t u$, where K_a and K_t are the current amplifier and the motor torque constant, respectively, and u represents the input voltage. The above modeling assumes that the bandwidth of the current loop response is much higher than the bandwidth of the mechanical response (B/J [rad/s]).

2.2.2. Lumped Mass-Spring-Damper, Hybrid, and Finite Element Models

In reality, feed drives are flexible systems that display a large number of vibration modes. These dynamics have been captured, with varying degrees of complexity, using methods like lumped (i.e., discrete-element) modeling, hybrid approaches, finite element models, and through modal analysis.

A two-mass discrete model, as shown in Figure 2.1, is often adequate for capturing the most significant dynamics of a ball-screw drive, including the rigid body motion and the 1st axial vibration mode, which is critical from the controls point of view. In a two-mass model, the first mass represents the inertia of the rotating components, for example, the motor, coupling, and the screw shaft. The second mass represents the inertia associated with the translating load side of the ball-screw drive, which is the nut, the table assembly, and the workpiece. The two-mass model has been widely used in the literature [8][9][10][11][12].

In the model, the viscous friction terms b_1 and b_2 represent the damping effect in the rotary bearings and linear guideways, respectively. The spring element represents the equivalent overall axial stiffness of the feed drive mechanism, and the damper represents the damping in the preloaded nut. The input torque produced by the servo motor is given by u , d_1 and d_2 are the disturbances acting on the motor and the table respectively. The table disturbance term occurs due to the cutting force, friction force (on the table/load side), or can also be used to capture the effect of unmodeled dynamics acting on the table.

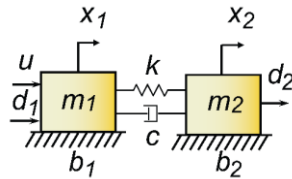


Figure 2.1: Two-inertia model.

Another approach to studying ball-screw drive dynamics is to decouple the response into rigid body motion and second-order resonators, which can be expressed as flexible modes:

$$\theta(s) = \underbrace{\frac{1}{s(Js + B)}}_{\text{Rigid body}} + \underbrace{\sum_{k=1}^N \frac{R_k}{s^2 + 2\zeta_k \omega_{n,k} s + \omega_{n,k}^2}}_{\text{flexible modes}} \quad (2.2)$$

In the above equation, $\omega_{n,k}$ and ζ_k are the natural frequency and damping ratio of the k th flexible mode. N is the number of modes considered in the model. R_k is the ‘residue’, also referred to as the modal participation factor. In some cases, when a mode is not at 0° or 180° in-phase with its excitation input (e.g., when the damping in the system is not proportionally distributed as a linear combination of stiffness and

mass matrices), R_k can assume the form of a complex number, to capture this phase shift. When the influence of external sensors, actuators, and control and filtering dynamics are considered, the numerator of the mode can be modified to a more general form as well, like as $R_k s + Q_k$. The frequency response of the plant can be constructed by applying $s \rightarrow j\omega$ in the above equation. At present, modal parameter estimation methods based on single and multiple degree-of-freedom systems have been commercialized in modal analysis packages. One such example is the rational fraction (Orthogonal) polynomial (RFOP) method [13] for SISO systems, which is a least-squares based method. This method has been developed into a global method, known as GRFOP, that enables SIMO systems to be successfully identified and modeled as high-order systems [13][14] as well.

Generally speaking, a ball-screw drive can be characterized as a system that possesses axial, rotational, and flexural eigenmodes [15] (see Figure 2.2). The low frequency axial and rotational modes have the most significant effect on the overall response of the mechanism. However, the modes at higher frequencies also have a somewhat smaller contribution, but they can still be excited by, and interact with, the feedback control system. The frequency, damping, and flexibility contributions of the modes can be highly dependent on the mounting conditions. Various discrete and hybrid models have been proposed to gain further understanding of the low-frequency modes. Varanasi and Nayfeh [16] introduced a hybrid modeling approach that observes the axial and rotational modes while ignoring the flexural dynamics. This model uses a distributed beam as the screw itself, based on the Euler-Bernoulli beam element. Other components in the mechanism are represented as lumped mass / spring elements. A different yet comparable study was conducted using a hybrid distributed–lumped model [17]. In another hybrid model introduced by Frey et al. [18], the feed drive was modeled using a combination of continuous (distributed) and lumped (discrete) mass elements. They separated the physical characteristics of the shaft into axial and rotational systems and studied the dominant effects via a simple lumped-mass model. Vicente et al. [19] proposed a model based on the Ritz series that could approximate the continuous field displacement of the ball-screw. Their model was used to predict the first lowest vibration mode. In addition to the axial and rotational modes of the screw, Dong and Tang [20] modeled the flexural dynamics of the screw as a Timoshenko beam.

More complicated models that are capable of capturing structural flexibility have also been proposed in the literature. As a means of structural analysis and optimization, the finite element method (FEM) continues to be an accepted and verified stage of the machine tool design [21]. This is also an efficient tool for capturing the essential dynamics of structures and has been applied for hybrid modeling of ball-screw drives. For instance, Zaeh et al. [21] proposed a FE model of the ball-screw drive system, in which the stiffness matrix between the screw and the nut represents the ball contact interface between these two components. They considered both the lateral and vertical motions of the balls. Their model was successful

in capturing the coupling between the torsional and axial dynamics of the ball-screw drive. Later, Okwudire and Altintas [22] developed a hybrid FE model in which the screw was modeled using Timoshenko beam elements, while the other parts including the table assembly, the coupling, and the motor shaft were modeled as lumped masses. Two advantage of their model was its ability to capture the lateral dynamics of the ball-screw-nut mechanism, in addition to the axial and torsional directions, and its ability to predict the system's response as a function of the table position.

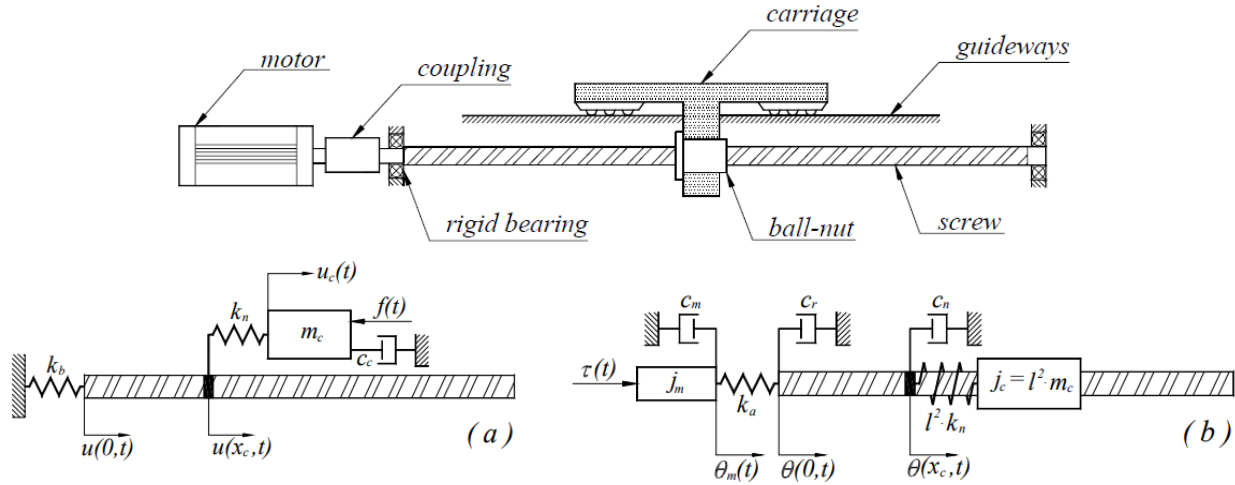


Figure 2.2: Schematic of the axial (a) and rotational (b) decoupled models [15].

2.2.3. Modal Analysis

Additionally to FE modeling, modal analysis is an efficient tool for studying the structural (vibratory) dynamics of feed drives, and it has been widely used in the field of machine tool design and analysis. For a ball-screw drive, modal analysis can reveal parameters that constitute each mode of vibration, such as natural frequency, damping ratio, and the associated mode shapes. Modal analysis is particularly critical from a control point of view, as it enables the vibration modes that can be excited by the actuation from the servo motor to be clearly identified. This, in turn, enables the control law to be designed in a way to avoid unwanted instability that could arise from the interaction of the control algorithm with the structural dynamics.

In addition to axial and torsional directions, vibration modes that run laterally to the feed direction are also critical, since their influence can be detected in the measurement (position feedback) system [23]. The peak-picking algorithm [24] is a simple and widely-used method for estimating modal parameters. In this method, it is recognized that a system's frequency response at the vicinity of a resonance mode is dominated, mainly by the contribution of that specific mode. The effects of the other modes remain

negligible. With this in mind, a system that behaves with multi-degree-of-freedom or, more realistically, a distributed system with infinite degrees of freedom can be treated as a superposition of multiple single-degree-of-freedom mass-spring-damper systems. While peak-picking is intuitively useful and practical, it is not as effective when the vibration modes of a system have close frequencies or when over-damped modes and additional dynamics (e.g., due to filtering) are also captured in the measurement. Figure 2.3 shows the excitation of a lateral vibration mode (i.e. due to the dynamic behavior of the guide system) at 300 Hz in a linear direct driven motion control system. Proper estimation of the modal frequency, damping, and residues allows for resonant dynamics within the bandwidth of the controller to be efficiently attenuated by adequate shaping of the control signal and those beyond the bandwidth to be suitably avoided, through notch or low-pass filtering approaches.

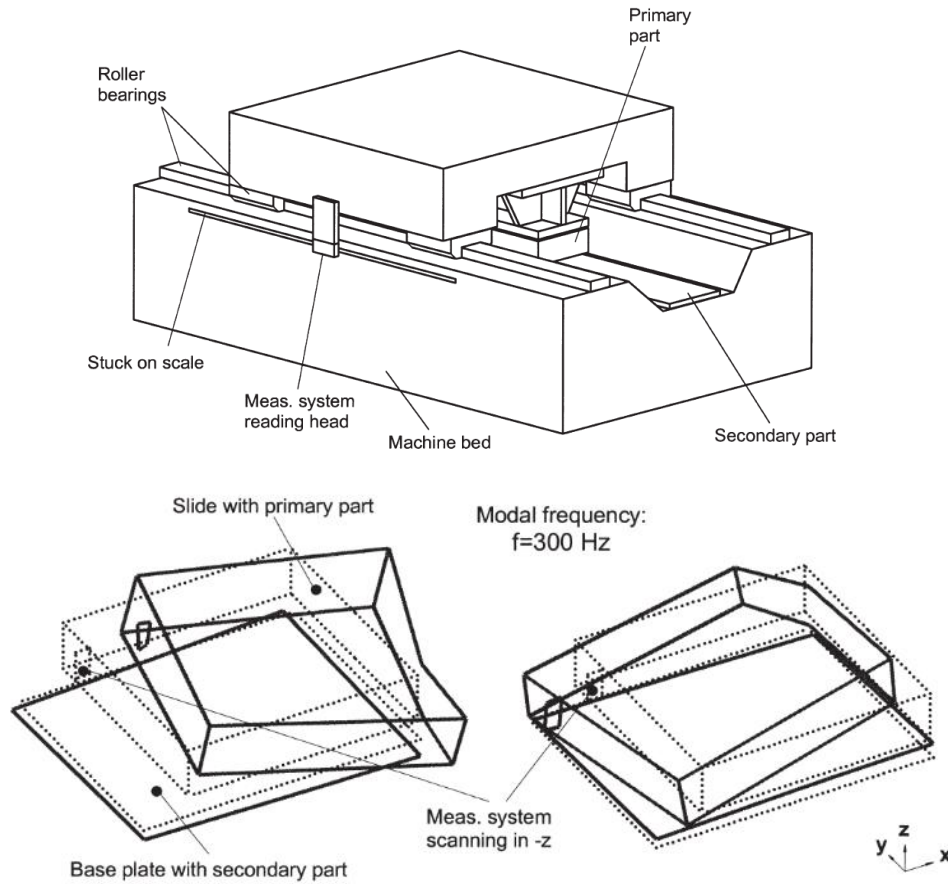


Figure 2.3: Drive system with linear direct drive and mode shape for natural frequency at 300 Hz [23].

2.2.4. Multivariable System Identification

System identification algorithms are widely used as efficient tools for estimating numerical models of dynamic systems from their respective experimental data. In this context, the identification of multi-input

multi-output (MIMO) models for mechatronic motion control systems can play a critical role in enabling more accurate simulation and higher performance control. However, estimating such models is not trivial, especially in the presence of challenging factors, such as high-order dynamics due to structural flexibilities, potential friction effects in the motion delivery mechanism, as well as filtering effects, which may originate from the sensor(s) and actuator(s), due to for example, conditioning circuitry on sensors or limited bandwidth of actuator power modules. The estimation of accurate linear time-invariant models is central to the application of model-based control techniques, such as linear quadratic Gaussian (LQG), and mixed sensitivity \mathcal{H}_2 and \mathcal{H}_∞ control [25].

Among mechatronic motion control systems, feed drives used in machine tools have received particular attention in both modeling and system identification efforts. A variety of first principle based models with different levels of complexity have been surveyed in the previous subsections, to capture the essential dynamics of feed drive systems in machine tools. These approaches assume a physical model and identify the system parameters from the observed data. However, the development of the mathematical descriptions for feed drives and other mechatronic actuation systems requires sophisticated modeling efforts, and the predicted models may often include uncertainties. The discrepancies between an identified model and the system's true response can also cause stability and robustness issues in the implementation of feedback control laws.

Other studies in the field of machine tools have focused on estimating dynamic models of the closed-loop trajectory tracking and disturbance (e.g., friction) response transfer functions directly, using in-process gathered time-domain motion control data [5][6][7][26]. For this purpose, simplified models of the feed drive systems were used, which assumed SISO plants and rigid body dynamics. Recently, Tseng et al. [27] developed a high-order MIMO extension of [26] for application to feed drives, which can capture vibration modes as well as coupling effects between the multiple input and output channels. This method works by matching the candidate models' time domain predictions to the experimental field data. They were able to reconstruct the servo error and acceleration response of a feed drive system, with a mechanical flexibility, achieving 2-3% RMS accuracy. In another effort to identify the feed drive models, an automated identification method was proposed by Kehne et al. [28] again targeting machine tool servo systems. They used a rational fraction polynomial [13] to estimate the total transfer function, considering a single-input single-output (SISO) ball-screw drive model, followed by solving an optimization problem.

General multi-input multi-output (MIMO) transfer function estimation methods such as `tfest` and `modalfit` functions in MATLAB [29][30][31] are capable of constructing models using measured MIMO frequency response data.

In the case of `tfest`, Sanathanan-Koerner (SK) [32] and Instrumental Variable (IV) [33] iterations are applied with orthonormal rational basis functions (OVF). The number of poles are specified and the number of zeros are determined automatically by the function. The numbers of zeros, input/output delays, and other estimation options (e.g., objective function, handling of initial conditions, numerical search method, etc.) can also be specified if needed [34]. However, achieving the commonality of pole locations, across multiple output-input channels, does not seem to be guaranteed. This can lead to shortcomings when working with multi-channel data, as pole (i.e., eigenvalue) commonality is an expected result of first-principles LTI modeling for mechatronic systems. This capability is captured with the methodology proposed in this thesis. Other algorithms in the `tfest` function that can be applied to initialize the values for the numerator and denominator of the estimated transfer functions are State Variable Filters ‘`svf`’, Generalized Poisson Moment Functions ‘`gpmf`’, Subspace state-space estimation ‘`n4sid`’ and the combination of all of the previous approaches using ‘`all`’.

Another commonly available solution is the `modalfit` function as a modal parameter estimation tool in the frequency-domain. It can be used to identify SISO or MIMO models. The number of structural resonances can be entered as an input, or selected by using the `modalsd` function, which generates a stability diagram for modal analysis using the least-squares complex exponential (LSCE) algorithm [24]. The `modalfit` function provides the option of using the peak-picking (PP) algorithm [24], the least-squares complex exponential (LSCE), as well as the least-squares rational function (LSRF) estimation method for modal parameter estimation [24]. Peak-picking assumes that each significant peak in the frequency-response function corresponds to precisely one natural mode (i.e., 2nd order transfer function), while the least-squares complex exponential method considers the impulse response of each pair of complex conjugate poles. In the LSRF and LSCE methods, the natural frequencies and damping ratios of several modes are analyzed simultaneously, and the parameters are estimated to obtain a ‘global fit’ across a broad frequency range.

The methods provided within the `modalfit` function work well in modeling frequency responses composed of the superposition of multiple lightly damped modes, which is applicable mainly to linear elastic mechanical structures. However, it has been observed as reported in Section 4.6, that these methods are not as effective in capturing models with additional poles which possess high damping ratio and which exhibit non-resonant behavior.

Upon surveying and testing `tfest` and `modalfit`, it was observed that the effectiveness of their corresponding system identification algorithms can diminish when attempting to construct multivariable models to MIMO frequency response data which originate from mechatronic systems containing a

combination of lightly and highly damped poles. This has been the principal motivation behind the algorithm developed in Chapter 4 of this thesis.

2.3. Friction Identification and Compensation

Friction is inevitable and exists in almost all motion control systems with mechanical contact. It is considered one of the major disturbances that affect a ball-screw drive's tracking performance, and it can produce undesired effects such as stick-slip and hysteresis. Friction consists of two main regimes, namely, the pre-sliding regime and the sliding regime. In the pre-sliding regime, the friction force is dominantly dependent on displacement. During sliding, it displays a dependency on velocity rather than displacement [35].

The Coulomb friction model, which is a simplified quantification of frictional force, has evolved into more sophisticated friction models. Static friction models comprising Coulomb, viscous, and Stribeck type effects are static maps that describe the relationship between frictional force and the relative velocity between two sliding surfaces. Such a model would only describe the behavior of friction during the sliding regime. One of the earliest attempts to describe the characteristics of friction in the pre-sliding regime was the Dahl model [36], which was proposed in the late 1960s. The Dahl model was further developed and refined by subsequent efforts, such as the LuGre friction model [37], which generalizes Dahl's model to capture the Stribeck effect and stick-slip motion.

Furthermore, Swevers et al. [38][39] proposed a more elaborate model, called the Leuven model, which includes the frictional properties of the LuGre model and an accurate description of the pre-sliding regime using a hysteresis function with non-local memory. Building on these earlier works, the generalized Maxwell-slip (GMS) model [35] was developed, which is one of the most recent dynamic models that best captures, both, the pre-sliding and sliding dynamics of friction. This model is essentially a hybrid of the LuGre model and the Maxwell-slip model that was used in the Leuven model. The GMS model is essentially made up of N -elementary slip-blocks and spring elements. Hence, GMS captures both the hysteresis effect and frictional memory observed during the pre-sliding phenomenon (i.e., when an element is in sticking state). It also captures the Stribeck-type velocity-dependent properties, when an element is over-stretched and transitions into the slipping state. Jamaludin [40] highlighted GMS model's effectiveness by using a GMS based feed-forward compensation to counteract the friction in an x-y cross-feed table. In this and other works [41][42], it has been shown that the nonlinear friction encountered in a ball-screw mechanism arises due to the Stribeck effect and rolling friction. Moreover, the static friction that exists in the interface between the screw and the nut deteriorates the circular contouring accuracy when a feed drive reverses velocity direction (e.g., at circular arc quadrants), and also when motion is first initiated from standstill. In

order to achieve better tracking performance, it is important to accurately identify and compensate for the friction in a feed drive.

The correct application of dynamic friction compensation reduces the large spikes normally seen in the instantaneous dynamic positioning error when the motion is initiated or terminated or at velocity reversal points. Figure 2.4 shows the schematic of the Maxwell-slip model with N-elementary components.

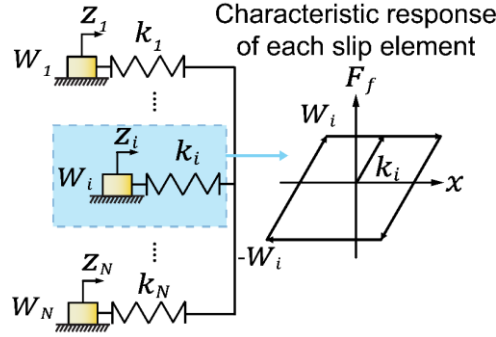


Figure 2.4: Schematic of the Maxwell-slip model with N-elementary blocks.

In the GMS model, the friction force can be described as a function of the position x , the velocity v of the moving part, and the average deflection of bristles that is denoted as the state variable z .

$$F_f = \mathcal{F}(z, v, x) \quad (2.3)$$

The dynamics of the internal state vector z can be described by the following differential equation.

$$\frac{dz}{dt} = \mathcal{G}(z, v, x) \quad (2.4)$$

Above $\mathcal{F}(\cdot)$ and $\mathcal{G}(\cdot)$ are general nonlinear functions. The sticking force in presliding is described by a spring element with stiffness k_i .

$$\frac{dF_i}{dt} = k_i v \quad (2.5)$$

Then, the following static model describes the steady-state behavior of the friction in sliding regime collectively when all elements are sliding.

$$S(v) = \text{sgn}(v) \left(F_c + (F_s - F_c) e^{-\left| \frac{v}{|v_s|} \right|^\delta} \right) \quad (2.6)$$

In Eq. (2.5) F_i is the elementary friction force. When each elementary force component F_i reaches a maximum value of $W_i = \alpha_i S(v)$ where $S(v)$ is the Stribeck friction and α_i is the saturation limit (for each element), that element enters slipping regime. The static and the Coloumb friction forces are denoted by F_s and F_c in Eq. (2.6). V_s and δ represent the Stribeck velocity and velocity shape factor. The following equation describes the dynamic behavior of an elementary slip-block:

$$\frac{dF_i}{dt} = \text{sign}(v) \cdot C \cdot \left(\alpha_i - \frac{F_i}{S(v)} \right) \quad (2.7)$$

The factor C in Eq. (2.7) shows the rate at which the friction force follows the Stribeck effect in the sliding regime. The total friction force can be stated as the summation of all the elementary components and the visous term σ .

$$F_f = \sum_{i=1}^N F_i(t) + \sigma v(t) \quad (2.8)$$

The influence of friction on the frequency response of servo systems has also been studied by Yoon and Trumper [43][44]. They developed a parameter identification method for the GMS friction model using frequency-domain measurements. They showed that as the input amplitude of the applied signal becomes smaller, the response has a smaller DC gain and the frequency of Dahl resonance becomes higher.

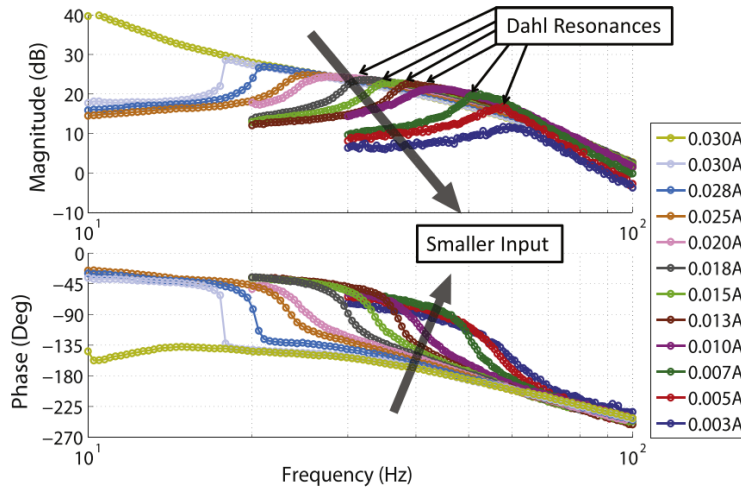


Figure 2.5: Input-amplitude-dependent frequency responses of the open-loop servo system with Dahl resonances [44].

2.4. Control for Precision Motion and Active Vibration Damping

Precision control and active vibration damping of flexible structures have been the focus of many studies on devices such as servo drives [45][46], hard disk drives [47][48][49], flexible robotic manipulators [50][51], and smart structures [52]. Many control techniques have been proposed to tackle this issue, including sliding mode control (SMC) and nonlinear methods [53], model predictive control (MPC) [54][55][56], positive position feedback [57], input shaping[58], and integral-based controllers [59].

As mentioned earlier, one of the main challenges in high-speed high-accuracy positioning of the ball-screw drive is the excitation of structural modes, by both external disturbances as well as the control input. The excitation of structural vibrations deteriorates the tracking performance and imposes limitations on the achievable bandwidth. Moreover, the unmodeled modes can interact with the reduced-order controller and can cause unstable behavior [60]. Hence, in order to achieve a wide bandwidth for the closed-loop system, stability issues originating from the interaction of a flexible ball-screw drive with the control law dynamics have to be resolved. When a vibration mode is not explicitly controlled or damped via feedback, the application of notch or low-pass filters can also be used to avoid exciting these modes, which may otherwise lead to instability. However, the addition of notch filters can further reduce the phase margin due to the notch filter's phase loss before its blocking frequency, and this can consequently affect a control system's overall robustness. Hence, good design is a trade-off between choosing the vibratory dynamics that are actively damped, and those that are suppressed, i.e., ignored.

In addition to actively damping out vibrations, the avoidance of vibration modes due to command generation must also be considered. Recently, extending the 'input shaping' concept that was earlier proposed for single-axis systems, Altintas and Khoshdarregi [61] presented a vibration avoidance and contouring error compensation algorithm that uses input-shaping filters on the commanded trajectory. They pre-compensated for the estimated contouring error from the closed-loop transfer function of the drive and the kinematics of the machine.

One of the critical physical restrictions in achieving successful active suppression of vibrations in flexible structures, such as machine tools, is the excitation of counter-phase modes (see Figure 2.6). The destabilization of counter modes prevents further improvement in the dynamic response of the system via use of loop shaping principles alone. Beudaert et al. [62] showed this could be seen as a significant limiting factor in the damping of chatter vibrations, which are caused by the interaction of the dynamic compliance with the cutting force process dynamics. Recently, they developed a tuning procedure for feed drive control that considers machine dynamics and chatter stability [63]. They reported up to 30% increase in productivity as a result of the new tuning technique.

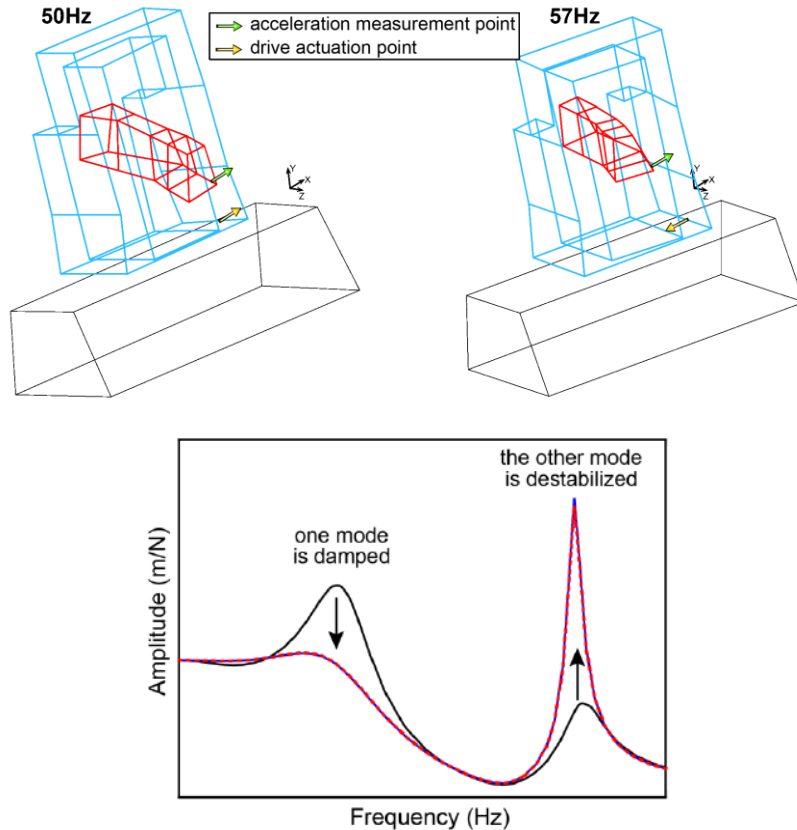


Figure 2.6: Excitation of the counter-phase mode in a vertical ram-type machining center [62].

They also showed limitations related to technical implementation, such as low sampling rate that causes significant phase lag, and noise issues can result in unsuccessful damping of the vibration modes.

2.4.1. Sliding Mode Control (SMC)

Sliding mode control (SMC) [53] is one of the most frequently studied approaches for vibration control in flexible systems, as its robustness helps provide stability in the presence of disturbances and parameter variations. The original sliding mode controller proposed by Utkin [53] has several drawbacks, most notably the high control authority (i.e., effort) and chattering issues. Chattering is undesirable since it involves high control activity at high frequency, and may excite the plant's high-frequency dynamics that have not been considered in the model. The concept of using 'sliding modes' was further developed by Slotine and Li [64] into an adaptive framework, in an attempt to address both the control signal continuity issue and provide the capability of tracking changing system parameters. SMC has been proposed for the control of ball-screw drives. Altintas and Erkorkmaz [65] used an adaptive sliding mode controller (ASMC) for high-speed positioning considering a rigid body model and disturbance force variations. Kamalzadeh

and Erkorkmaz [66] proposed a high-bandwidth ASMC and through experimental compensation of the first axial vibration mode (~133 Hz). This controller also incorporated feedforward compensation of friction, lead errors, as well as notch filtering of higher-order (torsional vibration) modes at 445, 1080, and 1755 Hz.

Okwudire and Altintas [67] proposed discrete-time adaptive sliding mode controller (DADSC) to compensate for vibration modes in ball-screw-driven and linear drives by using a MIMO model and by decoupling the disturbance estimation from the tracking performance. A mode-compensating adaptive back-stepping sliding-mode controller was proposed by Dong and Tang [12], who used a two-mass model to actively dampen out the first mode. They estimated the time-varying uncertainties and disturbances using a finite-term Fourier series. Hosseinabadi and Altintas [68] used a high-bandwidth active-vibration damping controller for CNC machine tools based on sliding-mode control with a damping network. They used a Kalman filter to minimize the noise in the estimation of acceleration and velocity from the encoder signals.

2.4.2. Pole-Placement Control

Pole-placement is a well-known technique for placing closed-loop system poles at desired locations in the s -plane by using appropriate feedback gains to achieve desired performance [69]. The state feedback gain of the pole-placement controller can be calculated using Ackerman's formula. A robust version of the pole-placement controller that is less sensitive to perturbations was proposed by Kautsky et al. [70]. The successful implementation of the pole-placement method for damping vibration in ball-screw drives has been reported by Erkorkmaz and Hosseinkhani [71]. They were able to use disturbance response optimization, in conjunction with pole-placement and loop shaping principles, to minimize the load (table) side disturbance response against cutting forces, and compensate for the phase delay caused by the power electronics using a lead filter (see Figure 2.7). In a precursor study, Gordon and Erkorkmaz [72] presented an active vibration damping by means of pole-placement, which was able to achieve higher bandwidth than the P-PI position-velocity cascade control approach, commonly used in industry. They also introduced a new pre-filtering technique to counteract the artefacts in the tracking error, which are correlated to the velocity, acceleration, jerk, and snap of the commanded trajectory due to existing imperfections in the control law discretization and open-loop dynamics inversion.

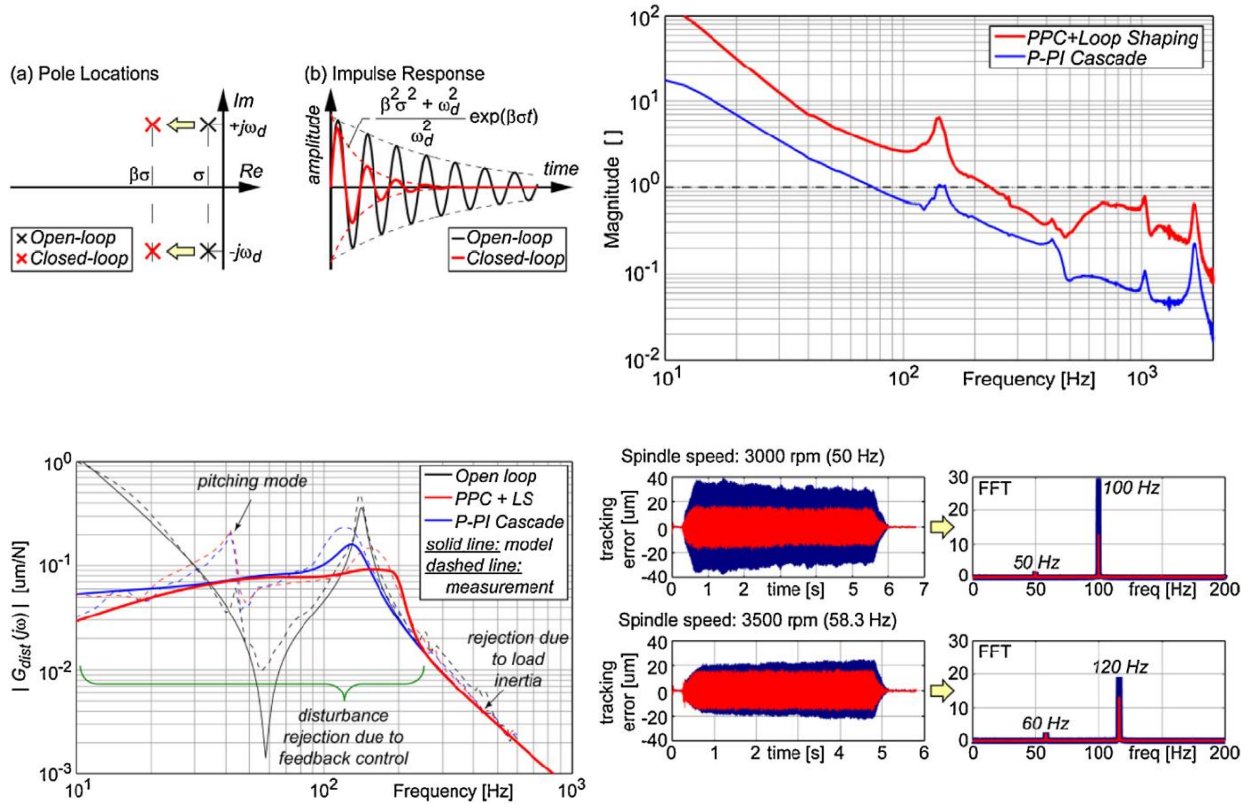


Figure 2.7: PPC versus P-PI [71]. Top left: Concept of damping via pole shifting. Top right: Loop transfer function gain comparison between mode-compensating PPC and P-PI. Bottom left: Optimization of table side cutting force response in PPC. Bottom right: Improvement in disturbance rejection during machining tests.

Hosseinkhani [73] proposed a pole-placement controller for multiple-mode vibration damping. Figure 2.8 shows the schematic of this design. In this approach, several vibration modes are modeled in modal coordinates, in addition to the rigid-body response. The controller uses a Kalman filter for estimating the unmeasurable states. Following the concept of low-authority vibration damping, the amount of leftward shift to be applied to each complex pole pair determines the extra damping to be injected at each mode. The integrated table position x_2 is also used as a state to ensure that the control law eliminates steady-state positioning at the load side. In an attempt to improve co-prime factorization stability, Glover–McFarlane loop shaping robustification was also incorporated [74].

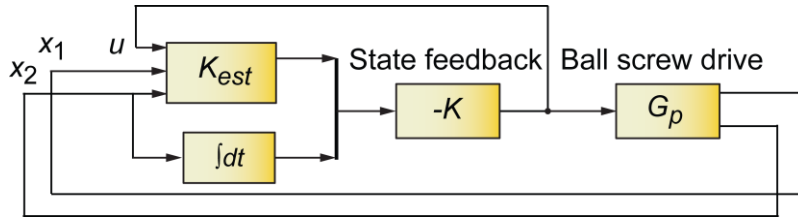


Figure 2.8: Multi-mode Pole Placement Controller (PPC) with a Kalman Filter observer [73].

This resulted in the oscillatory poles (whose locations were set during the pole placement step) to move back closer towards the imaginary axis and the ineffectiveness of the disturbance rejection controller. While this approach seems promising in simulation, its experimental implementation had suffered from several challenges. First, decoupled design of the state observer and feedback controller are required, which is not easy. Second, the selection of independent damping factors for each conjugate pole pair is not a trivial choice. Thus, due to the multitude of design choices, and difficulty in obtaining stable experimental implementation (which may have been related to the design choices) the multi-mode pole placement damping is theoretically interesting, but was found to be very difficult to implement experimentally.

2.4.3. Linear Quadratic Gaussian (LQG) Control

A linear quadratic Gaussian controller is a basic optimal controller used for linear and nonlinear systems with different applications, for example, in servo systems [75], flight and missile navigation control systems [76][77], and vibration (structural) control [78][79]. The controller is named as such because it is linear, the performance index or the cost is in quadratic form, and the disturbance signals and noise are assumed to be driven by Gaussian white noise.

Sencer et al. [80] proposed an optimal control design for high-speed feed drive systems based on a linear quadratic regulator (LQR) that uses load side feedback measurements to actively dampen the first vibration mode of the structure. In their state-space representation, they used an additional integral state similar to [73]. The addition of the integral term results in better low-frequency disturbance rejection on the load side by enforcing integral action. They also proposed a kinematic state observer design to fuse analog accelerometer measurements with linear encoder feedback to achieve high-fidelity state feedback and wide bandwidth non-collocated motion control [81]. This approach uses a ‘jerk’ feedback, in correspondence to a 4th order system, in damping vibrations of a single mode. However, its extension to feed drives with multiple vibration modes is not clear.

2.4.4. $\mathcal{H}_2/\mathcal{H}_\infty$ Control

The $\mathcal{H}_2/\mathcal{H}_\infty$ control was proposed in the 1980s to overcome the robustness issues associated with LQG control [82], as there are no guaranteed stability margins for LQG-controlled systems that incorporate both a Kalman filter and the LQR control law. One major drawback of the LQG controller is that the assumption of Gaussian white noise as an additional input to the system to represent uncertainty cannot always be considered valid. In contrast to the measurement noise, parametric uncertainty cannot be described using this assumption. Another main issue is that the parametric uncertainty between the input and output mapping of a dynamic system cannot always be described with extra state or output perturbations. This is due to the fact that the discrepancy in output, between the modeled and true plant, may in many cases be a function of the size of the applied input [83].

Several control designs that utilize this technique have been proposed for machine tool feed drives [84][85]. Braembussche et al. [86] used a scheme based on \mathcal{H}_∞ control for a linear motor and compared the robustness of the tracking performance with a discrete sliding mode controller for load (inertia) changes of up to 300%. Their results showed that the \mathcal{H}_∞ controller with standard weighting functions did not offer as robust a performance as SMC. To overcome this drawback, they proposed a new performance weighting function that was inspired by SMC. Dong et al. [87] used a gain-scheduled \mathcal{H}_∞ loop-shaping controller for the high-speed positioning of ball-screw drives. They also achieved vibration damping for the first axial mode in order to widen the controller bandwidth. Hanifzadegan and Nagamune [88] proposed a parallel-structure feedback controller for ball-screw drives that consists of both a tracking and structural vibration controller. The tracking and structural controller designs were based on gain scheduling adjacent \mathcal{H}_∞ designs. They demonstrated this approach's advantages over a conventional PID controller by incorporating vibration damping for the first flexible mode and reducing the effect of resonance mode. They also proposed a switching gain-scheduled control design for ball-screw drives [89] that can decrease the effect of 1st vibration mode by 45%. They did not consider vibration damping for higher-order (2nd, 3rd, etc.) modes. In their study, they used the linear parameter varying (LPV) framework to identify and compensate for dynamic model variations in the feed drive system, as a result of posture (i.e., displacement).

In the design of mixed sensitivity $\mathcal{H}_2/\mathcal{H}_\infty$ control laws, the selection of the sensitivity (i.e., performance) weighting function can have a significant impact on the achieved closed-loop response. While mainstream designs in literature typically employ weighting functions in the structure of a low-pass, band-pass, or high-pass filters, using a more targeted approach, such as directly employing the open-loop disturbance response of a mechanical system with flexibility, can help to achieve even more effective damping of structural vibrations as well as improved rejection of external disturbance forces. This concept

was explored in a master's thesis by Zeng [90] for damping the vibrations of fixed structures, such as rams, columns, and plate/shell type workpieces. In this thesis, as shown in Chapter 5, the application of targeted sensitivity weighting has been extended to the motion control (i.e., servo drive) problem, and successfully demonstrated for multiple mode vibration damping in a ball screw drive.

2.5. Suppression of Harmonic Positioning Errors using Adaptive Feedforward Cancellation (AFC)

As mentioned earlier, ball-screw drives provide a low cost means of achieving precision motion delivery in machine tools and various industrial automation applications. However, since their operation relies on mechanical contact, imperfections in the mating components as well as assembly errors can result in the deterioration of the achievable dynamic positioning accuracy. For example, inconsistencies in the helix angle of the screw, as well as alignment errors in the assembly of the mechanism, can cause harmonic positioning errors, commonly referred to as 'lead errors'. During high traversal speeds, imperfections in the groove of the threads can cause change in the effective lead over the length of the screw shaft. This consequently results in inaccurate and oscillatory motion. These errors are difficult to correct using classical feedback techniques, especially when the frequency of the error harmonics is close to or beyond that of the closed-loop bandwidth. Although model-based feedforward approaches are available for correction purposes [8], such compensation techniques may become ineffective when there are variations in the error characteristics, for example a change in the lead error profile due to thermal deformations or wear on the ball-screw.

Disturbances that are harmonic in nature, such as cutting force components in milling operations, can also contribute to repetitive positioning errors. The frequency of the first few harmonics in milling is typically beyond the closed-loop bandwidth of the servo control system. Thus, the feedback controller would be able to reduce the average value of the positioning error caused by the disturbance, but would be unable to compensate for the high-frequency oscillatory components. The ability to counteract these harmonics would undoubtedly improve the dynamic positioning accuracy of a drive system, and may also help improve the surface quality in manufactured parts [91].

The problem of harmonic disturbance cancellation is encountered in a multitude of engineering applications, ranging from noise control to precision mechatronic devices. Example applications include accuracy improvement in fast tool servos [46][92][93][94], hard disk drives [95][96], and robotic manipulators [97]. Due to its wide application range, there have been a number of solutions proposed for counteracting harmonic disturbances. Among them are the Internal Model Principle (IMP), Repetitive Control (RC), and Adaptive Feedforward Cancellation (AFC). IMP states that in order to asymptotically

reject an external disturbance [98], the controller must include a model of this disturbance. This is also the main idea behind the design of Repetitive Controllers (RC) [99][100]. In both IMP and RC, the controller gain is infinite at the frequency of the disturbance, as the controller has a pair of poles on the imaginary axis corresponding to that frequency. In these methods it is assumed that the fundamental disturbance frequency is known and not varying. Successful application of RC in mitigating the detrimental effects of harmonic cutting forces is reported in [91][101]. In [91], a vertical CNC machine is retrofitted with a dynamometer and a piezoelectric actuator. The dynamometer measures the component of the cutting force in the direction normal to the feed direction, while RC regulates this force by manipulating the radial depth of cut through the piezoelectric actuator. It was shown that this strategy is effective in improving the surface finish of the machined part, by reducing the magnitude of fluctuations in the cutting force. In comparison to the method in [91], the RC strategy proposed in [101] does not require additional hardware, such as a dynamometer or piezoelectric actuator, and acts directly upon the position error of the feed drive system. In this regard, it carries some similarity with the experimental approach that will be presented in this thesis. However, in this thesis, Adaptive Feedforward Cancellation (AFC) is proposed for harmonic error mitigation in ball-screw drives. AFC offers more flexibility and convenience in targeting specific harmonics with known frequency, compared to dealing with the design of a stable repetitive controller. Just as a feedback controller with integral action is theoretically able to apply unbounded input at zero frequency, which helps achieve zero steady state error at DC, AFC is able to apply unbounded input at a nonzero frequency ω_n , which helps remove the error component caused by a sinusoidal reference or disturbance input acting at this corresponding frequency [102].

Adaptive feedforward cancellation (AFC) [103][104] is a type of repetitive control that significantly improves periodic disturbance rejection, by injecting sinusoidal correction signals into a closed-loop system to cancel out harmonic components observed in the error signal. Although AFC, in general, can lead to a nonlinear compensator, it assumes the form of a linear time invariant (LTI) filter when the disturbance frequency is constant [105][106][107]. This makes it possible to use classical loop-shaping and analysis tools in designing an AFC. An extended form of AFC, for improving periodic disturbance rejection with time-varying frequency, was proposed by Guo and Bodson [108]. They showed that for certain adaptation laws, even if the disturbance frequency is time varying, the AFC still produces a linear but time-varying filter.

In [109], to tackle non-periodic disturbances which cannot be handled by the classical AFC method, Yabui et al. proposed an enhanced AFC implementation. They included a damping term in the denominator of the resonator, to ensure that the correction signal dissipates when the harmonic component of the error disappears. Yabui et al. also performed robustness analysis for the feedback system using the Nyquist

criterion [110]. In tuning the AFC resonator gain(s), they considered the implication of AFC on the loop sensitivity function.

Many of the earlier works on AFC focused on SISO (single-input single-output) plant configurations. However, ball-screw mechanisms usually have multiple output measurements. Typically, a rotational encoder mounted on the motor shaft provides feedback for velocity control, and a linear (translational) encoder scale mounted on the moving table provides sensing for the position control loop. Naturally, the dynamic response registered from each of these measurement points is different. Therefore, adequate implementation of AFC with a ball-screw drive requires consideration of the dual feedback dynamics, as reported by Hosseinkhani and Erkorkmaz in [111], which presents early results.

In this thesis, the earlier study in [111] has been systematically extended into a unified analysis considering the MIMO nature of ball-screw drives, and in a manner in which the impact of AFC on the response to different perturbation inputs can be analyzed with the help of a single frequency-dependent parameter (i.e., the response modification factor: α). The resulting work, also contained in Chapter 6 of this thesis, has been published in [112]. To the best of the authors' knowledge, this is the first time in which a systematic design procedure for AFC in conjunction with a ball-screw drive as a multi-output plant has been presented in literature.

2.5.1. Brief Review of AFC

In this section, a brief review of AFC is presented, in order to provide foundation to the developed new methodology and results in Chapter 6.

Figure 2.9a shows the typical integration of AFC within a feedback control loop. Here, $A = A(s)$ represents the AFC filter, K the feedback controller, and G the open loop plant (*for notation brevity, the Laplace and z-domain operators, i.e., s and z accompanying a transfer function or a signal name are omitted*). The AFC generates the cancellation signal c , which is injected back into the control loop on top of the regulation error e . The resulting signal is then applied to the feedback controller K . Figure 2.9b shows an alternate block diagram representation, which produces the same closed-loop dynamics as in Figure 2.9a (i.e., $x/r = [GK(1 + A)]/[1 + GK(1 + A)]$). As can be seen in Figure 2.9b, the correction signal c essentially perturbs the original command r , thus producing the modified command r^* . The modified command can then be considered to be fed into the original feedback control system (without AFC), which possesses the dynamics $x/r^* = GK/(1 + GK)$. Consequently, in tuning the AFC, the equivalent response

from the modified command r^* to the closed loop plant output x needs to be considered, as noted in the loop-shaping procedure outlined by Byl et al. [107]. This procedure relies on the principle that the stability of an LTI system does not depend on the reference input, but is a property of the system dynamics. Therefore, in the stability analysis conducted by inspecting the ‘loop’ transfer function, the influence of the original command input r can be neglected, as shown in Figure 2.9c. Then, the AFC block A and remainder dynamics $GK/(1 + GK)$ form a closed loop. Thus, the loop transfer function to be considered for the final closed-loop system’s stability analysis becomes $L = AGK/(1 + GK)$.

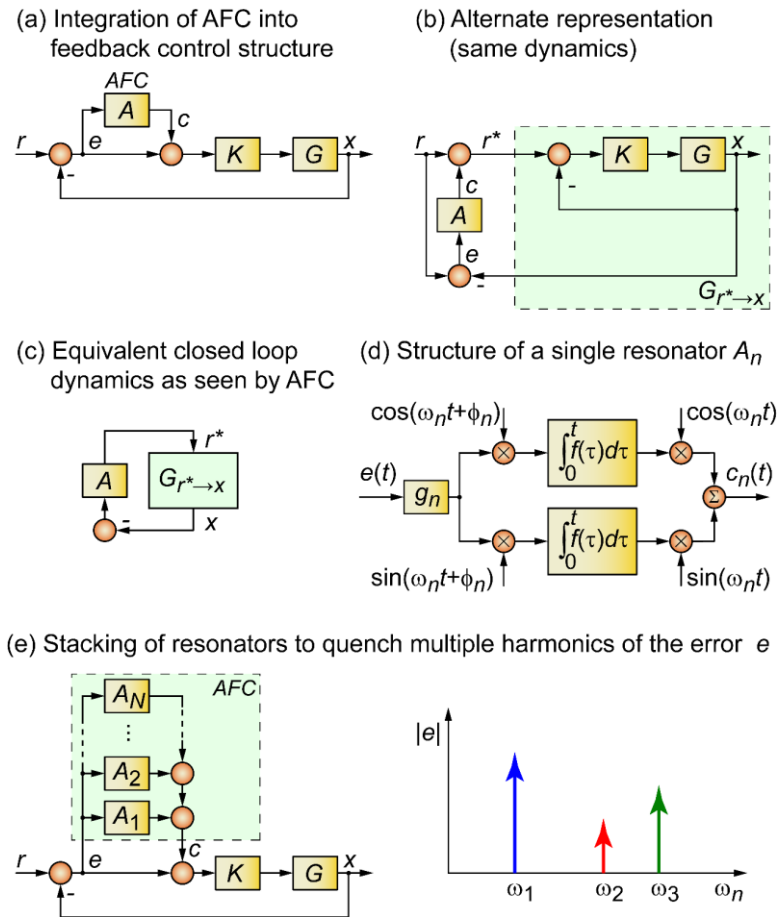


Figure 2.9: Brief review of AFC.

AFC can be comprised of one or more resonators, each designed to target a specific harmonic frequency in the regulation error. The structure of a single resonator $A_n(s)$, with target frequency ω_n , is shown in Figure 2.9d. The equivalence of the implementation in Figure 2.9d to the following LTI dynamics is shown in [107]:

$$A_n(s) = g_n \frac{s \cos \phi_n + \omega_n \sin \phi_n}{s^2 + \omega_n^2} \quad (2.9)$$

Above, g_n and ϕ_n are the constant gain and phase advance of the resonator, which need to be selected adequately to respond with sufficient strength and still preserve closed loop stability with a certain degree of robustness (e.g., stability margins). The implementation of multiple resonators to target multiple frequency components can be seen in Figure 2.9e, where the equivalent AFC transfer function for such a system can be stated as:

$$A(s) = \sum_{n=1}^N A_n(s) \quad (2.10)$$

The frequency response of an AFC resonator can be calculated for different values of ϕ_n (the phase advance parameter) using Eq. (2.9) as shown in Figure 2.10.

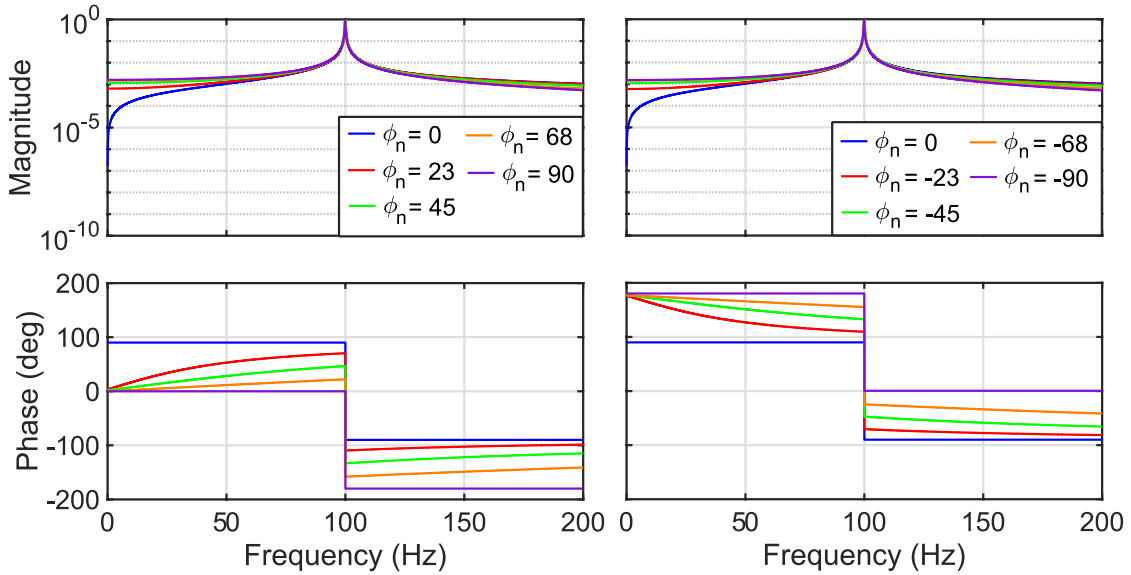


Figure 2.10: Frequency response of an AFC resonator with a pair of complex conjugate poles at 100 Hz for different values of the phase advance parameter.

The phase of an individual resonator changes sharply by -180° in the vicinity of ω_n , due to the absence of a damping factor in the denominator. This phase change is discontinuous, but is centered around the angle of $-\phi_n$ [107]. Considering Figure 2.9c, a given harmonic error component with frequency ω_n permeates through the closed loop response of $G_{r^* \rightarrow x}$ with a phase shift of $\angle G_{r^* \rightarrow x}(j\omega_n)$. If the resonator phase parameter is set to $\phi_n = \angle G_{r^* \rightarrow x}(j\omega_n)$, the AFC's averaged phase around this frequency becomes $-\angle G_{r^* \rightarrow x}(j\omega_n)$. It is important to note that the local gain provided by each resonator around its natural frequency overpowers the gain and phase contribution from the other resonators outside their resonance frequencies. This enables the phase shift of the loop (depicted in Figure 2.9c to be 0° around the resonator's

frequency. In other words, the timing of the cancellation signal is adjusted to take into consideration the phase latency (or lead) of the closed loop dynamics ahead of the injection point. Once this is achieved, the negative feedback realized by closing the loop enables the oscillatory signal to cancel itself out, as it is fed back through the AFC. Hence, following the guideline in [107], for each AFC the phase parameter is set to be $\phi_n = \angle G_{r^* \rightarrow x}(j\omega_n)$.

The final parameter in the AFC that must be set is the resonator gain g_n , which allows the disturbance rejection to be maximized. While the initial loop shaping procedure in [107] considered $L = G_{r^* \rightarrow x} \times A$ as the loop transfer function (Figure 2.9c) in setting the stability margins, a later implementation of AFC for diamond turning fast tool servos took into consideration the structure in Figure 2.9a ($L = GK(1 + A)$) as the loop transfer function [45]. Recalling the definition of $G_{r^* \rightarrow x}$, it can be verified that both analyses lead to the same characteristic equation.

From observation, it is known that higher gain leads to faster cancellation of the harmonic error. However, excessive values for g_n can also lead to problems with stability and loop robustness, which can be identified from the waterbed effect [25], or sensitivity integral. If the sensitivity function ($S = (1 + L)^{-1}$) is decreased in order to improve the disturbance rejection at a target frequency ($|S(j\omega_n)| \ll 1$) by increasing the resonator gain g_n , its magnitude will have to increase at other frequencies. At frequencies where $|S(\omega)| > 1$, the feedback control actually has a deteriorating effect on the closed-loop disturbance rejection, compared to the open-loop case.

In addition to potentially causing performance loss, excessive gain for the AFC can also lead to the excitation of other dynamics outside the target frequency, possibly triggering instability. Furthermore, the robust stability analysis of a multiple resonator structure is more complex than the case of tuning a single resonator at a time, as all resonator gains have to be considered simultaneously. Thus, the analysis and tuning method proposed in this thesis, which revolves around the definition of the ‘response modification factor α ’ (in Section 6.3), allows for the performance improvement versus deterioration to be gauged across the frequency spectrum when adjusting multiple AFC resonators. It also enables a robust stability margin to be maintained, based on an admissible peak sensitivity value.

2.6. Conclusions

The literature review in this chapter constitutes the background knowledge upon which this thesis is built. The literature related to modeling and identification of a feed drive system, using various approaches,

has been discussed. Also, the importance of modal analysis in the structural study of machine tools dynamics was highlighted. Furthermore, some of the static and dynamic friction models for motion control systems were explored. Accordingly, Chapter 3 of this thesis covers the initial modeling and identification for the main experimental setup, a precision ball screw drive. In Chapter 4, a new frequency-domain LTI MIMO model estimation algorithm is introduced, to address the challenge of estimating suitable models for CNC feed drive dynamics. The proposed new method can handle systems involving multiple actuation inputs, sensing outputs, a multitude of vibration modes, as well as a combination other (lightly-damped or well-damped) dynamics, and even direct- or derivative-like terms.

Various tracking and active vibration-damping control methods were reviewed in Section 2.4. Accordingly, in Chapter 5, a new control strategy is proposed to achieve high-bandwidth and superior (load-side) disturbance rejection, through multiple-mode vibration suppression in the inner loop, used alongside a loop-shaping based tracking controller in the outer loop. Finally, adaptive feedforward cancellation (AFC) for counteracting harmonic disturbances was reviewed in Section 2.5. This technique has been extended to match the multiple output nature of ball-screw drives, and a new AFC design method has been developed, capable of simultaneously adjusting multiple resonators while analyzing any potential performance degradation to any input sources (e.g., disturbances, mechanical imperfections, and noise) in a unified manner, as presented in Chapter 6.

Chapter 3

Modeling and Identification of Ball-Screw Driven Feed Drives

3.1. Introduction

Modeling and identification of the feed drive dynamics is a crucial step prior to designing a model-based motion controller. To achieve high motion precision, it is essential to consider nonlinear effects, such as friction, which deteriorates the positioning accuracy, or limitations on the available motor torque, such as drive saturation, due to the drive systems physics. Feed drive models can be constructed using a variety of methods, including a simplified rigid body approach for capturing low-frequency behavior, or more elaborate approaches, which also consider the influence mechanical flexibilities and vibration modes.

This chapter is organized as follows. Section 3.2 presents the experimental setup that was used for a majority of the validation studies in this thesis. Section 3.3 shows the frequency responses of the current loop dynamics, utilizing rotary and linear encoders and a pulse-width modulated (PWM) driver as the actuation system. In Section 3.4, a summary of modeling, and parameter estimation of for current loop dynamics is presented considering a high-bandwidth linear voltage amplifier. The identification of rigid body parameters is reported in Section 3.5. Section 3.6 shows the rotary and linear encoder frequency responses obtained using the linear amplifier for driving the motor. A two-inertia lumped model is used to capture the first axial mode of the feed drive system in Section 3.7. Sections 3.8 and 3.9 present a summary of friction identification for the experimental setup considering both a Stribeck-type model and then a generalized Maxwell slip (GMS) model. The identified models are demonstrated in friction compensation in Section 3.10. To better understand the high-frequency dynamics of the stage, vibration modal analysis was conducted and its results are discussed in Section 3.11. Finally, Section 3.12 covers the conclusions for this chapter.

3.2. Experimental Setup

Figure 3.1 shows the setup, which is a single-axis ball-screw (THK BNK 2020-3.6G0 + 1220 LC5-Y) driven by a 3kW AC servo motor (Omron R88M-K3K030H) permanent magnet synchronous motor (PMSM). The mechanism is a double start screw possessing 20 mm diameter and 20 mm lead (i.e., containing two 10 mm pitch helical grooves). The ball-screw has a simple free mounting arrangement, which is affected by thermal deflection. The screw shaft is attached to the servomotor by double-flex disc-type couplings to eliminate backlash and to tolerate possible misalignments between the screw and rotor shaft. The worktable moves along the two cylindrical guideways, which support four air bushings. As a

small deviation from the photograph in Figure 3.1, the two rotary encoders (Encoders 1 and 2) had been disassembled from the setup prior to the collection of the data.

The rotary encoder integrated into the motor (K3K030H) can generate up to 262144 pulses per rotation, based on quadrature signal output (i.e., Phases A and B, 20-bit resolution). When identification tests were first being conducted, as reported in Section 3.3, the rotary encoder resolution was set to produce 5000 sine waves (of quadrature type) per revolution. However, later on, when designing the current loop commutation, this resolution was reduced to allow sufficient decoding bandwidth in the motion control hardware (dSPACE DS3002 encoder interface) to ensure that encoder pulses can be counted without any loss.

The rotary encoder generates 5000 pulses/rev. Considering $400\times$ interpolation of the sinusoidal encoder signals, this achieves a measurement resolution equivalent to 10 nm to table translation. A linear encoder directly measures the table translation, which has 350 mm stroke length. After adequate interpolation of sinusoidal encoder signals, 10 nm of measurement resolution is obtained.

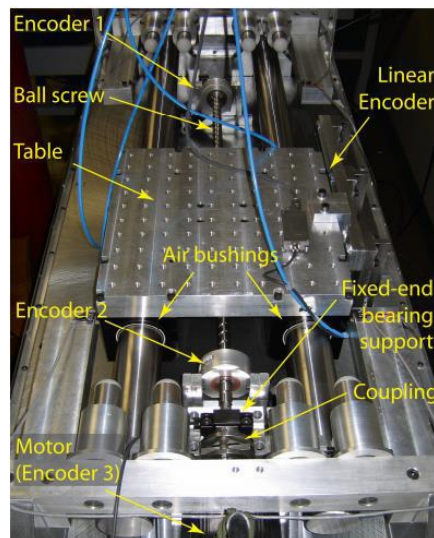


Figure 3.1: Single-axis ball-screw setup.

3.3. Frequency Response Measurements using a PWM Driver

As mentioned earlier, control bandwidth and disturbance suppression are limited by the mechanical resonances, resolution of the feedback device, time delay in the loop, and the current loop response time. To evaluate the achievable bandwidth by the PWM driver (Omron K3K030T), a frequency response measurement was conducted between the analog input voltage of the amplifier (representing the current or

torque command) and the output current, at a sampling frequency of 20 kHz. The torque commands are sent to the servo amplifier by a DS1005 dSPACE platform, as control signals ranging between -10...10 V. The motor torque constant and amplifier gain are 0.41 Nm/A and 2.33 A/V, respectively. Figure 3.2 shows the frequency response of the current loop dynamics generated with a sine-sweep excitation at 8 V and for frequencies between 10 Hz – 1 kHz. As can be seen, the bandwidth of the PWM driver is limited to 388 Hz. At this frequency, the phase margin is around 35°, indicating significant phase loss (-145°). The pure delay was estimated as 0.33 ms, by plotting the phase response on a linear frequency scale Figure 3.2.

In practical applications, the assumption of a perfectly linear system may not always be valid due to nonlinear effects, such as friction, hysteresis (e.g. due to backlash in the preloaded nut in a ball-screw), actuator saturation, etc. In this case, there are two basic options: (1) to obtain an FRF of the underlying linear system, by minimizing the nonlinear phenomena's impact on the response; (2) to try to find the best possible linear approximation of the nonlinear response data [113]. The first option is preferred if a linear model of the system already exists. In contrast, the second option is more applicable if the user wants to most accurately describe a relationship between the input and output, at the expense of losing some contextual or physics-based information about the nonlinearity causes. Different excitation signals have been recommended for addressing this issue [114].

Several methods were developed to visualize the nonlinearity in a system. For a linear system, the response is independent of its input amplitude, whereas, for a nonlinear system, the measured FRF would depend on the input amplitude and for example, the direction of frequency sweeping. For the ball-screw drive, a Gaussian white noise excitation signal was used at four, six, and eight-volt amplitudes to examine the consistency of the system's motion response. Figure 3.3 shows the rotary and linear encoder responses to this excitation. Here, the displacements have been scaled in terms of motor and screw shaft rotation in the unit of radian. Due to the roll-off effect in the current control loop, the accuracy of measurements at frequencies higher than 400 Hz is reduced, and the effect of friction and backlash-like motion loss in the preloaded nut are also dominant. This is because as smaller displacements are generated, static friction cannot always be fully overcome, and the transmission of rotary screw motion to the table displacement does not occur perfectly. Based on this measurement, the observable natural frequencies were, at first glance, identified to be at 135 Hz, 276 Hz, 673 Hz, 1192 Hz, and 1632 Hz. Later, vibration modal analysis carried out in Section 3.11 provides further insight into the mode shapes of some of these frequencies.

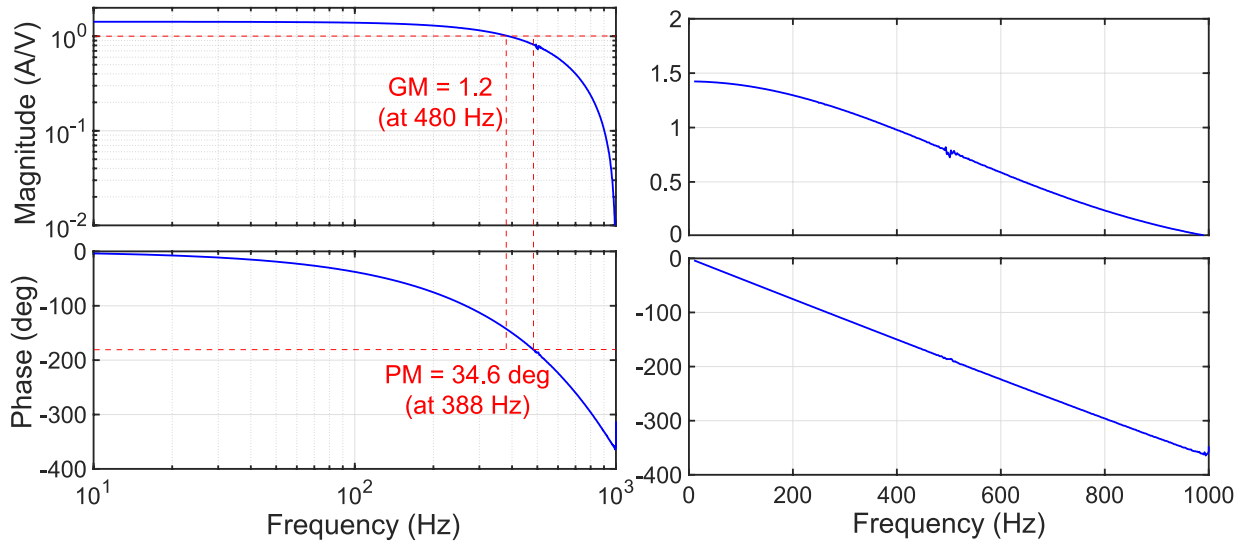


Figure 3.2: Current loop frequency response measurement using the PWM driver in logarithmic (left) and linear scale (right).

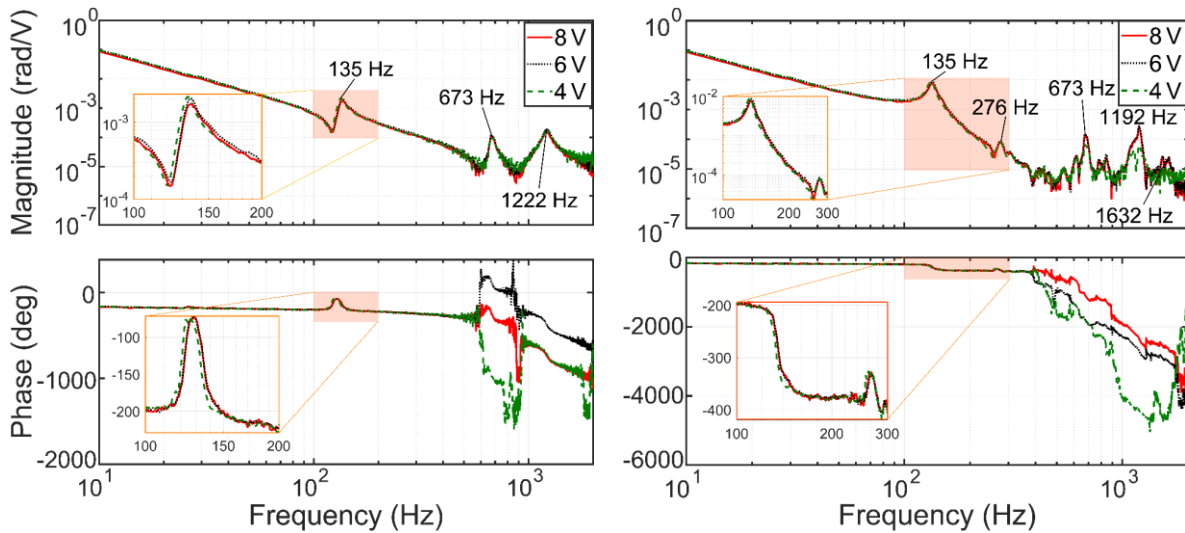


Figure 3.3: Rotary (left) and linear encoder (right) position frequency responses.

3.4. Modeling and Identification of the Current Loop Dynamics upon Retrofitting the Setup with a Linear Amplifier

A high-bandwidth amplifier is required to shorten the transient response time, which can be used to improve the tracking accuracy and disturbance suppression by enabling a higher bandwidth feedback controller design. The main advantage of PWM drivers over linear amplifiers is their transfer efficiency [115], since much less power dissipation has to take place in the electronics, in the form of heat, when in modulating the armature voltage applied to the actuator. However, in spite of their lower efficiency, linear amplifiers can generate smoother motion, lower noise levels, and negligible distortion in the generated

armature voltage, in comparison with PWM drivers. For these reasons, a LA-1555T Varedan linear amplifier was integrated into the experimental setup to achieve higher bandwidth for current control, compared to the existing Omron PWM driver described in Section 3.3. Table 3.1 shows the specifications of the permanent magnet synchronous motor (PMSM) used in the setup, for which the LA-1555T was selected.

Table 3.1: 3-phase PMSM motor specification.

Variable	Description Unit	Value	Unit
L_s	Inductance (direct and quadrature) $L_s = L_d = L_q$	0.004	[H]
R_s	Winding resistance (direct and quadrature) $R_s = R_d = R_q$	0.035	[Ω]
K_t	Torque constant	0.41	[N · m/A]
J_m	Motor inertia	Estimated	[kg · m ²]
Z_p	Number of pole pairs	5	[]
B_m	Viscous friction coefficient of motor	Estimated	[N · s/rad]
λ_0	Back-emf constant	0.19	[V/rad/s]
ω_e	Electrical speed	–	[rad/s]
ω_r	Rotary encoder angular velocity	–	[rad/s]

Some of the most widely used vector control techniques of PMSM are field-oriented control (FOC) [116] and direct torque control (DTC) [117]. FOC is the most adopted vector control method in the industry. In this section, the control of the PMSM using FOC technique is described.

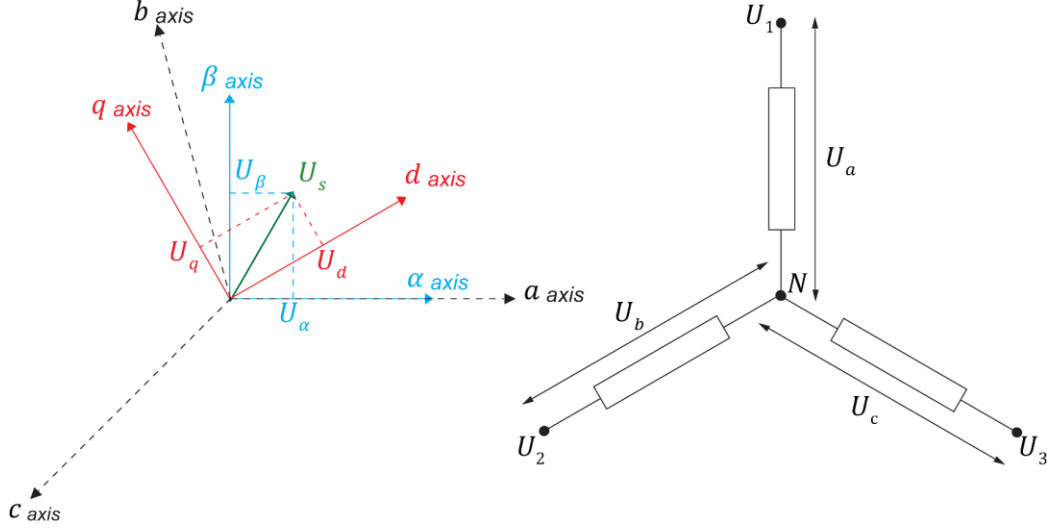


Figure 3.4: Illustration of space vector (abc), stationary ($\alpha - \beta$) and synchronous ($d - q$) reference frames.

In Figure 3.4, abc frame represents the space vector, which has three equally spaced stator windings with a neutral connection in the center. The tip voltages have the following relationship with the space vector components:

$$U_1 - U_a = U_2 - U_b = U_3 - U_c \quad (3.1)$$

This can be stated in the matrix form as follows.

$$\begin{bmatrix} U_a \\ U_b \\ U_c \end{bmatrix} = A_{abc}^{123} = \frac{1}{3} \begin{bmatrix} 2 & -1 & -1 \\ -1 & 2 & -1 \\ -1 & -1 & 2 \end{bmatrix} \begin{bmatrix} U_1 \\ U_2 \\ U_3 \end{bmatrix} \quad (3.2)$$

The transformation between the three phases of variables to their components in the $\alpha - \beta$ frame is done by Clarke transformation as shown below [118].

$$\begin{bmatrix} U_\alpha \\ U_\beta \end{bmatrix} = A_{\alpha\beta}^{abc} = \frac{2}{3} \begin{bmatrix} 1 & -\frac{1}{2} & -\frac{1}{2} \\ 0 & \frac{\sqrt{3}}{2} & -\frac{\sqrt{3}}{2} \end{bmatrix} \begin{bmatrix} U_a \\ U_b \\ U_c \end{bmatrix} \quad (3.3)$$

The transformation of components in the $\alpha\beta$ frame to its components in rotating dq reference frame is achieved by the Park transformation. The voltage relation between the two reference frames is described as.

$$\begin{bmatrix} U_d \\ U_q \end{bmatrix} = A_{dq}^{\alpha\beta} = \begin{bmatrix} \cos \theta_e & \sin \theta_e \\ -\sin \theta_e & \cos \theta_e \end{bmatrix} \begin{bmatrix} U_\alpha \\ U_\beta \end{bmatrix} \quad (3.4)$$

Combining Clarke transformation with Park transformation gives the Park-Clarke transformation from the three-phase values to the rotating dq reference frame, which can be stated by.

$$\begin{bmatrix} U_d \\ U_q \end{bmatrix} = A_{dq}^{abc} = \frac{2}{3} \begin{bmatrix} \cos \theta_e & \cos(\theta_e - \frac{2\pi}{3}) & \cos(\theta_e - \frac{4\pi}{3}) \\ -\sin \theta_e & -\sin(\theta_e - \frac{2\pi}{3}) & -\sin(\theta_e - \frac{4\pi}{3}) \end{bmatrix} \begin{bmatrix} U_a \\ U_b \\ U_c \end{bmatrix} \quad (3.5)$$

The following can represent the complete model of the PMSM.

$$\frac{di_d}{dt} = \frac{1}{L_d} (U_d - R_s i_d + \omega_e L_q i_q) \quad (3.6)$$

$$\frac{di_q}{dt} = \frac{1}{L_q} (U_q - R_s i_q - \omega_e \lambda_0) \quad (3.7)$$

$$\frac{d\omega_e}{dt} = \frac{Z_p}{J_m} \left(\frac{3}{2} Z_p \lambda_0 i_q - \frac{B_m}{Z_p} \omega_e - T_L \right) \quad (3.8)$$

Above i_d, i_q, U_d, U_q are direct and quadrature current and voltages, R_s, L_d, L_q are stator winding resistance and dq axis inductances. ω_e is the electrical angular velocity. Z_p is the number of pole pairs, and λ_0 is the back-emf constant. The inertia and viscous damping of the motor are represented by J_m and B_m respectively and T_L is the load torque. Knowing that $L_d = L_q = L_s$, the electrical characteristic can be represented in the Laplace domain as,

$$G(s) = \frac{i_d(s)}{U_d(s)} = \frac{i_q(s)}{U_q(s)} = \frac{1}{L_s s + R_s} \quad (3.9)$$

The current loop controller is typically a proportional integral (PI) type and can be represented by the following transfer function:

$$G_c(s) = \frac{K_p s + K_i}{s} \quad (3.10)$$

The simplified electrical dynamics with PI controller is shown in Figure 3.5. In the block diagram, the equivalent rotor back electromagnetic force which acts as a disturbance is denoted by U_{emf} . The reference and measured current signals are shown by i_r and i , respectively.

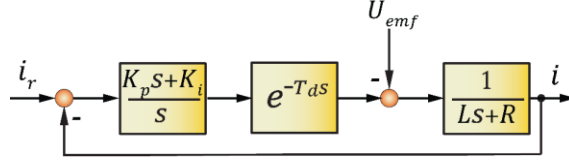


Figure 3.5: Simplified electrical dynamics with PI controller.

The linear amplifier has a low-pass filter with cut-off frequency, which was 30 kHz in the case of the Varedan amplifier. The maximum sampling frequency by dSPACE in the experiments was 30 kHz. As the cut-off of this filter is very high, in PI current control parameter setting, its influence can be neglected.

$$G_{filter}(s) = \frac{\omega_{nf}^2}{s^2 + 2\zeta_f \omega_{nf} s + \omega_{nf}^2} \quad (3.11)$$

By analysis of the block diagram in Figure 3.5, it is expected that a PI-controlled current response will have 2nd order dynamics with natural frequency ω_n and damping ζ . Additionally, there will also be a zero in the numerator, designated with $2\pi f_z$.

$$G(s) = \frac{\omega_n^2}{s^2 + 2\zeta \omega_n s + \omega_n^2} \frac{(s + 2\pi f_z)}{2\pi f_z} = \frac{(\frac{\omega_n^2}{2\pi f_z} s + \omega_n^2)}{s^2 + 2\zeta \omega_n s + \omega_n^2} \quad (3.12)$$

The PI control parameters are correlated to the natural frequency and damping ratio of the system as:

$$\omega_n^2 = \frac{K_i}{L} \rightarrow K_i = L\omega_n^2 \quad (3.13)$$

$$2\zeta \omega_n = \frac{K_p + R}{L} \rightarrow K_p = 2\zeta \omega_n L - R \quad (3.14)$$

Based on the experimental response of the current loop, the transmission zero frequency f_z can be adjusted to better match the observed frequency response function (FRF), thus helping account for the influence of additional or unmodeled dynamics. It is also expected that the measurement may contain a pure constant delay (T_d), which again can be estimated from the frequency response measurement phase graph.

$$G_{delay}(s) \cong e^{-T_d s} \quad (3.15)$$

The delay can also be modeled by a second order Padé approximation, which can be used in performing simulations to corroborate the model with the observed time-domain signals.

$$G_{delay}(s) \cong \frac{1 - \frac{T_d}{2}s + \frac{T_d^2}{12}s^2}{1 + \frac{T_d}{2}s + \frac{T_d^2}{12}s^2} \quad (3.16)$$

The effective quadrature rate from the encoder at maximum translational velocity of the ball-screw is about 52 MHz ($= 262144$ [pulses/rev] $\times 4$ [quadrature edges/pulse] $\times 1000$ [mm/s] $\times 1/20$ [rev/mm]). Such high frequency can cause problems for achieving the commutation control law around the linear amplifier. Moreover, the maximum input analog frequency the dSPACE board (DS3002) can process is 750 kHz. To overcome this issue, the resolution of the encoder was lowered to 2500 pulses/rev, to generate encoder signals at maximum frequency of 500 kHz in the worst-case scenario.

Figure 3.6 shows the overall schematic of the experimental setup, which includes the dSPACE platform, the linear amplifier, the PWM driver, and the permanent magnet synchronous motor. As can be seen from the figure, the PWM driver is only used to decode the rotary encoder data into an analog signal that can be sent to the dSPACE system. The commutation of the PMSM is carried out using the dSPACE and linear amplifier. The two-input sinusoidal command signals are sent to the linear amplifier from the dSPACE. The current sensors on the linear amplifier (LEM-LAH 25-NP) are used as the feedback in the current loop diagram. It is worth noting that this is a synthesized current monitor and does not reflect the full bandwidth of the current signals. This signal shows some quantization, and it is used primarily for diagnostic monitoring. For this reason, additional current transducers (Tamura-LA01P035S05) were added to the experimental setup, to measure the actual current response of the system as shown in Figure 3.6. While in the actual implementation the three phases were measured separately, only two current transducers are sufficient to obtain the current in the third phase.

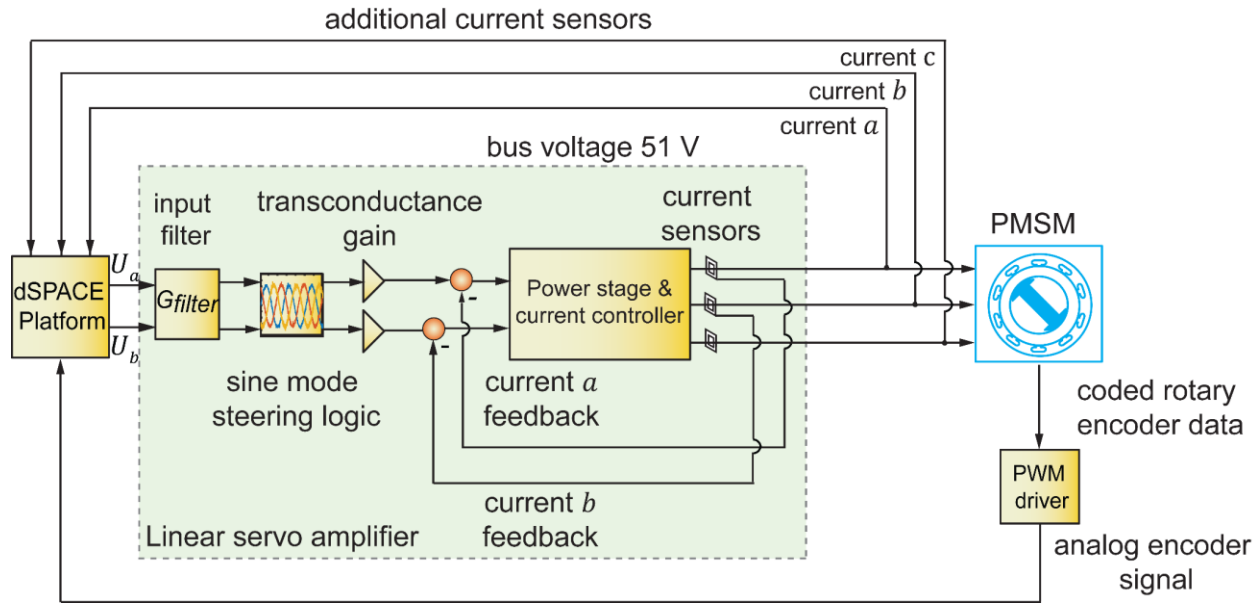


Figure 3.6: Schematic of the current-loop implementation.

The linear amplifier in sinusoidal mode requires an external controller to properly commutate the two-phase current commands for the motor, as low voltage signal U_a, U_b , as shown in Figure 3.6. The third command signal is generated internally in the amplifier. Figure 3.7 shows the block diagram of the current loop with a PI controller and PMSM dynamics. The rotary encoder signal is used for the commutation using the inverse of Park transformation.

Since the encoder is an incremental type, a homing procedure is required to synchronize the electrical angle $\theta_e = Z_p \theta_r$ of the PMSM with the stator phases. This angle is essential to transform the dq frame inputs into the two-phase sine inputs (inverse Park transformation). The z-index pulse of the rotary encoder is obtained by the slow rotation of the rotor using sinusoidal waves with 120-degree phase shifts as inputs in abc -frame. Once the index pulse is generated, the input signal is changed to a constant. Consequently, the rotor locks magnetically and is aligned with the nearest active stator winding. While one winding has a constant current value, the other two have half of this amount in the negative direction. The abrupt change of current value to a constant (i.e., step) causes an oscillation in the position response of the rotor. In the implementation, a stabilization time is considered to let this oscillation dissipate.

The PI control parameters were identified from the servo motor current loop frequency response measurement using the values from Table 3.1 and estimated parameters (inertia and viscous damping).

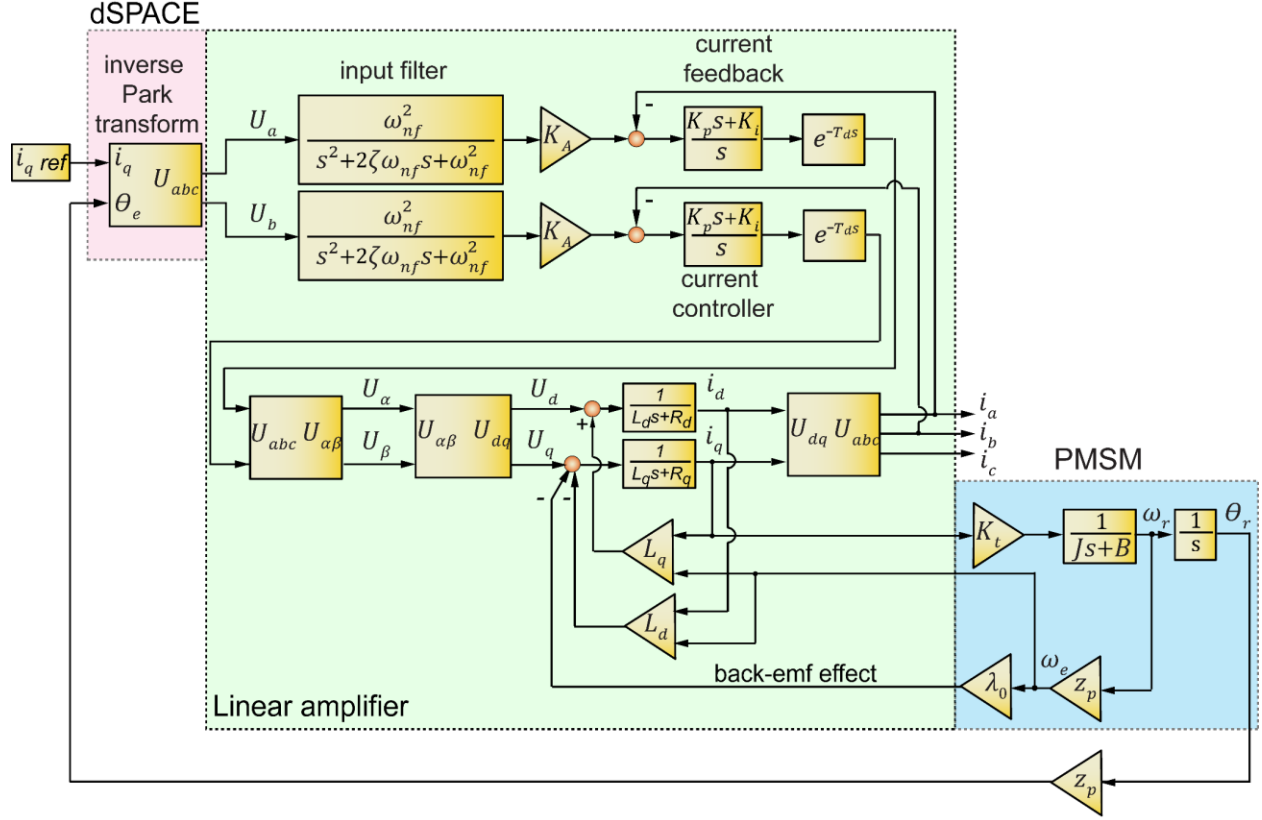


Figure 3.7: Block diagram of the current-loop controller and PMSM dynamics.

The total dynamics of the system includes the effect of the controller, open-loop plant, a second order low-pass filter and the estimated pure constant delay. The measurement was carried out with a sampling frequency of 20 kHz using a band-passed (between 1 Hz -10 kHz) white noise excitation at 0.5 V amplitude. The amplitude of the input signal was chosen sufficiently small so that nonlinear distortion (slew rate limiting) is avoided. Considering the band-limited white noise excitation $x(t)$ as a complex, wide-sense stationary (i.e. its mean and autocorrelation functions are time invariant), random process with the autocorrelation function $R_{xx}(\tau)$, the continuous-time Fourier transform of its autocorrelation function is defined by [119]:

$$P_{xx}(\omega) = \int_{-\infty}^{\infty} R_{xx}(\tau) e^{-j\omega\tau} d\tau \quad (3.17)$$

The power spectral density (PSD) of the output $y(t)$, induced by the input excitation signal $x(t)$ is given by [119]:

$$P_{yy}(\omega) = |H_{xy}(\omega)|^2 P_{xx}(\omega) \quad (3.18)$$

Above, $H_{xy}(\omega)$ is the frequency response measurement for the SISO system in Eq. (3.9). The magnitude-squared coherence is a function of the power spectral densities, $P_{xx}(\omega)$, $P_{yy}(\omega)$, and the cross power spectral density $P_{xy}(\omega) = \int_{-\infty}^{\infty} R_{xy}(\tau)e^{-j\omega\tau}d\tau$ of x and y signals [119]:

$$C_{xy}(\omega) = \frac{|P_{xy}(\omega)|^2}{P_{xx}(\omega)P_{yy}(\omega)}, \quad 0 \leq C_{xy}(j\omega) \leq 1 \quad (3.19)$$

Figure 3.8 shows the measured current loop from DC to 10 kHz with a resolution of 1 Hz (left column) and the magnitude-squared coherence function (right column) of the measurement. In order to enhance the spectral estimation, Welch’s overlapped averaged periodogram method [120] was applied using the `cpsd` command in MATLAB. The measurement data series of ten seconds (for both input and output vectors) was divided into ten frames with 50% overlap. A Hanning window was applied to minimize the leakage effect. The estimated transfer function $G(s)$ (Eq. (3.12)) is overlaid on top of the experimental data. As can be seen, the theoretical transfer function captures the dynamics of the measured current loop up to about 5 kHz. The bandwidth of the current loop controller is significantly higher with the linear amplifier (~ranging between 1.5 ... 5 kHz) compared to using the PWM driver (388 Hz). The measured time delay from the FRF is approximately 0.0394 ms, which is about one-tenth of the delay measured by the PWM driver (0.33 ms). Table 3.2 shows a summary of the current loop identified parameters based on the measured data shown in Figure 3.8.

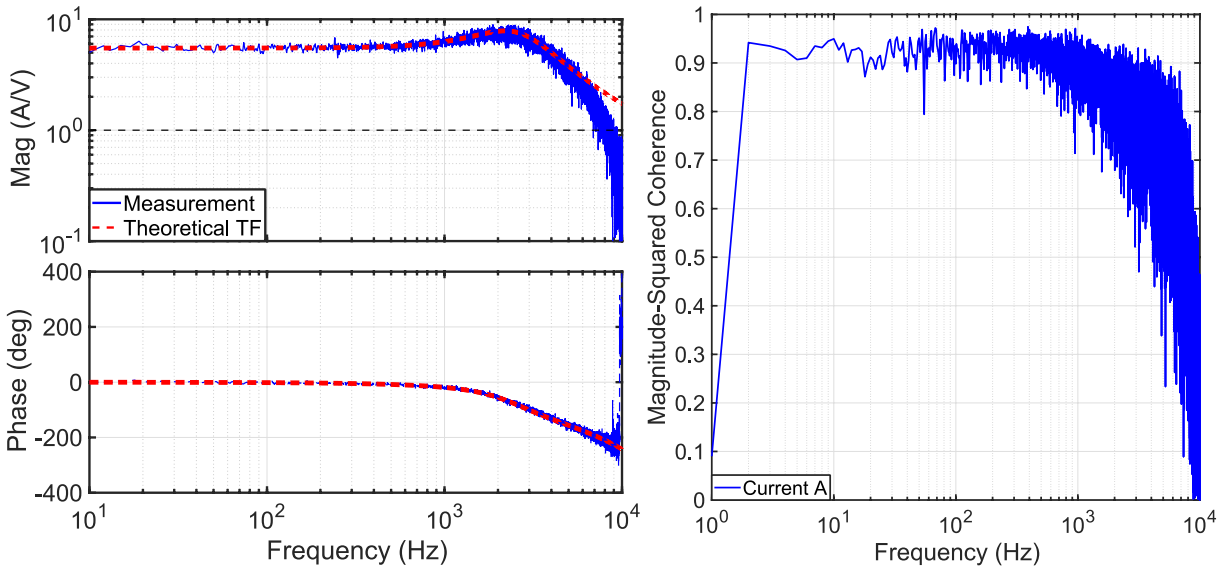


Figure 3.8: Measured and estimated FRF of the current loop dynamics (left), coherence of the FRF (right).

Table 3.2: Summary of the identified current loop dynamics.

Parameter	Value	Unit
K_p	69.47	[V/A]
K_i	1.06	[V/(A · μs)]
T_d	0.0394	[ms]
K_a	5.5	[A/V]
f_z	1600	[Hz]
ω_n	2594	[Hz]
ζ	0.53	[]
BW	1.5 ... 5	[kHz]

A time-domain simulation was run to further validate the modeling of the current loop response using a chirp signal with linearly increasing frequency as the input. The instantaneous frequency of the excitation is expressed by:

$$f(t) = f_0 + kt \quad (3.20)$$

Above, f_0 is the starting frequency, t is the current time, and k is the rate of frequency change. It can be calculated from the following:

$$k = \frac{f_1 - f_0}{T} \quad (3.21)$$

In the above equation, f_1 is the final frequency, and T is the final time. The linear chirp signal can be stated by [121]:

$$d(t) = A \cdot \sin\left(2\pi \cdot \left(f_0 t + k \frac{t^2}{2}\right)\right) \quad (3.22)$$

where A is the amplitude. The slew rate ($di_a/dt = U_a/L$) limits the maximum rate of change of the output of the amplifier. This effect was considered in the time-domain simulation to emulate the dynamics of the current loop more precisely. Then, an experiment was performed using a similar excitation signal ($A = 0.5 V$ amplitude chirp signal 1 Hz-10 kHz). As can be observed from Figure 3.9, the simulated response is in good agreement with the experimental data up to 1.2 kHz, while it begins to deviate at higher frequencies. Due to slew rate limiting, small-amplitude input signals result in a higher bandwidth than larger amplitudes, since the distortion effect (slew rate = $2\pi f V_{peak}$) becomes less dominant. This effect has been shown in

Figure 3.10. The minimum achievable bandwidth of the current loop dynamics is 1523 Hz at the $V_{peak}=8V$ which is approximately four times higher than the bandwidth of the PWM driver.

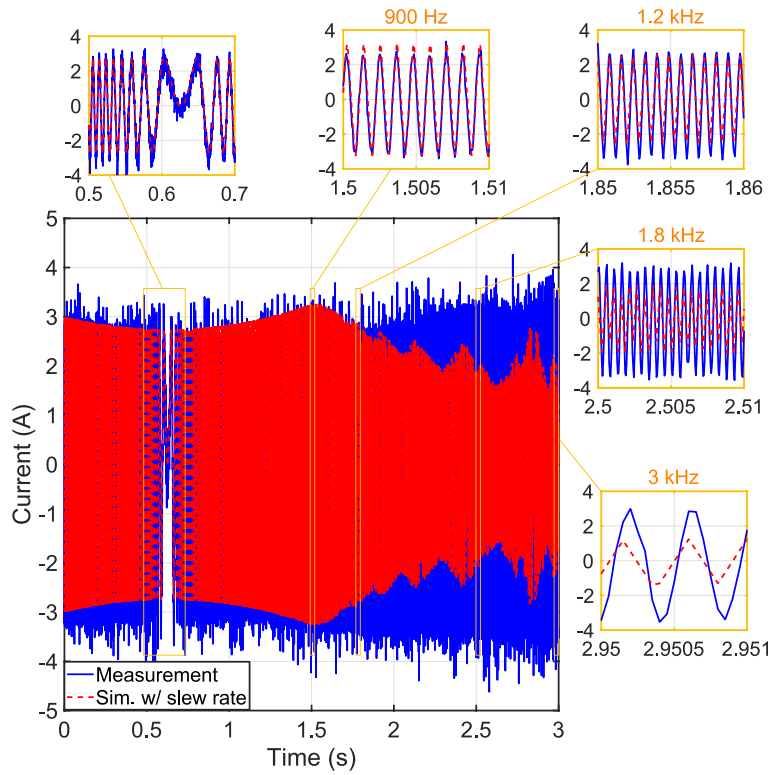


Figure 3.9: Measured and simulated current loop responses using a chirp excitation signal.

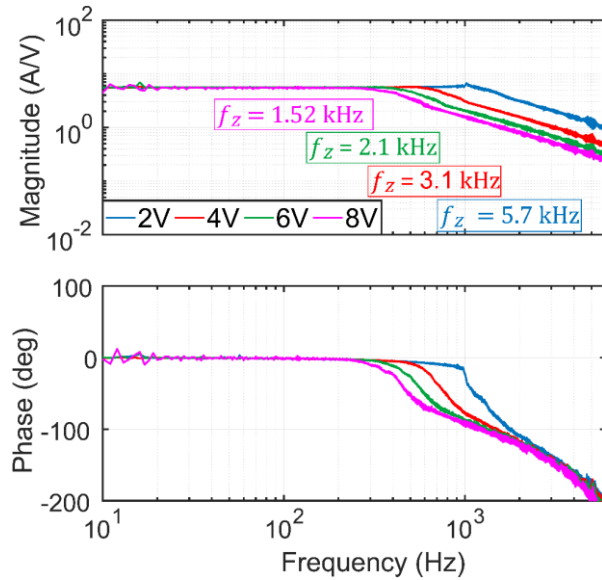


Figure 3.10: Measured frequency response of the linear amplifier current loop dynamics at different output voltages.

Figure 3.11 and Table 3.3 show a comparison between the performance of the linear amplifier and the PWM driver. Time delay effect imposes an upper bound limit on achievable bandwidth of the closed-loop system ($\omega_{cl} < 1/\tau_{delay}$), and this directly affects the performance of tracking and disturbance rejection.

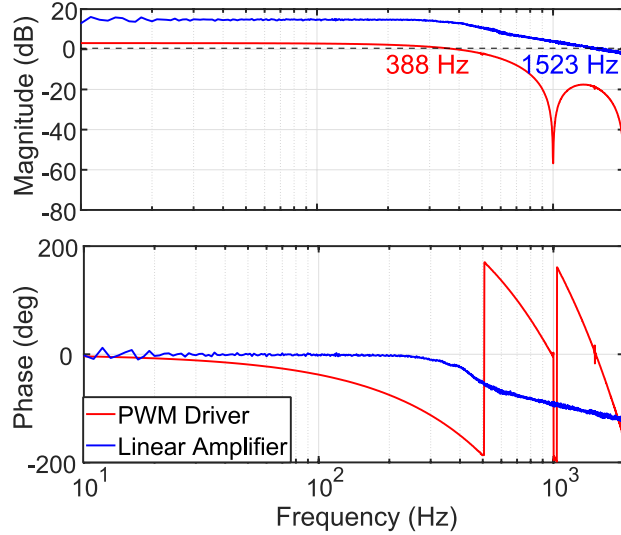


Figure 3.11: Measured linear amplifier vs measured PWM current loop frequency responses.

Table 3.3: Current loop dynamics linear amplifier vs. PWM driver.

Parameter	Linear amplifier	PWM driver
Bandwidth	1.523 kHz	388 Hz
Time delay	0.0394 ms	0.33 ms

3.5. Identification of Rigid Body Dynamics

A method similar to that described by Erkorkmaz and Altintas [4] was used to perform the identification of rigid-body dynamics, using a Least-Squares (LS) parameter identification. The transfer function between the amplifier input voltage U_q (i.e., motor torque command) and angular velocity of the motor rotor ω can be described by the following expression.

$$\frac{\omega}{U_q} = \frac{K_t K_a}{B_m} \frac{\frac{B_m}{J_m}}{s + \frac{B_m}{J_m}} \quad (3.23)$$

The discrete-time form of Eq. (3.23) using the zero-order hold equivalent discretization transformation can be stated as.

$$\frac{B(1 - e^{-AT_s})}{z - e^{-AT_s}} = \frac{Q}{z - P} \quad (3.24)$$

In the above equation, $A = -\frac{1}{T_s} \ln P$, $B = \frac{Q}{1-e^{AT_s}}$ where $P = e^{-AT_s}$ and $Q = B(1 - e^{-AT_s})$. To obtain the difference equation Eq. (3.24) is inverse transformed.

$$\omega_{k+1} = P\omega_k + QU_{q,k} \quad (3.25)$$

A Coulomb friction term model (d_f) is added to Eq. (3.25) to reduce the input amplitude dependent bias in the estimation of the system parameters,

$$d_f(\omega_k) = A(\omega_k) \cdot d^+ + B(\omega_k) \cdot d^- \quad (3.26)$$

$$\omega_{k+1} = P\omega_k + Q(U_{q,k} - d_f(\omega_k)) \quad (3.27)$$

In Eq. (3.26) d^+ , and d^- are the Coulomb coefficients in positive and negative directions of motion. The following equation shows the construction of the regressor matrix Φ , for the parameter estimate vector θ . The output (ω) and input (U_q) vectors are Y and U respectively.

$$\underbrace{\begin{bmatrix} y_2 \\ y_3 \\ \vdots \\ y_n \end{bmatrix}}_Y = \underbrace{\begin{bmatrix} y_1 & u_1 & -Ay_1 & -By_1 \\ y_2 & u_2 & -Ay_2 & -By_2 \\ \vdots & \vdots & \vdots & \vdots \\ y_{n-1} & u_{n-1} & -Ay_{n-1} & -By_{n-1} \end{bmatrix}}_{\Phi} \underbrace{\begin{bmatrix} P \\ Q \\ Qd^+ \\ Qd^- \end{bmatrix}}_{\theta} + \underbrace{\begin{bmatrix} e_2 \\ e_3 \\ \vdots \\ e_n \end{bmatrix}}_E \quad (3.28)$$

The estimated parameters are $\theta = (\Phi^T \Phi)^{-1} \Phi^T Y$, $d^+ = K_t K_a \cdot (\theta_3 / \theta_2)$, $d^- = K_t K_a \cdot (\theta_4 / \theta_2)$, $B_m = K_t K_a / B$, and $J_m = B_m / A$. $\theta_1, \dots, \theta_4$ represent the entries of the estimated parameter vector. In this estimation, the PWM driver was used as the actuation system, with input application and data collection from the setup at 20 kHz. The applied excitation is shown in Figure 3.12. The estimated rotor inertia (see Table 3.4) is in close agreement with the manufacturer's data sheet ($9.5 \times 10^{-4} \text{ kg} \cdot \text{m}^2$).

Table 3.4: Estimated inertia and viscous coefficients of the servo motor.

Parameter	Value	Unit
J_m	9.57×10^{-4}	$\text{kg} \cdot \text{m}^2$
B_m	0.0069	$(\text{Nm})/(\text{rad/s})$

Considering the peak torque (9.55 Nm), the motor torque constant (0.41 Nm/A), and the maximum control signal amplitude (10 V), the PWM amplifier gain is $K_a = 2.3293 \text{ A/V}$. Figure 3.12 illustrates the predicted and measured velocity responses, prediction errors, and input signals used for estimation of the ball-screw drive's rigid body parameters. A moving average filter was applied to smoothen the velocity

estimation obtained by differentiating the rotary encoder readings. While the estimated value of inertia remains constant at different amplitudes of excitation, the estimation of viscous damping and Coulomb coefficients vary slightly. For that reason, the Stribeck curve in Section 3.8 is used to further adjust the viscous damping term and to correct for overestimation. The Coulomb coefficients can also be obtained from the friction curve in the sliding regime. Table 3.5 shows the estimated rigid body parameters of the ball-screw drive using the PWM driver as the actuation system. In later sections, the inertia and viscous damping values are also further adjusted to match the low-frequency characteristics of the frequency response measurements.

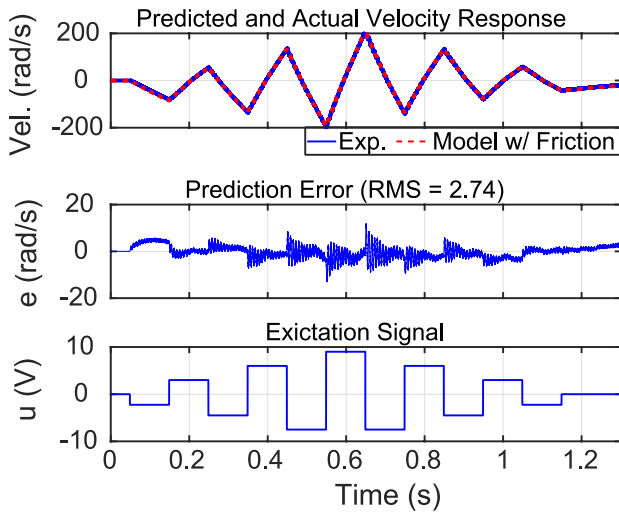


Table 3.5: Estimated rigid body parameters of the ball-screw drive.

Parameter	Value	Unit
J	0.0022	$kg.m^2$
B	0.0052	$Nm/(rad/s)$
d_{coul}^+	0.119	Nm
d_{coul}^-	-0.134	Nm

Figure 3.12: Predicted and actual velocity responses, prediction error, and the input signal.

3.6. Frequency Response Measurement using Linear Amplifier

Due to the high power dissipation in the linear amplifier, the application of the random type (Gaussian white noise) resulted in imperfect quality frequency response measurements. Thus, the frequency response of the ball-screw drive was obtained using a sine-sweep test at 4 V amplitude excitation and frequencies between 10...1600 Hz. The data was collected at 15 kHz. Indeed, stepped-sine excitation enabled enough power to be applied at each frequency to generate meaningfully detectable motion. The measurement was carried out while the axis was stationary. Figure 3.13 show the position and acceleration responses registered from the rotary and linear encoders. As can be seen, the rotary encoder response is affected by the noise at high frequencies.

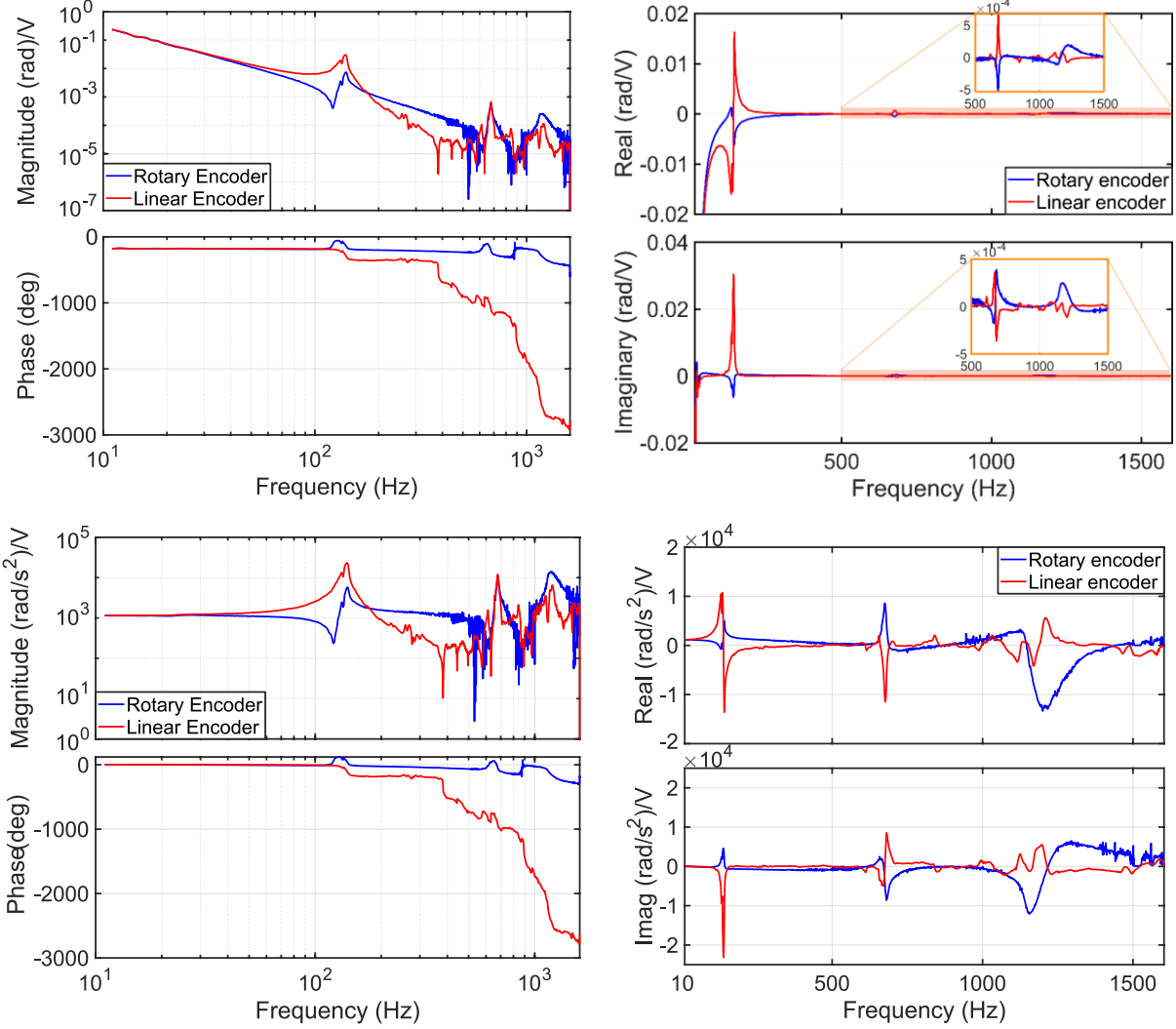


Figure 3.13: Rotary and linear encoder position (upper-hand panels) and acceleration (lower-hand panels) frequency responses.

3.7. Modeling and Identification of a Lumped Two-Inertia System Model

The rotary and linear encoder responses of the ball-screw drive to the inputs of actuation (i.e., control) u and disturbance d was measured using stepped-sine motor torque commands and impact hammer testing. The resulting FRF data was used to identify a two-inertia discrete element model similar to the one shown in Figure 2.1. In the sweep sine measurements, the high-bandwidth linear amplifier (see Section 3.4) was used to provide the actuation system. According to measured FRFs, the first axial mode of vibration was observed at 132 Hz, with a damping ratio of 0.02. Based on this mode, the parameters for the two lumped-mass model were identified as: $m_1 = 5.49 \times 10^{-4} V/(rad/s^2)$, $m_2 = 1.51 \times 10^{-4} V/(rad/s^2)$, $b_1 = 4 \times 10^{-4} V/(rad/s)$, $b_2 = 0 V/(rad/s)$ (air guideway system), $k = 81.4549 V/rad$, and $c =$

0.0075 V/(rad/s). These values were obtained by trial-and-error tuning of the mass ratio (knowing the total inertia) and comparing the synthesized FRF's with the measured ones, for both amplifier torque command input (u , measured by sine sweeping), and the tableside disturbance force input (d , measured by impact hammer testing). The axial stiffness of the ball-screw mechanism k_{axial} includes a combination of the system's relevant axial flexibilities, namely the axial rigidity due to the bearing and its mounting support $k_{bearing}$; the equivalent axial rigidity of the ball-screw shaft k_{shaft} ; and the rigidity of the preloaded nut k_{nut} . This results in $k_{axial}^{-1} = k_{shaft}^{-1} + k_{bearing}^{-1} + k_{nut}^{-1}$.

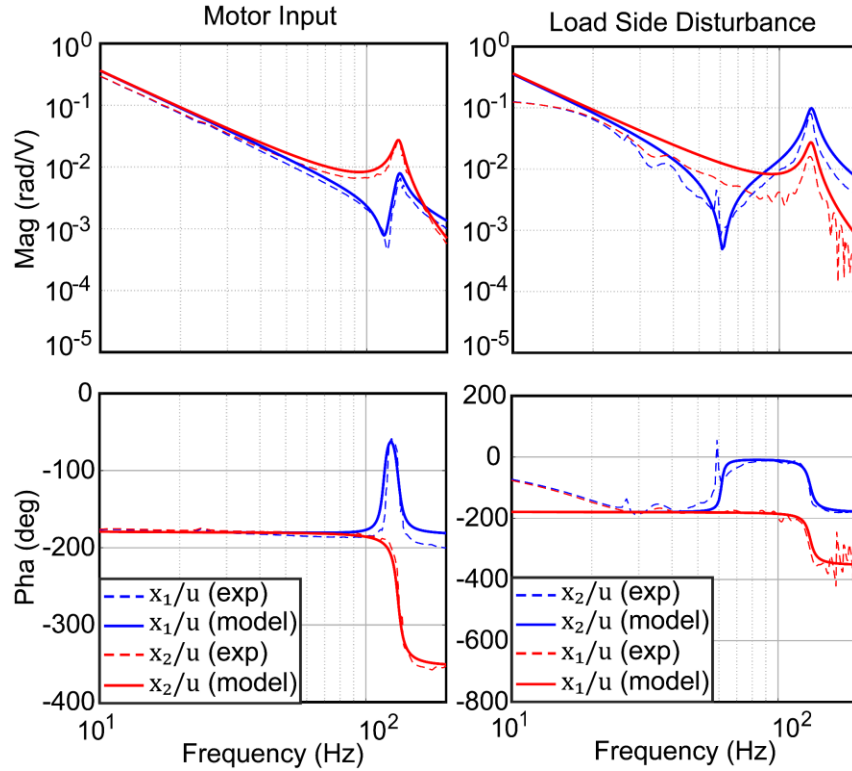


Figure 3.14: Measured (dashed line) and modeled (solid line) open-loop FRFs.

Considering Figure 3.14, the identified model is in reasonable agreement with the experimental data for the control input and load side disturbance. Selecting the state vector as $x = [x_2 \quad \dot{x}_2 \quad x_1 \quad \dot{x}_1]^T$ yields the following state-space system:

$$\underbrace{\begin{bmatrix} \dot{x}_2 \\ \ddot{x}_2 \\ \dot{x}_1 \\ \ddot{x}_1 \end{bmatrix}}_x = \underbrace{\begin{bmatrix} 0 & 1 & 0 & 0 \\ -\frac{k}{m_2} & -\frac{c+b_2}{m_2} & \frac{k}{m_2} & \frac{c}{m_2} \\ 0 & 0 & 0 & 1 \\ \frac{k}{m_1} & \frac{c}{m_1} & -\frac{k}{m_1} & -\frac{c+b_1}{m_1} \end{bmatrix}}_A \underbrace{\begin{bmatrix} x_2 \\ \dot{x}_2 \\ x_1 \\ \dot{x}_1 \end{bmatrix}}_x + \underbrace{\begin{bmatrix} 0 \\ 0 \\ 0 \\ \frac{1}{m_1} \end{bmatrix}}_B \underbrace{u}_u + \underbrace{\begin{bmatrix} 0 \\ 1 \\ 0 \\ 0 \end{bmatrix}}_W \underbrace{d}_d \quad (3.29)$$

3.8. Identification of a Stribeck-Type Friction Model using a Kalman Filter

A proportional derivative (PD) controller was designed with a low crossover frequency of 7 Hz to estimate the static friction from the experimental setup. The low crossover frequency, achieved via small feedback gains, allows sufficient motor torque to be generated to overcome static friction and initiate primarily rigid-body motion, while leaving the feed drive's mid- and high-frequency pole locations relatively unaltered. The worktable was jogged at constant velocities in forward and backward motion while capturing the control input signal. The following captures the state-space formulation of the system, including an equivalent disturbance input to represent friction.

$$\begin{bmatrix} \dot{\theta}(t) \\ \dot{\omega}(t) \end{bmatrix} = A_c \begin{bmatrix} \theta(t) \\ \omega(t) \end{bmatrix} + [B_c \quad -B_c] \begin{bmatrix} u(t) \\ d(t) \end{bmatrix}, A_c = \begin{bmatrix} 0 & 1 \\ 0 & P_v \end{bmatrix}, \text{ and } B_c = \begin{bmatrix} 0 \\ K_v \end{bmatrix} \quad (3.30)$$

Above, θ and ω are the angular position and velocity, and A_c and B_c are the continuous system and input matrices. In the above equation, P_v and K_v are defined by $P_v = -B/J$, and $K_v = K_a K_t/J$. The discrete-time state-space model can be described by the following, using the zero-order hold equivalent discretization transformation [69].

$$\underbrace{\begin{bmatrix} \theta(k+1) \\ \omega(k+1) \end{bmatrix}}_{x(k+1)} = A_d \underbrace{\begin{bmatrix} \theta(k) \\ \omega(k) \end{bmatrix}}_{x(k)} + [B_d \quad -B_d] \underbrace{\begin{bmatrix} u(k) \\ d(k) \end{bmatrix}}_{U(k)} \quad (3.31)$$

Above, A_d , B_d , C_d are the discrete-time state transition, input and output matrices. For better estimation of the input torque, a Kalman filter [122] was designed which considers the rigid body feed drive model. In designing the Kalman filter, the disturbance dynamics was considered an integrated white noise process (e.g., random walk): $d(k) = d(k-1) + w_d(k)$. Thus, the Kalman filter can be expressed as a discrete-time system, given by the following:

$$\underbrace{\begin{bmatrix} \hat{\theta}(k) \\ \hat{\omega}(k) \\ \hat{d}(k) \end{bmatrix}}_{\hat{z}(k)} = \underbrace{(1 - K_{obs}C_d)A_d}_{A_z} \underbrace{\begin{bmatrix} \hat{\theta}(k-1) \\ \hat{\omega}(k-1) \\ \hat{d}(k-1) \end{bmatrix}}_{\hat{z}(k-1)} + \underbrace{(1 - K_{obs}C_d)B_d}_{B_z} \underbrace{\begin{bmatrix} u(k-1) \\ U(k-1) \end{bmatrix}}_{U(k-1)} + K_{obs} \underbrace{\begin{bmatrix} \theta_m(k) \\ \omega_m(k) \end{bmatrix}}_{Y_m(k)} \quad (3.32)$$

In the Eq. (3.32), K_{obs} represents the observer gain. A_z , and B_z , are the augmented model state, and input matrices for rigid body dynamics. \hat{d} is the estimated disturbance, which is mainly attributed to friction, and $\hat{\theta}$, $\hat{\omega}$, θ_m , and ω_m are the estimated and measured angular position and velocity signals, respectively. Further details of the state-space modeling and Kalman filter design for friction estimation can be found in [4].

In the design of the Kalman filter, the process input perturbation and measurement noise statistical properties also need to be determined or tuned. The input to the current amplifier is generated by a 16-bit DAC converter between ± 10 V. The resolution of the input voltage is $\delta_u = 20/2^{16}$ V. Thus, assuming a uniform random distribution of input error, caused by the DAC quantization, the variance for the input can be calculated as $R_{\tilde{u}} = (\delta_u)^2/12 = 7.61 \times 10^{-9}$ V². The detailed derivation can be found in [4]. The resolution of the encoder after 400 times interpolation of the sinusoidal signal is $\delta_\theta = 2\pi/(5000 \times 400)$ rad, which is equivalent to 10 nm of the worktable linear motion. The position measurement variance can be calculated as $R_{\tilde{\theta}} = (\delta_\theta)^2/12 = 8.2247 \times 10^{-13}$ rad². The variance of the perturbation $R_{w_d} = var\{w_d\}$ in the random walk disturbance model $d(k+1) = d(k) + w_d(k)$ is used as a tuning parameter, and adjusted to give a quick estimate of the detected friction force while avoiding an excessively oscillatory or noisy signal. Its value was tuned to be 7.7×10^{-10} [V²]. The optimal observer gain K_{obs} can thus be computed by iterating the following equation.

$$\begin{aligned}
P_{k|k-1} &= A_d P_{k-1|k-1} A_d^T + W R_w W^T \\
K_{obs}(k) &= P_{k|k-1} C_d^T [C_d P_{k|k-1} C_d^T + R_v]^{-1} \\
P_{k|k} &= [I - K_{obs}(k) C_d] P_{k|k-1}
\end{aligned} \tag{3.33}$$

Above $R_w = diag\{R_{\tilde{u}}, R_{w_d}\}$ and $R_v = R_{\tilde{\theta}}$. The first part of the above equation is the propagation of the covariance of state estimation. W matrix indicates how the process noise vector $[\tilde{u} \quad w_d]^T$ affects the state transition. In the second line, optimal gain is computed to minimize $tr\{P_{k|k}\}$, i.e. the covariance of state estimation error. In the last line, the state estimation error is updated based on the calculated optimal gain. In iterating the calculation, $P_{k|k}$ is initially set to a large value of, e.g., $\alpha I = 10^{10}$. For the identified system model and specified covariance terms, the observer gain was eventually obtained as $K_{obs} = [0.0791 \quad 43.1409 \quad -6.5674]^T$. Using the resulting Kalman filter, Figure 3.15 shows the measured and estimated disturbance signals at 15 mm/s and 100 mm/s jogging speeds.

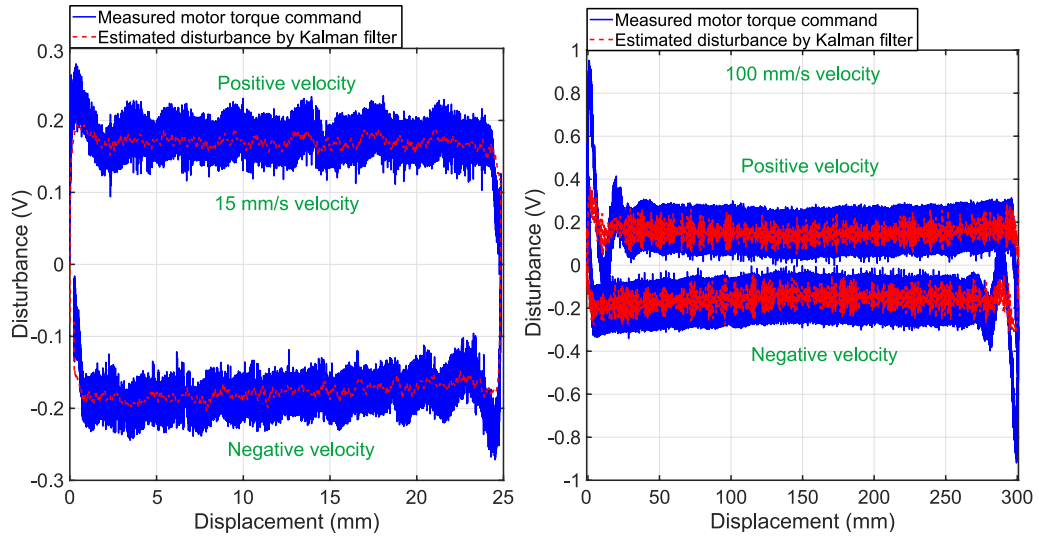


Figure 3.15: Measured motor torque command and estimated disturbance with Kalman filtering at 15 mm/s and 100 mm/s.

The identified Stribeck curve for velocities between zero and 350 mm/s is shown in Figure 3.16. The over-estimated viscous damping from rigid body identification was further modified by (Δb) by considering the negative slope in the originally estimated Stribeck curve (black dotted characteristic). With this correction, the value of B was updated from 1.6×10^{-3} to $9.02 \times 10^{-4} \text{ Nm}/(\text{rad}/\text{s})$. Then, the updated viscous damping was used once more in augmented state formulation, and re-design of the Kalman filter, which then yielded the updated Coulomb friction characteristic in Figure 3.16 shown with the blue dotted line.

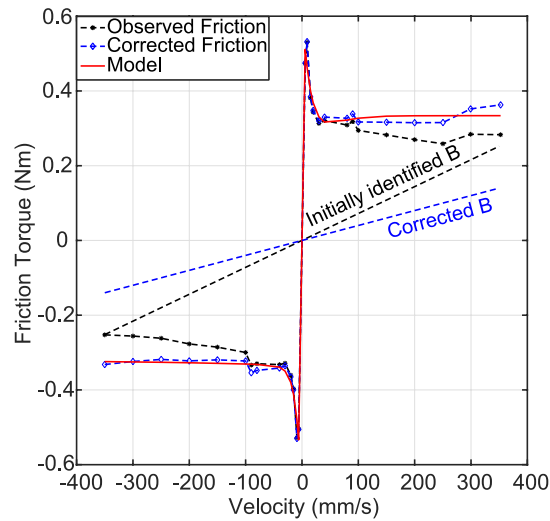


Figure 3.16: Stribeck curve.

The friction parameters were identified based on the following model, also used in [4].

$$d = \begin{cases} A^+ e^{-v/V_1^+} + B^+ e^{-v/V_2^+} + d_{coul}^+, & v > 0 \\ A^- e^{-v/V_1^-} + B^- e^{-v/V_2^-} + d_{coul}^-, & v < 0 \end{cases} \quad (3.34)$$

The static friction terms can be stated as:

$$d_{stat} = \begin{cases} A^+ + B^+ + d_{coul}^+, & v > 0 \\ A^- + B^- + d_{coul}^-, & v < 0 \end{cases} \quad (3.35)$$

In the above equations d_{coul} and d_{stat} are the Coulomb and static friction terms, and A, B, V_1 , and V_2 are the exponential term coefficients and velocity constants. The positive and negative subscripts denote the direction of the motion. Table 3.6 shows the identified parameters from the Eq. (3.34) and (3.35).

Table 3.6: Identified Stribeck friction parameters.

A^+	B^+	V_1^+	V_2^+	d_{coul}^+	d_{stat}^+
(Nm)	(Nm)	(mm/s)	(mm/s)	(Nm)	(Nm)
0.662	-0.37	38.98	60.1	0.334	0.6263
A^-	B^-	V_1^-	V_2^-	d_{coul}^-	d_{stat}^-
(Nm)	(Nm)	(mm/s)	(mm/s)	(Nm)	(Nm)
-0.373	-0.015	21.26	524.78	-0.321	-0.71

The parameters were estimated using least squares involving both nonlinear and linear iterations. This model is later used in Chapter 5 and Chapter 6 for feedforward compensation of the Stribeck effect of friction, in the controller design.

3.9. Identification of Friction Considering the Generalized Maxwell-Slip (GMS) Model

The GMS friction model is used to capture the pre-sliding behavior of systems with noticeable stick-slip behavior. In this context, it has also been applied to the ball-scrw drive. Load side displacement measurements were realized while applying sinusoidal torque command excitations at different amplitudes with a relatively low frequency (0.1 Hz). The data obtained helps identify the so-called ‘virgin curve’ used to build the GMS model [35]. Figure 3.17 shows the transition from pre-sliding to sliding regime, through gradual increase in the excitation amplitude.

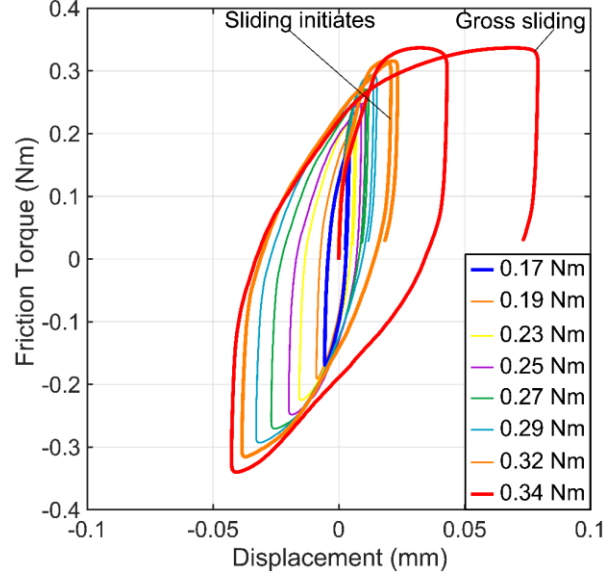


Figure 3.17: Experimental friction torque vs. load side displacement at different amplitudes of excitation (frequency of excitation: 0.1 Hz).

The estimated breakaway torque and corresponding displacement are at 0.327 Nm, and 0.031 mm. Here a GMS model with seven elementary slip-blocks is chosen that consists of seven α_i and k_i (incremental torque contribution factors and stiffness values) parameters estimated from the piecewise linear approximation of the virgin curve (Figure 3.18). Each elementary component slips when the friction force equals the maximum value $W_i = \alpha_i S(v)$ for that element (see Eq. (2.7)). Table 3.7 shows the summary of the identified pre-sliding parameters. A factor of $C = F_s/\tau_c = 13.53 \text{ Nm/s}$ with a time constant of $\tau_c = 0.05 \text{ s}$ was used to denote the rate at which the friction force transitions from pre-sliding into the Stribeck sliding regime.

$$\begin{aligned}
 k_a &= k_1 + k_2 + \dots + k_7 \\
 k_b &= k_2 + k_3 + \dots + k_7 \\
 k_c &= k_3 + k_4 + \dots + k_7 \\
 k_d &= k_4 + k_5 + \dots + k_7 \\
 k_e &= k_5 + k_6 + k_7 \\
 k_f &= k_6 + k_7 \\
 k_g &= k_7
 \end{aligned}
 \tag{3.36}$$

Table 3.7: Identified pre-sliding GMS model parameters.

α_i	$k_i(\text{Nm/mm})$
0.2147	97.19
0.1289	19.37
0.0835	4.68
0.0782	2.2
0.0717	1.19
0.1804	2.22
0.2427	2.47

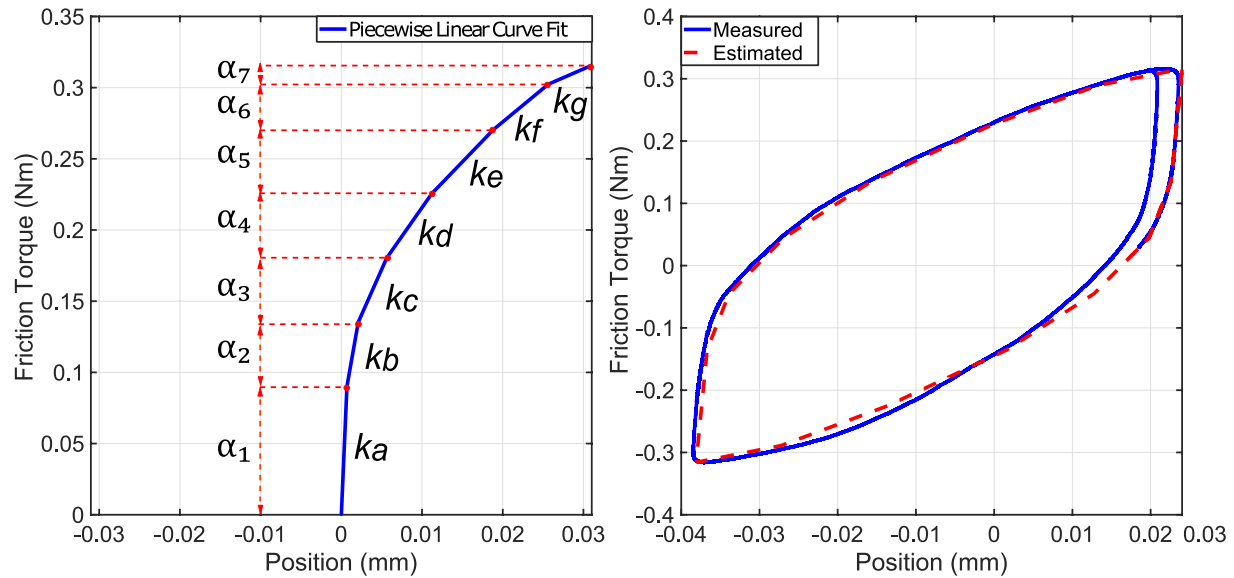


Figure 3.18: Virgin curve with selected knots for identification of stiffness in pre-sliding regime (left), and the measured and estimated virgin curves (right).

The steady-state behavior of the friction in sliding regime is described by Eq. (2.6). Figure 3.19 shows the measured and fitted static friction curves. Table 3.8 shows the summary of the static friction identified parameters. The effect of viscous friction is added as a separate term using the corrected estimation term from Section 3.8.

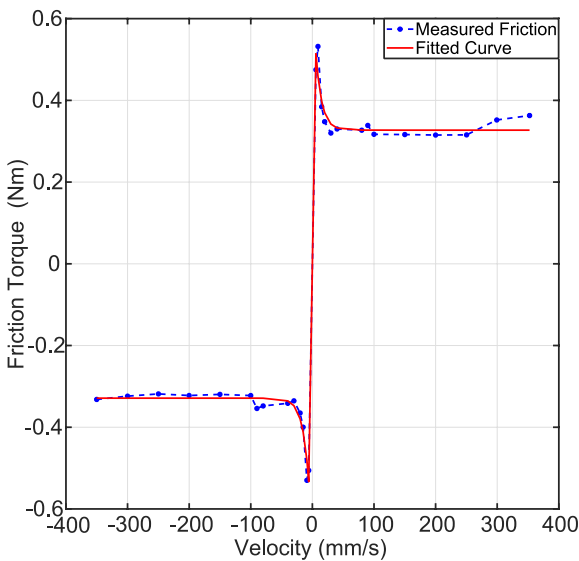


Table 3.8: Identified sliding GMS model parameters.

$F_s(Nm)$	$F_c(Nm)$	$V_s(mm/s)$	δ
0.6765	0.3270	31.83	1

Figure 3.19: The Stribeck curve used in GMS model.

3.10. Friction Compensation using Stribeck-Type Model vs. GMS Model

In order to verify the effectiveness of the estimated friction model, especially in representing and compensating the actual friction, a closed-loop tracking experiment was conducted using a jerk-limited motion profile with 200 mm/s translational speed, 816.5 mm/s² acceleration, and 5000 mm/s³ jerk values. The feedback loop is based on the P-PI cascade controller, which will be presented in Section 5.3. Figure 3.20 shows the tracking results without feedforward friction compensation, compensation using the Stribeck model from Section 3.8, and compensation using the GMS model from Section 3.9.

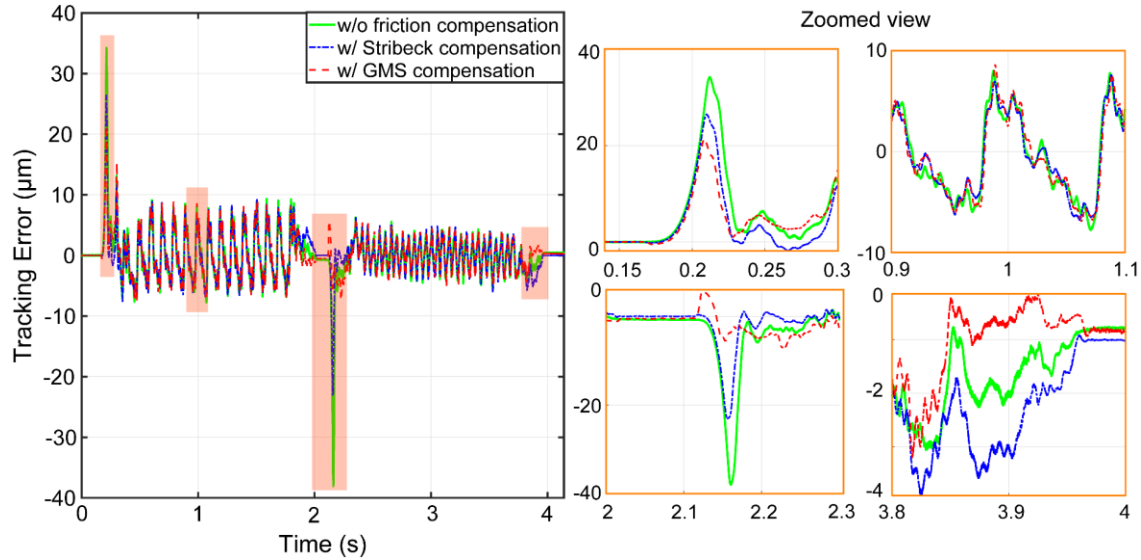


Figure 3.20: Tracking error profile without compensation, with Stribeck model-based compensation, and with GMS model-based compensation.

The summary of the tracking experiment is shown in Table 3.9. As can be seen, the GMS friction model makes an additional 14.9 % improvement over the Stribeck model for the maximum value of the tracking error. However, the improvement in the RMS of the tracking error (7.1 %) is less since the GMS model behaves like the Stribeck model in the sliding regime. This can be verified from the zoomed views of the tracking error profile. While the GMS feedforward compensation significantly reduces the peak value of the tracking error, especially when transitioning from the sticking regime, the higher velocity part of the compensation is identical that of Stribeck-based compensation. This portion of the tracking error also has a noticeable harmonic component, due to the lead (i.e., helix) imperfections in the ball-screw as well as potential mechanism and sensor misalignments. The harmonic error, however, is compensated separately using AFC in Chapter 6.

Table 3.9: Friction compensation using Stribeck-type model vs GMS model.

Tracking error (RMS) (μm)			Max. tracking error (μm)		
w/o comp.	w/ Stribeck	w/ GMS	w/o comp.	w/ Stribeck	w/ GMS
4.2	3.6 (14.3%)	3.3 (21.4%)	34.2	26.5 (22.5%)	21.4 (37.4%)

3.11. Vibration Modal Analysis

A vibration modal analysis of the ball-screw setup was carried out using two different methods. First, the peak-picking method [24] was applied for modal parameter estimation and then the PolyMAX method [123] was used to analyze the vibratory behavior. In the peak-picking method (similar to circle fitting in the complex numbers' domain), the modes are locally fitted and their estimated transfer functions are stacked, while in the PolyMAX method (similar to least squares complex exponential (LSCE) method) the natural frequencies and damping ratios of several modes are analyzed simultaneously, and parameters are estimated to achieve a good fit across the frequency spectrum of interest. The data acquisition of the first method (peak-picking method) was performed using CutPRO software, MalTF module. Ideally, modal analysis should be unaffected by the roving of the accelerometer or the hammer, if the measurement artefact is a linear elastic system. This is due to the reciprocity principle applicable to such systems, implying that a compliance transfer function for exciting at point A and measuring at point B should be identical to the case where the actuation and measurement points are switched ($G_{AB}(\omega) = G_{BA}(\omega)$).

For expediency, the measurements were carried out by roving of the hammer along specific points on the feed drive table geometry, while the accelerometer was fixed at one reference point, which ideally should not be a nodal (zero) vibration point for any of the vibration modes of interest. The FRFs were captured along different planes of motion, in order to accumulate enough spatial information about each observed mode. In this method, the mode shapes associated with each vibration mode were drawn manually on 2D planes as shown in the left-hand panel of Figure 3.26. While slower and less accurate compared to using automated modal analysis algorithms, such practice of manually estimating modal parameters and sketching out mode shapes is especially helpful in establishing a solid intuitive understanding of the plant's modal characteristics, and also in verifying the accuracy of the automatically fitted modes by an algorithm, such as PolyMAX, afterwards.

Figure 3.21 shows the locations of the impact points and the accelerometer, as placed on the feed drive's moving table, in different testing scenarios.

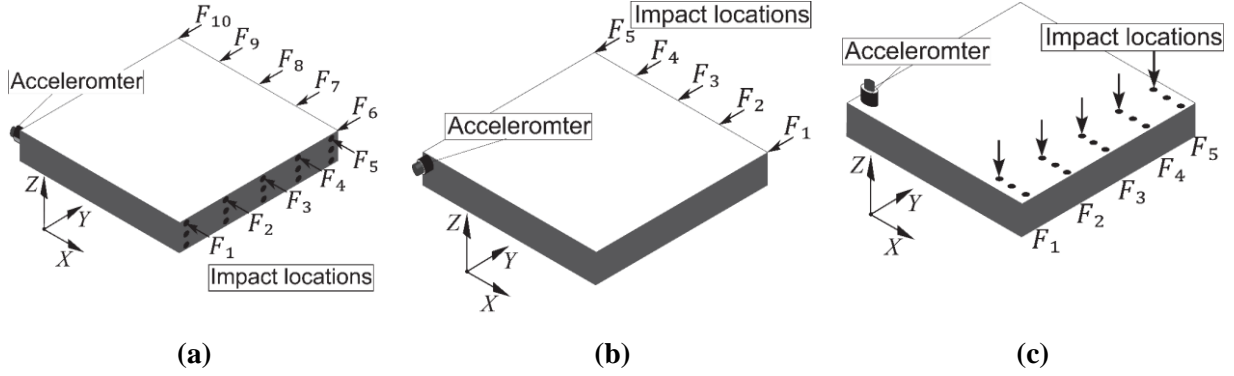


Figure 3.21: Impact locations for peak-picking method (a) Impact in x and y-direction and measuring in the x-direction (axial), (b) Impact and measurement in the y-direction (lateral) (c) Impact and measurement in the z-direction.

A Dytran 5802A impact sledgehammer with 1.36 kg head weight was used to excite the table up to 1 kHz with a 0.5 Hz measurement resolution. The sensitivity of the impact hammer is 0.24279 mV/N. The accelerometer, in this case, was a one-dimensional Dytran 3035 with a sensitivity of 98.8 mV/g. The measurement spectrum was verified by inspecting the coherence function of the recorded impact force.

The accelerance FRF is defined as the acceleration magnitude per force at each frequency as:

$$\alpha(\omega) = \frac{\ddot{x}(\omega)}{F(\omega)} = -\omega^2 \frac{x(\omega)}{F(\omega)} \quad (3.37)$$

The accelerance can be approximated as the superposition N of second-order systems as follows:

$$\alpha(\omega) = \sum_{i=1}^N -r_i^2 \phi_i'(r_i) = \sum_{i=1}^N \frac{-r_i(\omega)^2 K_i'}{1 - r_i(\omega)^2 + j2\zeta_i r_i(\omega)} \quad (3.38)$$

Above, $\phi_i(r_i) = G(r) + jH(r)$ and $\phi_i'(r_i) = \omega_{n,i}^2 \phi_i(r_i)$. Each second-order summand has real and imaginary parts which are expressed as:

$$-r^2 \omega_n^2 \phi(r) = -r^2 \omega_n^2 G(r) - r^2 \omega_n^2 jH(r) \quad (3.39)$$

Above, $\omega_{n,i}$ is the i th mode's natural frequency, ζ_i is the damping ratio, and K_i is the i th modal contribution factor ($K_i' = \omega_{n,i}^2 K_i = 1/m_i$, where m_i is the modal mass, and $K_i'/\omega_{n,i}^2 = 1/k_i$, where k_i is the modal stiffness). $r_i(\omega) = \omega/\omega_{n,i}$ is the normalized excitation frequency with respect to $\omega_{n,i}$.

In order to obtain the modal parameters via peak picking from the measured accelerance responses, for each mode, the natural frequency ω_n is identified by inspecting the frequency of the local peak in the imaginary portion of the response [24][124]. Then, the frequencies ω_1 and ω_2 are recorded, corresponding

to the local maximum and minimum in the real component of the response within the vicinity of $\omega_n \cong \omega_{min}$ (assuming small ζ , typically $\zeta \leq 0.1$). The damping ratio, which indicates how sharply or gradually the FRF for a single mode transitions from spring-like behavior into mass-like behavior (or basically how narrow or wide the shape of the resonance is) can be practically identified from the real component of acceleration (acceleration per unit force) plot as $\zeta = (\omega_2^2 - \omega_1^2)/4\omega_n^2$ (see Figure 3.22) [124]. Once the damping ratio for each mode is calculated, the real and imaginary parts of the identified second-order FRF are overlaid on top of the measurements and the modal stiffness's values can be adjusted to match the magnitude of the transition in the real part and the peak in the imaginary part. Figure 3.23 illustrates some of the reconstructed (i.e., synthesized) FRFs after model fitting, for the measurements obtained at different impact points, based on manual modal analysis accomplished by applying the above summarized parameter estimation method.

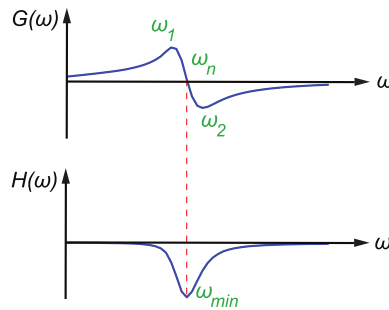


Figure 3.22: Second-order accelerance plot.

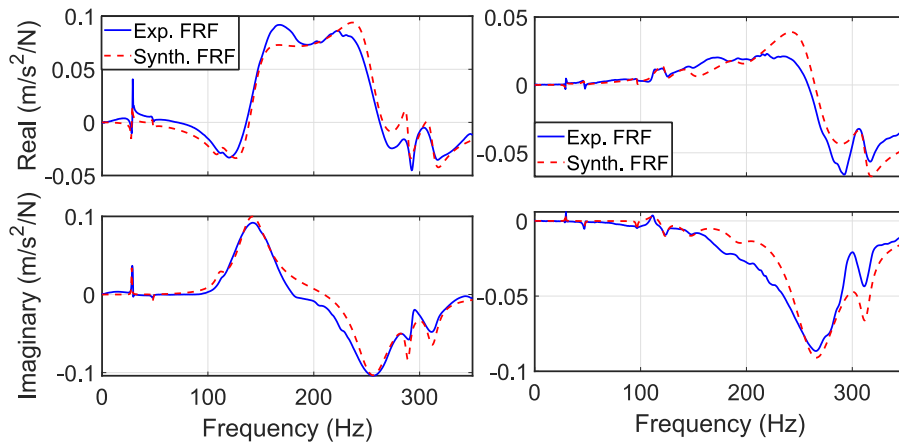


Figure 3.23: Experimental and synthesized FRF for impact point F_1 in the x- (left), and y-direction (right).

As mentioned earlier, the PolyMAX or polyreference least-squares complex frequency-domain method allows for the estimation of natural frequencies and damping ratios for multiple vibration modes simultaneously. Using the PolyMAX method, the modal parameters were also estimated in LMS Test.Lab

software. In this measurement, accelerometer roving was applied and the hammer was considered as the reference point. A tri-axial PCB 356A02 accelerometer (x-axis sensitivity: 10.02 mV/g, y-axis sensitivity: 9.86 mV/g, z-axis sensitivity: 9.92 mV/g) was placed at the eight corners of the table for each measurement, while the same 3-pound (1.36 kg) impact hammer was used. Using the LMS software and the modeled 3D geometry of the feed drive table, the mode shapes could be estimated and presented as automated 3D animations using the FRF collected from the various measurement points (P_1, \dots, P_8). Figure 3.24 shows the impact location and accelerometer roving for PolyMAX modal parameter estimation method. Figure 3.25 shows the measured and synthesized frequency responses for point 1 (P_1) in x, y, and z-directions.

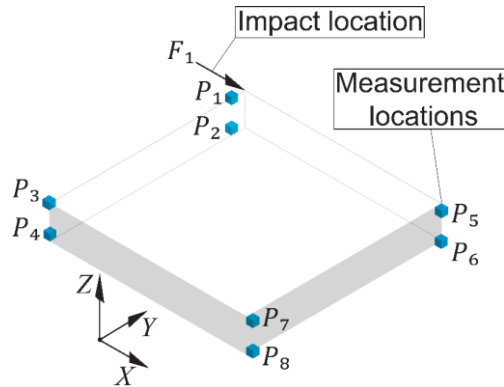


Figure 3.24: Accelerometer roving and impact location for PolyMAX method.

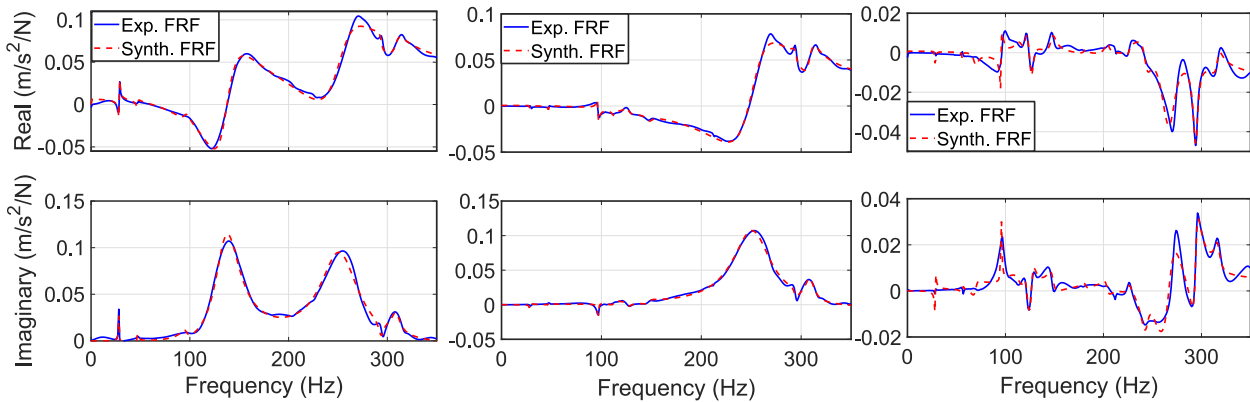


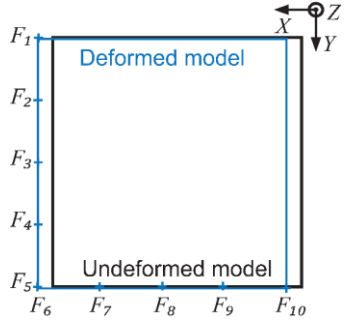
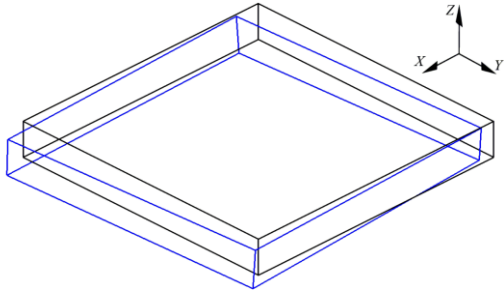
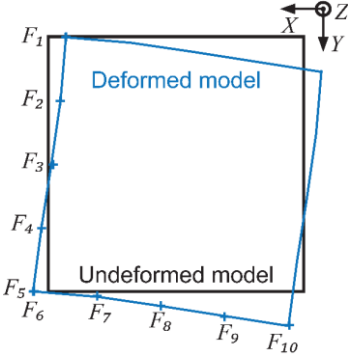
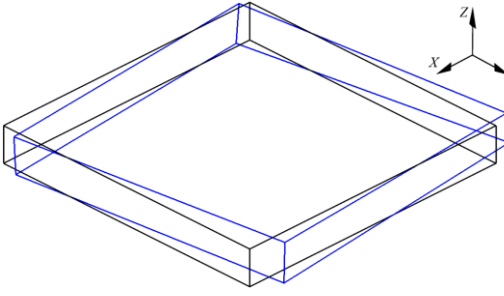
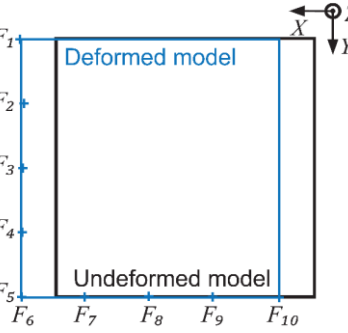
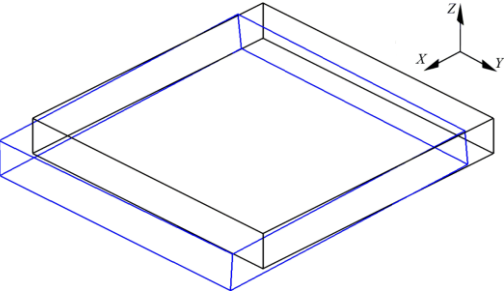
Figure 3.25: Experimental and synthesized FRF for impact point P_1 in the x- (left), y- (middle), and z- directions (right).

For comparative purposes, the mode shapes on 2D planes (estimated manually), and planar projections of the results from the LMS Test.Lab software are presented in Figure 3.26. This figure shows the main vibration modes in 1-350 Hz frequency range. According to the mode shapes, the first mode at 28 Hz belongs to the machine base frame. The second vibration mode at 48 Hz is predominantly the yawing-

pitching motion of the table pivoted by the guideway blocks (see Figure 3.1). This vibration mode can be excited by load side disturbances (e.g., cutting forces). The 141 Hz component in the frequency response is the axial vibration mode, which can interact with the control law and result in instability. Considering the FRFs shown in Figure 3.13, this mode is the most significant in the rotary and linear encoder measurement responses, especially in the 10-300 Hz range, which overlaps with the target control servo control bandwidth.

The modes at 255 Hz (yaw), 289 Hz (yaw & roll), and 312 Hz (yaw & pitch), which have lateral z-direction components to the feed drive motion, pose limitations on the achievable controller bandwidth as mentioned earlier in [23]. It is already very difficult to control these modes using excitation from the ball screw drive, and their relatively higher frequency further complicates the ability to stabilize them actively. Another observation is that the first two vibration modes (machine base & yawing-pitching motion) appear to have much lower damping ratios (≈ 0.01) compared to the first axial and yaw modes (≈ 0.1). They are also barely visible in the open-loop servo system response FRFs in Figure 3.13. However, their consideration in control law design, as shown in Chapter 5, can make a dramatic improvement in the achievable load-side disturbance rejection.

The modal analysis carried out is foundational to interpreting the physical significance of the measured FRFs, and the dynamic models estimated with the MIMO identification algorithm developed in Chapter 4. This is because while MIMO transfer function fitting can be useful for model-based control synthesis purposes, the true physical and spatial nature of the individual modes is unfortunately not contained in this data. This information is invaluable in understanding, which modes can be successfully controlled, or excited by the inputs of concern, and which modes present physical limitations that cannot be overcome by active controls. Such modes are best left unmodified, either through careful selection of the controller synthesis performance weights to achieve attenuation in the loop gain, or by placing, as needed, suitable low-pass or notch filters.

Manual Modal Analysis	Automated Modal Analysis
	
$\omega_1 = 28 \text{ Hz}, \zeta_1 = 0.011$	$\omega_1 = 28 \text{ Hz}, \zeta_1 = 0.0106$
	
$\omega_2 = 48 \text{ Hz}, \zeta_2 = 0.0125$	$\omega_2 = 47 \text{ Hz}, \zeta_2 = 0.0172$
	
$\omega_3 = 141 \text{ Hz}, \zeta_3 = 0.1$	$\omega_3 = 136 \text{ Hz}, \zeta_3 = 0.112$

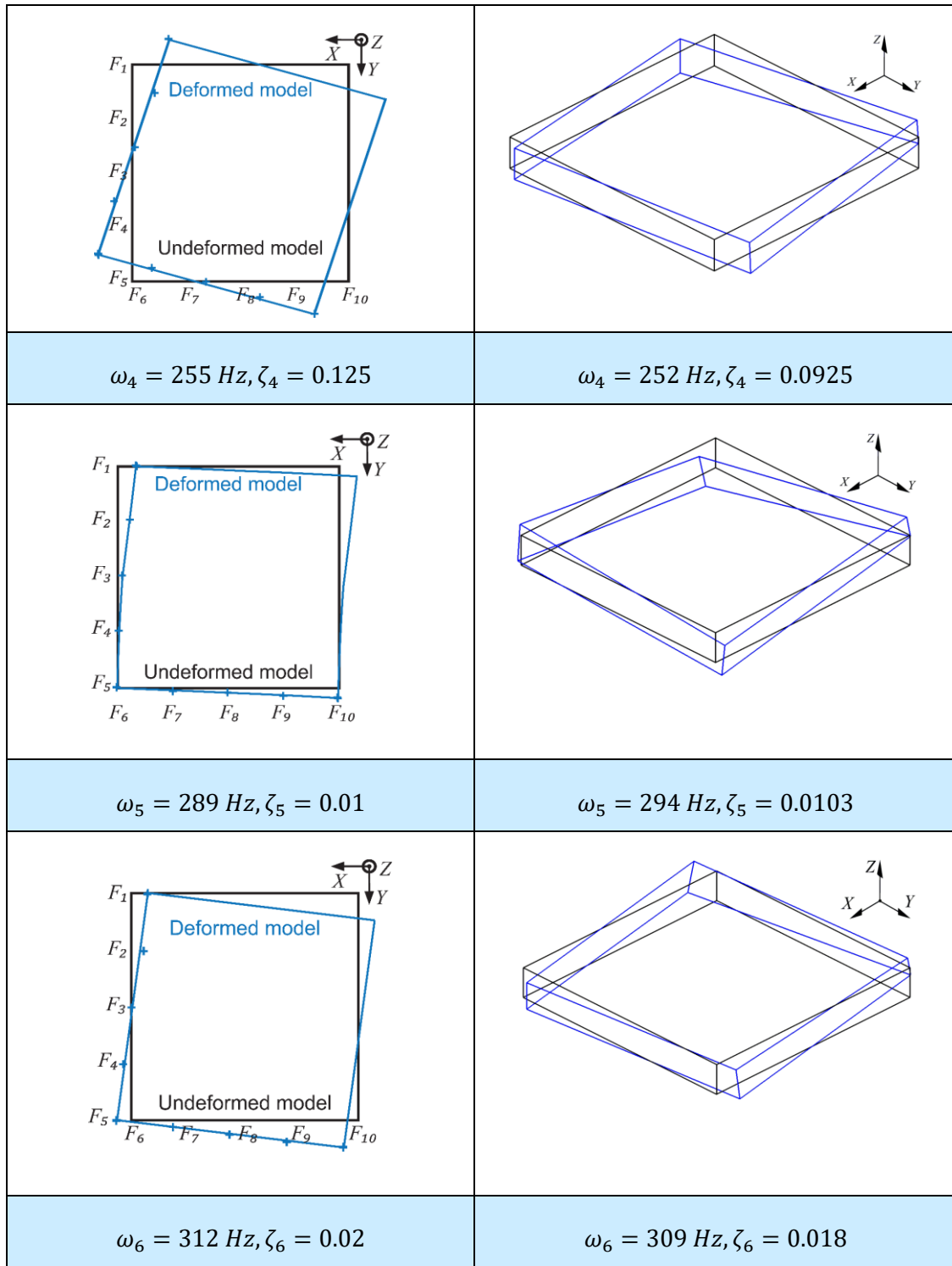


Figure 3.26: Mode shapes of the ball-screw drive, estimated by manual (left) and automated (right) modal analysis methods.

3.12. Conclusions

In this chapter, thorough modeling and identification for the principal experimental setup, a precision ball-screw drive, has been accomplished.

First, the dynamic modeling and identification of the current loop has been realized. For that reason, a PWM driver was initially used to capture the frequency response measured from the rotary and linear encoders. Later, a high bandwidth linear amplifier was integrated to the setup, with the required 3-phase commutation being achieved digitally, in order to command the current loop closed within this amplifier. This step provided nearly 4-fold improvement in the current loop bandwidth, from 388 Hz to 1523 Hz.

Next, rigid body parameters were estimated from time-domain data to capture the low-frequency behavior of the drive system. A two-inertia model was identified to capture both the rigid body and the 1st axial mode vibration dynamics. This model is suitable for vibration damping-based precision positioning control laws, such as pole placement (PPC), which are among the state-of-the-art that was accomplished by earlier researchers prior to this thesis. The identified state-space representation, with rotational and translational encoder feedback, is both controllable and observable. However, the limitation of the two-mass model is that only a single vibration mode can be modeled and compensated. As demonstrated in the latter parts of this thesis, by using the open-loop FRFs measured in this chapter, and the new MIMO model identification algorithm and controller design developed in Chapter 4 and Chapter 5, several vibration modes will be modeled and experimentally compensated simultaneously, to achieve even better disturbance rejection results compared to PPC and the industry-standard P-PI position-velocity cascade control.

The friction, which is one of the main (non-machining) disturbances in the feed drive system, was also identified using both a Stribeck-type static friction model, as well as the generalized dynamic-type Maxwell-slip model, which in the author's best knowledge is currently the most accurate friction model for motion control systems in the literature.

In the last section, vibration modal analysis of the experimental setup was carried out to reveal the spatial behavior of the ball screw drive's vibrations at different frequencies, thus allowing the establishment of deeper insight into the physics of the setup when interpreting the frequency characteristics of the modeling, identification, and controller design results. Essentially, the most significant mode is at 148 Hz, coinciding with the axial vibrations of the ball-screw mechanism. Lower frequency modes were identified at 28 and 48 Hz, which are typically ignored when designing servo controllers. Other modes at 255, 289, and 312 Hz are difficult to damp actively, due to the challenge of exciting these modes through the motor, and also their relatively high frequency, as they require much higher level of energy input.

Chapter 4

Linear Time-Invariant (LTI) Model Identification Algorithm for Mechatronics Systems based on Multi-Input Multi-Output (MIMO) Frequency Response Data

4.1. Introduction

In this chapter, a new MIMO frequency-domain identification algorithm is introduced to estimate the MIMO models, capturing the effects of lightly and highly damped poles on the frequency response, as well as potential direct-transmission or derivative-like terms, and also pure time-delay. To compare the effectiveness of the proposed algorithm with the existing methods, `tfest` and the `modalfit` functions from the MATLAB System Identification [29] and Signal Processing Toolboxes [31] were selected as candidates for performance benchmarking.

In the following, Section 4.2 presents the details of the MIMO model estimation algorithm. Section 4.3 shows step-by-step progression of the algorithm via experimental data from a T-type gantry mechanism for precision motion delivery. The evaluation of the algorithm on a ball screw driven feed drive system is presented in Section 4.4. In Section 4.5, an industry-scale H-type gantry flatbed router is used as the last experimental setup in the evaluation of the system identification algorithm. These case studies have produced models with output-input channels sizes of 2×2 , 1×1 , 2×2 , 4×4 , and 2×1 . Finally, the performance of the newly proposed algorithm is compared with MATLAB's `tfest` function as a general transfer function estimation method, and `modalfit` function as a modal parameter estimation method. The performance of the newly proposed algorithm is compared against MATLAB's `tfest` function as a general transfer function estimation method, and `modalfit` function as a modal parameter estimation tool in Section 4.6. The conclusions of this chapter are presented in Section 4.7.

4.2. MIMO LTI Model Identification Algorithm

4.2.1. Formulation of the MIMO model and overview of the identification algorithm

The general form for a MIMO LTI dynamic system with N_i input channels, clustered in input vector $\mathbf{u} = [u_1 \ \dots \ u_{N_i}]^T$, and N_o output channels, denoted with output vector $\mathbf{y} = [y_1 \ \dots \ y_{N_o}]^T$, can be represented in the Laplace domain with the following expression:

$$\mathbf{y}(s) = \mathbf{G}'(s)\mathbf{u}(s) \rightarrow \begin{bmatrix} y_1(s) \\ \vdots \\ y_{N_o}(s) \end{bmatrix} = \underbrace{\begin{bmatrix} G'_{11}(s) & \dots & G'_{1N_i}(s) \\ \vdots & \ddots & \vdots \\ G'_{N_o1}(s) & \dots & G'_{N_oN_i}(s) \end{bmatrix}}_{\mathbf{G}'} \begin{bmatrix} u_1(s) \\ \vdots \\ u_{N_i}(s) \end{bmatrix} \quad (4.1)$$

In the MIMO model identification algorithm presented henceforth any particular entry $G'_{k_o k_i}(s)$ of the matrix transfer function \mathbf{G}' , which links the input in channel k_i to the response in channel k_o , is assumed to have the following form:

$$G'_{k_o k_i}(s) = G_{k_o k_i}(s) \cdot e^{-T_d s} \quad , \text{ where:} \quad (4.2)$$

$$G_{k_o k_i}(s) = \sum_{k=1}^{n_c} \frac{\beta_k^{k_o k_i} s + \alpha_k^{k_o k_i}}{s^2 + 2\zeta_k \omega_k s + \omega_k^2} + \sum_{k=1}^{n_r} \frac{\gamma_k^{k_o k_i}}{s + p_k} + \delta_0^{k_o k_i} + \delta_1^{k_o k_i} s + \dots + \delta_{d_{k_o k_i}}^{k_o k_i} s^{d_{k_o k_i}}$$

In the above expression, n_c represents the total number of complex conjugate poles, and n_r the number of real poles. As all input and output channels belong to the same physical system, the characteristic equation (i.e., pole locations) are assumed to be common among all input/output transfer functions. The delay term, $e^{-T_d s}$ allows for the detection and removal of any possible pure delay that may be common to all channels (e.g., due ADC/DAC conversion and/or computational latencies encountered in the instrumentation or real-time control platform). Hence, $G_{k_o k_i}(s)$ (without the ‘prime’ symbol) is used to represent the component of the transfer function with the pure delay effect removed. ω_k and ζ_k represent the natural frequency and damping ratio for to the k th complex conjugate pole pair. $-p_k$ represents the location of the k th real pole. $\beta_k^{k_o k_i}$, $\alpha_k^{k_o k_i}$, and $\gamma_k^{k_o k_i}$ define the participation factors (i.e., ‘weights’) needed to combine the contribution of each pole’s response (real or complex conjugate) in constituting the overall response exhibited by the dynamics $G_{k_o k_i}$.

The expansion $\delta_0^{k_o k_i} + \delta_1^{k_o k_i} s + \dots + \delta_{d_{k_o k_i}}^{k_o k_i} s^{d_{k_o k_i}}$ enables the optional inclusion of direct transmission or time derivative-like terms up to order $d_{k_o k_i}$. Their inclusion and order can be individually enabled or disabled, and separately defined for each transfer function channel $G_{k_o k_i}(s)$. For example, if acceleration response is being modelled in response to a force input, $\delta_0^{k_o k_i}$ would be nonzero. Similarly, if an accelerometer signal is considered as the output in response to a position command for a limited frequency range, $\delta_2^{k_o k_i}$ needs to be chosen as nonzero in order to enable the term $\delta_2^{k_o k_i} s^2$. For strictly proper transfer functions, these terms ($\delta_k^{k_o k_i}$, $k = 0, 1, \dots, d_{k_o k_i}$) are all set to zero. Enabling such optional direct terms is

to allow the proposed identification algorithm to work successfully with experimental data gathered simultaneously from a variety of sensors.

In an LTI dynamic system, complex conjugate poles can either possess light damping ($\zeta_k \leq \zeta_c$, e.g. $\zeta_c \approx 0 \dots 0.2$) and lead to easily noticeable resonances in the frequency response function (FRF), or assume higher damping values ($\zeta_c < \zeta_k < 0.707$) making their resonances subtle and spread over wider frequency band. In the damping interval $0.707 \leq \zeta_k < 1.0$, no resonance is generated, but the presence of complex conjugate poles still affects the magnitude and phase characteristics [127].

Typical practice in frequency domain system identification is to discern the resonances (local magnitude maxima) contributed by the most significant vibration modes, sometimes via manual inspection, and to select frequency ranges around these modes to be used in local model fitting. In the expression for $G_{k_o k_i}(s)$, the dynamics contributed by the complex conjugate poles can be separated into two groups:

Group 1: n_{c1} pole pairs which lead to resonances that can be clearly distinguished and selected by a user or an automated algorithm. This facilitates semi-decoupled estimation of the modal parameters like ω_k , and ζ_k from the rest of the dynamics.

Group 2: $n_{c2} = n_c - n_{c1}$ pole pairs, which lead to either subtle resonances or none at all. They exhibit a more gradual magnitude and phase transition, thus are more difficult to spot via manual inspection. These poles can still be estimated via numerical methods, such as the fitting of a higher order transfer function. In this case, these poles are estimated together with the dynamics contributed by other nearby poles, which also exert their influence in the frequency range of interest in a superposed manner.

Based on the above separation, $G_{k_o k_i}(s)$ in Eq. (4.2) can be rewritten in the following form:

$$G_{k_o k_i}(s) = \underbrace{\sum_{k=1}^{n_{c1}} \frac{\beta_k^{k_o k_i} s + \alpha_k^{k_o k_i}}{s^2 + 2\zeta_k \omega_k s + \omega_k^2}}_{C_{k_o k_i}(s)} + \underbrace{\sum_{k=n_{c1}+1}^{n_c} \frac{\beta_k^{k_o k_i} s + \alpha_k^{k_o k_i}}{s^2 + 2\zeta_k \omega_k s + \omega_k^2}}_{L_{k_o k_i}(s)} + \underbrace{\sum_{k=1}^{n_r} \frac{\gamma_k^{k_o k_i}}{s + p_k}}_{R_{k_o k_i}(s)} + \underbrace{\delta_0^{k_o k_i} + \delta_1^{k_o k_i} s + \dots + \delta_{d_{k_o k_i}}^{k_o k_i} s^{d_{k_o k_i}}}_{D_{k_o k_i}(s)} \quad (4.3)$$

where:

$C_{k_o k_i}(s)$: Dynamics due to complex conjugate poles which cause significant resonance

$L_{k_o k_i}(s)$: Dynamics due to complex conjugate poles with little or no resonance

$R_{k_o k_i}(s)$: Dynamics due to real poles (no resonance)

$D_{k_o k_i}(s)$: Dynamics due to direct transmission and/or derivative-like effects

Another way of expressing $G_{k_o k_i}(s)$ would be to combine the dynamics of all terms, excluding the complex conjugate poles with significant resonance contribution, into a single rational transfer function

$T_{k_o k_i}(s)$:

$$G_{k_o k_i}(s) = \underbrace{\sum_{k=1}^{n_{c1}} \frac{\beta_k^{k_o k_i} s + \alpha_k^{k_o k_i}}{s^2 + 2\zeta_k \omega_k s + \omega_k^2}}_{C_{k_o k_i}(s)} + \underbrace{\frac{b_0^{k_o k_i} s^{m_{k_o k_i}} + b_1^{k_o k_i} s^{m_{k_o k_i}-1} + \dots + b_{m_{k_o k_i}}^{k_o k_i}}{s^n + a_1 s^{n-1} + \dots + a_n}}_{T_{k_o k_i}(s)} \quad (4.4)$$

$$= C_{k_o k_i}(s) + T_{k_o k_i}(s)$$

By inspecting the number of the complex and real poles n_{c1} , n_{c2} , n_r , and the presence and order (denoted by $d_{k_o k_i}$) of any direct terms in Eq. (4.3), it can be verified that the numerator and denominator orders ($m_{k_o k_i}$ and n) for the rational transfer function $T_{k_o k_i}(s)$ in Eq. (4.4) must satisfy:

$$n = 2n_{c2} + n_r \quad (4.5)$$

$$m_{k_o k_i} = \begin{cases} 2n_{c2} + n_r - 1 & \text{if } \delta_0 = 0, \delta_1 = 0, \dots, \delta_d = 0 \Rightarrow \text{no direct terms} \\ 2n_{c2} + n_r + d_{k_o k_i} & \text{if } \delta_0 \neq 0 \text{ or } \dots \text{ or } \delta_d \neq 0 \Rightarrow \text{highest order direct term: } d_{k_o k_i} \end{cases}$$

Considering the different formats in Eq. (4.2)-(4.4) to represent $G_{k_o k_i}(s)$, the following observations can be made:

⇒ Eq. (4.2) is useful for reconstructing the overall response from the simultaneous influence of all terms, especially during the task of further optimizing the locations of the poles once their approximate value and type (complex or real) are determined. For a candidate set of pole locations being tested, this formulation enables the best fitting participation factors ($\alpha_k^{k_o k_i}$, $\beta_k^{k_o k_i}$, $\gamma_k^{k_o k_i}$, $\delta_k^{k_o k_i}$) to be conveniently calculated using LS (Least Squares) parameter estimation.

⇒ Eq. (4.3) is helpful in estimating complex conjugate poles, which have very low damping ($\zeta_k < \zeta_c$). Such poles exert strong influence on $G_{k_o k_i}(s)$ within a narrow frequency band centered around their resonance [79]. In this format, the dynamics contributed by each oscillatory mode ‘ r ’ ($r \in \{1, \dots, n_{c1}\}$)

are estimated by distinguishing their influence from those of the other lightly damped poles. The remainder dynamics are captured with the terms $L_{k_o k_i}(s)$, $R_{k_o k_i}(s)$, and $D_{k_o k_i}(s)$.

⇒ Eq. (4.4) enables the estimation of the combined remainder dynamics contributed by the complex poles with significant damping, the real poles, and the direct or derivative-like terms, using a single rational transfer function $T_{k_o k_i}(s)$ to capture their influences. Comparing Eq. (4.3) and (4.4), it can be seen that $T_{k_o k_i}(s) = L_{k_o k_i}(s) + R_{k_o k_i}(s) + D_{k_o k_i}(s)$. Estimation of $T_{k_o k_i}(s)$ is accomplished after the estimated dynamics with the lightly damped poles in $C_{k_o k_i}(s)$ are subtracted from the measured FRFs, which have also been corrected for pure delays.

Based on the above formulations, the proposed identification strategy is presented, from a bird's eye view, as illustrated in Figure 4.1.

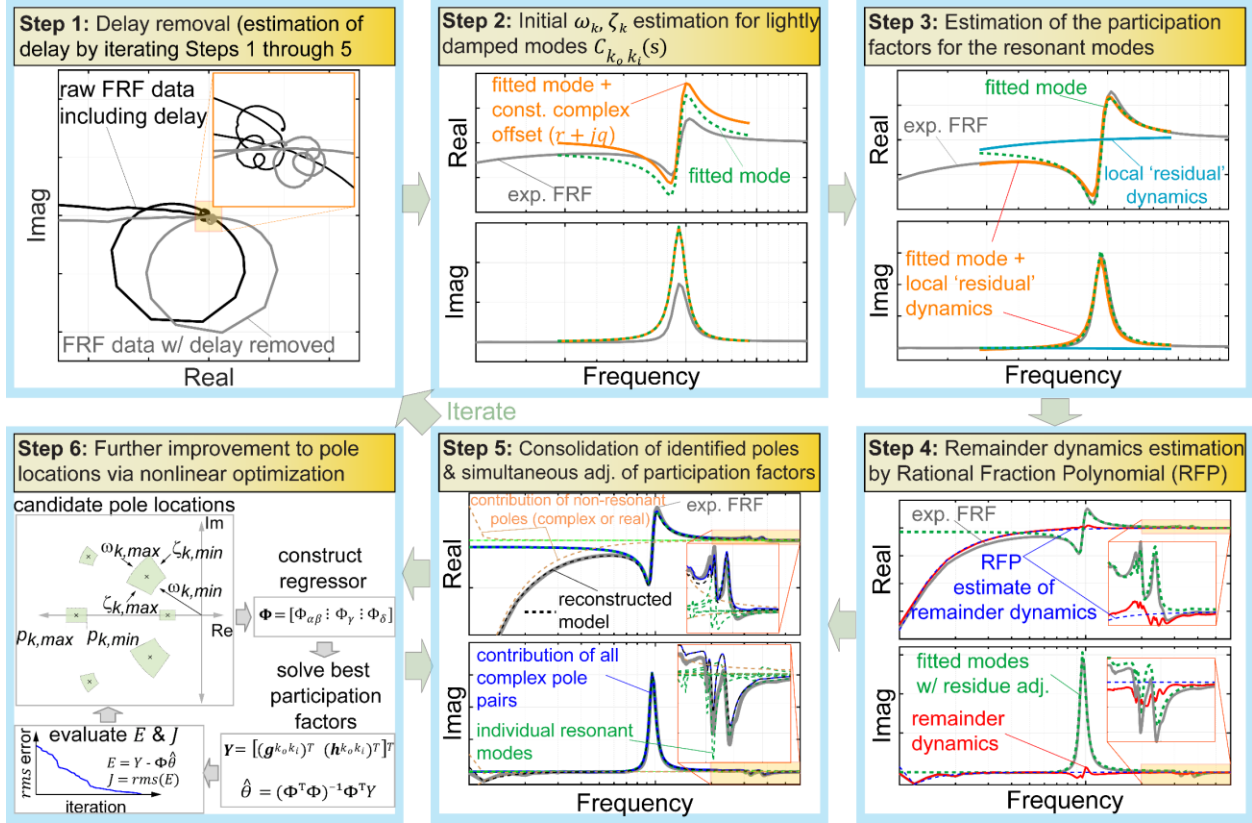


Figure 4.1. Flow chart for the proposed identification algorithm.

Considering Figure 4.1, in Step 1 the pure delay is estimated and removed from the FRF measurement data. In Step 2, the lightly damped (resonant) modes are determined by using a 'mode indicator function', and their natural frequency (ω_k) and damping ratio (ζ_k) are individually estimated. In Step 3, the

corresponding participation factors ($\beta_k^{k_o k_i}$ and $\alpha_k^{k_o k_i}$) for the resonant modes are calculated. In Step 4, the remainder dynamics represented with the expression $T_{k_o k_i}(s)$ (in Eq. (4.4)) are estimated, by removing the influence of the lightly damped modes determined in Steps 2 and 3 from the delay-corrected measurement FRF. In Step 5, all estimated dynamics are consolidated and reformatted into the form in Eq. (4.2) (i.e., separating the contributions of complex conjugate poles, real poles, and direct or derivative-like terms). In this step, the participation factors ($\alpha_k^{k_o k_i}$, $\beta_k^{k_o k_i}$, $\gamma_k^{k_o k_i}$, $\delta_k^{k_o k_i}$) are also updated to yield a further optimal fit, in the presence of each of the dynamic terms weighted by these terms. Finally, in Step 6, a nonlinear optimization is invoked targeting further improvement to the model, by perturbing the pole locations into new candidate locations and updating the best fitting participation factors for each candidate set of poles.

As currently described, the algorithm puts the same level of weighting on every output/input channel data. However, in a situation where the MIMO transfer function entries for $G_{k_o k_i}$ may have significantly different magnitude, for example due to a variety of different physical outputs and/or input sources being considered, the best practice would be to apply prior scaling to the raw MIMO frequency response data, to ensure that a good numerical fit can be achieved across all output/input channels [25][27]. On the other hand, if certain entries for the estimated MIMO transfer function require a higher degree of accuracy in fitting, adequate weighting to further emphasize certain output/input channels can also be introduced into the objective functions which are minimized during Steps 2-6, similar to the concept of Weighted Least Squares (WLS) [128]. To keep the presentation in this thesis focused on the main identification algorithm, the topics of signal scaling and objective function weighting have been kept outside the scope of this thesis.

4.2.2. Details of the algorithm considering an LTI model

The mathematical details of each step are presented in the proceeding subsections (4.2.2.1–4.2.2.6). The direct application of each step to experimental data, obtained from a MIMO mechatronic system, is demonstrated in Section 4.3.

4.2.2.1. Step 1: Time delay estimation and removal

To correctly estimate the poles and zeros of a transfer function, any pure delay originating from the electro-mechanical system’s dynamics itself, the associated instrumentation, or the real-time data acquisition and control system must be accurately identified and removed. Otherwise, the phase lag introduced by such delays can cause an error in the estimation of the poles and zeros. In Figure 4.1, the first panel labeled ‘Step 1’ clearly illustrates this effect, in which the real and imaginary components of the FRF may get shifted, or even switch polarity, due to the influence of pure delay.

The methodology in this thesis assumes one single delay value τ_d , which applies to all input/output channels, per Eq. (4.2). While it is possible to extend the idea to consider different delay values for different input/output channels, in the scope of experimental validations performed in this research, a single delay value was sufficient.

It is assumed that frequency response measurements for the SISO or MIMO system to be identified are available as an array of complex numbers $\mathbf{H}'_1, \dots, \mathbf{H}'_N \in \mathbb{C}^{N_o \times N_i}$ at discrete frequency values ω_i [rad/s] for $i = 1, \dots, N$. If the pure delay amount is known or estimated, then its frequency response $H_{delay}(\omega_i)$ can be computed as follows:

$$H_{delay}(\omega_i) = \exp(-j\omega_i T_d) = \cos(T_d \omega_i) - j \cdot \sin(T_d \omega_i) \quad (4.6)$$

Hence, the FRF measurement can be corrected for the assumed pure delay as:

$$\begin{aligned} \mathbf{H}_i &= [H_{delay}(\omega_i)]^{-1} \mathbf{H}'_i = [\cos(T_d \omega_i) + j \sin(T_d \omega_i)] \cdot \mathbf{H}'_i = \underbrace{\text{Re}\{\mathbf{H}_i\}}_{\mathbf{g}_i} + j \underbrace{\text{Im}\{\mathbf{H}_i\}}_{\mathbf{h}_i} \\ &= \mathbf{g}_i + j\mathbf{h}_i \end{aligned} \quad (4.7)$$

In scalar form, the delay-corrected FRF relating output channel k_o to input in channel k_i can be expressed as:

$$H_{k_o k_i}(\omega_i) = g^{k_o k_i}(\omega_i) + j h^{k_o k_i}(\omega_i) = g_i^{k_o k_i} + j h_i^{k_o k_i} \quad (4.8)$$

In implementing the identification algorithm in Figure 4.1, τ_d is iterated by testing a range of predefined delay values $\tau_d \in [\tau_{d,\min}, \tau_{d,\max}]$, and executing Steps 1 through 6. The candidate for τ_d , which leads to the smallest discrepancy between the experimental FRF data and the frequency response for the overall estimated model, is identified as the best estimate of the system's pure delay. Naturally, having a close initial value obtained through inspection of the raw FRF measurements for a linearly decreasing trend in the phase also helps in the estimation.

4.2.2.2. Step 2: Initial estimation of natural frequency and damping ratio for resonant modes

After having removed the pure delay in Step 1, frequencies belonging to the lightly damped poles are determined by inspecting the Complex Mode Indicator Function (CMIF). The MIMO frequency response $\mathbf{H}_i = \mathbf{H}(\omega_i)$ can be expressed for each frequency ω_i as a Singular Value Decomposition (SVD) [25]:

$$\mathbf{H}(\omega_i) = [\mathbf{U}(\omega_i)] \cdot [\mathbf{\Sigma}(\omega_i)] \cdot [\mathbf{V}(\omega_i)]^H \quad (4.9)$$

Above, $[\mathbf{V}(\omega_i)]_{N_i \times N_i} = [\mathbf{v}_1(\omega_i) \ \dots \ \mathbf{v}_{N_i}(\omega_i)]$ and $[\mathbf{U}(\omega_i)]_{N_o \times N_o} = [\mathbf{u}_1(\omega_i) \ \dots \ \mathbf{u}_{N_o}(\omega_i)]$ are, in the mentioned order, unitary matrices containing the input and output singular vectors as a function of frequency. The singular value matrix $[\mathbf{\Sigma}(\omega_i)]_{N_o \times N_i}$, which has non-zero entries only along its diagonal, contains the gains which relate how different input combinations (i.e., directions), defined with the input singular vectors $\mathbf{v}_k(\omega_i)$, propagate into the output channels via the output singular vectors $\mathbf{u}_k(\omega_i)$. Using the SVD, the CMIF is computed as [24]:

$$[\mathbf{CMIF}(\omega_i)]_{N_i \times N_i} = [\mathbf{\Sigma}(\omega_i)]^T \cdot [\mathbf{\Sigma}(\omega_i)] \quad (4.10)$$

Sample CMIFs for a SISO and a 2x2 MIMO dynamic system are shown in Figure 4.2. These belong to the single motor (x-axis) and double motor (y-axis) responses of the linear motor driven T-type gantry, shown in Figure 4.4.

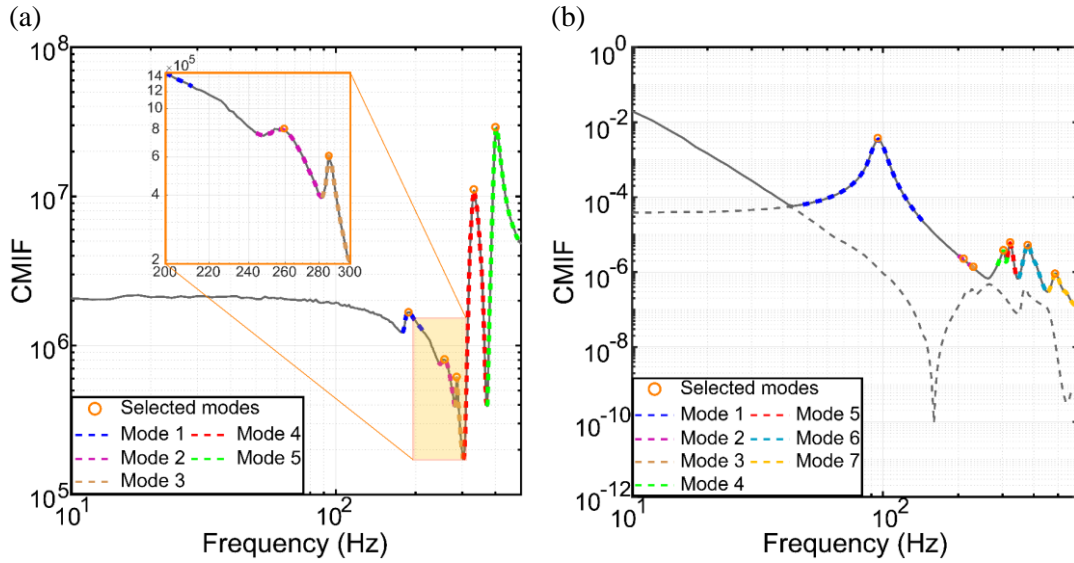


Figure 4.2: Use of the CMIF in identifying resonant frequencies and selecting frequency ranges to fit individual modes: (a) acceleration response to torque command for single-axis linear motor drive. (b) position response to torque command due a dual linear motor driven gantry axis.

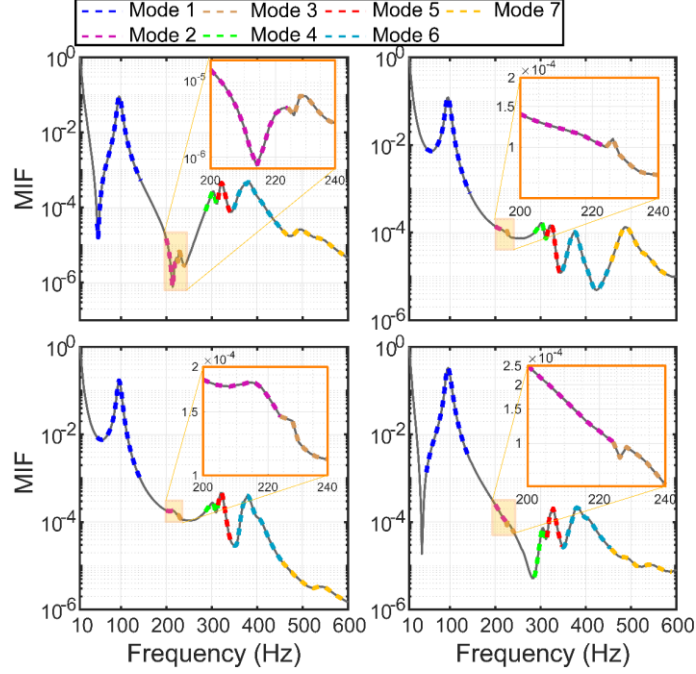


Figure 4.3: Use of the SISO MIF in identifying resonant frequencies and selecting frequency ranges to fit individual modes: position response to torque command for a dual linear motor-driven gantry axis.

The normalized MIF of the individual SISO transfer functions for the 2×2 MIMO dynamic system in Figure 4.2b is illustrated in Figure 4.3. The SISO MIFs are used as supplementary information for revealing more modes than the dominant ones. In this case, the 2nd and the 3rd modes can be observed more visibly from Figure 4.3.

$$MIF_{k_o k_i}(\omega_i) = \mathbf{H}_{k_o k_i}(\omega_i) \circ \bar{\mathbf{H}}_{k_o k_i}(\omega_i) \quad (4.11)$$

Above, the operator ‘ $A \circ B$ ’ designates Hadamard (i.e., element-wise) product of two arrays. The normalized MIF can be expressed by $MIF_{k_o k_i}(\omega_i) \circ (1/\max(MIF_{k_o k_i}(\omega_i)))$.

Inspection of the CMIF reveals the frequencies at which resonance is observed, attributed to the lightly damped modes. The CMIF also aids in the selection of suitable frequency ranges to approximately identify the parameters for these modes in a decoupled manner (i.e., one mode at a time). For example, around the vicinity of mode k , the frequency response data can be selected by indexing the range $[i_k^-, i_k^+]$, where $1 \leq i_k^- < i_k^+ \leq N$. The extracted frequency array $\boldsymbol{\omega}$ and corresponding real and imaginary response arrays \mathbf{g} and \mathbf{h} are defined as:

$$\boldsymbol{\omega} = [\omega_{i_k^-} \quad \dots \quad \omega_{i_k^+}]^T, \quad \mathbf{g} = [g(\omega_{i_k^-}) \quad \dots \quad g(\omega_{i_k^+})]^T = [g_{i_k^-} \quad \dots \quad g_{i_k^+}]^T \quad (4.12)$$

$$\mathbf{h} = [h(\omega_{i_k^-}) \quad \dots \quad h(\omega_{i_k^+})]^T = [h_{i_k^-} \quad \dots \quad h_{i_k^+}]^T, \quad \text{number of data points: } N_k = i_k^+ - i_k^- + 1$$

As known from vibration modal analysis and control literature [24][79], the frequency response of a system near one of its lightly damped modes (i.e., complex conjugate poles) with natural frequency ω_k can be approximated by the response contributed solely by that mode; which constitutes most of the magnitude contribution around ω_k , when the damping ratio associated with that mode ζ_k is relatively small (e.g., <0.05). However, as can be verified from Eq. (4.3), other poles at frequencies below and above this mode also present a frequency response influence around ω_k . For the purpose of estimating ω_k and ζ_k , which is done in a narrow frequency band around the resonance, the response contributed by the other dynamics (which demonstrate more gradual transition in the same frequency band) can be captured using a constant complex offset ($r^{k_o k_i} + jq^{k_o k_i}$). Thus, the FRF of the model in Eq. (4.3) can be approximated as:

$$\underbrace{G_{k_o k_i}(\omega)}_{\text{FRF of model}} \cong \underbrace{\frac{j\omega\beta_k^{k_o k_i} + \alpha_k^{k_o k_i}}{\omega_k^2 - \omega^2 + j2\zeta_k\omega_k\omega}}_{\text{mode 'k' - which is being fitted}} + \underbrace{\frac{r_k^{k_o k_i} + jq_k^{k_o k_i}}{\text{offset contributed}}}_{\text{by poles other than of mode 'k'}}, \quad \text{for } \omega \approx \omega_k \quad (4.13)$$

Equating the real and imaginary components of the model FRF with those obtained from the delay-corrected measurement ($H_{k_o k_i}(\omega) = g^{k_o k_i}(\omega) + jh^{k_o k_i}(\omega)$), ω_k and ζ_k can be solved by setting up a Least Squares parameter estimation problem. For notation simplification, initially considering only the SISO case, the output/input channel designations (i.e., superscript or subscript of ' $k_o k_i$ ') are dropped. Also, for mathematical convenience, two new auxiliary variables are defined as:

$$u = \omega_k^2, \quad v = 2\zeta_k\omega_k \quad \Leftrightarrow \quad \omega_k = \sqrt{u}, \quad \zeta_k = v/(2\sqrt{u}) \quad (4.14)$$

The model error, representing the discrepancy between the measurement and the model prediction can be expressed as $E(\omega) = H(\omega) - G(\omega)$. This should, in the ideal case, be equal to zero:

$$E(\omega) = H(\omega) - G(\omega) = g(\omega) + jh(\omega) - r - jq - \frac{j\omega\beta + \alpha}{u - \omega^2 + j\omega v} = 0 \quad (4.15)$$

Eq. (4.15) implies that both the real and imaginary components of $E(\omega)$ should be zero, leading to:

$$\left. \begin{aligned} \text{Re}\{E(\omega)\} = 0 &\Rightarrow \omega^{-2}g(\omega)u - \omega^{-2}ru + r - \omega^{-1}h(\omega)v + \omega^{-1}qv - \omega^{-2}\alpha = g(\omega) \\ \text{Im}\{E(\omega)\} = 0 &\Rightarrow \omega^{-2}h(\omega)u - \omega^{-2}qu + q + \omega^{-1}g(\omega)v - \omega^{-1}rv - \omega^{-1}\beta = h(\omega) \end{aligned} \right\} \quad (4.16)$$

The unknown variables that need to be identified can be ordered inside a parameter vector, defined as:

$$\boldsymbol{\theta} = [u \ v \ ru \ qu \ rv \ qv \ r \ q \ \alpha \ \beta]^T \quad (4.17)$$

This enables for the expressions in Eq. (4.16) to be written in a regressor (Φ') - parameter ($\boldsymbol{\theta}$), and observation/output (\mathbf{Y}') format, which is regularly used in Least Squares parameter estimation [128]:

$$\begin{aligned} \Phi' &= \left[\begin{array}{cccccccccc} \omega^{-2}g(\omega) & -\omega^{-1}h(\omega) & -\omega^{-2} & 0 & 0 & \omega^{-1} & 1 & 0 & -\omega^{-2} & 0 \\ \omega^{-2}h(\omega) & \omega^{-1}g(\omega) & 0 & -\omega^{-2} & -\omega^{-1} & 0 & 0 & 1 & 0 & -\omega^{-1} \end{array} \right] \\ \mathbf{Y}' &= [g(\omega) \ h(\omega)]^T \end{aligned} \quad (4.18)$$

In Eq. (4.18), the regressor and output expressions are based on an FRF value at only a single frequency, ω . Generalizing this formulation to consider the selected data range in arrays $\boldsymbol{\omega}$, \mathbf{g} , \mathbf{h} in Eq. (4.12), the regressor matrix (Φ) and output (observation) vector (\mathbf{Y}) can be re-written in the following format:

$$\begin{aligned} \Phi &= \left[\begin{array}{cccccccccc} \boldsymbol{\omega}^{\circ-2} \circ \mathbf{g} & -\boldsymbol{\omega}^{\circ-1} \circ \mathbf{h} & -\boldsymbol{\omega}^{\circ-2} & \mathbf{0} & \mathbf{0} & \boldsymbol{\omega}^{\circ-1} & \mathbf{1} & \mathbf{0} & -\boldsymbol{\omega}^{\circ-2} & \mathbf{0} \\ \boldsymbol{\omega}^{\circ-2} \circ \mathbf{h} & \boldsymbol{\omega}^{\circ-1} \circ \mathbf{g} & \mathbf{0} & -\boldsymbol{\omega}^{\circ-2} & -\boldsymbol{\omega}^{\circ-1} & \mathbf{0} & \mathbf{0} & \mathbf{1} & \mathbf{0} & -\boldsymbol{\omega}^{\circ-1} \end{array} \right] \\ \mathbf{Y} &= [\mathbf{g}^T \ \mathbf{h}^T]^T \end{aligned} \quad (4.19)$$

$\boldsymbol{\omega}^{\circ X}$ represents the Hadamard power operator which takes each entry in vector $\boldsymbol{\omega}$ to its X th power. $\mathbf{1}$ and $\mathbf{0}$ are arrays full of ones and zeros, respectively, with the adequate dimensions ($N_k \times 1$).

The optimal parameter set can be solved using the Least Squares formulation [128], leading to:

$$\hat{\boldsymbol{\theta}} = [\hat{u} \ \hat{v} \ \hat{ru} \ \hat{qu} \ \hat{rv} \ \hat{qv} \ \hat{r} \ \hat{q} \ \hat{\alpha} \ \hat{\beta}]^T = (\Phi^T \Phi)^{-1} \Phi^T \mathbf{Y} \quad (4.20)$$

The only two parameters of interest in this step are u and v , which help determine a close estimate for the natural frequency ω_k and damping ratio ζ_k , per Eq. (4.14). The other eight parameters (ru, \dots, β) are discarded. The mode participation factors α and β , are estimated later in Step 3 of the overall algorithm (Figure 4.1), using the ω_k, ζ_k values computed during this current step, and are further refined during Steps 5 and 6 of the overall algorithm.

To extend this idea to the case of working with MIMO FRF data, the output/input channel designation ' $k_o k_i$ ' is reintroduced into the notation. Hence, the following measurement data is assumed to be available and preselected in the vicinity of ω_k for each output/input channel pair:

$$\begin{aligned}
\boldsymbol{\omega} &= [\omega_{i_k^-} \quad \dots \quad \omega_{i_k^+}]^T, \quad \mathbf{g}^{k_o k_i} = [g^{k_o k_i}(\omega_{i_k^-}) \quad \dots \quad g^{k_o k_i}(\omega_{i_k^+})]^T = [g_{i_k^-}^{k_o k_i} \quad \dots \quad g_{i_k^+}^{k_o k_i}]^T \\
\mathbf{h}^{k_o k_i} &= [h^{k_o k_i}(\omega_{i_k^-}) \quad \dots \quad h^{k_o k_i}(\omega_{i_k^+})]^T = [h_{i_k^-}^{k_o k_i} \quad \dots \quad h_{i_k^+}^{k_o k_i}]^T, \\
1 &\leq k_o \leq N_o, \quad 1 \leq k_i \leq N_i
\end{aligned} \tag{4.21}$$

Considering Eq. (4.13), the first two entries of $\boldsymbol{\theta}$ in Eq. (4.17) ($u = \omega_k^2$ and $v = 2\zeta_k \omega_k$) have to be common across all output/input channels. However, the other entries for the parameter vector (i.e., the terms $(r^{k_o k_i} u), \dots, (\beta^{k_o k_i})$ per Eq. (4.17)), are specific to the output-input channel designation $k_o k_i$. Hence, the parameter vector in Eq. (4.17) can be partitioned into a common portion $\boldsymbol{\theta}_{uv}$, and channel-specific individual portions $\boldsymbol{\xi}^{k_o k_i}$:

$$\begin{aligned}
\boldsymbol{\theta}^{k_o k_i} &= [\boldsymbol{\theta}_{uv}^T \quad \vdots \quad \boldsymbol{\xi}^{k_o k_i T}]^T, \quad \boldsymbol{\theta}_{uv} = [u \quad v]^T \\
\boldsymbol{\xi}^{k_o k_i} &= [r^{k_o k_i} u \quad q^{k_o k_i} u \quad r^{k_o k_i} v \quad q^{k_o k_i} v \quad r^{k_o k_i} \quad q^{k_o k_i} \quad \alpha^{k_o k_i} \quad \beta^{k_o k_i}]^T
\end{aligned} \tag{4.22}$$

Reapplying Eq. (4.18) - (4.19), the regressor matrix Φ can thus be written for the output/input response pair $k_o k_i$ in partitioned form, according to the definition of $\boldsymbol{\theta}^{k_o k_i}$ in Eq. (4.22). Also, the notation for the output (observation) array \mathbf{Y} can be augmented with the superscript $k_o k_i$, to designate the output/input channels to which the data applies:

$$\begin{aligned}
\Phi^{k_o k_i} &= [\Phi_{uv}^{k_o k_i} \quad \vdots \quad \Gamma], \quad \Phi_{uv}^{k_o k_i} = \begin{bmatrix} \omega^{\circ-2} \circ \mathbf{g}^{k_o k_i} & -\omega^{\circ-1} \circ \mathbf{h}^{k_o k_i} \\ \omega^{\circ-2} \circ \mathbf{h}^{k_o k_i} & \omega^{\circ-1} \circ \mathbf{g}^{k_o k_i} \end{bmatrix} \\
\Gamma &= \begin{bmatrix} -\omega^{\circ-2} & \mathbf{0} & \mathbf{0} & \omega^{\circ-1} & \mathbf{1} & \mathbf{0} & -\omega^{\circ-2} & \mathbf{0} \\ \mathbf{0} & -\omega^{\circ-2} & -\omega^{\circ-1} & \mathbf{0} & \mathbf{0} & \mathbf{1} & \mathbf{0} & -\omega^{\circ-1} \end{bmatrix}, \quad \mathbf{Y}^{k_o k_i} = \begin{bmatrix} \mathbf{g}^{k_o k_i} \\ \mathbf{h}^{k_o k_i} \end{bmatrix}
\end{aligned} \tag{4.23}$$

Now, considering a $N_o \times N_i$ MIMO system's response, the complete set of regressors (Φ), parameters ($\boldsymbol{\theta}$), and output arrays (\mathbf{Y}) needed to define and solve a LS parameter estimation problem can be written as:

$$\Phi = \begin{bmatrix} \Phi_{uv}^{11} & \Gamma & \mathbf{0} & & & & & & \mathbf{0} \\ \vdots & \mathbf{0} & \ddots & & & & & & \mathbf{0} \\ \Phi_{uv}^{1N_i} & & & \Gamma & & & & & \\ \vdots & & & & \ddots & & & & \\ \Phi_{uv}^{N_o 1} & & & & & \Gamma & & & \\ \vdots & & & & & & \ddots & & \mathbf{0} \\ \Phi_{uv}^{N_o N_i} & \mathbf{0} & \mathbf{0} & & & & \mathbf{0} & \Gamma & \end{bmatrix}, \quad \mathbf{Y} = \begin{bmatrix} \mathbf{Y}_{uv}^{11} \\ \vdots \\ \mathbf{Y}_{uv}^{1N_i} \\ \vdots \\ \mathbf{Y}_{uv}^{N_o 1} \\ \vdots \\ \mathbf{Y}_{uv}^{N_o N_i} \end{bmatrix}, \quad \boldsymbol{\theta} = \begin{bmatrix} \boldsymbol{\theta}_{uv} \\ \boldsymbol{\xi}^{11} \\ \vdots \\ \boldsymbol{\xi}^{1N_i} \\ \vdots \\ \boldsymbol{\xi}^{N_o 1} \\ \vdots \\ \boldsymbol{\xi}^{N_o N_i} \end{bmatrix} \tag{4.24}$$

Above, the symbol $\mathbf{0}$ represents a block array of zeros with the adequate dimension of $(2N_k \times 8)$. The optimal solution in the MIMO case, similar to that in Eq. (4.20), assumes the form:

$$\hat{\boldsymbol{\theta}} = [\hat{u} \quad \hat{v} \quad ; \quad (\hat{\xi}^{11})^T \quad \dots \quad (\hat{\xi}^{1N_i})^T \quad \dots \quad (\hat{\xi}^{N_o1})^T \quad \dots \quad (\hat{\xi}^{N_oN_i})^T]^T = (\boldsymbol{\Phi}^T \boldsymbol{\Phi})^{-1} \boldsymbol{\Phi}^T \mathbf{Y} \quad (4.25)$$

Once again only the first two terms (\hat{u} , \hat{v}) are of interest are kept, which now enable the optimal estimates $\hat{\omega}_k$ and $\hat{\zeta}_k$ based on the available multi-channel frequency response data in the selected range $[\omega_{i_k^-}, \omega_{i_k^+}]$. If data from certain measurement channels are missing (e.g., $\overline{k_o k_i}$), then their corresponding block entries can be removed from the construction of $\boldsymbol{\Phi}$, \mathbf{Y} , and $\boldsymbol{\theta}$ in Eq. (4.24), and estimation of the best-fit natural frequency and damping can still proceed with partially available data.

4.2.2.3. Step 3: Estimation of the participation factors for the resonant modes

Once approximate values for ω_k and ζ_k are determined, the next step is to find close values for the participation factors $\beta_k^{k_o k_i}$ and $\alpha_k^{k_o k_i}$. In doing so, the frequency response of the model is approximated by the contribution coming from the mode of interest, as well as residual terms. In this case, the residual terms are further refined compared to the earlier step of just considering a complex offset, as shown in Eq. (4.26).

$$G_{approx}^{k_o k_i}(\omega) = \underbrace{\frac{\bar{a}}{(j\omega)^2} + \frac{\bar{b}}{j\omega} + \bar{c} + (j\omega)\bar{d}}_{\text{residual terms}} + \underbrace{\frac{j\omega\beta_k^{k_o k_i} + \alpha_k^{k_o k_i}}{\omega_k^2 - \omega^2 + j2\zeta_k\omega_k\omega}}_{\text{mode being fitted}} \quad (4.26)$$

While the main purpose of this step is to estimate only the participation factors ($\beta_k^{k_o k_i}$ and $\alpha_k^{k_o k_i}$) at the mode of interest, frequency response contributions from other dynamics also need to be captured and isolated adequately, to avoid biasing the estimates for β and α terms. As noticeable, rather than using only a complex constant offset to capture the residual dynamics, as is done in Step 2, a more elaborate structure is proposed. For example, as noted in [24], vibration modes with lower frequency than ω_k would collectively contribute a mass-like (i.e., double-integrator) influence, which can be captured with the $(j\omega)^{-2}\bar{a}$ term. Vibration modes with higher frequency than ω_k would collectively contribute a stiffness-like effect, which can be captured with real scalar constant \bar{c} . Furthermore, to keep the removal of residual dynamics as general as possible, a single integrator and single derivative type term ($(j\omega)^{-1}\bar{b}$ and $(j\omega)\bar{d}$) are also included. This is because realistic mechatronic systems may have additional dynamics originating from well-damped poles, sensors, actuators, or various filtering and feedback control effects. The combined influence of such effects are captured and kept apart from $\beta_k^{k_o k_i}$ and $\alpha_k^{k_o k_i}$ by estimating their contributions

through the coefficients \bar{a} , \bar{b} , \bar{c} , \bar{d} . However, these auxiliary coefficients are not stored permanently. After fulfilling their principal duty of helping in the estimation of $\beta_k^{k_o k_i}$ and $\alpha_k^{k_o k_i}$, they are discarded.

To facilitate convenience in the formulation and computations, an auxiliary frequency response function G_2 is defined, representing a scaled version of the current mode's receptance (i.e., dynamic compliance) characteristic:

$$G_2(\omega) = \frac{1}{\omega_k^2 - \omega^2 + j2\zeta_k \omega_k \omega}, \text{ where: } g_2(\omega) = \text{Re}\{G_2(\omega)\}, h_2(\omega) = \text{Im}\{G_2(\omega)\} \quad (4.27)$$

Thus, the real and imaginary components of $G_{approx}^{k_o k_i}(\omega)$ in Eq. (4.26) can be re-expressed as,

$$\begin{aligned} \text{Re}\{G_{approx}^{k_o k_i}(\omega)\} &= g_2(\omega)\alpha_k^{k_o k_i} - \omega h_2(\omega)\beta_k^{k_o k_i} - \omega^{-2}\bar{a} + \bar{c} \\ \text{Im}\{G_{approx}^{k_o k_i}(\omega)\} &= h_2(\omega)\alpha_k^{k_o k_i} + \omega g_2(\omega)\beta_k^{k_o k_i} - \omega^{-1}\bar{b} + \omega\bar{d} \end{aligned} \quad (4.28)$$

The objective is to represent the delay-corrected experimental FRF data for output/input channel $k_o k_i$ with the approximation $G_{approx}^{k_o k_i}(\omega)$. For a single frequency ω , this can be expressed in regressor (Φ') - parameter (θ), and observation/output (Y') format, suitable for Least Squares parameter estimation [128] as,

$$\begin{aligned} \Phi' &= \begin{bmatrix} g_2(\omega) & -\omega h_2(\omega) & -\omega^{-2} & 0 & 1 & 0 \\ h_2(\omega) & \omega g_2(\omega) & 0 & -\omega^{-1} & 0 & \omega \end{bmatrix} \\ \theta &= [\alpha_k^{k_o k_i} \quad \beta_k^{k_o k_i} \quad \bar{a} \quad \bar{b} \quad \bar{c} \quad \bar{d}] \\ Y' &= [g^{k_o k_i}(\omega) \quad h^{k_o k_i}(\omega)]^T \end{aligned} \quad (4.29)$$

Expanding this formulation to the selected frequency array ω and the FRF real and imaginary component arrays $\mathbf{g}^{k_o k_i}$ and $\mathbf{h}^{k_o k_i}$ (per Eq. (4.21)), the regressor matrix (Φ) and output (observation) vector (Y) can be re-written in the following manner (using the Hadamard product and power operators, as earlier defined and used for Step 2):

$$\begin{aligned} \Phi &= \left[\begin{array}{cccccc} \mathbf{g}_2 & -\omega \circ \mathbf{h}_2 & -\omega^{\circ-2} & \mathbf{0} & \mathbf{1} & \mathbf{0} \\ \mathbf{h}_2 & \omega \circ \mathbf{g}_2 & \mathbf{0} & -\omega^{\circ-1} & \mathbf{0} & \omega \end{array} \right] \\ Y &= [(\mathbf{g}^{k_o k_i})^T \quad (\mathbf{h}^{k_o k_i})^T]^T \end{aligned} \quad (4.30)$$

In Eq. (4.30), the arrays \mathbf{g}_2 and \mathbf{h}_2 are obtained by enumerating the frequency array ω in the expression for G_2 in Eq. (4.27), and afterwards taking the real and imaginary components of the frequency response of

$G_2(\boldsymbol{\omega})$ in the mentioned order. The terms $\mathbf{0}$ and $\mathbf{1}$ represent arrays of zeros and ones of suitable dimension, ($N_k \times 1$).

The optimal solution for the parameter vector, in this step, is obtained as,

$$\hat{\boldsymbol{\theta}} = [\hat{\alpha}_k^{k_o k_i} \quad \hat{\beta}_k^{k_o k_i} \quad : \quad \hat{a} \quad \hat{b} \quad \hat{c} \quad \hat{d}]^T = (\boldsymbol{\Phi}^T \boldsymbol{\Phi})^{-1} \boldsymbol{\Phi}^T \mathbf{Y} \quad (4.31)$$

Since ω_k and ζ_k define the complex conjugate pole locations that are fixed to be common across all output/input channel pairs, estimation of the mode participation factor $\beta_k^{k_o k_i}$ and $\alpha_k^{k_o k_i}$ for different input/output channels is simply achieved by updating the output/observation vector $\mathbf{Y} = [(\mathbf{g}^{k_o k_i})^T \quad (\mathbf{h}^{k_o k_i})^T]^T$ in Eq. (4.30) with the correct FRF data for $k_i = 1, \dots, N_i$, and $k_o = 1, \dots, N_o$, and re-applying the solution in Eq. (4.31). Naturally, to save on computational time, the left pseudo-inverse matrix $(\boldsymbol{\Phi}^T \boldsymbol{\Phi})^{-1} \boldsymbol{\Phi}^T$ may also be reused after its computation for the first mode.

Hence, while all available output/input channels of FRF data need to be simultaneously considered during the estimation of ω_k and ζ_k in Step 2, the participation factors for a given mode are then solved independently for each output/input channel combination.

4.2.2.4. Step 4: Estimation of the remainder dynamics using the Rational Fraction Polynomial (RFP) method

While Steps 2 and 3 distinguish and identify the resonant modes, the remainder dynamics typically comprising real poles, complex conjugate poles with higher damping (i.e., not displaying noticeable resonance), and possibly direct and derivative-like terms, cannot be estimated by simply curve fitting in localized frequency ranges. The estimation of these dynamics, spread typically over a wider frequency range, needs to consider a broad spectrum which can be coincident with the measurement range $\boldsymbol{\omega} = [\omega_1 \quad \dots \quad \omega_N]^T$.

Recalling from Eq. (4.4) ($G_{k_o k_i} = C_{k_o k_i} + T_{k_o k_i}$), $C_{k_o k_i}$ represents the contribution of resonant modes and $T_{k_o k_i}$ the remainder dynamics. Before $T_{k_o k_i}$ can be estimated from experimental data, the influence of so-far identified and modeled resonant modes must be subtracted, as shown in Eq. (4.32).

$$H_{remainder}^{k_o k_i}(\omega) = g^{k_o k_i}(\omega) + jh^{k_o k_i}(\omega) - \sum_{k=1}^{n_{c1}} \frac{j\beta_k^{k_o k_i} \omega + \alpha_k^{k_o k_i}}{\omega_k^2 - \omega^2 + j2\hat{\zeta}_k \hat{\omega}_k \omega} \quad (4.32)$$

$$g_r^{k_o k_i}(\omega) = \text{Re}\{H_{remainder}^{k_o k_i}(\omega)\} \quad , \quad h_r^{k_o k_i}(\omega) = \text{Im}\{H_{remainder}^{k_o k_i}(\omega)\}$$

Above, $g^{k_o k_i}(\omega) + jh^{k_o k_i}(\omega)$ represents the delay-corrected MIMO frequency response data at each discrete frequency ω , as defined in Eq. (4.8). The summation term (Σ) represents the contribution of the identified lightly damped modes, i.e., $C_{k_o k_i}$ as defined in Eq. (4.3). The objective is to match this ‘remainder’ frequency response ($H_{rem}^{k_o k_i}$) with a suitable rational transfer function $T_{k_o k_i}$, as defined in Eq. (4.4).

The proceeding mathematical derivation first focusses on estimating the transfer function for a single channel $T_{k_o k_i}(s)$ of the generalized remainder dynamics. In developing the initial solution, to keep the derivations simple, the channel superscripts (or subscripts) $k_o k_i$ are dropped, similar to the approach in explaining the formulation for Step 2 (Section 4.2.2.2). Additionally, while in the general case the numerator order $m_{k_o k_i}$ for $T_{k_o k_i}$ can be different for each output/input channel pair (per Eq. (4.5)), for simplicity this order is also just denoted as m . Proceeding the derivation of model fitting for a single SISO transfer function entry, in the generalization to the MIMO case, adequate output/input channel and numerator order designations are also reintroduced.

In the ideal case, at each frequency ω the response of the rational fraction polynomial $T(\omega) = T_{k_o k_i}(\omega)$ should match the remainder measurement FRF (i.e., $H_{rem}(\omega) = g_r(\omega) + jh_r(\omega)$):

$$T(\omega) = \frac{b_0(j\omega)^m + b_1(j\omega)^{m-1} + \dots + b_{m-1}(j\omega) + b_m}{(j\omega)^n + a_1(j\omega)^{n-1} + a_2(j\omega)^{n-2} + \dots + a_{n-1}(j\omega) + a_n} = g_r(\omega) + jh_r(\omega) \quad (4.33)$$

Arranging Eq. (4.33) leads to:

$$b_m + (j\omega)b_{m-1} + (j\omega)^2 b_{m-2} + \dots + (j\omega)^{m-1} b_1 + (j\omega)^m b_0 - [a_n + (j\omega)a_{n-1} + (j\omega)^2 a_{n-2} + \dots + (j\omega)^{n-1} a_1 + (j\omega)^n] \cdot [g_r(\omega) + jh_r(\omega)] = 0 \quad (4.34)$$

The real and imaginary terms of Eq. (4.34) can be separated from one another. During this process, to allow for the right-hand side to represent the actual components of the transfer function being fitted, the equation is normalized by multiplying both sides with ω^{-n} . Additionally, depending on the integer value of n , the right-hand side of the real and imaginary components will possess either g_r or h_r terms, with

either positive or negative sign. To enable for the correct entry to occur with correct sign, two auxiliary functions are defined:

$$\sigma(n) = \begin{cases} +1 & , \quad n = 0,4,8, \dots \\ -1 & , \quad n = 2,6,10, \dots \\ 0 & , \quad n = 1,3,5,7, \dots \end{cases} \quad \rho(n) = \begin{cases} +1 & , \quad n = 3,7,11, \dots \\ -1 & , \quad n = 1,5,9, \dots \\ 0 & , \quad n = 0,2,4,6, \dots \end{cases} \quad (4.35)$$

As a result, the real and imaginary components of Eq. (4.34) can now be expressed in the following manner (after performing some algebra to facilitate neater organization):

$$\begin{aligned} \text{Re}\{T(\omega) - (g_r(\omega) + jh_r(\omega))\} &= 0 \Rightarrow \\ & -\omega^{-n}g_r a_n + \omega^{-n+1}h_r a_{n-1} + \omega^{-n+2}g_r a_{n-2} - \omega^{-n+3}h_r a_{n-3} - \omega^{-n+4}g_r a_{n-4} + \dots \\ & + \omega^{-n}b_m - \omega^{-n+2}b_{m-2} + \omega^{-n+4}b_{m-4} - \omega^{-n+6}b_{m-6} + \dots = \sigma_r(n) \cdot g_r + \rho_r(n) \cdot h_r \\ \text{Im}\{T(\omega) - (g_r(\omega) + jh_r(\omega))\} &= 0 \Rightarrow \\ & -\omega^{-n}h_r a_n - \omega^{-n+1}g_r a_{n-1} + \omega^{-n+2}h_r a_{n-2} + \omega^{-n+3}g_r a_{n-3} - \omega^{-n+4}h_r a_{n-4} - \dots \\ & + \omega^{-n+1}b_{m-1} - \omega^{-n+3}b_{m-3} + \omega^{-n+5}b_{m-5} - \omega^{-n+7}b_{m-7} + \dots \\ & = -\rho_r(n) \cdot g_r + \sigma_r(n) \cdot h_r \end{aligned} \quad (4.36)$$

Thus, for a single frequency ω , fitting of the remainder dynamics as a rational polynomial (transfer function) $T(s)$ can be expressed in regressor (Φ') - parameter (θ), and observation/output (Y') format for LS parameter estimation [128]:

$$\begin{aligned} \Phi'(\omega) &= [\Phi'_a(\omega) \quad \vdots \quad \Phi'_b(\omega)] \\ \theta &= [\theta_a^T \quad \vdots \quad \theta_b^T]^T \\ Y'(\omega) &= [\sigma_r(n) \cdot g_r(\omega) + \rho_r(n) \cdot h_r(\omega) \quad \vdots \quad -\rho_r(n) \cdot g_r(\omega) + \sigma_r(n) \cdot h_r(\omega)]^T \end{aligned}$$

where:

$$\theta_a = [a_n \quad a_{n-1} \quad \dots \quad a_1]^T, \quad \theta_b = [b_m \quad b_{m-1} \quad \dots \quad b_0]^T \quad (4.37)$$

$$\Phi'_a(\omega) = \begin{bmatrix} -\omega^{-n}g_r & \omega^{-n+1}h_r & \omega^{-n+2}g_r & -\omega^{-n+3}h_r & -\omega^{-n+4}g_r & \dots \\ -\omega^{-n}h_r & -\omega^{-n+1}g_r & \omega^{-n+2}h_r & \omega^{-n+3}g_r & -\omega^{-n+4}h_r & \dots \\ \underbrace{\hspace{2cm}}_{a_n} & \underbrace{\hspace{2cm}}_{a_{n-1}} & \underbrace{\hspace{2cm}}_{a_{n-2}} & \underbrace{\hspace{2cm}}_{a_{n-3}} & \underbrace{\hspace{2cm}}_{a_{n-4}} & \dots \end{bmatrix}$$

$$\Phi'_b(\omega) = \begin{bmatrix} \omega^{-n} & 0 & -\omega^{-n+2} & 0 & \omega^{-n+4} & \dots \\ \underbrace{0}_{b_m} & \underbrace{\omega^{-n+1}}_{b_{m-1}} & \underbrace{0}_{b_{m-2}} & \underbrace{-\omega^{-n+3}}_{b_{m-3}} & \underbrace{0}_{b_{m-4}} & \dots \end{bmatrix}$$

The formulation in Eq. (4.37) can now be expanded to use the frequency response data in arrays ω , \mathbf{g}_r , \mathbf{h}_r , defined in Eq. (4.21), via adequate Hadamard (i.e., element-wise) product and power operators.

$$\boldsymbol{\omega} = [\omega_1 \quad \dots \quad \omega_N]^T, \quad \mathbf{g}_r = [g_r(\omega_1) \quad \dots \quad g_r(\omega_N)]^T, \quad \mathbf{h}_r = [h_r(\omega_1) \quad \dots \quad h_r(\omega_N)]^T \quad (4.38)$$

In this case, the regressor matrix (Φ) and observation/output vector (\mathbf{Y}) take the proceeding forms:

$$\Phi = [\Phi_a \quad \vdots \quad \Phi_b]$$

$$\mathbf{Y} = \begin{bmatrix} \sigma_r(n) \cdot \mathbf{g}_r + \rho_r(n) \cdot \mathbf{h}_r \\ -\rho_r(n) \cdot \mathbf{g}_r + \sigma_r(n) \cdot \mathbf{h}_r \end{bmatrix}$$

where:

$$\Phi_a = \begin{bmatrix} -\underbrace{\omega^{(-n)} \circ \mathbf{g}_r}_{a_n} & \underbrace{\omega^{(-n+1)} \circ \mathbf{h}_r}_{a_{n-1}} & \underbrace{\omega^{(-n+2)} \circ \mathbf{g}_r}_{a_{n-2}} & -\underbrace{\omega^{(-n+3)} \circ \mathbf{h}_r}_{a_{n-3}} & -\underbrace{\omega^{(-n+4)} \circ \mathbf{g}_r}_{a_{n-4}} & \dots \\ -\underbrace{\omega^{(-n)} \circ \mathbf{h}_r}_{a_n} & -\underbrace{\omega^{(-n+1)} \circ \mathbf{g}_r}_{a_{n-1}} & \underbrace{\omega^{(-n+2)} \circ \mathbf{h}_r}_{a_{n-2}} & \underbrace{\omega^{(-n+3)} \circ \mathbf{g}_r}_{a_{n-3}} & -\underbrace{\omega^{(-n+4)} \circ \mathbf{h}_r}_{a_{n-4}} & \dots \end{bmatrix} \quad (4.39)$$

$$\Phi_b = \begin{bmatrix} \underbrace{\omega^{(-n)}}_{b_m} & \mathbf{0} & -\underbrace{\omega^{(-n+2)}}_{b_{m-2}} & \mathbf{0} & \underbrace{\omega^{(-n+4)}}_{b_{m-4}} & \dots \\ \mathbf{0} & \underbrace{\omega^{(-n+1)}}_{b_{m-1}} & \mathbf{0} & -\underbrace{\omega^{(-n+3)}}_{b_{m-3}} & \mathbf{0} & \dots \end{bmatrix}$$

Thus, the optimal parameter solution for a single output/input channel has the structure:

$$\hat{\boldsymbol{\theta}} = [\hat{\boldsymbol{\theta}}_a^T \quad \vdots \quad \hat{\boldsymbol{\theta}}_b^T]^T = [\hat{a}_n \quad \hat{a}_{n-1} \quad \dots \quad \hat{a}_1 \quad \vdots \quad \hat{b}_m \quad \hat{b}_{m-1} \quad \dots \quad \hat{b}_0]^T = (\Phi^T \Phi)^{-1} \Phi^T \mathbf{Y} \quad (4.40)$$

Extension of the above formulation to the MIMO case requires the consideration of the commonality of the poles, as also done in Section 4.2.2.2. Hence, $\boldsymbol{\theta}_a$ portion of the parameter vector in Eq. (4.37) has to be the same across all output/input channels. The size and entries of the numerator vector $\boldsymbol{\theta}_b^{k_o k_i}$, however, can be different for each output/input channel pair ($k_o k_i$). The size of the numerator vector, and its corresponding regressor matrix $\Phi_b^{k_o k_i}$, will be $m_{k_o k_i} + 1$.

Using the formulation developed through Eqs. (4.35)-(4.41), the output (\mathbf{Y}), model prediction ($\Phi \boldsymbol{\theta}$), and model prediction error (\mathbf{E}) terms for a single output/input channel pair ($k_o k_i$) can be expressed as,

$$\mathbf{Y}^{k_o k_i} = [\Phi_a^{k_o k_i} \quad \Phi_b^{k_o k_i}] \cdot \begin{bmatrix} \boldsymbol{\theta}_a \\ \boldsymbol{\theta}_b^{k_o k_i} \end{bmatrix} + \mathbf{E}^{k_o k_i} \quad (4.41)$$

In constructing $\mathbf{Y}^{k_o k_i}$, $\Phi_a^{k_o k_i}$, and $\Phi_b^{k_o k_i}$, the expressions in Eq. (4.39) is applied by substituting the occurrences of \mathbf{g}_r , \mathbf{h}_r , and m with $\mathbf{g}_r^{k_o k_i}$, $\mathbf{h}_r^{k_o k_i}$, and $m_{k_o k_i}$ respectively. The superscript ' $k_o k_i$ ' is appended to the terms \mathbf{Y} , Φ_a , and Φ_b . Following this step, the LS parameter estimation for the MIMO case can be formulated by concatenating the occurrences of Eq. (4.41) for the available output/input channels ($1 \leq$

$k_o \leq N_o$, $1 \leq k_i \leq N_i$), and factoring the common denominator (i.e. system poles) related portion of the parameter vector (θ_a) accordingly.

$$\underbrace{\begin{bmatrix} \mathbf{Y}^{11} \\ \vdots \\ \mathbf{Y}^{1N_i} \\ \vdots \\ \mathbf{Y}^{N_o1} \\ \vdots \\ \mathbf{Y}^{N_oN_i} \end{bmatrix}}_Y = \underbrace{\begin{bmatrix} \Phi_a^{11} & \Phi_b^{11} & \dots & \mathbf{0} & \dots & \mathbf{0} & \dots & \mathbf{0} \\ \vdots & \vdots & \ddots & \vdots & \dots & \vdots & \dots & \vdots \\ \Phi_a^{1N_i} & \mathbf{0} & \dots & \Phi_b^{1N_i} & \dots & \mathbf{0} & \dots & \mathbf{0} \\ \vdots & \vdots & \dots & \vdots & \ddots & \vdots & \dots & \vdots \\ \Phi_a^{N_o1} & \mathbf{0} & \dots & \mathbf{0} & \dots & \Phi_b^{N_o1} & \dots & \mathbf{0} \\ \vdots & \vdots & \dots & \vdots & \dots & \vdots & \ddots & \vdots \\ \Phi_a^{N_oN_i} & \mathbf{0} & \dots & \mathbf{0} & \dots & \mathbf{0} & \dots & \Phi_b^{N_oN_i} \end{bmatrix}}_{\Phi} + \begin{bmatrix} \theta_a \\ \theta_b^{11} \\ \vdots \\ \theta_b^{1N_i} \\ \vdots \\ \theta_b^{N_o1} \\ \vdots \\ \theta_b^{N_oN_i} \end{bmatrix}_{\theta} + \begin{bmatrix} \mathbf{E}^{11} \\ \vdots \\ \mathbf{E}^{1N_i} \\ \vdots \\ \mathbf{E}^{N_o1} \\ \vdots \\ \mathbf{E}^{N_oN_i} \end{bmatrix}_E \quad (4.42)$$

Above, the $\mathbf{0}$ terms represent block arrays of zeros with adequate dimensions (i.e., $2N \times (m_{k_o k_i} + 1)$). The optimal solution for the parameter vector is thus found as [128]:

$$\hat{\theta} = \left[(\hat{\theta}_a)^T \quad ; \quad (\hat{\theta}_b^{11})^T \quad \dots \quad (\hat{\theta}_b^{1N_i})^T \quad \dots \quad (\hat{\theta}_b^{N_o1})^T \quad \dots \quad (\hat{\theta}_b^{N_oN_i})^T \right]^T = (\Phi^T \Phi)^{-1} \Phi^T Y \quad (4.43)$$

Thus, an overall fit for the remainder dynamics (excluding the resonant modes) is established using the available multi-channel FRF data. While the choice for the denominator order n , and the numerator orders for each channel $m_{k_o k_i}$ are not trivial, in the developed approach these are determined in a semi-automated manner. The implementation iterates through different integer values for n and $m_{k_o k_i}$, within preset bounds, while applying Steps 4 and 5 of the algorithm shown in Figure 4.1. Afterwards, the user is presented with topology visualization for the objective function (i.e., RMS of modeling error) as a function of n and $m_{k_o k_i}$, which facilitates the selection of reasonably low values for these orders which still enabling good modeling accuracy.

4.2.2.5. Step 5: Consolidation of lightly and highly damped pole and joint fitting of participation factors

In this step, the participation factors ($\beta_k^{k_o k_i}$, $\alpha_k^{k_o k_i}$, $\gamma_k^{k_o k_i}$, and $\delta_k^{k_o k_i}$) for the candidate pole locations and potential direct or derivative-like terms, identified so far, are simultaneously adjusted, now considering a broad spectrum of frequency response data that is available. This is performed to further improve the model fitting over Steps 2-4, particularly considering that Steps 2-3 use only narrow frequency range data near the resonances, and that the expressions for $C_{k_o k_i}$ and $T_{k_o k_i}$ were so far estimated sequentially, not simultaneously.

The expression of $T_{k_o k_i}$ in Eq. (4.4) can be put into the form $T_{k_o k_i}(s) = L_{k_o k_i}(s) + R_{k_o k_i}(s) + D_{k_o k_i}(s)$ as in Eq. (4.3). If the numerator order $m_{k_o k_i}$ is equal to or higher than the denominator order n , polynomial deconvolution is also applied to determine the quotient (i.e., direct or derivative-like terms $D_{k_o k_i}$) and the remainder $F_{k_o k_i}$:

$$T_{k_o k_i}(s) = \frac{\overbrace{f_0^{k_o k_i} s^{n-1} + f_1^{k_o k_i} s^{n-2} + \dots + f_{n-1}^{k_o k_i}}^{\text{Remainder: } F_{k_o k_i}(s)}}{\underbrace{s^n + a_1 s^{n-1} + \dots + a_n}_{\text{Poles of RFP: } P'(s)}} + \underbrace{\delta_0^{k_o k_i} + \delta_1^{k_o k_i} s + \dots + \delta_{d_{k_o k_i}}^{k_o k_i} s^{d_{k_o k_i}}}_{\text{Quotient: } D_{k_o k_i}(s)} \quad (4.44)$$

Afterwards, solving and grouping the poles of $P'(s)$ based on whether they are complex conjugate or real establishes the locations for the n_{c2} complex and n_r real poles contained within $L_{k_o k_i}(s)$ and $R_{k_o k_i}(s)$. In software such as MATLAB, deconvolution and pole finding can be achieved with commands like ‘deconv’, ‘pole’, ‘damp’, and ‘residue’. The latter, given $F_{k_o k_i}$, can also determine the numerator coefficients for the expressions of $L_{k_o k_i}$ and $R_{k_o k_i}$. After combining all complex conjugate poles into one set ($n_c = n_{c1} + n_{c2}$), the formulation for $G_{k_o k_i}$ in Eq. (4.2) can be applied to concurrently solve the unknown coefficients (i.e., β ’s, α ’s, γ ’s, and δ ’s). At this point, a candidate set of poles is either given or identified in terms of ζ_k , ω_k , and p_k values, and also the existence and structure ($d_{k_o k_i}$) of any direct terms has been determined for each output/input channel pair. Thus, the frequency response contribution of each term is computed and used to setup a LS parameter estimation problem.

Considering Eq. (4.2), for each frequency ω the response contribution from each complex conjugate pole pair $-\zeta_k \omega_k \pm j\omega_k \sqrt{1 - \zeta_k^2}$ (for $k = 1, \dots, n_c$) at can be represented by defining the auxiliary function $G_{2,k}$, similar to that in Eq. (4.27).

$$G_{2,k}(\omega) = \frac{1}{\omega_k^2 - \omega^2 + j2\zeta_k \omega_k \omega} , \text{ with: } g_{2,k}(\omega) = \text{Re}\{G_{2,k}(\omega)\} , h_{2,k}(\omega) = \text{Im}\{G_{2,k}(\omega)\} \quad (4.45)$$

Above, the subscript ‘ k ’ is included to designate the separate contribution of each complex mode, as they all have to be considered simultaneously. Similarly, the frequency response from a real pole at $-p_k$ for $k = 1, \dots, n_r$ can be represented with the auxiliary function $G_{1,k}$:

$$G_{1,k}(\omega) = \frac{1}{j\omega + p_k} , \text{ with: } g_{1,k}(\omega) = \text{Re}\{G_{1,k}(\omega)\} , h_{1,k}(\omega) = \text{Im}\{G_{1,k}(\omega)\} \quad (4.46)$$

Substituting $(j\omega)$ in the place of ‘s’ in Eq. (4.2), and by considering the auxiliary functions defined in Eqs. (4.45) and (4.46), the real and imaginary components of the frequency response of $G_{k_o k_i}(\omega)$ can thus be expressed as,

$$\begin{aligned}
\text{Re}\{G_{k_o k_i}(\omega)\} &= \sum_{k=1}^{n_c} (g_{2,k}(\omega) \cdot \alpha_k^{k_o k_i} - \omega h_{2,k}(\omega) \cdot \beta_k^{k_o k_i}) + \sum_{k=1}^{n_r} g_{1,k}(\omega) \cdot \gamma_k^{k_o k_i} \\
&\quad + \delta_0^{k_o k_i} - \omega^2 \delta_2^{k_o k_i} + \omega^4 \delta_4^{k_o k_i} - \omega^6 \delta_6^{k_o k_i} + \dots \\
\text{Im}\{G_{k_o k_i}(\omega)\} &= \sum_{k=1}^{n_c} (h_{2,k}(\omega) \cdot \alpha_k^{k_o k_i} + \omega g_{2,k}(\omega) \cdot \beta_k^{k_o k_i}) + \sum_{k=1}^{n_r} h_{1,k}(\omega) \cdot \gamma_k^{k_o k_i} \\
&\quad + \omega \delta_1^{k_o k_i} - \omega^3 \delta_3^{k_o k_i} + \omega^5 \delta_5^{k_o k_i} - \omega^7 \delta_7^{k_o k_i} + \dots
\end{aligned} \tag{4.47}$$

The objective in this adjustment step is to have $G_{k_o k_i}(\omega)$ match the delay-corrected experimental data as closely as possible. Thus, the LS parameter estimation problem can be defined by introducing the arrays for the parameters ($\boldsymbol{\theta}$), the regressors ($\boldsymbol{\Phi}'(\omega)$), and the output measurements ($\mathbf{Y}'(\omega)$), as shown in the proceeding equations:

$$\begin{aligned}
\text{Parameter vector: } \boldsymbol{\theta} &= [\boldsymbol{\theta}_{\alpha\beta}^T \quad \boldsymbol{\theta}_{\gamma}^T \quad \boldsymbol{\theta}_{\delta}^T]^T \\
\boldsymbol{\theta}_{\alpha\beta} &= [\alpha_1^{k_o k_i} \quad \beta_1^{k_o k_i} \quad \dots \quad \alpha_{n_c}^{k_o k_i} \quad \beta_{n_c}^{k_o k_i}]^T \\
\boldsymbol{\theta}_{\gamma} &= [\gamma_1^{k_o k_i} \quad \gamma_2^{k_o k_i} \quad \dots \quad \gamma_{n_r}^{k_o k_i}]^T \\
\boldsymbol{\theta}_{\delta} &= [\delta_0^{k_o k_i} \quad \delta_1^{k_o k_i} \quad \dots \quad \delta_{d_{k_o k_i}}^{k_o k_i}]^T
\end{aligned} \tag{4.48}$$

$$\begin{aligned}
\text{Regressor matrix: } \boldsymbol{\Phi}'(\omega) &= [\boldsymbol{\Phi}'_{\alpha\beta}(\omega) \quad \boldsymbol{\Phi}'_{\gamma}(\omega) \quad \boldsymbol{\Phi}'_{\delta}^{k_o k_i}(\omega)] \\
\boldsymbol{\Phi}'_{\alpha\beta}(\omega) &= [\boldsymbol{\Phi}'_{\alpha\beta,1}(\omega) \quad \boldsymbol{\Phi}'_{\alpha\beta,2}(\omega) \quad \dots \quad \boldsymbol{\Phi}'_{\alpha\beta,n_c}(\omega)] \\
\boldsymbol{\Phi}'_{\alpha\beta,k}(\omega) &= \begin{bmatrix} g_{2,k}(\omega) & -\omega h_{2,k}(\omega) \\ h_{2,k}(\omega) & \omega g_{2,k}(\omega) \end{bmatrix}, \text{ where: } k = 1, \dots, n_c \\
\boldsymbol{\Phi}'_{\gamma}(\omega) &= [\boldsymbol{\Phi}'_{\gamma,1}(\omega) \quad \boldsymbol{\Phi}'_{\gamma,2}(\omega) \quad \dots \quad \boldsymbol{\Phi}'_{\gamma,n_r}(\omega)] \\
\boldsymbol{\Phi}'_{\gamma,k}(\omega) &= \begin{bmatrix} g_{1,k}(\omega) \\ h_{1,k}(\omega) \end{bmatrix}, \text{ where: } k = 1, \dots, n_r \\
\boldsymbol{\Phi}'_{\delta}^{k_o k_i}(\omega) &= \begin{bmatrix} 1 & 0 & -\omega^2 & 0 & \omega^4 & 0 & -\omega^6 & 0 & \dots \\ 0 & \omega & 0 & -\omega^3 & 0 & \omega^5 & 0 & -\omega^7 & \dots \end{bmatrix}, \text{ size: } 2 \times (d_{k_o k_i} + 1)
\end{aligned} \tag{4.49}$$

$$\text{Output vector: } \mathbf{Y}'(\omega) = [g^{k_o k_i}(\omega) \quad h^{k_o k_i}(\omega)] \tag{4.50}$$

As applied earlier in Steps 3 and 4, the extension of the LS formulation in Eq. (4.48)-(4.50) to the data in the frequency range $\boldsymbol{\omega} = [\omega_1 \ \dots \ \omega_N]^T$ is realized by replacing the product and power operations with their Hadamard (i.e., element-wise) counterparts, leading to the regressor matrix (Φ) and output vector (Y) for the whole frequency range.

$$\begin{aligned} \text{Regressor matrix: } \Phi &= [\Phi_{\alpha\beta} \quad \vdots \quad \Phi_{\gamma} \quad \vdots \quad \Phi_{\delta}^{k_o k_i}] \\ \Phi_{\alpha\beta} &= [\Phi_{\alpha\beta,1} \quad \Phi_{\alpha\beta,2} \quad \dots \quad \Phi_{\alpha\beta,n_c}] \ , \ \Phi_{\alpha\beta,k} = \begin{bmatrix} \mathbf{g}_{2,k} & -\boldsymbol{\omega} \circ \mathbf{h}_{2,k} \\ \mathbf{h}_{2,k} & \boldsymbol{\omega} \circ \mathbf{g}_{2,k} \end{bmatrix} \ , \text{ where: } k = 1, \dots, n_c \\ \Phi_{\gamma} &= [\Phi_{\gamma,1} \quad \Phi_{\gamma,2} \quad \dots \quad \Phi_{\gamma,n_r}] \ , \ \Phi_{\gamma,k} = \begin{bmatrix} \mathbf{g}_{1,k} \\ \mathbf{h}_{1,k} \end{bmatrix} \ , \text{ where: } k = 1, \dots, n_r \\ \Phi_{\delta}^{k_o k_i} &= \begin{bmatrix} \mathbf{1} & \mathbf{0} & -\boldsymbol{\omega}^{\circ 2} & \mathbf{0} & \boldsymbol{\omega}^{\circ 4} & \mathbf{0} & -\boldsymbol{\omega}^{\circ 6} & \mathbf{0} & \dots \\ \mathbf{0} & \boldsymbol{\omega} & \mathbf{0} & -\boldsymbol{\omega}^{\circ 3} & \mathbf{0} & \boldsymbol{\omega}^{\circ 5} & \mathbf{0} & -\boldsymbol{\omega}^{\circ 7} & \dots \end{bmatrix} \ , \text{ size: } 2N \times (d_{k_o k_i} + 1) \end{aligned} \quad (4.51)$$

$$\text{Output vector: } Y = \begin{bmatrix} \mathbf{g}^{k_o k_i} \\ \mathbf{h}^{k_o k_i} \end{bmatrix} \quad (4.52)$$

In Eq. (4.51), the arrays $\mathbf{g}_{2,k}$, $\mathbf{h}_{2,k}$ and $\mathbf{g}_{1,k}$, $\mathbf{h}_{1,k}$ are obtained by enumerating the frequency array $\boldsymbol{\omega} = [\omega_1 \ \dots \ \omega_N]^T$ in the expressions for $G_{2,k}$ in Eq. (4.45) and $G_{1,k}$ in Eq. (4.46), and afterwards taking the real and imaginary components of the frequency response of $G_{2,k}(\boldsymbol{\omega})$ and $G_{1,k}(\boldsymbol{\omega})$, in the mentioned order. The terms $\mathbf{0}$ and $\mathbf{1}$ represent arrays of zeros and ones of suitable dimension, ($N \times 1$). The expressions $\mathbf{g}^{k_o k_i}$ and $\mathbf{h}^{k_o k_i}$ in Eq. (4.52) represent the real and imaginary components of the delay-corrected frequency response measurement described in Eqs. (4.7) and (4.8), corresponding to the frequency array $\boldsymbol{\omega}$. Thus,

$$\begin{aligned} \boldsymbol{\omega} &= [\omega_1 \ \dots \ \omega_N]^T \ , \ \mathbf{g}^{k_o k_i} = [g^{k_o k_i}(\omega_1) \ \dots \ g^{k_o k_i}(\omega_N)]^T = [g_1^{k_o k_i} \ \dots \ g_N^{k_o k_i}]^T \\ \mathbf{h}^{k_o k_i} &= [h^{k_o k_i}(\omega_1) \ \dots \ h^{k_o k_i}(\omega_N)]^T = [h_1^{k_o k_i} \ \dots \ h_N^{k_o k_i}]^T \end{aligned} \quad (4.53)$$

The optimal solution for the participation factors, thus considering the simultaneous contribution of all poles (complex and real) as well as direct or derivative-like terms in Eq. (4.2), is obtained by [128],

$$\hat{\boldsymbol{\theta}} = [\hat{\boldsymbol{\theta}}_{\alpha\beta}^T \quad \hat{\boldsymbol{\theta}}_{\gamma}^T \quad \hat{\boldsymbol{\theta}}_{\delta}^T]^T = (\Phi^T \Phi)^{-1} \Phi^T Y \quad (4.54)$$

Thus, the estimates $\hat{\alpha}_k^{k_o k_i}$, $\hat{\beta}_k^{k_o k_i}$, $\gamma_k^{k_o k_i}$, and $\hat{\delta}_k^{k_o k_i}$ can be extracted per Eq. (4.48). Since the pole locations are common for all output/input channels the participation factors for each channel pair $k_o k_i$ can be solved independently. Also, considering Eq. (4.49), a portion of the regressor matrix $[\Phi_{\alpha\beta} \quad \vdots \quad \Phi_{\gamma}]$ can

be re-used. However, the third part of Φ , i.e., $\Phi_{\delta}^{k_o k_i}$, and the output vector Y in Eq. (4.52) still need to be updated with the correct structure before using each new data set.

It is important to note that in the developed algorithm, the treatment of root multiplicity has not been incorporated; neither in the main model structure in Eq. (4.2), nor in its conversion from Eq. (4.44). This is because sufficiently accurate models for most mechatronic systems can still be typically identified using only distinct poles, which can also be located arbitrarily close if needed. The implementation of root multiplicity would add another level of complexity to the overall identification algorithm. Hence, currently this limitation is acknowledged and root multiplicity was kept out of the research scope in this thesis. However, is still considered as an interesting future improvement idea.

4.2.2.6. Step 6: Nonlinear optimization by perturbing pole locations

During this step, further potential improvement is sought to the model by perturbing the pole locations using a nonlinear optimization algorithm.

The pole locations determined initially during Steps 2 and 4 are used as initial guess values in a global optimization algorithm available with MATLAB [129]. While different algorithms are available in [129], the one utilized in this study was ‘fmincon’ which combines Sequential Quadratic Programming (SQP), suitable for converging accurately to local minima, alongside a systematic procedure for trying out different SQP starting conditions. In an earlier work, pole search in conjunction with LS projection-based updating of numerator terms was applied to identify MIMO LTI models based on time-domain data [27]. In this study, the global optimization is utilized for *frequency-domain* model fitting, in an integrated manner with the methodology outlined in Figure 4.1.

The search variables are the pole parameters \mathbf{x} , defined within pre-determined lower and upper bounds (\mathbf{x}^{lb} and \mathbf{x}^{ub} , respectively).

$$\mathbf{x} = [\omega_1 \quad \zeta_1 \quad \dots \quad \omega_{n_c} \quad \zeta_{n_c} \quad \vdots \quad p_1 \quad \dots \quad p_{n_r}]^T, \text{ such that } \mathbf{x}^{lb} \leq \mathbf{x} \leq \mathbf{x}^{ub} \quad (4.55)$$

For each candidate pole set, the corresponding participation factors are using Step 5, as described in the preceding subsection. Afterwards, the fitness of the model is determined by evaluating an objective function, which computes the root-mean square (RMS) value for the model fitting error in a multi-channel sense.

During the repeated application of Step 5, for each output-input channel pair $k_o k_i$, as the solution for the parameter vector (of participation factors) is constructed and solved, the residual (i.e., fitting error) vector $\mathbf{E}^{k_o k_i}$ is also estimated.

$$\mathbf{E}^{k_o k_i} = \mathbf{Y}^{k_o k_i} - \mathbf{\Phi}^{k_o k_i} \hat{\boldsymbol{\theta}}^{k_o k_i} \quad , \quad k_o = 1, \dots, N_o \quad , \quad k_i = 1, \dots, N_i \quad (4.56)$$

Above, $\mathbf{\Phi}^{k_o k_i}$, $\mathbf{Y}^{k_o k_i}$, and $\hat{\boldsymbol{\theta}}^{k_o k_i}$ correspond to the terms of $\mathbf{\Phi}$, \mathbf{Y} , and $\hat{\boldsymbol{\theta}}$ from Eqs. (4.51), (4.52), and (4.54), in the mentioned order. Once the frequency domain modeling error is determined for each channel pair, an overall objective function J which considers the RMS of model fitting errors from all channels is computed, by concatenating the individual error vectors:

$$\mathbf{E} = [(\mathbf{E}^{11})^T \quad \dots \quad (\mathbf{E}^{1N_i})^T \quad \dots \quad (\mathbf{E}^{N_o 1})^T \quad \dots \quad (\mathbf{E}^{N_o N_i})^T]^T \quad , \quad J = \text{rms}(\mathbf{E}) \quad (4.57)$$

Considering the definition of root mean square operator: (i.e., $\text{rms}(\mathbf{e}) = \sqrt{\left(\frac{1}{N}\right) \sum e_i^2}$), the objective function J can also be computed by taking the RMS of individual objective function values $J^{k_o k_i}$ calculated for each output-input channel pair, by applying the RMS to their corresponding model fitting error vectors:

$$J = \text{rms}(\mathbf{J}_{array}) \quad (4.58)$$

where: $\mathbf{J}_{array} = [J^{11} \quad \dots \quad J^{1N_i} \quad \dots \quad J^{N_o 1} \quad \dots \quad J^{N_o N_i}]^T \quad , \quad J^{k_o k_i} = \text{rms}(\mathbf{E}^{k_o k_i})$

The algorithm is stopped upon the error converging below a set tolerance, or the maximum number of iterations exceeding their limit.

4.3. Experimental Validation on a Precision T-Type Gantry Machine

In this section, the application of the algorithm is demonstrated step-by-step, using frequency response data collected from a T-type precision x-y gantry stage, which is shown in Figure 4.4. The stage is driven by ironless linear motors (ETELILM06-060-3RB) powered by 3-phase pulse width modulated (PWM) amplifiers (DSC2P154-32) which operate in current-control mode. 1 V of current command generates 20.38 N of force from each actuator (Motor force constant $K_t = 46.4$ N/A, peak force $F_p = 1247$ N, maximum input voltage $V_p = 10$ V, and the amplifier gain $K_A = 0.4392$ A/V). As shown in the figure, the guideways are all air bearing type, provided by New Way Precision. Thus, any perceivable nonlinear stick-slip friction effect is eliminated. The encoders are Heidenhain LIP 581C, which provide a measurement resolution, after signal interpolation, of 10-20 nm. The data collection was performed using a modular DS 1005 dSPACE platform, by injecting distinct sine wave excitation at different frequencies (with 2 Hz increments) from

one actuator at a time, and measuring the displacement response from the encoders at sampling a frequency of 15 kHz. Due to the lack of nonlinear stick-slip friction, the tests could be conducted while the axes were all stationary. Further details about the setup can be found in [130].

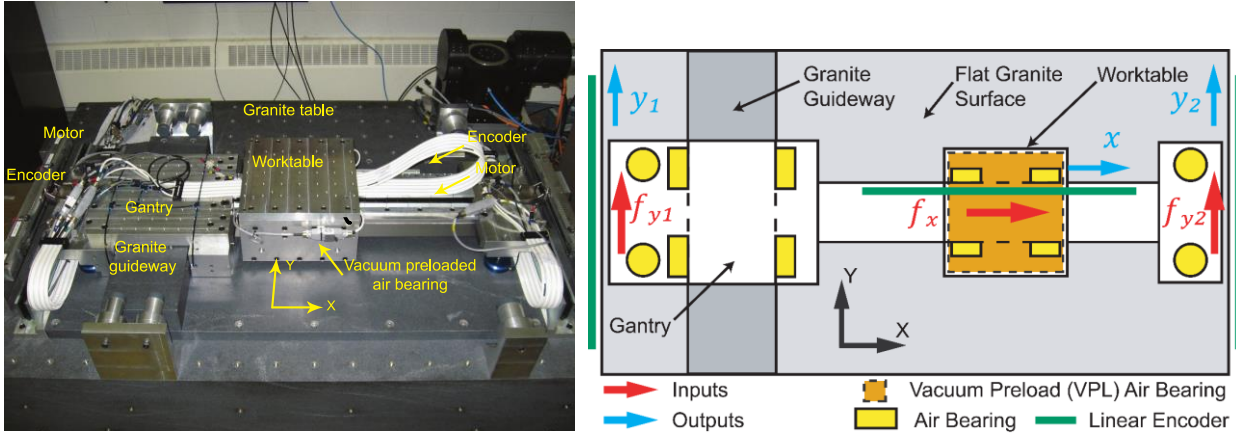


Figure 4.4: Linear motor driven T-type gantry and worktable (left) and the schematic of the setup (right) [130].

4.3.1. MIMO Identification of Y-Axis

The gantry-style y-axis is a two-input two-output system with a strong dynamic coupling between the left-hand and right-hand actuators. The four air bearings around the granite guideway exhibit the behavior of a torsional spring, creating a yaw vibration mode at around 96 Hz. In the data collection, systems inputs 1 and 2 coincide with the current (i.e., force) commands (f_{y_1} , f_{y_2}) applied to the left- and right-hand actuators' amplifiers. Outputs 1 and 2 correspond to the position measurements (y_1 , y_2) obtained from the left- and right-hand linear encoders.

Figure 4.5 shows the raw frequency response data, in which the influence of delay can also be clearly seen as a linearly decreasing component with frequency in the individual phase plots ($\angle H'_{11}$, $\angle H'_{12}$, $\angle H'_{21}$, $\angle H'_{22}$). By iterating through Steps 1 to 5 in constant delay increments of 0.1 ms, the value of the pure delay was determined to be 1 ms, and ultimately removed from the measurement data per Section 4.2.2.1.

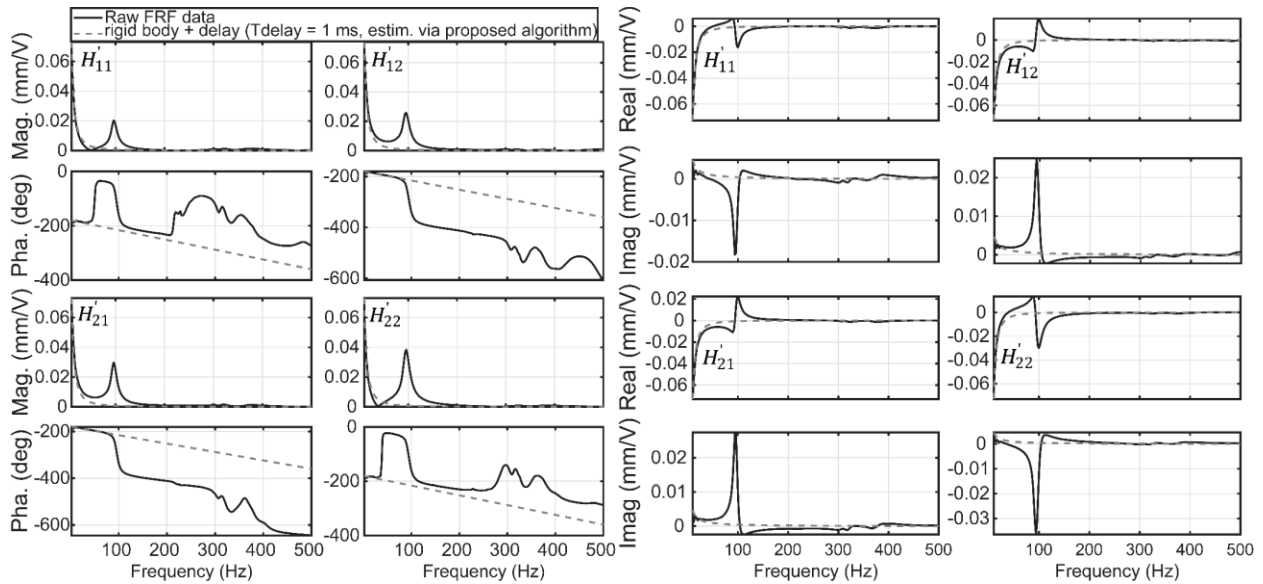


Figure 4.5: Raw FRFs, also containing the system's pure delay in the measurement.

Figure 4.6 shows the measured frequency response data before and after the delay removal (i.e., **Step 1** of the algorithm). A clearer comparison of the raw FRFs and their delay-corrected counterparts are shown in the right-hand panels of Figure 4.6. While the Bode plots on the left hand are shown with logarithmic magnitude to discern the general shape, the right hand plots showing fitting consistency are presented as real and imaginary components for more convenient comparison. As can be seen, correction of the delay has a dramatic impact on the contents of the real and imaginary components of the FRFs, especially at frequencies beyond 200 Hz where the delay-induced phase lag exceeds 57.6° .

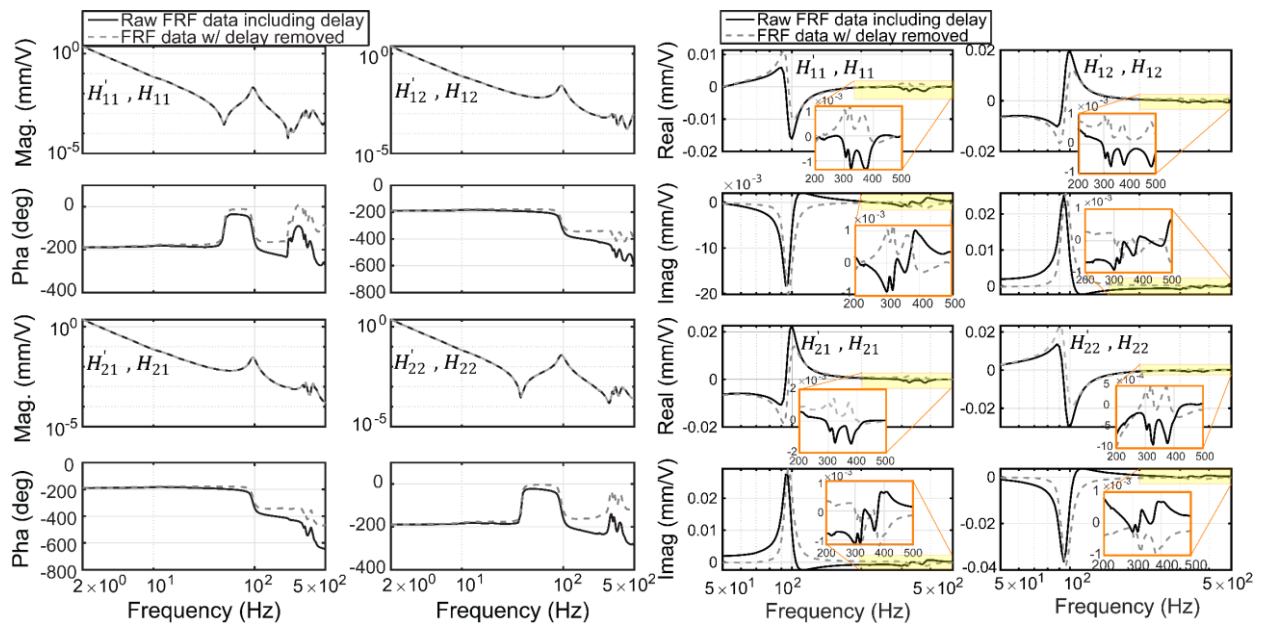


Figure 4.6: Frequency response data before and after the removal of pure delay (Step 1).

The application of **Steps 2** and **3** (i.e., fitting of the modes and approximate participation factors in the vicinity of observed resonances) is shown in Figure 4.7. As can be seen, the FRF reconstructed solely with the estimates of these components already captures most of the trends in the experimental data.

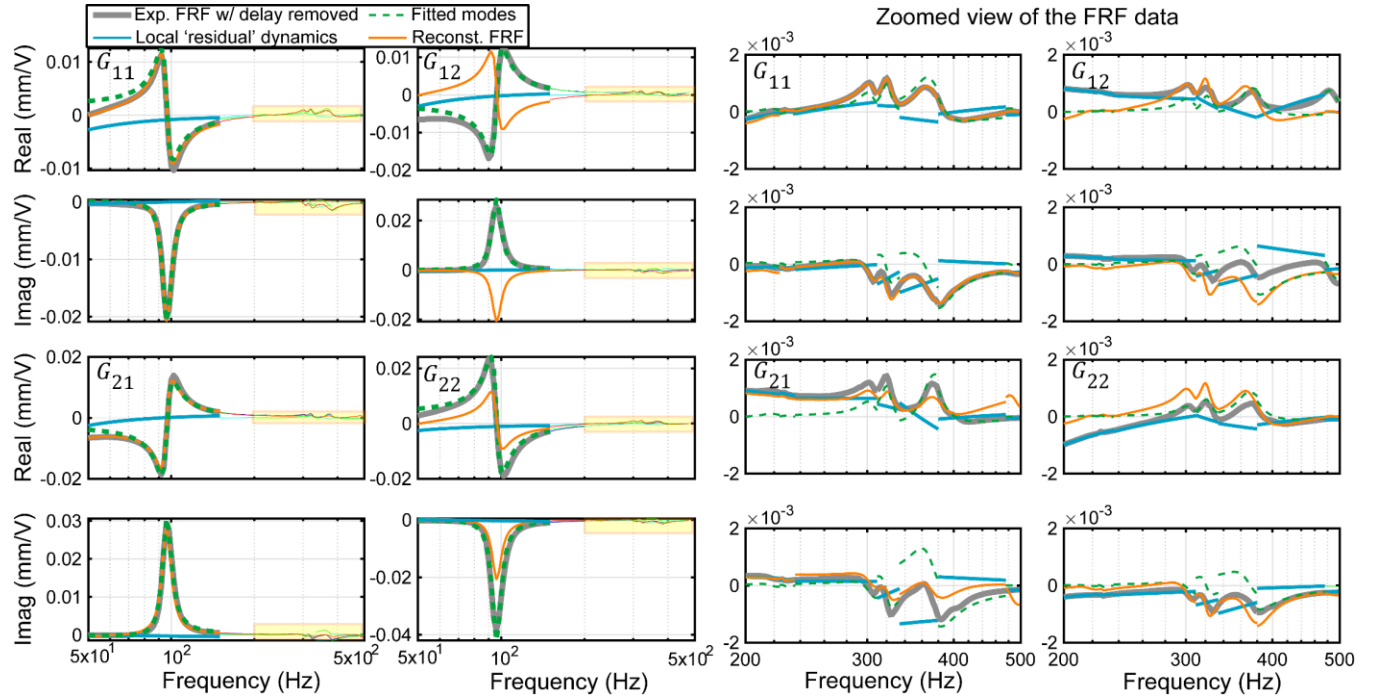


Figure 4.7: Fitting of vibration modes and residual FRFs (left) and zoomed view (right) (Steps 2 and 3).

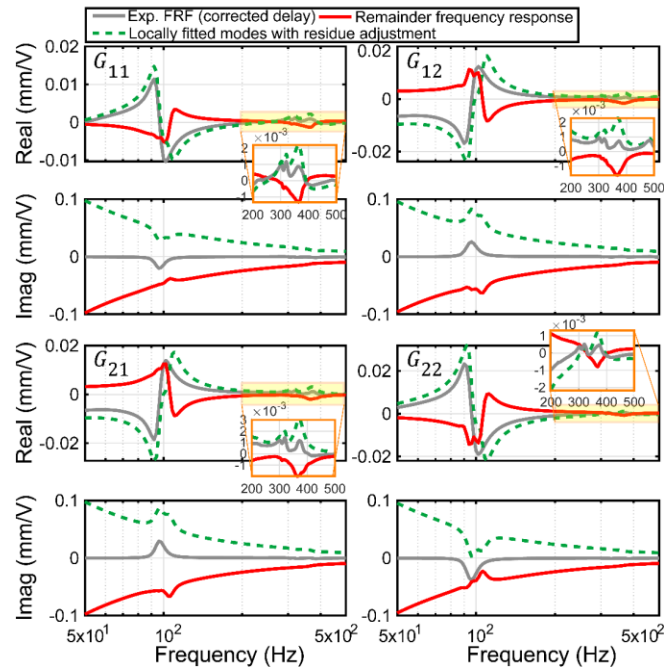


Figure 4.8: Subtraction of fitted modes to reveal remainder frequency response contributions (start of Step 4), shown from 50 Hz onwards.

Figure 4.8 shows the subtraction of the identified resonant modes from the delay-corrected FRF data, which constitutes the first part of **Step 4**. This reveals the remainder dynamics that must be matched by the RFP estimation. Fitting of the remainder dynamics ($T_{k_o k_i}$) via RFP estimation, i.e., completion of **Step 4**, is shown in Figure 4.9. While the most significant trends are well-captured in the fitting, especially with the imaginary components of G_{11} , G_{12} , G_{21} , G_{22} , and with the low frequency portion of the real parts of these transfer functions, the fitting for frequencies beyond 40 Hz, at this time, is not ideal. This is attributed to two factors. The first is that the identified and subtracted modes are only local approximations around their resonances, without considering at this time a global improvement in all participation factors. This is believed to be the cause of the fitting errors around 96, 303, 321, and 373 Hz, which coincide with such modes, as listed in Appendix A.1. The second factor is that the RFP algorithm in Step 4 places the highest emphasis in reducing the fitting error where the response magnitude is largest. Since the gantry drive (ideally) has no friction, it displays double-integrator type behavior. Thus accurate fitting of the low frequencies, and the imaginary component of the response (which is an order of magnitude larger than the real component), becomes the priority. However, as will be shown in Steps 5 and 6, these discrepancy problems are largely mitigated by the simultaneous (global) adjustment of all participation factors, and ultimately further refinement of pole locations via nonlinear optimization.

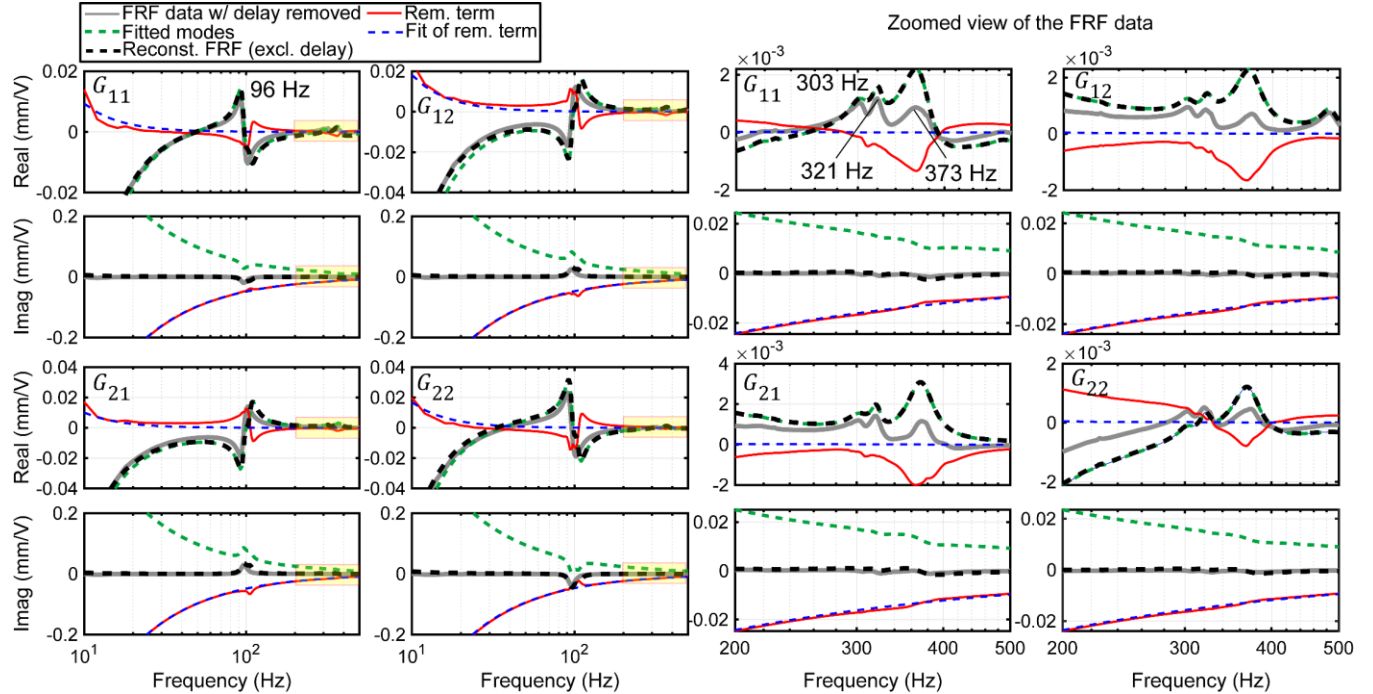


Figure 4.9: Fitting of the remainder dynamics $T_{k_o k_i}$ (Step 4).

The application of **Step 5**, i.e. consolidation of complex vs. real poles and simultaneous adjustment of all participation factors, is shown in Figure 4.10. As can be seen, a significant improvement is obtained for both the magnitude and phase components of all four responses. Additionally, the topologies for the RMS of MIMO fitting error per Eq. (4.58), including the global minimum values, are shown in Figure 4.11. These were computed through iterations of different system delay values (e.g., 0.0008, 0.0009, 0.0010, and 0.0011 s), as well as denominator and numerator orders (i.e., n and $m = m_{11} = m_{12} = m_{21} = m_{22}$) for the remainder dynamics. It can be seen that 3rd order remainder dynamics with 2nd order numerators yield the best possible (and minimal order) realization for the poles not captured with the resonant modes. This is reasonable, as two of the orders are attributed to the double-integrator-like behavior of the stage, and the third may be originating from the current loop. As the algorithm is iterated through Steps 1-5 in assumed delay increments of 0.1 ms, the delay value of $T_d = 0.0010$ s yields the best overall fit. Thus, at this point the parameters T_d , n , and m are fixed and the algorithm can proceed to **Step 6**.

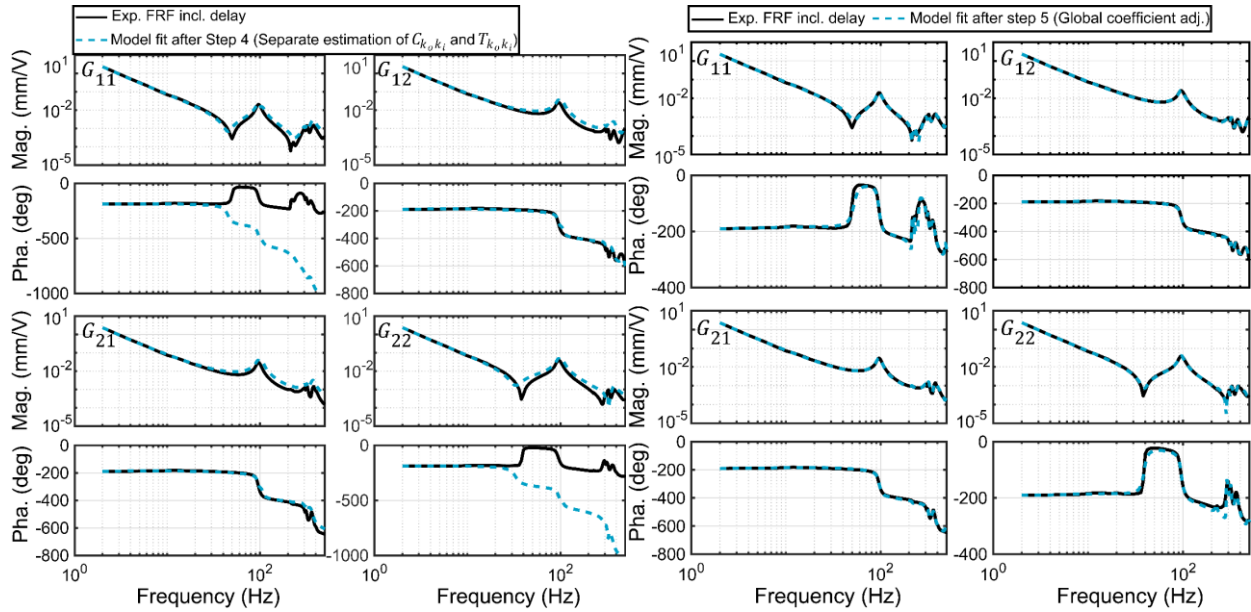


Figure 4.10: Measured and fitted model before (shown in left hand panels) and after (shown in right hand panels) pole consolidation and simultaneous fitting of all participation factors (Step 5).

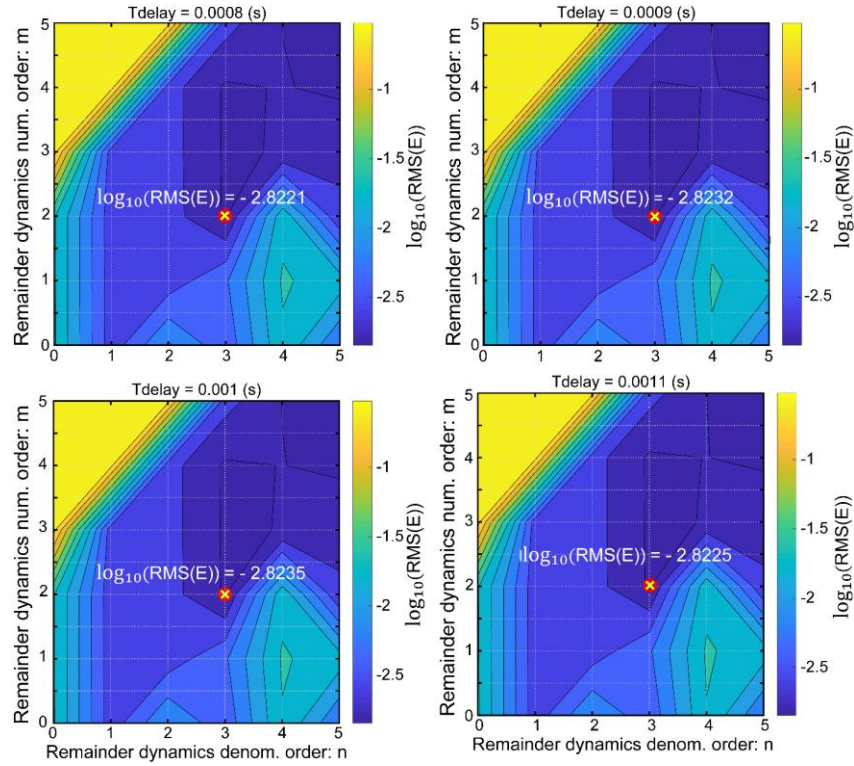


Figure 4.11: Topologies of RMS values for the MIMO fitting error, obtained by iterating different values for the assumed pure delay (T_d) and denominator / numerator model orders for the remainder dynamics (Steps 1-5).

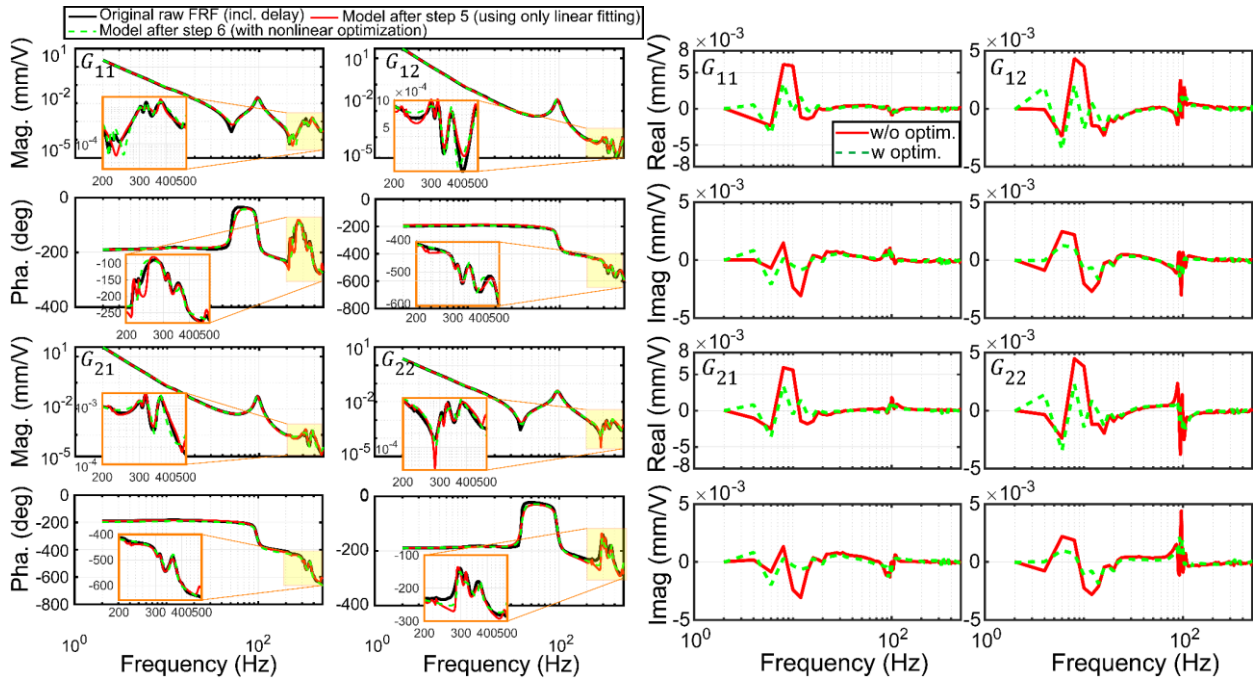


Figure 4.12: Experimental FRF (including delay) and fitted model before and after the nonlinear optimization of the pole locations. (left), and the corresponding real and imaginary response fitting errors (right) (Step 6).

Finally, the outcome of pole location nonlinear optimization, via **Step 6**, is shown in Figure 4.12. The left hand panels show the magnitude and phase components for the actual and fitted responses. The right hand panels show the real and imaginary components of the fitting errors, before and after the nonlinear pole adjustment. Additionally, the system poles estimated before and after Step 6 are summarized in Table A.1.1 in Appendix A.1. As can be seen, while several of the poles only change location by a relatively lower amount, the complex poles at 217.1, 228.68, and 369.8 Hz are replaced with new ones at 10.76, 124.41, 3696 Hz. Most importantly, the MIMO RMS value for the fitting error, per Eq. (4.58), is reduced from 0.0015 to 0.0010 mm/V, which is a 33% improvement achieved in Step 6, of course by also recursively invoking Step 5 during the nonlinear search.

4.3.2. SISO Identification of the X-Axis

The proposed model identification algorithm has also been tested on the x-axis response of the same setup. In this case, with a single actuator and encoder the plant model is SISO. The fit was configured to capture the acceleration response, by considering numerically differentiated encoder signals with respect to time, in computing the FRFs. The measurement data and model fits obtained at Steps 5 and 6 are shown in Figure 4.13. As can be seen, the estimated model replicates very closely the measured FRF at both steps, and further improvement is observed for Step 6, upon inspecting the RMS of fitting error value, which decreases from 94.5 (mm/s²)/V to 28.1 (mm/s²)/V, thus achieving additional 70% enhancement, reported in Appendix A.2. The summary of the identified parameters are also presented in the same appendix. The original FRF and final fitted model (at Step 6) are also shown in polar plot (Nyquist) format in Figure 4.14. It is interesting to note that the optimum estimate for the delay, in this case, is 0.5 ms, after also having used 0.1 ms search steps. This could possibly originate from having used different real-time data collection scripts on the dSPACE platform, which less delay being induced when lower data collection channels are used. Nevertheless, the achieved overall fit, as can be seen, is quite close for a wide frequency range.

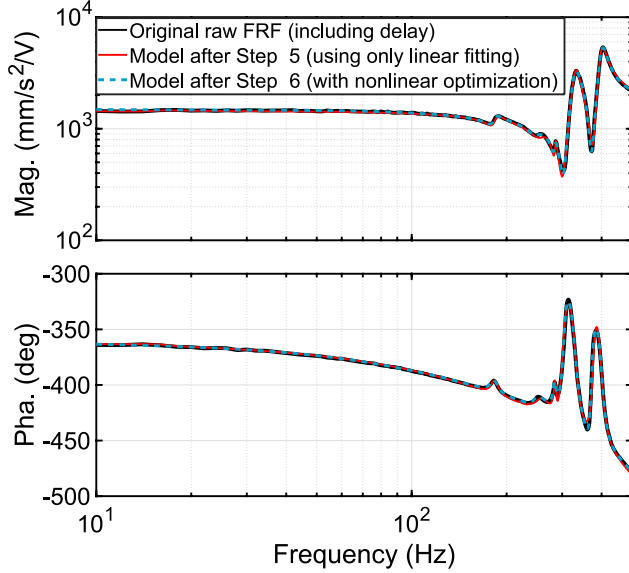


Figure 4.13: Experimental FRF (including delay) and fitted model before (RMS(E) = 94.57) & after the optimization (RMS(E) = 28.13).

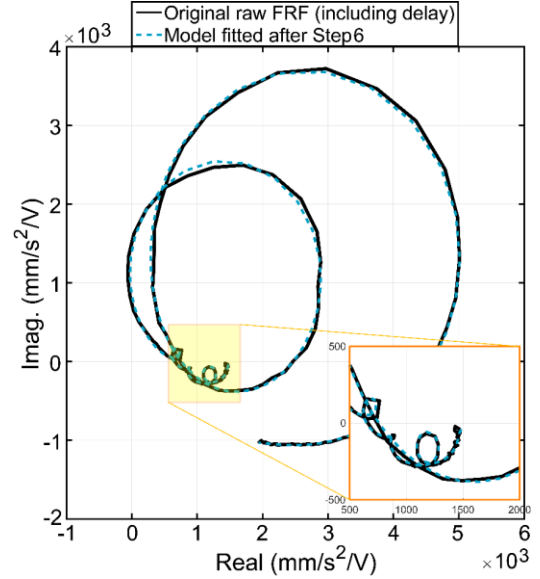


Figure 4.14: Nyquist diagram for experimental FRF and fitted model at Step 6.

4.4. Experimental Validation on a Single-Axis Ball Screw Drive

The second validation was performed with data from a precision ball-screw motion mechanism, which was introduced in Section 3.2. As mentioned, the ball-screw drive has air bushing type guideway system. Thus, the effect of nonlinear stick-slip friction is greatly mitigated and it only originates from the rotational bearings supporting the motor and screw, and the interface between the screw and nut, which contains recirculating ball elements. The schematic of the setup is shown in Figure 4.15.

The motor is powered via a Varedan LA-1555T amplifier introduced in Section 3.4. The real-time controller used is dSPACE DS1005, which performs command signal generation to the linear amplifier and the required data collection from the encoders on the setup. The system is considered as a two-input two-output plant. The inputs are, u_1 : motor torque command at the current amplifier input, and u_2 : the disturbance force applied on the table side. The outputs are, x_1 : the displacement registered from the rotational encoder (Encoder 3) at the back of the motor, and x_2 : the linear scale measurement of the table translation. The motor encoder signals were collected using specialized circuitry built into the Omron K3K030T driver. The translation was measured using a Heidenhain LIF 101 R linear scale. The current input commands to the amplifier are analog voltage signals between -10 ... 10 V. In representing the motor torque command, 1 V input corresponds to 708.4291 N of force at table translation level.

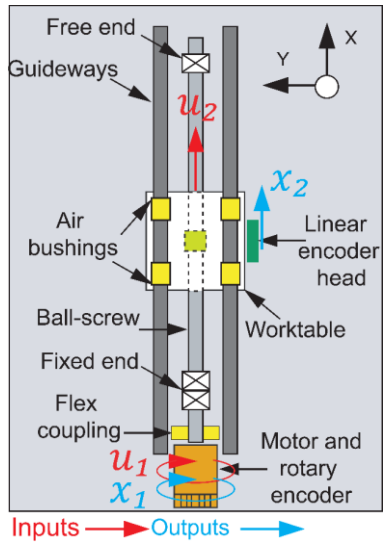


Figure 4.15: Schematic of the Single-axis ball-screw drive and worktable.

The frequency response functions for the first input were obtained by applying sinusoidal motor current commands to the amplifier and measuring the rotary and linear encoder position responses at 15 kHz sampling frequency. The disturbance input response was measured by applying impact excitation with a force sensor instrumented hammer (Dytran 5800, sensitivity: 2.36 mV/N). In representing the disturbance force, its unit was also scaled in terms of equivalent motor torque command in Volt acting at the amplifier input (i.e., $1 \text{ V} \cong 708.4291 \text{ N}$).

Figure 4.16 shows the measured FRF, and fitted 2×2 MIMO model FRFs in both Bode and Nyquist forms. As can be seen, the model is once again in very close agreement with the experimental data. The summary of the identified parameters is provided in Appendix A.3.

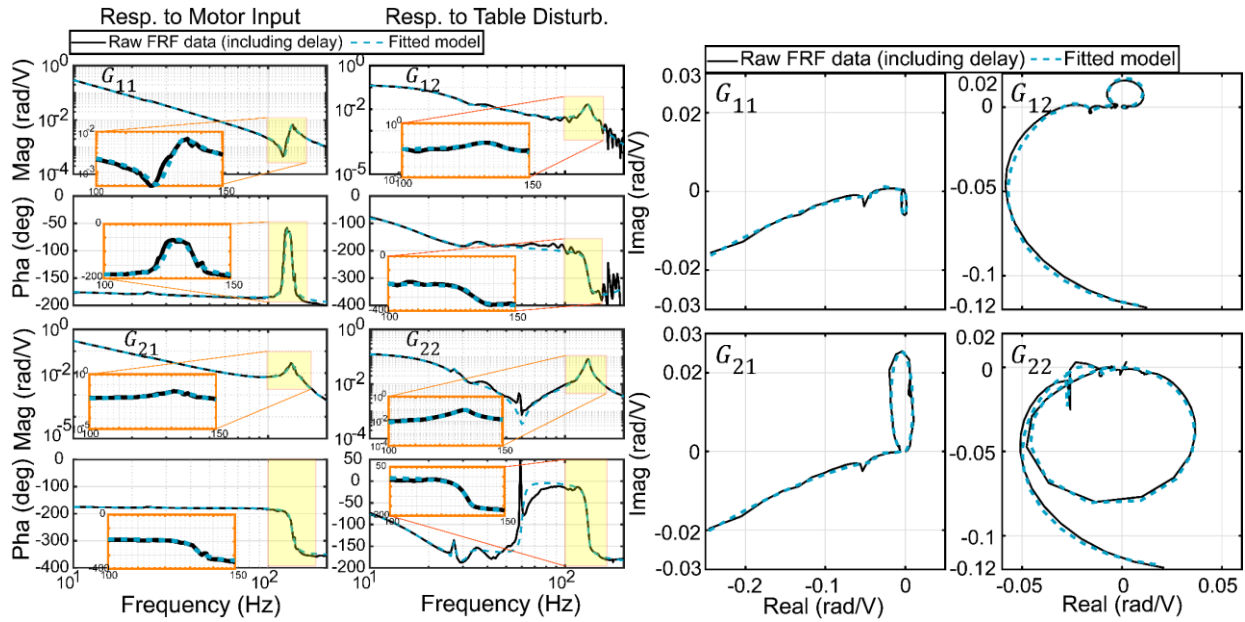


Figure 4.16: Measured MIMO FRF and fitted model (after Step 6) for the single-axis ball screw drive.

4.5. Experimental Validation on a 3-Axis H-Type Gantry Machine

The third validation was performed on a 3-axis H-type CNC gantry equipped with ball-screw drives and supported by linear bearing guideways. The experimental setup is shown in Figure 4.17.

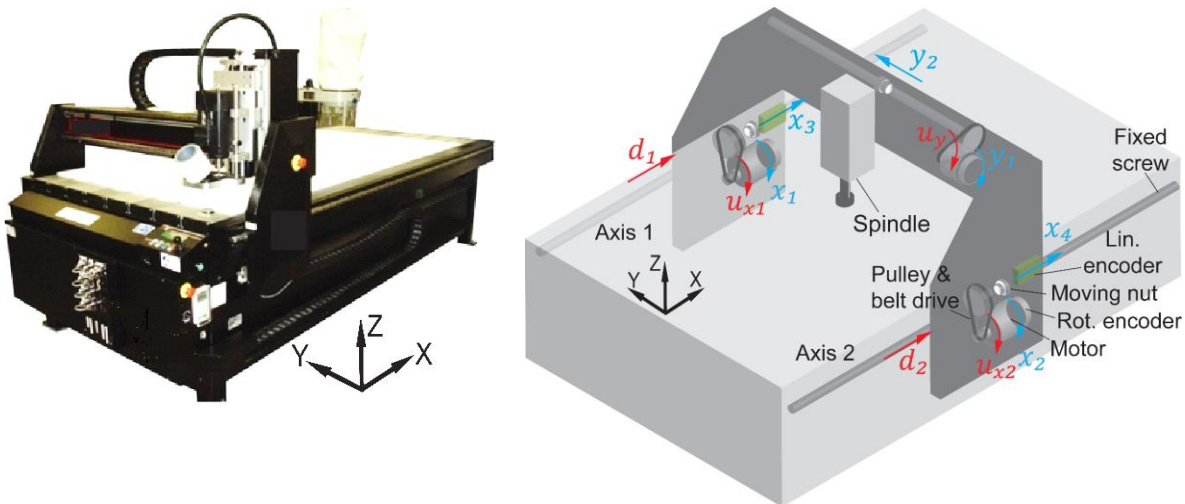


Figure 4.17: 3-axis H-type CNC router (left) and schematic view of actuation and measurement points (right).

The gantry x-axis has two drives, on the left-hand side and right-hand side. Both have stationary screws, which do not rotate, and the actuation is obtained by rotating the nut on each side using a pulley-synchronous belt mechanism. The y-axis, which has shorter travel, comprises a rotating screw and

translating nut. It too utilizes a pulley-synchronous belt mechanism, this time between the motor and screw. All axis are driven by Pittman 14207S008 brush commutated DC motors. The (vertical) z-axis has been kept outside the scope of the identification results reported in this work.

The rotary encoders mounted on the motors have a resolution of 500 pulses/rev with quadrature interpolation. Considering the 25 mm lead of the ball-screws, and the pulley ratio of 4.8 at each drive, a position measurement resolution equivalent to 2.6 μm of translation is achieved by the rotary encoders. Additionally, both sides of the x-axis gantry, and the y-axis, were retrofitted with LIDA 485 type linear encoders from Heidenhain. These generate sinusoidal signals with 20 μm period. With 4-fold quadrature decoding, and reliable ADC interpolation of 100-fold, the achieved measurement resolution, including electrical noise effects, was around 50 nm. A modular DS 1103 dSPACE platform was used for the measurements at a sampling frequency of 5 kHz.

Due to the strong mechanical coupling between the left- and right-hand sides, and the existence of a multitude of vibration modes, the x-axis has been measured and identified as a 4 \times 4 MIMO dynamic system. Of interest are both the command (i.e., motor actuation) response, and also the response to disturbance input forces at both the left- and right-hand sides. Considering the 3D schematic in Figure 4.17, the first two inputs to the plant correspond to the motor voltage commands applied at the amplifier inputs for both sides: u_{x1} and u_{x2} . The last two inputs are the external disturbance forces that can be applied or modeled at the moving columns of the gantry, shown with d_1 and d_2 . These two inputs can be used to independently simulate the dynamic response to the nonlinear stick-slip friction acting at the guideway on each side, or in gauging the impact of the machining forces, as they would be reflected to the feed drive system. The excitation of the disturbance inputs was achieved using an impact sledgehammer with 1.36 kg proof mass (Dytran 5802A, sensitivity of 0.24279 mV/N). In all cases, the disturbance force was also represented in terms of the equivalent voltage signal that would be applied at the amplifier input, in which 1 V corresponds to 7.2456 N of translational force. Similarly, the system outputs considered are, respectively, the rotary encoder measurements (x_1 and x_2) and linear encoder measurements (x_3 and x_4), obtained from the left-hand and right-hand sides, in the mentioned order. In the case of the y-axis, the system model was cast as being a SIMO (single-input multi-output) 2 \times 1 system, with the input being the motor voltage command (u_y) and the outputs being the rotary encoder and linear encoder measurements (y_1, y_2).

Due to large amount of stick-slip friction in the feed drive mechanisms, the actuation input related frequency response measurement for the x- and y-axes was performed using the two-stage indirect method [121][131][132], with the axes being in motion while following a constant-velocity trajectory. This helps to remove the influence of the sticking dynamics typically observed in guideways with friction. The closed-

loop system response was measured by injecting an additional excitation signal on top of the control signal (i.e., at the plant input), and by evaluating its impact on the outputs of interest. From this data, and with knowledge of the stabilizing feedback controller \mathbf{K} and its frequency response $\mathbf{K}(\omega)$, the open-loop MIMO FRF $\mathbf{H}(\omega)$ is estimated from the closed-loop frequency response. The testing procedure and open loop FRF estimation are explained in Appendix A.6.

In performing the FRF measurements for the actuation inputs, a simple proportional controller with low feedback gain was used, achieving a cross-over frequency of 3 Hz and 4 Hz in x- and y-axes, respectively. The small feedback gain allows for sufficient motor torque generation to overcome the sticking friction in order to achieve the primary rigid-body motion, while leaving the electromechanical system's mid- and high-frequency pole locations relatively unaltered. During post-processing of the measurement, the dynamic contribution of the controller is also removed from the measured closed-loop FRFs, as detailed in Appendix A.4. However, this decoupling is realized under the assumption of linearity. Thus, keeping the cross-over frequency low also allows various nonlinear phenomena to be avoided, such as actuator saturation or limit cycles due to the interaction of measurement quantization or friction effects with high feedback gain.

As the excitation signal, in the x-axis white noise perturbation, band-passed between 1...400 Hz, was applied to each side of the gantry, one at a time. In the y-axis, chirp type excitation, between 1...400 Hz, was applied. The FRF's were then computed by relating the cross-power spectrum with the auto-power spectrum, and applying suitable averaging using Welch's method [120].

In measuring the disturbance response, impact hammer testing with the machine covers removed was not possible while the axes were in motion, due to safety interlocks built into machine. Hence, the disturbance response FRFs for the gantry ($H_{13}, H_{23}, H_{33}, H_{43}, H_{14}, H_{24}, H_{34}, H_{44}$) were measured while the axis was stationary. In the case of the y-axis, the disturbance response measurement was not obtained. Such measurements are already presented for a single axis ball screw in Section 4.4, and the dual gantry x-axis in this section.

Figure 4.18 and Figure 4.19 show the experimentally measured FRFs and fitted MIMO (4×4) model FRFs for the gantry. The model fitting was based on imposing common pole location across all output/input channels, as explained in Section 4.2. Additionally, Figure 4.20 shows the visualization of the first two vibration modes of the gantry, determined by performing modal analysis on the machine structure. The identified model parameters and participation factors are summarized in Appendix A.4. It is important to note the large amount of friction present in the system, which results in the complex conjugate poles, especially related to the low frequency response of the gantry, to assume significant damping values

($\zeta_k > 0.1$). The nonlinear influence of friction can also be spotted in the FRF measurements shown in Figure A.6.2 in Appendix A.6, which were conducted under different input excitation amplitudes. At higher excitation magnitude, the apparent low frequency gain for the plant increases due to the Coulomb / Stribeck type friction assuming a less dominant role in relation to the motor actuation torques.

Since the response to the disturbance inputs (channels 3 and 4 for inputs: d_1, d_2) were measured while the axis was stationary, the influence of static friction is also clear in the low frequency asymptote for the corresponding gain plots. Thus, the slope is close 0 db/dec (demonstrating spring-like behavior), rather than -20 db/dec (which would represent motion capability against viscous friction). Comparing the estimated poles and mode shape visualization (Figure 4.20), it is seen that the pole pair at 25.9 Hz corresponds to axial-like movement of the gantry, and the pole pair at 46.6 Hz relates to yaw motion. The physical interpretation of the other poles merit further investigation, but this is not fully in the scope of the presented MIMO model fitting algorithm. Overall, it can be seen that the model fitting is in fairly close agreement with the experimental FRF measurements.

Figure 4.21 presents the measurement and SIMO (2×1) model FRFs for the y-axis. The parameters are summarized in Appendix A.5. Once again, a very close fit is achieved.

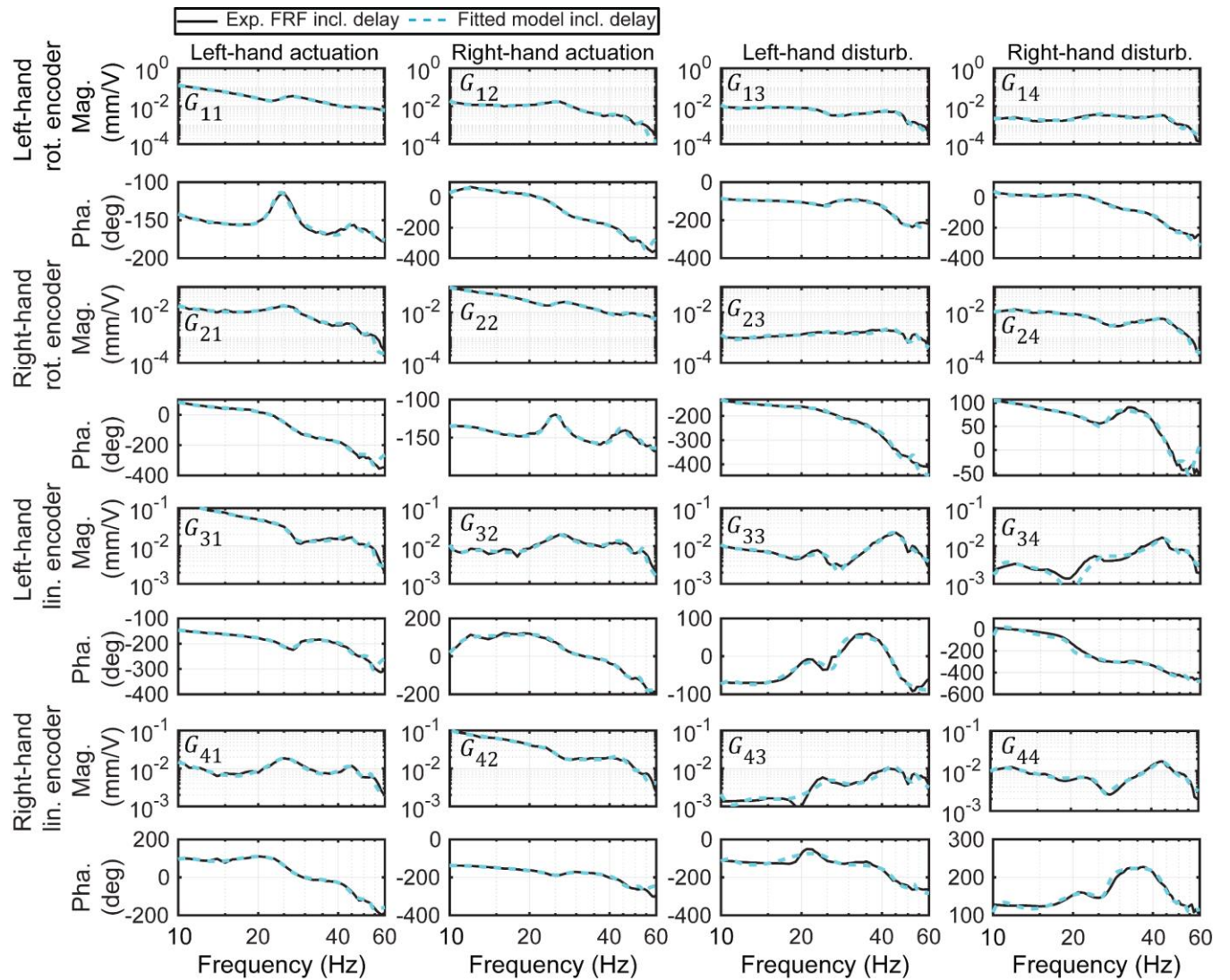


Figure 4.18: Raw FRF data and fitted model for the x-axis of the CNC router.

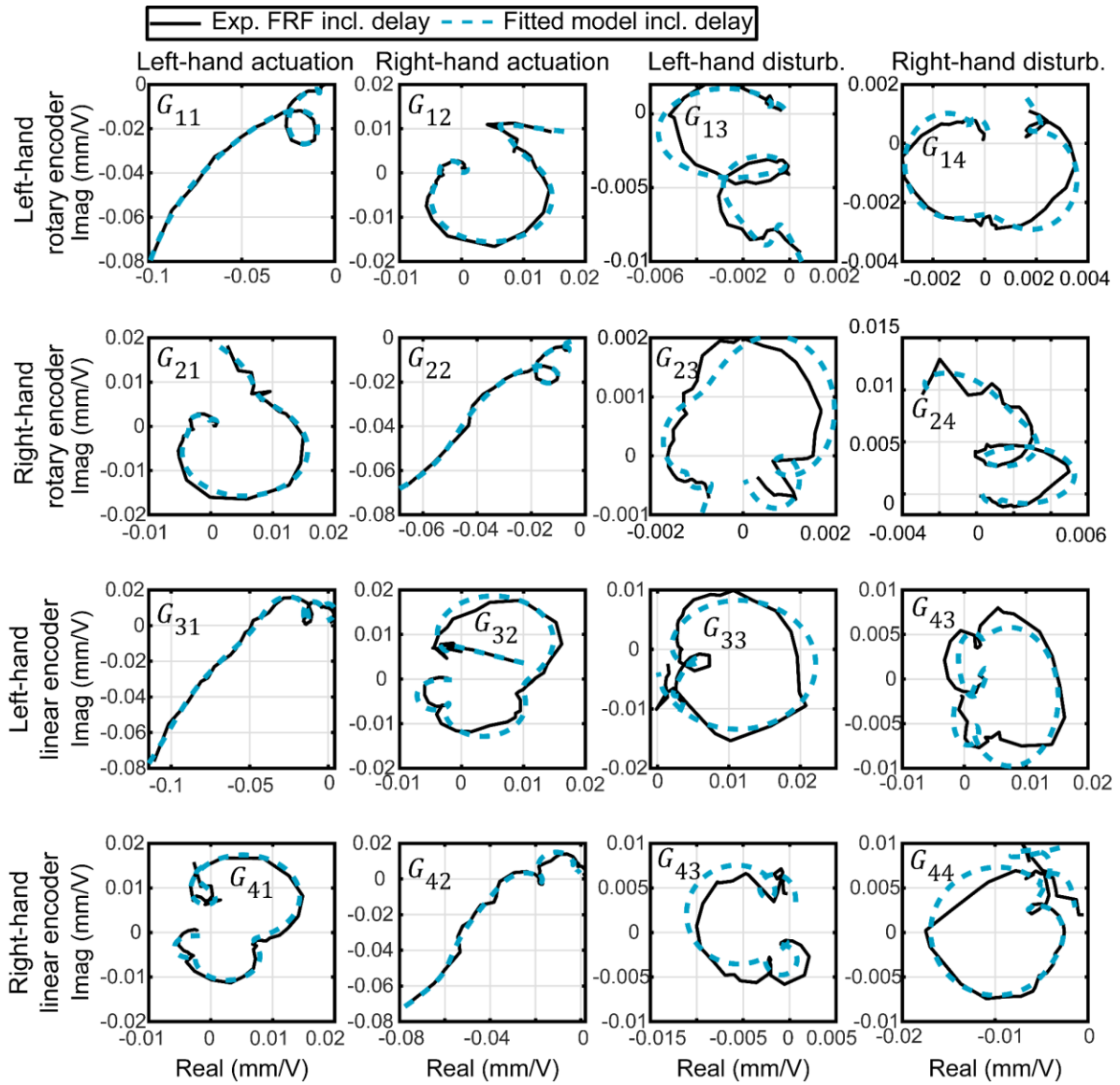


Figure 4.19: Nyquist plots of the experimental FRF including delay and fitted model.

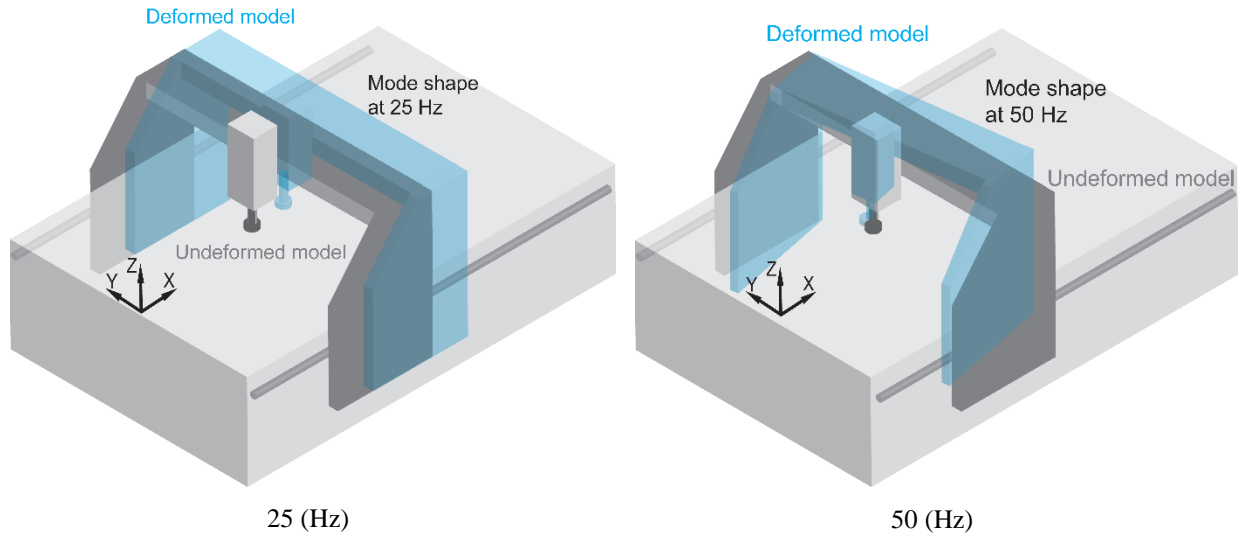


Figure 4.20: Mode shape visualization for the gantry x-axis.

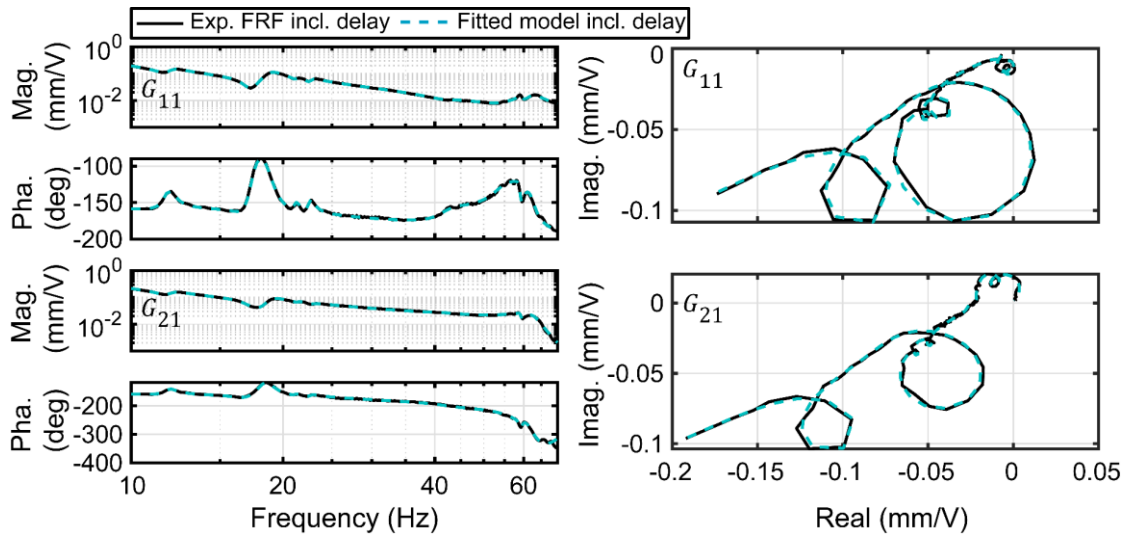


Figure 4.21: FRF (left), Nyquist plots (right) of the raw data including delay and fitted model for the y-axis of the CNC gantry machine.

4.6. Comparison of Proposed MIMO Algorithm with MATLAB's `tfest` and `modalfit` Functions

This section presents a comparison of the fitting results between the proposed algorithm and two widely used algorithms available in MATLAB, which are `tfest` and `modalfit`.

For a consistent comparison between the proposed algorithm and `tfest`, both algorithms were configured to use the same nonlinear optimization solver (i.e. `fmincon`). The poles of the system were constrained to be on the left-hand plane, to guarantee the stability of the identified models. Different

denominator degrees were examined in order to obtain the case with the least fitting error. While `tfest` can estimate MIMO models, the identified characteristic equation (i.e., pole locations) for the individual transfer function entries is not necessarily common across all output/input channels. However, as mentioned earlier, pole (i.e., eigenvalue) commonality is an expected result of first-principles based LTI modeling for mechatronic systems. This essential attribute is captured with the proposed MIMO identification algorithm. In addition to Instrumental Variable (`iv`) approach, other available algorithms in `tfest` (i.e. `svf`, `gpmf`, `n4sid`) were also examined to obtain the lowest fitting error between the measured frequency responses and the estimated model.

In the second case, the `modalfit` function, as a modal parameter estimation tool in frequency-domain, was used to identify models for SISO and MIMO feed drive systems. Since the function `modalfit` does not capture the effect of remainder dynamics (excluding resonances), increasing the order of the estimated model does not necessarily reduce the fitting error to the experimentally measured FRF. In using `modalfit`, all three available methods (`lsce`, `lsrf` – global fitting, `pp` – peak picking) were examined to achieve similar results.

In the proceeding comparisons, the data obtained from the T-type gantry, presented in Section 4.3, was used.

The first comparison is in fitting a SISO model based on the x-axis acceleration response, discussed in Section 4.3.2. For consistency, the model order for each method; `tfest`, `modalfit`, and the proposed algorithm, was set to be the same, as $n = 18$. This was the model order optimally determined in Section 4.3.2 for the corresponding setup data. In using `tfest`, the delay estimate obtained from the proposed MIMO algorithm was applied as an additional parameter. `modalfit`, on the other hand, does not allow the specification of pure system delay.

Figure 4.22 shows the experimental FRFs and fitted models using all three methods. For convenience, frequency-wise fitting errors are also displayed. The RMS values for the fitting errors, computed using Eq. (4.58), are summarized in Table 4.1. As can be seen, `tfest` generally works better than `modalfit`, achieving lower fitting error ($\text{RMS}(E) = 25.2844 \text{ (mm/s}^2\text{)/V}$ vs. $\text{RMS}(E) = 1511.2 \text{ (mm/s}^2\text{)/V}$). This is primarily due to its ability to capture a wider variety of poles, not just the lightly damped complex conjugate pairs. Due to the inability to capture remainder dynamics or system delay, there is significant mismatch in the imaginary component of the model identified using `modalfit`. On the other hand, it is seen that the model estimated with the proposed algorithm yields slightly higher fitting error than `tfest` method

($\text{RMS}(E) = 28.126 \text{ (mm/s}^2\text{)/V}$ vs. $\text{RMS}(E) = 25.2844 \text{ (mm/s}^2\text{)/V}$), while it shows significantly lower fitting error when compared to `modalfit` method, demonstrating 98.14% improvement.

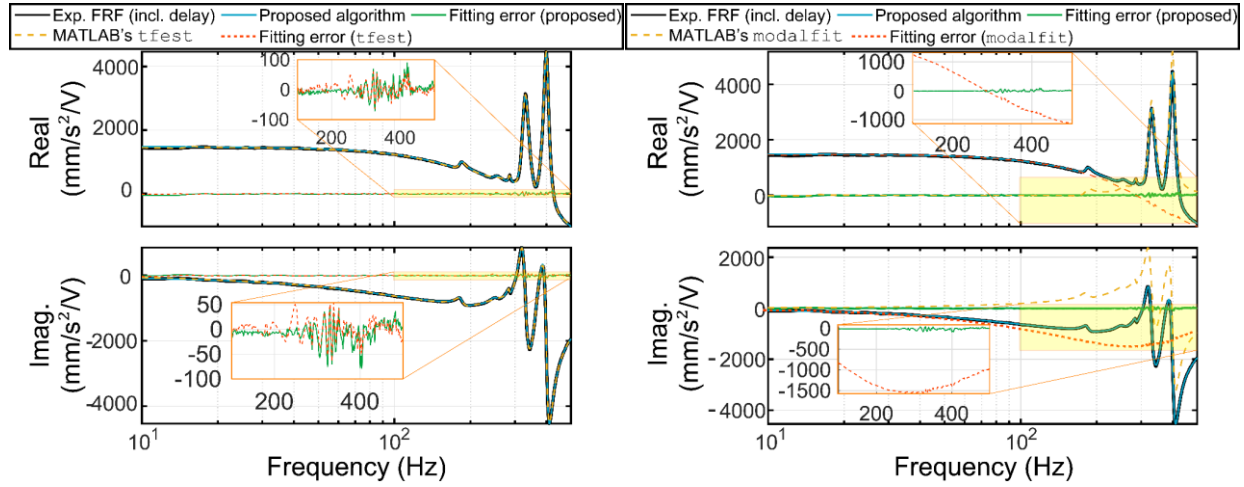


Figure 4.22: Raw FRF data and fitted models using `tfest` (left) `modalfit` (right) vs. the proposed algorithm.

Table 4.1: Comparison between the proposed algorithm, `tfest` and `modalfit` (SISO case).

Fitting algorithm	RMS error (mm/s ²)/V	Order
Proposed	28.126	18
<code>tfest</code>	25.2844	18
<code>Modalfit (lsrf)</code>	1511.2	18

The second comparison is in fitting a MIMO model based on the y-axis displacement response of the high precision gantry discussed in Section 4.3.1. The model order identified earlier with the proposed algorithm ($n=23$) was propagated into this comparison as well in configuring `tfest`. However, `modalfit` requires an even model order. For the use of this function, the model order was rounded up to 24. Figure 4.23 and Figure 4.24 show the original MIMO FRF data, the model fitted using the proposed MIMO estimation algorithm, and in the mentioned order: overlays of the models fitted using `tfest` and `modalfit`. Once again, frequency-wise fitting errors are also presented. Table 4.2 shows the comparison of fitting error RMS values, per Eq. (4.58), computed for all three methods.

Similar to the SISO case, `tfest` achieves lower fitting error in comparison to `modalfit` ($\text{RMS}(E) = 0.2242 \text{ mm/V}$ vs. $\text{RMS}(E) = 0.3032 \text{ mm/V}$). However, the proposed algorithm achieves even lower fitting error, $\text{RMS}(E) = 0.001004 \text{ mm/V}$. Compared to the result of `tfest`, this is an additional 99.55% improvement.

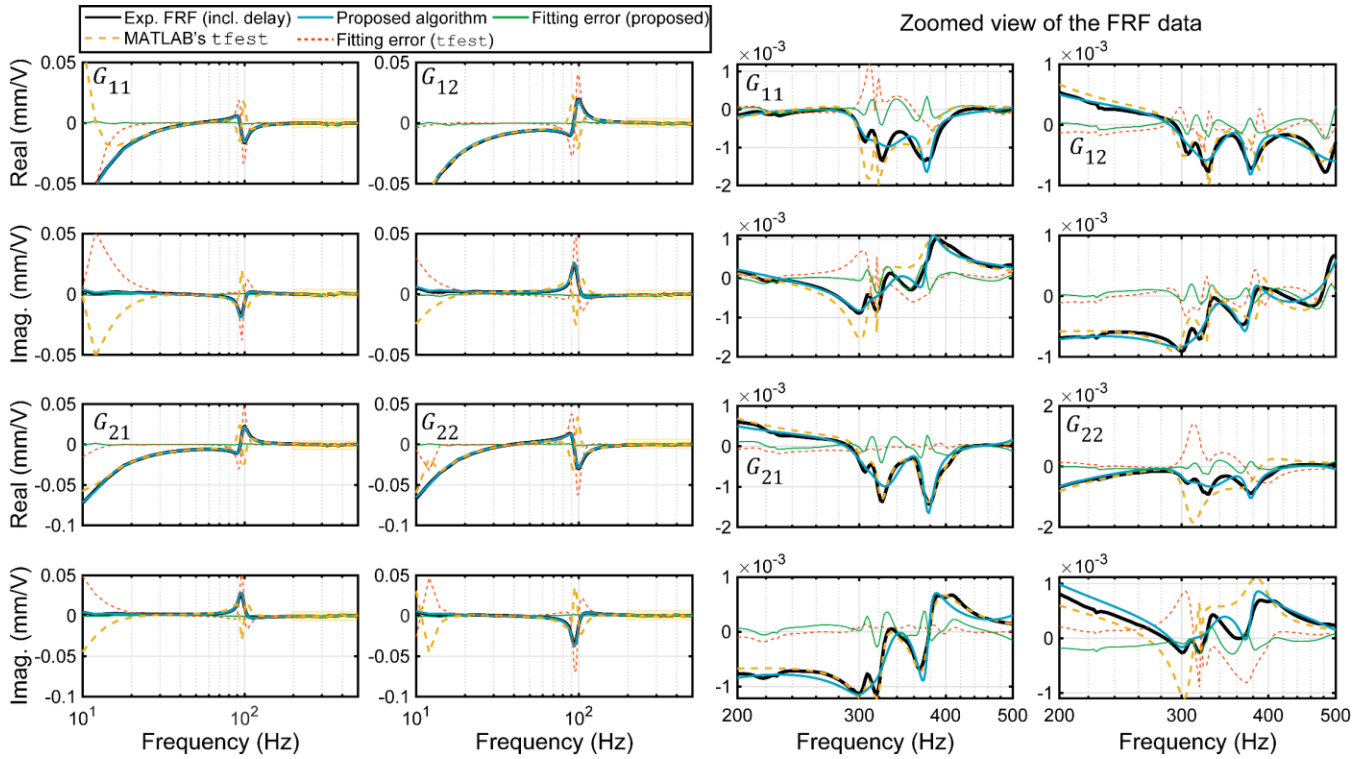


Figure 4.23: Raw FRF data and fitted models using the proposed algorithm vs. `tfest`.

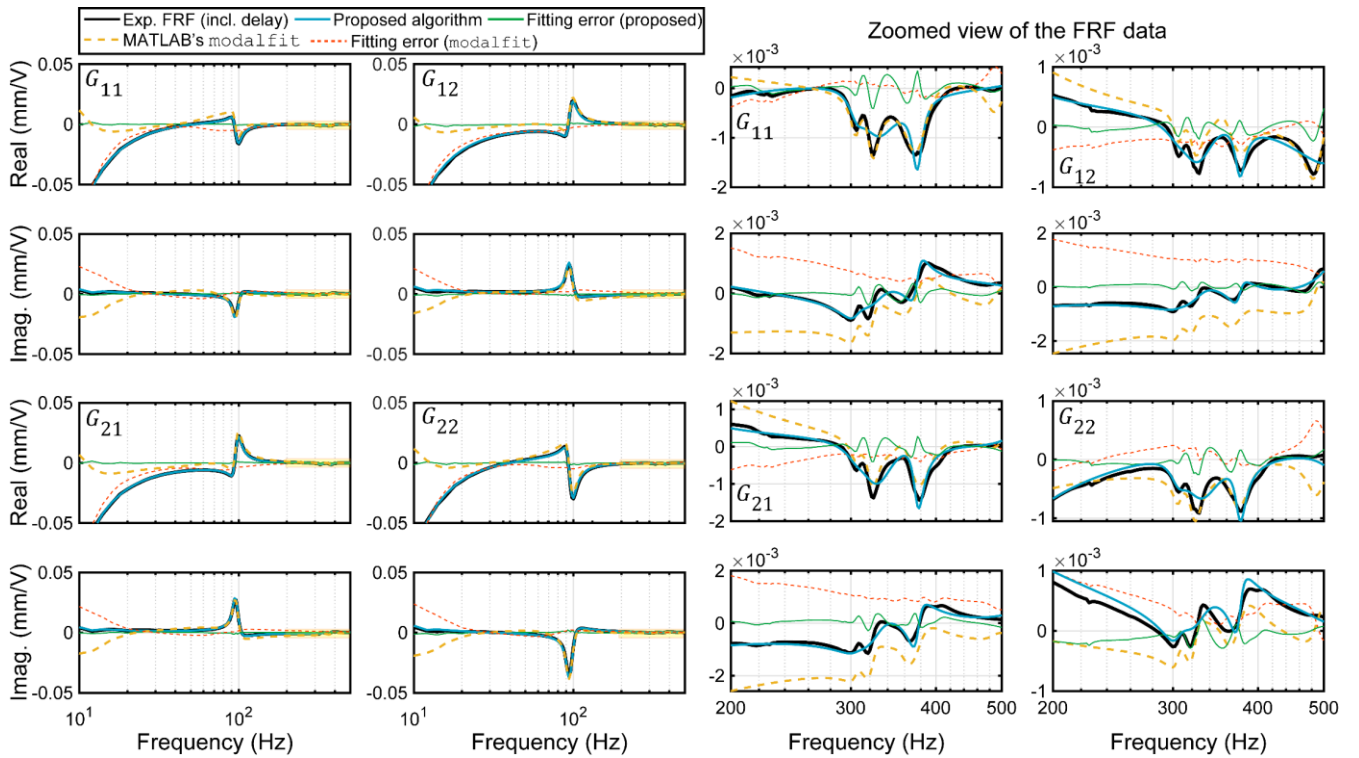


Figure 4.24: Raw FRF data and fitted models using the proposed algorithm vs. `modalfit`.

Furthermore, through its ability to enforce the commonality of pole locations across all designated output and input channels, the proposed algorithm is able to estimate a minimal order MIMO LTI model with ideally the least amount of ‘superfluous modes’. In mainstream identification practice, superfluous modes can originate from estimating and attempting to merge multiple SISO realizations, obtained from different output-input channel combinations, into a single MIMO model. However, the proposed algorithm simultaneously considers all available multivariate data, and systematically optimizes the pole locations and participation factors, to achieve a constrained-order model with the best possible fit across all transfer function entries. Such a compact and carefully optimized MIMO model can provide significant advantages in controller design and implementation, especially in the implementation of model-based methods like state-feedback, pole-placement, LQG, and H_2/H_∞ optimal control. As can be observed from Table 4.2, for the y-axis of the gantry, the fitting error of the model constructed by concatenation of the individual SISO transfer functions is significantly lower than the model considering the MIMO system for the same order. The stability was enforced for the identification of each SISO transfer function. Due to lack of constraint on the commonality of the system’s poles, the minimal realization of the identified MIMO system by `tfest` function results in 92 states as compared to 46 states estimated by the proposed algorithm (considering the data from all the input/output channels). There were some cases where `tfest` achieved better fitting results compared to the proposed algorithm. However, these were obtained only when the optimization of `tfest` was not constrained to enforce left-hand plane poles and in each of these cases, the model estimated by `tfest` was unstable. These cases are shown in Appendix A.7. The convergence result was the same regardless of the solver algorithm chosen.

Overall, the presented SISO and MIMO benchmark studies demonstrate that the proposed MIMO identification algorithm is able to achieve two order of magnitude improvement in the frequency-domain fitting compared to some of the well-established algorithms currently available in MATLAB’s `tfest` and `modalfit`. In addition, the MIMO models estimated with the proposed method are highly suitable for model-based controller design.

Table 4.2: Comparison between the proposed algorithm, `tfest` and `modalfit` (MIMO case).

Fitting algorithm	RMS error (mm)/V	Order
Proposed	0.001004	23
<code>tfest</code> (Concatenation of SISO models)	0.1121	23 (2×2)
<code>tfest</code> (MIMO model)	0.2242	23 (2×2)
<code>modalfit</code> (<code>lsrf</code>)	0.3032	24

4.7. Conclusions

This chapter has presented a new frequency-domain MIMO LTI model identification algorithm, which can be used for mechatronic systems with multiple actuation and disturbance inputs, as well as multiple sensor and measurement channels. The algorithm is particularly successful in identifying models for systems with mixed dynamics, comprising delays, lightly damped (highly resonant) as well as well-damped (lightly-resonant or non-resonant) complex conjugate and real poles. The systematic procedure has first been described from bird's eye view (Section 4.2.1), then with full-detailed formulation (Section 4.2.2), and afterwards in the context of step-by-step numerical implementation with experimental MIMO data (Section 4.3).

As case studies of different mechatronic systems, the proposed method has been successfully validated in model identification for: i) A T-type precision gantry with linear motors and air bearings (2×2 MIMO y-axis, 1×1 SISO x-axis); ii) A precision ball screw with air bushing (2×2 MIMO with different types of actuation inputs (motor and impact hammer) and rotary and linear encoders outputs, and ; iii) An industrial flatbed router with long ball-screws, significant friction, and belt-pulleys transmission systems (4×4 MIMO x-axis: motor and impact hammer inputs, rotary, linear outputs, plus, 2×1 SISO y-axis).

In all cases, it is seen that the proposed algorithm, made up of: Iterating for the system delay estimate (Step 1), Initially decoupled estimation of the resonant modes and remainder dynamics (Steps 2-4), Consolidation of all dynamics and joint adjustment of all participation factors (Step 5), and, Nonlinear optimization of the pole locations (Step 6), has achieved very close fits to the experimental data. Furthermore, the method has been benchmarked against two of the most widely used estimation algorithms available through MATLAB, `tfest` and `modalfit`. The proposed algorithm has demonstrated two order-of-magnitude or better (i.e., 99.55% - 99.67%) improvement over the results obtained with these methods in MIMO case. The use of the identified models, obtained via the proposed approach, is now being investigated in MIMO control design strategies.

Chapter 5

Control for Precision Motion and Active Vibration Damping

5.1. Introduction

Aside from fundamental limitations, such as time delays and non-minimum phase zeros, the excitation of structural resonances by the control input remains one of the limiting factors in achieving high servo-bandwidth control in motion control systems, such as machine tool feed drives. This is especially true if the modes that are excited have poor controllability or observability in relation to the feedback controller output and input, or lie in a frequency range where the required control action exceeds the actuators' capabilities, or the sensor's feedback quality diminishes. The latter two points are especially prevalent in dealing with high-frequency vibration modes, for which the required damping effort can be excessive, and the signal-to-noise ratio deteriorates due to relatively small motions registered, when using industry-standard displacement (encoder) signals for feedback.

While most servo control architectures with active damping capability typically consider only one vibration mode at a time [55][71][72][80], namely the most dominant axial mode in ball-screw drives, the existence of other modes at lower and higher frequencies can have a diminishing effect on the achievable closed-loop control performance, especially in terms of rejecting external (e.g., cutting force or friction) type disturbances on the load side for a wide frequency range. The rejection of such disturbances, nevertheless, plays a critical role in improving both the dynamic positioning accuracy of a production machine [71][133][134] (i.e., the manufactured part quality), and also the stability of a machining process (i.e., productivity), by reducing the susceptibility of the feed drive system to cause unstable machining chatter vibrations due to exhibiting a high value for dynamic compliance [63][135].

In this chapter, a new tracking and vibration damping control strategy is proposed in order to attenuate multiple vibration modes and obtain superior disturbance rejection in ball-screw drive systems. *In the best of the author's knowledge, this study is the first time in literature in which multiple vibration modes for a ball-screw drive are successfully modelled and actively attenuated with experimental validation.* The proposed controller includes an inner loop that is synthesized using the mixed-sensitivity optimization method based on the \mathcal{H}_2 or \mathcal{H}_∞ norm to achieve active vibration damping, and an outer loop designed using loop shaping principles to achieve suitable tracking of trajectory commands. The vibration damping controller synthesis, which is at the heart of the proposed design, is made possible especially due to the high-fidelity MIMO model that could be estimated from FRF data of a ball-screw, using the algorithm developed in Chapter 4. In addition to the two-loop structure, suitable feedforward control terms to

overcome repeatable disturbances, such as friction, and to correct for trajectory following distortions, are also included into the overall control structure.

The performance of the proposed controller is compared against the industry-standard P-PI position-velocity cascade controller, and the vibration-damping pole-placement controller (PPC) [72] in tracking and disturbance rejection experiments. The benchmarked controllers (i.e. P-PI position-velocity & PPC) are designed, and optimally tuned based on a two-inertia model of the feed drive system described in Section 3.7.

In the following, Section 5.2 introduces a motivating case study to highlight the importance of considering structural vibrations when designing servo control laws for machine tool feed drive systems.

Section 5.3 reviews the design of the industry standard P-PI position-velocity cascade controller, which will be used as the first benchmark (i.e., baseline) in this chapter. Section 5.4 describes a more recent vibration damping based position controller presented in the literature based on the pole-placement method, considered as the second benchmark. Afterwards, the general formulation of the mixed-sensitivity \mathcal{H}_2 and \mathcal{H}_∞ optimization problem is reviewed in Section 5.5, which is used in synthesizing the proposed control law's vibration damping functionality. Setting this work apart from earlier applications of \mathcal{H}_2 and \mathcal{H}_∞ control for feed drives, in this thesis, multiple vibration modes are targeted instead of just one.

The design and integration of the tracking controller and active vibration-damping optimal controller is discussed in Section 5.6. Section 5.7 compares the proposed control synthesis against the conventional weighting approach used in sensitivity function parameterization. The former directly aims to minimize the load-side compliance transfer function, whereas the latter typically adopts a conventional filter structure that is reported and proposed in literature.

Lastly, Section 5.8 evaluates the performance of the proposed design (mixed-sensitivity with \mathcal{H}_2 or \mathcal{H}_∞ based vibration damping, in conjunction with Loop Shaping (LS)) against the two benchmarked controllers (P-PI and PPC). Section 5.9 presents the conclusions for this chapter.

5.2. Case Study Demonstrating Limiting Influence of Vibration Modes

Figure 5.1c shows an H-type gantry machine, which was measured and described in Chapter 4 in the context of model estimation. Considering the ball-screw driven y-axis (i.e., cross-axis), which contains feedback measurement from a rotary encoder on the motor, and a linear encoder mounted along the axis, the outcomes of applying a similar control strategy, but with different feedback points, are shown in Figure 5.1 and Figure 5.3, in terms of loop stability and sensitivity, and in terms of time- and frequency-domain servo error and control signals. The frequency response measurements obtained for the gantry in Chapter 4 were used in the stability and sensitivity analyses per [25]. The control structure, shown in Figure 5.2, is a PID controller with feedforward friction and open-loop rigid body dynamics compensation. The plants outputs y_1 and y_2 are the rotational and translational feedback channels. The input represents the motor armature voltage commanded to the actuator's amplifier input. The feedback gains were originally designed to achieve 20 Hz crossover frequency and 35° phase margin, by considering only a single-mass rigid-body based model of the feed drive system ($G = \frac{y}{u} = \frac{1}{s(ms+b)}$). It is known, from the measurements presented in Chapter 4 that the true frequency response is indeed more complex.

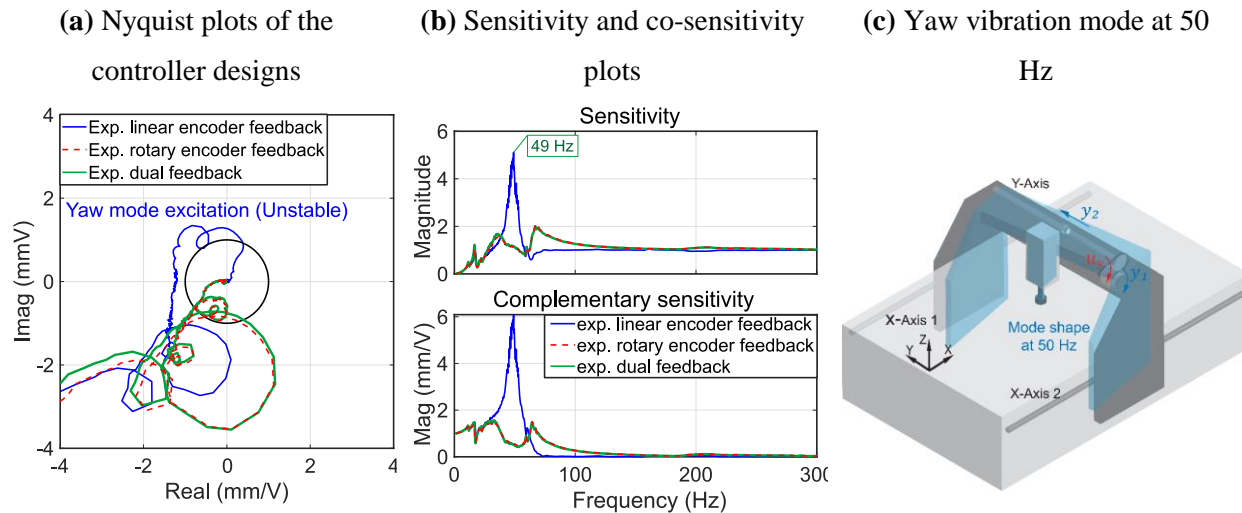


Figure 5.1: Frequency-domain analysis of y-axis PID control feedback loop closed using different measurement signals.

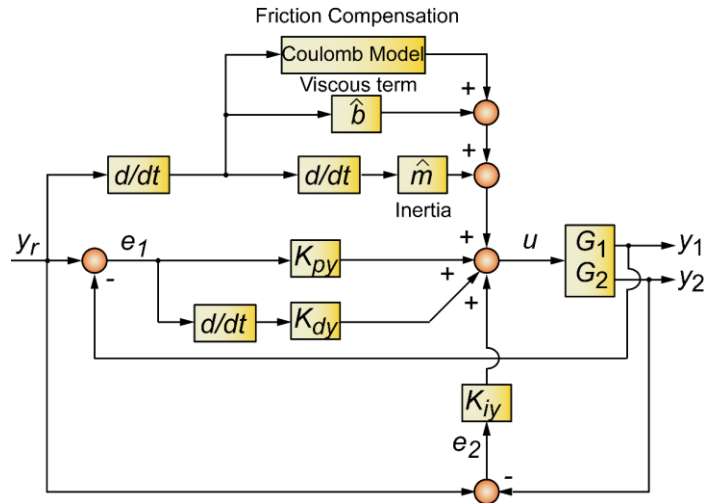
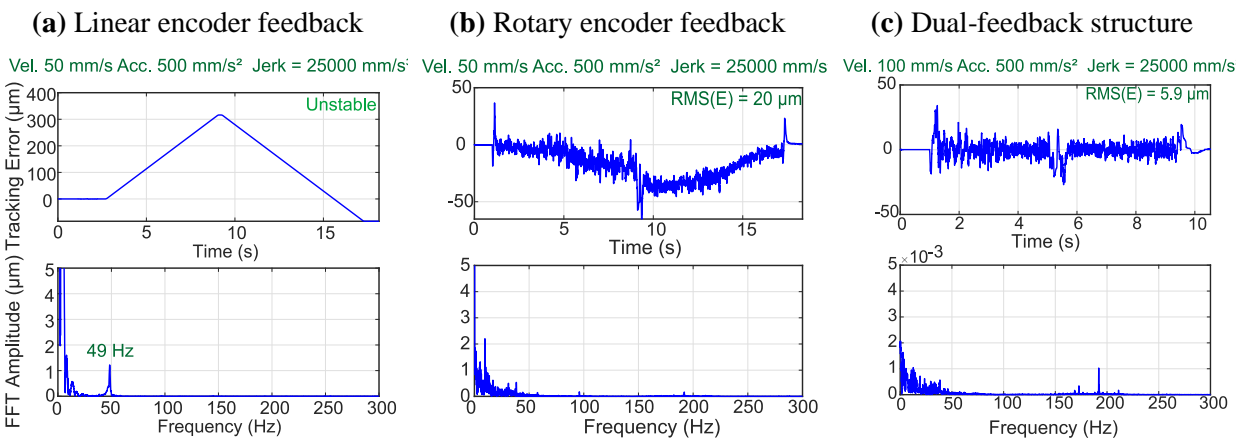


Figure 5.2: Block diagram of the dual-feedback loop-shaping PID controller.

In the first case, when translational feedback (y_2) is used as the sole plant output, the control loop is unstable, with the source of instability being associated with the frequency of 49 Hz, as seen in the sensitivity and complementary sensitivity magnitude plots in Figure 5.1b. Modal analysis performed on the setup reveals that at 50 Hz, the parallel x-axes of the gantry constitutes a yaw-type vibration mode (Figure 5.1c). Clearly, this behaviour cannot be captured with a simplified rigid-body based plant model. Although the actuation and feedback are obtained from the perpendicular y-axis, as a result of the mechanical cross-talk between the axes, in this feedback configuration, the y-axis servo system and yaw-vibration mode affecting the x-axis couple together to form an unstable system. This is seen with the highly oscillatory control signal in Figure 5.3a, followed by emergency software shut-down of axis power, which results in the commanded motion profile not being tracked, as seen in the servo error profile.



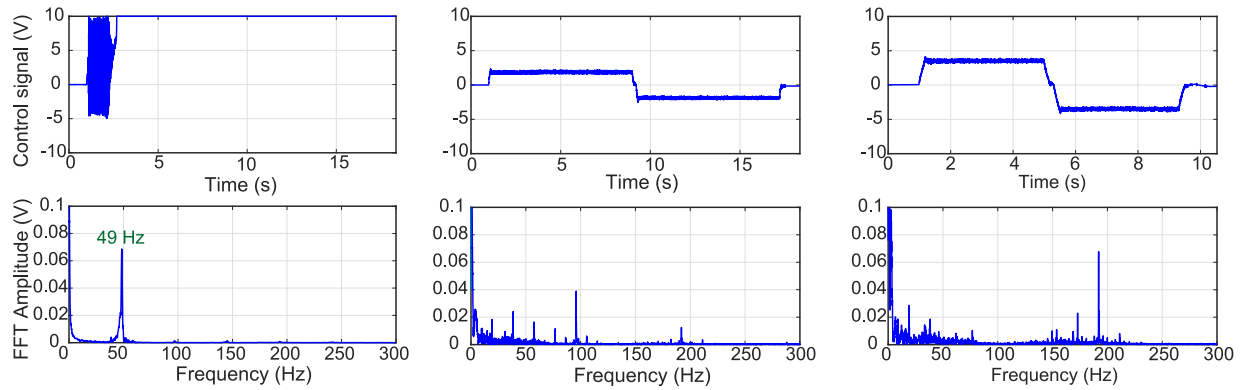


Figure 5.3: Tracking error profiles and control signals using different feedback structure.

In the second case, if only rotational feedback is used, which is less sensitive to the yaw vibration mode, the control loop can then be stabilized, as shown in Figure 5.1b. However, as seen in the servo error profile in Figure 5.3b, which is estimated using the table translational motion ($e = y_{ref} - y_2$), closing the loop from the rotary encoder alone can result in positioning drift to accumulate along the travel due to various factors, such as the misalignment of the ball-screw mechanism, backlash, and through longer time durations, the effect of thermal deformations.

In the third case, using the rotary encoder to close the ‘high-frequency’ component of the feedback loop (i.e., the PD-control terms, similar to the concept of using PI-type velocity control) and applying linear encoder feedback for the ‘low frequency’ portion, (i.e., the integral control action in position control), a good stabilization is obtained providing immunity against the external vibration mode (Figure 5.1b), and the low-frequency drift in the servo positioning error is also prevented, as can be verified from Figure 5.3c. Indeed, there is nearly 70% improvement in accuracy compared to the second case, in spite of the commanded velocity having doubled over case two (from 50 to 100 mm/s). This is the main reason that in the practical application of ball-screw drives, the rotational feedback is used to close the velocity control loop (typically with PI-control) to achieve high bandwidth control with reduced influence from vibration modes, and translational feedback is used to control the position control loop (usually with P-control) to accomplish better steady-state positioning accuracy.

In addition to clarifying the use of different feedback points in feed axes, this example shows the critical influence of vibration modes on the stability and performance of a servo control system. In some cases, adequate choice of feedback locations can help avoid the excitation of a vibration mode, or even achieve its suppression in comparison to the open-loop case as will be shown in the proceeding subsections. However, due to the non-collocated nature of sensor and actuator placement in feed drives, this approach

typically has the limitation of being effective against perhaps one or two modes at a time, thus motivating the study for more advanced, and ideally model-based, controller design techniques.

Further, complementary to the vibration modes originating from the active drive elements (e.g., ball screw, bearings, motor, guideways, sensor mounting), the flexibilities arising from large components in machine tools such as columns and rams, or the joints, contribute to low eigenfrequencies, as seen with the 50 Hz yaw mode example in this case study. Based on the observations in Section 3.11, the responses of a feed drive often contains highly as well as lightly damped modes with close frequency. For example, in the case of the single-axis ball-screw drive (Section 3.11), there are three vibration modes at 255 Hz, 289 Hz, and 312 Hz, which exhibit seemingly similar combinations of yaw-roll and yaw-pitch motions. Additionally, machine tool / feed drive structures are also susceptible to possessing counter-phase modes, which are very difficult to stabilize via manual loop shaping or simple dual-sensor placement strategies. All of these factors necessitate a more powerful, systematic, and, holistic approach to feed drive controller design in dealing with structural vibrations. The ideal approach needs to incorporate adequate system identification, when possible active compensation, and when not possible, suitable suppression or avoidance, of detected vibration modes that may be inclined to interact with the servo system's feedback law. Thus, the proposed methodology that will be presented in Sections 5.6 and 5.7 was developed to achieve this goal.

5.3. Benchmark #1 Industry-Standard P-PI Position-Velocity Cascade Controller

The P-PI position-velocity cascade controller is the most widely used structure by the machine tool industry to achieve high tracking accuracy and disturbance suppression. To a certain extent, this structure is also used in industrial robots. Figure 5.4 depicts the dual-feedback structure of the P-PI controller. The velocity feedback is taken from the rotary encoder directly on the motor. This way, structural modes appear mostly as anti-resonances, thereby not leading to limitations in terms of increasing the feedback gain and bandwidth. On the other hand, the position feedback is typically taken from a linear encoder close to the location of the workpiece-tooltip interface. This leads to more accurate measurement and regulation of the actual cutting motion, but creates the challenges of amplified resonances and additional phase lag in the feedback loop, which can be a limiting factor on the achievable motion bandwidth. P-PI position-velocity cascade control is typically tuned in industry following guidelines that emphasize maximizing the bandwidth of individual loops to enhance the dynamic accuracy. Certain filters and trade-offs in the bandwidth are also considered to ensure stability of the overall system. As an alternate tuning methodology, Beudaert et al. [63] proposed tuning the velocity loop gain directly to maximize the damping factors of

vibration modes, which are most prone to causing chatter vibrations during machining. While this can lead to more productive rough machining operations with better chatter stability, it has a negative impact on the dynamic positioning accuracy.

In this thesis, as the objective is to improve the dynamic accuracy as much as possible, the benchmarking is done with respect to the design methodology that maximizes the bandwidth of the P-PI control system while ensuring that the robustness and stability margins are satisfied.

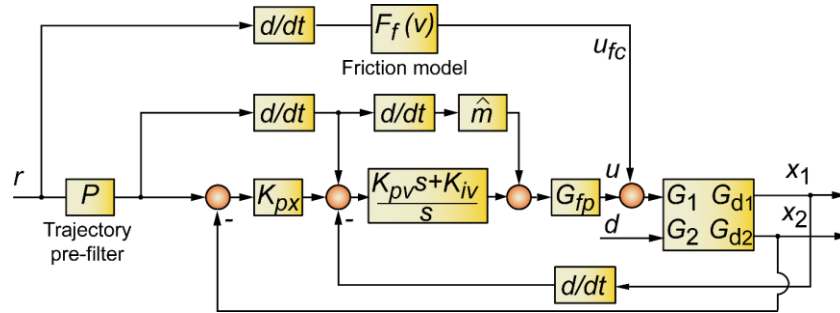


Figure 5.4: Dual-feedback P-PI position-velocity cascade control structure.

The P-PI controller design is achieved based on the two-inertia model of the drive system to actively damp its first axial vibration mode (see Section 3.7). The gain tuning procedure follows the guideline in [136]. First, the inner loop of the controller (velocity loop) is designed to achieve five percent overshoot in the step response. Then, the proportional gain in the outer position loop is increased incrementally until an overshoot is observed in the position. Lastly, feedforward terms are added to further improve the tracking accuracy of the motion. The feedforward terms include velocity (using the estimated viscous damping coefficient), acceleration, a trajectory pre-filter [130] (to remove un-compensated velocity, acceleration, and jerk artefacts from the servo error), and Stribeck model-based friction compensation.

5.4. Benchmark #2 PPC Vibration Damping Controller

As the second benchmark, a vibration-damping pole-placement controller was chosen. The feedback controller design follows the method proposed by Gordon and Erkorkmaz [72]. With this method, the objective is to widen the bandwidth of the controller by increasing the dynamic stiffness near the first axial vibration mode, while also achieving high tracking and disturbance rejection for the low-frequency range. The state-space model includes five states. Two of the poles are placed to increase the decay ratio in the vibratory response without modification to the damped oscillation frequency, as this would directly affect

the control effort. To further move the poles to the left side of the s -plane, a shifting factor is defined for the real component of the complex conjugate poles. This idea is similar to the concept of low authority LQG vibration control [79]. The state-space model can be expressed by:

$$\begin{aligned} \underbrace{\begin{bmatrix} \dot{x}_1 \\ \dot{x}_2 \\ \ddot{x}_1 \\ \ddot{x}_2 \end{bmatrix}}_{\dot{z}} &= \underbrace{\begin{bmatrix} 0 & 0 & 1 & 0 \\ 0 & 0 & 0 & 1 \\ -k/m_1 & k/m_1 & -(c+b_1)/m_1 & c/m_1 \\ k/m_2 & -k/m_2 & c/m_2 & -(c+b_2)/m_2 \end{bmatrix}}_A \underbrace{\begin{bmatrix} x_1 \\ x_2 \\ \dot{x}_1 \\ \dot{x}_2 \end{bmatrix}}_z + \\ &\underbrace{\begin{bmatrix} 0 & 0 & 0 \\ 0 & 0 & 0 \\ 1/m_1 & 1/m_1 & 0 \\ 0 & 0 & 1/m_2 \end{bmatrix}}_B \underbrace{\begin{bmatrix} u \\ d_1 \\ d_2 \end{bmatrix}}_U, \\ \underbrace{\begin{bmatrix} x_1 \\ x_2 \end{bmatrix}}_y &= \underbrace{\begin{bmatrix} 1 & 0 & 0 & 0 \\ 0 & 1 & 0 & 0 \end{bmatrix}}_C z \end{aligned} \quad (5.1)$$

The low-frequency disturbance rejection was enhanced by applying an additional state that represents the integral of load-side position ($x_{2i}(t) = \int_0^t x_2(\tau) d\tau$). The pole-placement controller takes the form of a simple PD-PID structure, which applies weighting to the rotary encoder (x_1) and linear encoder (x_2) feedback channels:

$$K_{ppc}(s) = \left[\underbrace{K_{x_1} + K_{v_1}s}_{K_1}, \quad \underbrace{K_{x_2} + \frac{K_{i_2}}{s} + K_{v_2}s}_{K_2} \right] \quad (5.2)$$

The shifted poles (p_1, p_2) in the s -plane will become:

$$p_1, p_2 = -\beta\sigma_1 \pm j\omega_d \quad (5.3)$$

In the above equation $\beta \geq 1$ is the shifting factor, ω_d is the damped natural frequency, and σ_1 is the real component of the complex conjugate poles for the open-loop plant. The three remaining poles $\{p_3, p_4, p_5\}$ are related to rigid body dynamics.

$$\begin{aligned} p_3, p_4 &= -\zeta_2\omega_2 \pm j\omega_2\sqrt{1 - \zeta_2^2} \\ p_5 &= -\omega_2 \end{aligned} \quad (5.4)$$

Due to its low order, the state feedback gain for the pole-placement controller can be calculated using Ackerman's formula. Figure 5.5 shows the structure of the vibration damping pole-placement controller. In the controller design, different shifting factors and pole locations were examined to achieve the

maximum crossover frequency, while adhering to a peak sensitivity requirement. A shifting factor of $\beta = 4$ and desired rigid-body pole locations at $\omega_2 = 30$ Hz and $\zeta_2 = 0.7$, were found to be successful in this respect. The plant inversion based on the two-inertia model was used as a feedforward term to improve the tracking accuracy.

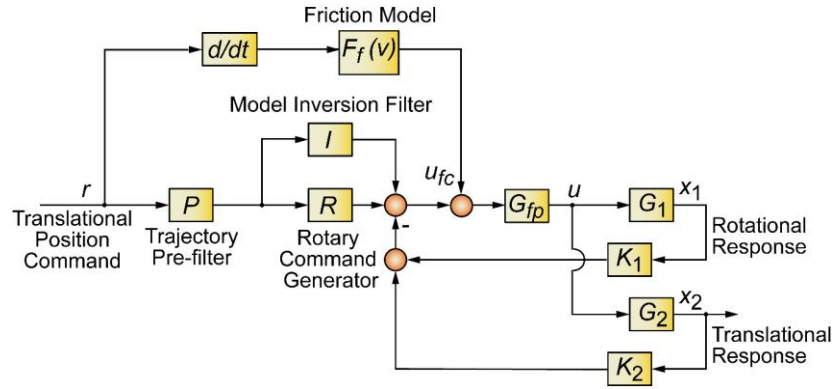


Figure 5.5: Vibration-damping pole-placement control structure [72].

As mentioned, this pole-placement controller design can only be successfully used to suppress a single vibration mode. While the two-inertia model is helpful in performing simulation studies and gaining insight into various dynamic interactions, it has its limitation in handling more realistic feed drive dynamics, which have both low and high frequency modes outside the main axial mode. Another limitation of the pole-placement controller is the choice of feedback sensors. In cases where more actuation and feedback points are available (e.g., gantry drive, multiple position / velocity/ acceleration sensors etc.), the extendibility of this approach is not clear.

5.5. Mixed-Sensitivity \mathcal{H}_2 and \mathcal{H}_∞ Optimization Problem

This subsection briefly reviews the \mathcal{H}_2 and \mathcal{H}_∞ optimization based controller synthesis problem, which will be used in subsequent sections in vibration damping controller design.

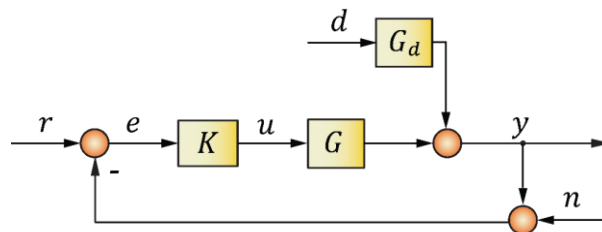


Figure 5.6: Structure of a feedback control system.

The typical structure of an LTI feedback control system is shown in Figure 5.6, where G and G_d represent the actuation and disturbance inputs of the plant, K the feedback controller, y the true plant output, d the disturbance input, n the measurement noise, r the command input, and u the feedback control signal. The dynamics blocks and signals can be SISO or MIMO. Based on the above, the closed-loop system output (y) and the control effort (u) can be expressed in terms of the three main inputs (r, d, n) as.

$$\begin{aligned} y &= (I + GK)^{-1}GK \cdot r + (I + GK)^{-1}G_d \cdot d - (I + GK)^{-1}GK \cdot n \\ u &= K(I + GK)^{-1} \cdot r - K(I + GK)^{-1}G_d \cdot d - K(I + GK)^{-1} \cdot n \end{aligned} \quad (5.5)$$

In the expression for u , the term $K(I + GK)^{-1}$ originates from the expression for $(I + KG)^{-1}K$. The two are equivalent per the ‘push-through’ rule [25], which can be verified by multiplying the matrix inverse form of one with the un-inverted form of the other to obtain the unity matrix. The expression $(I + GK)^{-1}$, also referred to as the *sensitivity* (S) plays a critical role in determining how feedback control improves the disturbance response at certain frequencies ($(I + GK)^{-1}G_d$) compared to the open-loop case (G_d). Indeed, at frequencies where the maximum matrix gain (i.e. upper singular value) is less than one, $\bar{\sigma}(S(\omega)) < 1$, improvement via feedback control is obtained. However, this is limited in frequency range due to the expected ‘waterbed’ effect [25]. Very high values of sensitivity ($\bar{\sigma}(S(\omega)) > 2$) also indicate stability and robustness problems. The term $KS = K(I + GK)^{-1}$, on the other hand, represents the amount of control effort that is generated as a result of command inputs and especially measurement noise at each frequency. This function has to be limited, in order to avoid an excessively ‘active’ control law, that would be detrimental in terms of causing actuator saturations and/or high-frequency high-amplitude outputs, which can be very detrimental to the electromechanical system, and also lead to the excitation of high frequency dynamics that were not originally considered in the controller design.

Hence, the mixed-sensitivity \mathcal{H}_2 and \mathcal{H}_∞ control synthesis problem is based on minimizing a stacked version of the two expressions (i.e., S over KS), as shown with Eq. (5.6) [137][138]:

$$\min_{K \text{ stabilizing}} \left\| \begin{array}{c} (I + GK)^{-1} \\ K(I + GK)^{-1} \end{array} \right\|_{2 \& \infty} \quad (5.6)$$

Further information about system and signal norms can be found in [25]. Given a plant in terms of state-space matrices $A \in R^{n \times n}$, $B \in R^{n \times n_u}$, $C \in R^{n_y \times n}$, and $D \in R^{n_y \times n_u}$, the continuous-time linear time-invariant plant can be described as:

$$\begin{aligned} \dot{x}(t) &= Ax(t) + Bu(t) \\ y(t) &= Cx(t) + Du(t) \end{aligned} \quad (5.7)$$

The MIMO transfer function for the above LTI can be stated as $G(s) = C(sI - A)^{-1}B + D$:

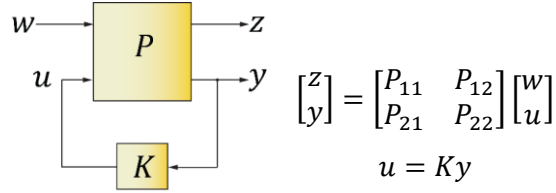


Figure 5.7: General control configuration.

In a more generalized formulation, as shown in Figure 5.7, the input channels can be expanded into exogenous disturbances (w) and controlled inputs (u). Exogenous disturbances may contain generalized command inputs, disturbances, and sensor noise. Similarly, the output channels can be expanded into outputs for evaluating performance (z), versus outputs used in feedback control (y). In defining the performance outputs (z), certain weighting functions, like W_e and W_u , can be included into the structure, as shown in Figure 5.8. These are used to define weights for S and KS in the standard mixed-sensitivity \mathcal{H}_2 & \mathcal{H}_∞ control configuration, which help shape the frequency-dependent bounds for this function. In this case, the ‘generalized plant’ expression, P , can be written in state-space form as:

$$\begin{aligned} \dot{x}(t) &= Ax(t) + B_1w(t) + B_2u(t) \\ z(t) &= C_1x(t) + D_{11}w(t) + D_{12}u(t) \\ y(t) &= C_2x(t) + D_{21}w(t) + D_{22}u(t) \end{aligned} \tag{5.8}$$

The P and K state-space systems, defined in matrix form, are expressed as:

$$P := \begin{pmatrix} [A] & [B_1 & B_2] \\ [C_1] & [D_{11} & D_{12}] \\ [C_2] & [D_{21} & D_{22}] \end{pmatrix}, K := \begin{pmatrix} A_f & B_f \\ C_f & D_f \end{pmatrix} \tag{5.9}$$

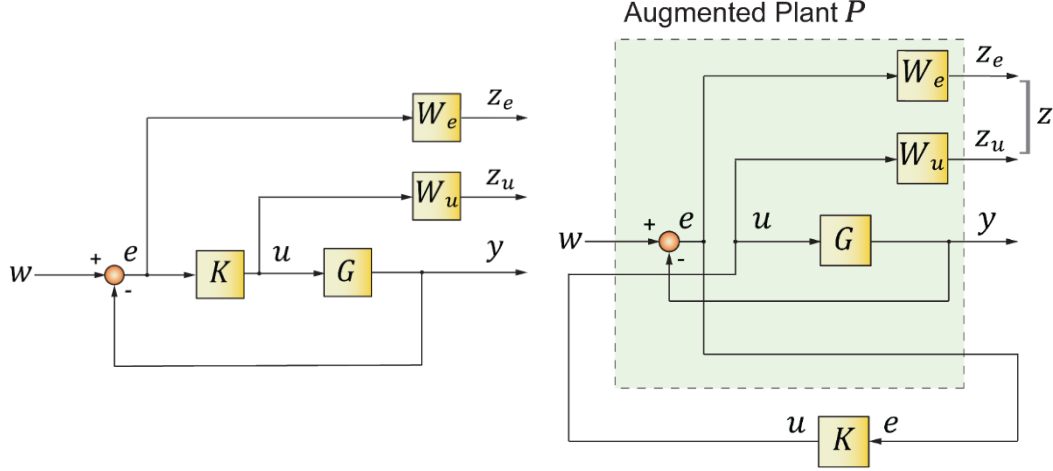


Figure 5.8: Standard mixed-sensitivity \mathcal{H}_2 and \mathcal{H}_∞ control configuration.

The closed-loop system matrix A_{cl} (i.e. a Hurwitz matrix) and closed-loop transfer function matrix T_{cl} (in state-space realization) are given as:

$$A_{cl} := \begin{pmatrix} A + B_2 D_f C_2 & B_2 C_f \\ B_f C_2 & A_f \end{pmatrix} \quad (5.10)$$

$$T_{cl} := \begin{pmatrix} \begin{bmatrix} A + B_2 D_f C_2 & B_2 C_f \\ B_f C_2 & A_f \end{bmatrix} & \begin{bmatrix} B_1 + B_2 D_f D_{12} \\ B_f D_{21} \end{bmatrix} \\ \begin{bmatrix} C_1 + D_{12} D_f C_2 & D_{12} C_f \end{bmatrix} & \begin{bmatrix} D_{11} + D_{12} D_f D_{21} \end{bmatrix} \end{pmatrix} \quad (5.11)$$

The following assumptions need to be satisfied in \mathcal{H}_2 and \mathcal{H}_∞ controller synthesis:

- (A, B_2) is stabilizable and (C_2, A) is detectable.
- D_{12} and D_{21} have full rank.
- $\begin{bmatrix} A - j\omega I & B_2 \\ C_1 & D_{12} \end{bmatrix}$ has full rank for $\forall \omega \in \mathbb{R}$.
- $\begin{bmatrix} A - j\omega I & B_1 \\ C_2 & D_{21} \end{bmatrix}$ has full rank for $\forall \omega \in \mathbb{R}$.
- $D_{11} = 0$ and $D_{22} = 0$.

The last assumption ($D_{11} = 0$ and $D_{22} = 0$) makes P_{11} , and P_{22} , respectively, strictly proper.

The following weighting function [139] is often used to synthesize the mixed-sensitivity controller by suppressing the peak of the sensitivity function $S(s) = (I + K(s)G(s))^{-1}$:

$$\frac{1}{W_e(s)} = \frac{s + \omega_b \varepsilon}{s/M_s + \omega_b} \quad (5.12)$$

The sensitivity peak is typically limited by M_s (e.g. $M_s < 2$ (6 dB)) to ensure sufficient module margin (i.e., distance between the MIMO Nyquist plot, obtained via $\det(I + GK)$ and the origin), which acts as a stability margin measure. The low frequency gain of the inverse of the weighting function W_e^{-1} is determined by ε , showing the amount of improvement targeted via controls. Generally, ω_b influences the closed-loop bandwidth and it is chosen to be high enough to ensure faster disturbance rejection and better command tracking response. Figure 5.9 presents a visualization of how such a weighting function (or its inverse W_e^{-1}) can be used to impose a bound on the sensitivity function $S(\omega)$.

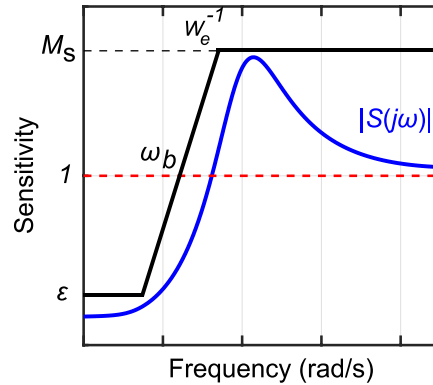


Figure 5.9: Conventional sensitivity shaping function.

In the vibration controller in this thesis, the $\mathcal{H}_2/\mathcal{H}_\infty$ stacked sensitivity optimization algorithms available in MATLAB, which have their origins in the works of Zhou, Glover, and Doyle [139], have been applied.

5.6. Proposed Control Design for Multiple-Mode Vibration Damping and Tracking Control of Feed Drive Systems

In this section, a new high-bandwidth control design is proposed for tracking and active vibration suppression in CNC feed drives. Figure 5.10 shows the overall control scheme. The vibration damping is based on a mixed-sensitivity \mathcal{H}_2 and \mathcal{H}_∞ control synthesis leading to the inner loop feedback controller K_{H_2/H_∞} , which can actively damp multiple modes of vibration. Successful synthesis of K_{H_2/H_∞} is achieved using the feed drive model estimated with the proposed MIMO model identification algorithm in Chapter 4. In order to achieve rapid response to control commands, which enhances disturbance suppression, the linear amplifier detailed in Chapter 3 was used as the source of power for the motor. The tracking controller is based on a loop shaping filter C_f , comprising a lead-lag controller. Lag compensation increases the control gain to further improve the low-frequency disturbance rejection, while the lead filter boosts the phase margin around the target crossover frequency. A filter pack G_{fp} helps to avoid the excitation of

unmodeled or high frequency dynamics. Additionally, a friction model F_f and trajectory pre-filter P_f are used in feedforward, to further improve the tracking accuracy with knowledge of the expected motion commands. The performance of the proposed controller has been validated in high-speed tracking experiments and closed-loop disturbance response measurements. The proposed controller design is also compared against the two benchmark controllers (P-PI and PPC) detailed earlier Sections 5.3 and 5.4.

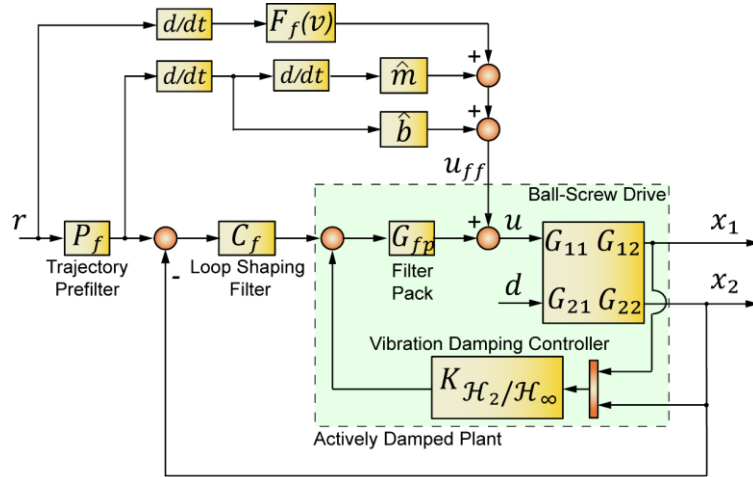


Figure 5.10: Vibration damping and tracking controller design.

5.6.1. Feed Drive Model

Considering the ball-screw drive dual-feedback structure, the setup is modeled as a two-input two-output system. The inputs are motor torque command (control input (u)) and load side disturbance force (d). Rotational and translational position feedback measurements (x_1 and x_2 , respectively) are the outputs of the system. The identified MIMO model can be stated in transfer matrix form as:

$$\begin{bmatrix} x_1(s) \\ x_2(s) \end{bmatrix} = \begin{bmatrix} G_{11}(s) & G_{12}(s) \\ \frac{G_{21}(s)}{G_u(s)} & \frac{G_{22}(s)}{G_d(s)} \end{bmatrix} \begin{bmatrix} u(s) \\ d(s) \end{bmatrix} \quad (5.13)$$

Above, G_{11} , G_{12} and G_{21} , G_{22} are the rotary and linear encoders' responses to motor command and load side disturbance inputs. The identified model (using the method in Chapter 4) is a 12th order strictly proper transfer matrix. The identified model captures the effect of the base frame vibration mode at 26 Hz and the first axial vibration mode at 138 Hz.

An additional mode was also measured at 37 Hz, which is very clear in the encoder response measurement. However, during the experimental modal analysis in Section 3.11, this mode could not be spotted with the mounted accelerometers. Instead, another mode at 48 Hz was captured, demonstrating predominantly yawing-pitching motion. While the experimental modal analysis was conducted using

impact hammer excitation with the axis being stationary, and therefore susceptible to stick-slip friction, the controlled input FRF measurement was performed with the motor by applying higher excitation amplitudes, thus reducing the effect of friction. It is believed that the 37 Hz resonance measured with the motor corresponds to the 48 Hz mode measured with the impact hammer. The perceived increase in the natural frequency with the hammer measurement is attributed to the Dahl resonance effect [43][44], which becomes prevalent under the influence of friction. In any case, the model identification algorithm in Chapter 4 estimated other poles, as listed in Appendix A.3, but not the 37 Hz resonance in fitting a MIMO model to match all input/output channels. Other poles locations seemed to play a more dominant role in coming up with an overall close fit.

Figure 5.11 shows the disturbance response measurement of the load side and the corresponding mode shapes. The anti-resonance frequency ω_{AR} at 60 Hz corresponds to $\omega_{AR} = \sqrt{k_{axial}/m_1}$ in the two-inertia system (Figure 2.1), which is the resonance constituted by the primary side inertia and equivalent axial stiffness. This corresponds to the frequency at which the primary side absorbs the most amount of energy applied to the secondary load side.

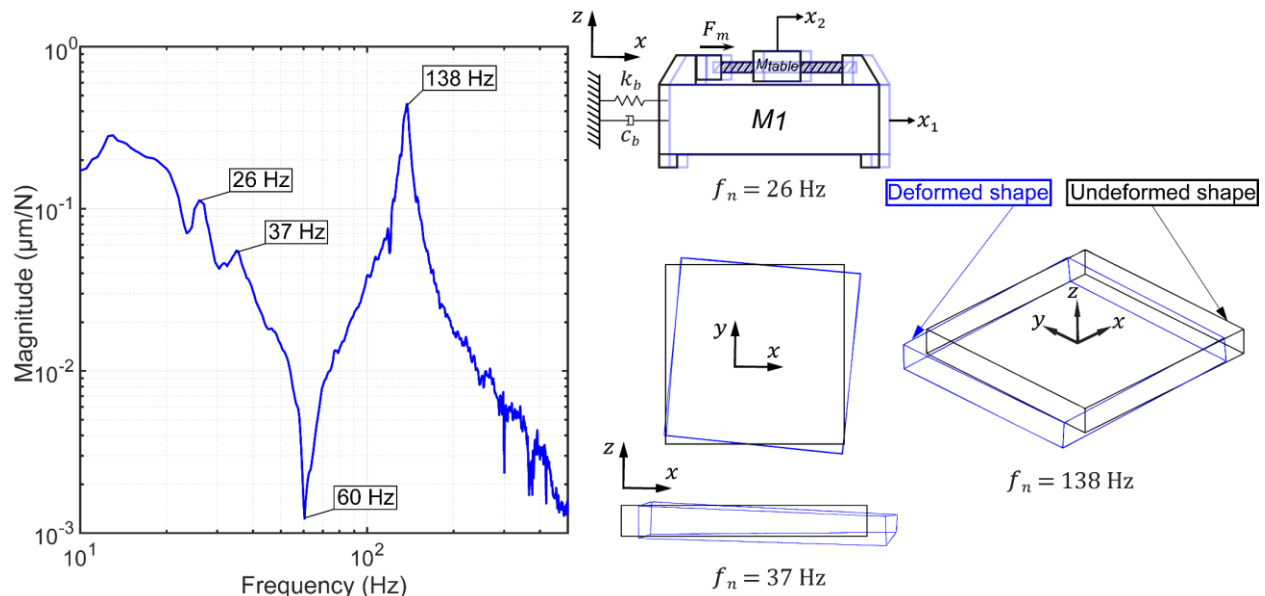


Figure 5.11: Worktable disturbance FRF obtained by impact hammer test, the mode shapes, and their corresponding frequencies.

Considering a generalized MIMO model describing the output/input channel pairs $k_o k_i$, the identified model takes the structure:

$$G_{k_o k_i}(s) = \sum_{k=1}^{n_c} \frac{\beta_k^{k_o k_i} s + \alpha_k^{k_o k_i}}{s^2 + 2\zeta_k \omega_k s + \omega_k^2} + \sum_{k=1}^{n_r} \frac{\gamma_k^{k_o k_i}}{s + p_k} + \delta_0^{k_o k_i} + \delta_1^{k_o k_i} s + \dots + \delta_d^{k_o k_i} s^{d_{k_o k_i}} \quad (5.14)$$

The identified system parameters can be found in Appendix A.3. It is interesting to note that while some poles have very small damping (26.8, 131.1, 134.1 Hz), other poles have more significant damping and therefore do not display very noticeable resonance (e.g., poles at 16.5 and 30.3 Hz). No direct terms ($\delta_0 = 0, \delta_1 = 0, \dots, \delta_d = 0$) were estimated, since only rotary and linear encoder (displacement) measurements were used in the system identification and no direct transmission and/or derivative-like effects were observed.

The state space realization of the feed drive model can be stated in the structure in Eq. (5.7), where $x = [x_1, x_2, \dots, x_{24}]^T$, $u = [u_1, u_2]^T$, $y = [y_1, y_2]^T$ represent the state, input, and output vectors. $u_1 = u$ corresponds to the motor input. $u_2 = d$ is the load side disturbance. y_1, y_2 are the rotary and linear encoder displacement outputs. The system matrices can be written as:

$$A = \begin{bmatrix} A_1 & 0_{12 \times 12} \\ 0_{12 \times 12} & A_2 \end{bmatrix}, A_n = \begin{bmatrix} a_{n1,1} & a_{n1,2} & \dots & a_{n1,11} & a_{n1,12} \\ a_{n2,1} & 0 & \dots & 0 & 0 \\ 0 & a_{n3,2} & \ddots & \vdots & \vdots \\ \vdots & \ddots & \ddots & 0 & 0 \\ 0 & \dots & 0 & a_{n12,11} & 0 \end{bmatrix}, n = 1, 2. \quad (5.15)$$

$$B = \begin{bmatrix} b_{1,1} & 0_{12 \times 1} \\ 0 & b_{2,2} \\ 0 & 0 \\ \vdots & \vdots \\ 0 & 0 \end{bmatrix}, C = \begin{bmatrix} c_{1,1} & c_{1,2} & \dots & c_{1,24} \\ c_{2,1} & c_{2,2} & \dots & c_{2,24} \end{bmatrix}, D = 0_{2 \times 2}$$

The contribution of each complex conjugate pole pair (Eq. (5.14)) of the identified system to the ∞ -norm of the plant model are shown in Figure 5.12. From this figure we can observe the system norm (the largest of the mode norms) [79] to be $\|G\|_\infty \cong 63.73$, based on the available frequency range data. At this point, the possibility of attempting model order reduction (from 12th order to 10th order) was investigated, by truncating the mode at 30.3 Hz.

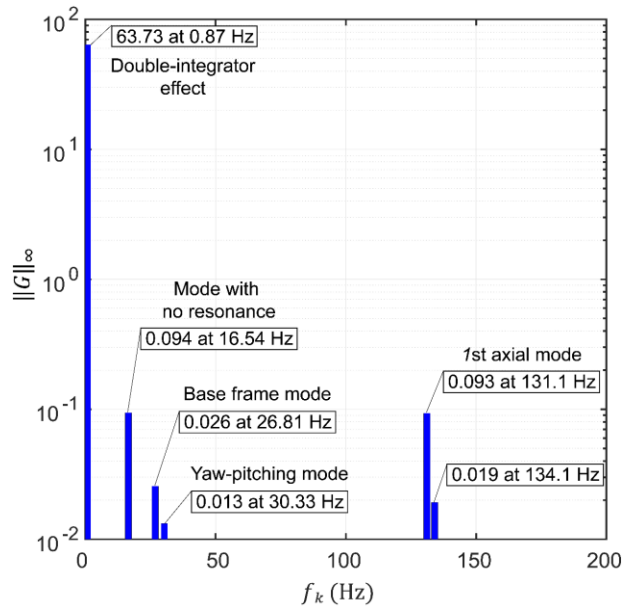


Figure 5.12: $\|G\|_\infty$ of the system modes.

The low frequency complex conjugate poles at 0.87 Hz contribute to mass-like (i.e. double-integrator) influence on the system response. While this formulation is only approximate, the low frequency high feedback gain achieved via loop shaping for the position tracking control loop, overcomes any complication this approximation may cause in the control of the ball screw drive.

Figure 5.13 shows the reduced model fit (10th order) versus the full-order system (12th order). The reduced-order approximation of the feed drive system was obtained by truncating the least important states (i.e. mode with the smallest norm). The `balred` function in MATLAB was used for model order reduction. The minimal state-space realization of the reduced-order model leads to 10 states.

As can be seen, the reduced-order mode shows significant deterioration in fitting results, particularly around the identified natural frequencies (see Figure 5.14). In this figure H represents measurement and G represents the estimated model. For that reason, the full-order model was used for control synthesis analysis.

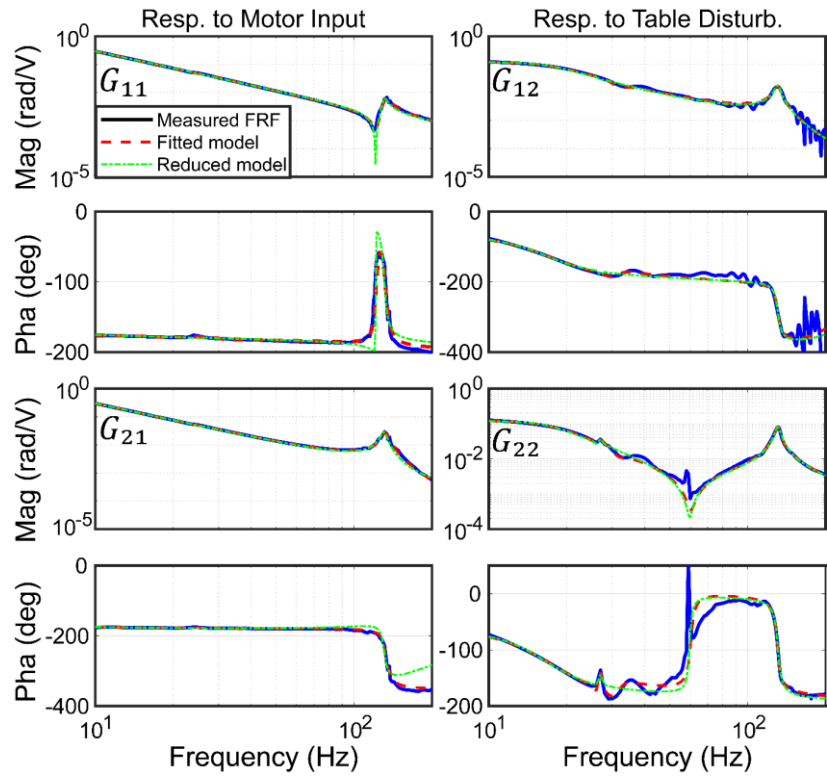


Figure 5.13: Model order reduction through truncation.

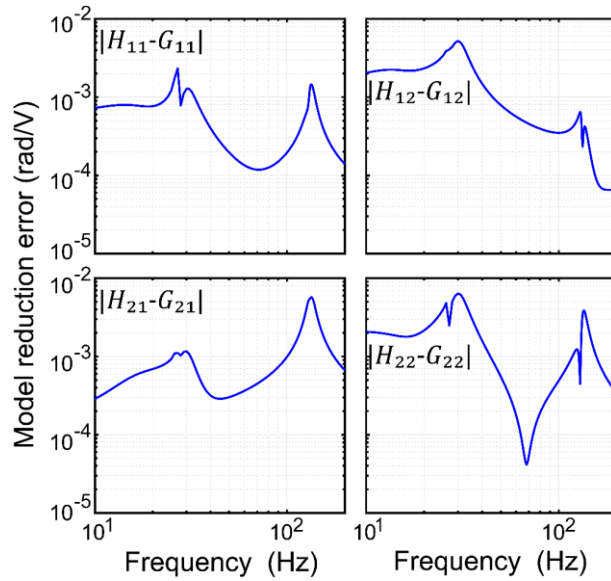


Figure 5.14: Model reduction error for output-input channel terms $|H_{k_o k_i}(\omega) - G_{k_o k_i}(\omega)|$.

5.6.2. Mixed-Sensitivity \mathcal{H}_2 and \mathcal{H}_∞ Control for Multiple-Mode Vibration Suppression

The objective is to find a feedback controller $K = [K_1 \ K_2]$ that minimizes the effect of disturbance force on the load-side d to the position x_2 in the frequency range of $0 \leq \omega \leq \omega_{max}$, both in terms of peak value and the overall shape. The closed-loop disturbance response for the feed drive system can be described by the following:

$$G_{dist}(s) = S_{21}(s)G_{12}(s) + S_{22}(s)G_{22}(s) \ , \quad S = \begin{bmatrix} S_{11}(s) & S_{12}(s) \\ S_{21}(s) & S_{22}(s) \end{bmatrix} = (I + GK)^{-1} \quad (5.16)$$

To facilitate stability analysis using the SISO form of the Nyquist criterion, while the system has two outputs (rotary and linear encoder feedback), it can be simplified into a SISO form ($L = K_1G_1 + K_2G_2$) using block manipulation [72] as shown in Figure 5.15. Hence the stability of any dual-channel feedback controller for the ball-screw drive has been analyzed with this approach in this thesis.

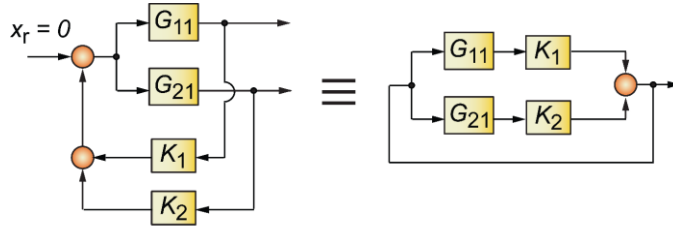


Figure 5.15: Block diagram manipulation for closed-loop analysis [72].

Following the established mixed sensitivity design rules, weighting functions are used to characterize load-side disturbance response, measurement noise, and control input.

Regarding the performance (or servo error) weighting function W_e , differing from classical choice of weighting functions which are typically low-pass, band-pass, or high-pass [25], in this work the load side disturbance response (G_{22}) has been adopted to shape the sensitivity function to achieve $\underbrace{\max}_{\text{for all } \omega} |S(j\omega)| \leq |W_e^{-1}(j\omega)|$. The outcome of this is the direct reduction of the load-side mechanical compliance through feedback control. Eq. (5.17) describes the corresponding weighting function.

$$W_e = \alpha_F \frac{G_{22}}{\|G_{22}\|_{2/\infty}} \quad (5.17)$$

Above, $\alpha_F \in \mathbb{R}$ is used as the improvement factor to minimize the peak value or area below of load side disturbance response G_{22} . The norm term ($\|G_{22}\|_{2/\infty}$) in the denominator decouples the design choice

from the representation units or magnitude of G_{22} , allowing a some-what non-dimensional assignment for the ‘improvement factor’ α_F . Hence, the above weighting function directs the mixed sensitivity optimization to focus primarily on attenuating the mechanical resonances by shaping the closed-loop sensitivity S , rather than trying to achieve a wide-band overall improvement in the sensitivity function.

The control input weighting function W_u can affect the closed-loop bandwidth and can be used to limit the controller gain around the crossover frequency. This weighting function was determined as a constant value through observation from multiple time-domain simulations. Simulations were conducted to maximize vibration suppression on the load side of the feed drive system G_{22} while actuator saturation is avoided for expected command trajectories and disturbance input forces. The measurement noise weighting functions W_{n_1} , W_{n_2} were selected as first-order low-pass filters, since the encoders pick up high-order modes in the high-frequency range, which are not the intention of feedback control.

$$W_{n_1} = W_{n_2} = k_{W_n} \frac{\omega_{W_n}}{s + \omega_{W_n}} \quad (5.18)$$

Overall, the weighting functions required the selection of the terms: α_F , W_u , k_{W_n} , and ω_{W_n} . Most importantly, the open loop load-side direct compliance G_{22} was integrated into the automatic selection of the performance weight W_e , by a simple improvement factor α_F , as mentioned earlier. Considering the system plant as in Eq. (5.13), the augmented plant with the weighting functions is described by the following weighting matrix:

$$\begin{bmatrix} z_e \\ z_u \\ x_1 \\ x_2 \end{bmatrix} = \underbrace{\begin{bmatrix} W_e G_{22} & 0 & 0 & W_e G_{21} \\ 0 & 0 & 0 & W_u \\ G_{12} & W_{n_1} & 0 & G_{11} \\ G_{22} & 0 & W_{n_2} & G_{21} \end{bmatrix}}_{P(s)} \begin{bmatrix} d \\ n_1 \\ n_2 \\ u \end{bmatrix} \quad (5.19)$$

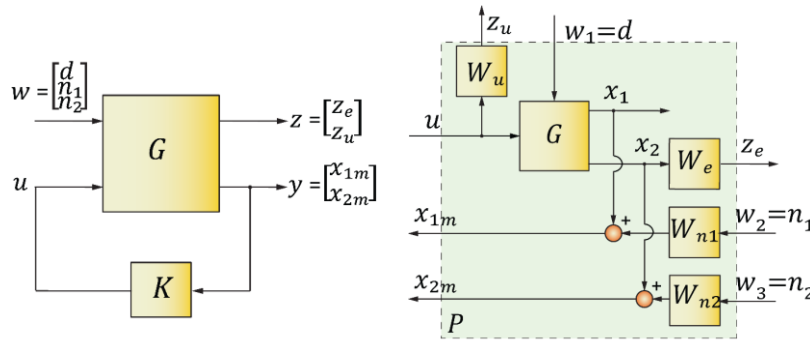


Figure 5.16: Augmented plant with the sensitivity weighting function W_e , control input weighting function W_u , and measurement noise weighting functions W_{n_1} , W_{n_2} .

Figure 5.16 shows the augmented plant with the corresponding weighting functions. By partitioning the interconnected system $P(s)$ the following are set:

$$\begin{aligned} P_{11} &= \begin{bmatrix} W_e G_{22} & 0 & 0 \\ 0 & 0 & 0 \end{bmatrix}, P_{12} = \begin{bmatrix} W_e G_{21} \\ W_u \end{bmatrix} \\ P_{21} &= \begin{bmatrix} G_{12} & W_{n_1} & 0 \\ G_{22} & 0 & W_{n_2} \end{bmatrix}, P_{22} = \begin{bmatrix} G_{11} \\ G_{21} \end{bmatrix} \end{aligned} \quad (5.20)$$

The response of the generalized plant P under the closed-loop influence of the feedback controller K can be found by applying the lower linear fractional transformation:

$$\mathcal{F}_l(P, K) = [P_{11} + P_{12}K(I - P_{22}K)^{-1}P_{21}] \quad (5.21)$$

To compute the stabilizing \mathcal{H}_2 or \mathcal{H}_∞ optimal controllers for the augmented plant P , `h2syn` and `hinfsyn` functions from MATLAB's Robust Control Toolbox were used [140]. Therefore, the optimal feedback control calculation is done offline. For the ball-screw drive this calculation takes only a few seconds on a personal computer. Afterwards, the vibration-damping controller can be implemented as an LTI state-space system. One problematic feature of optimally synthesized $\mathcal{H}_2/\mathcal{H}_\infty$ controllers is their relatively high order, containing the orders of the plant and all weighting functions. Hence, it is common to attempt to reduce the controller order, after an optimal control law has been synthesized. In controller order reduction, the main concern is preserving the stability and performance of the closed-loop system. In order to guarantee the stability of the controller itself, the pole locations of the reduced-order feedback controller K_r were inspected to be on the left-hand side of the s-plane. The balanced truncation method was used for order reduction [141]. Figure 5.17 shows the frequency response of the full-order (\mathcal{H}_2 : 44 and \mathcal{H}_∞ : 50 states) and reduced order (\mathcal{H}_2 : 16 and \mathcal{H}_∞ : 16 states) synthesized vibration damping controllers.

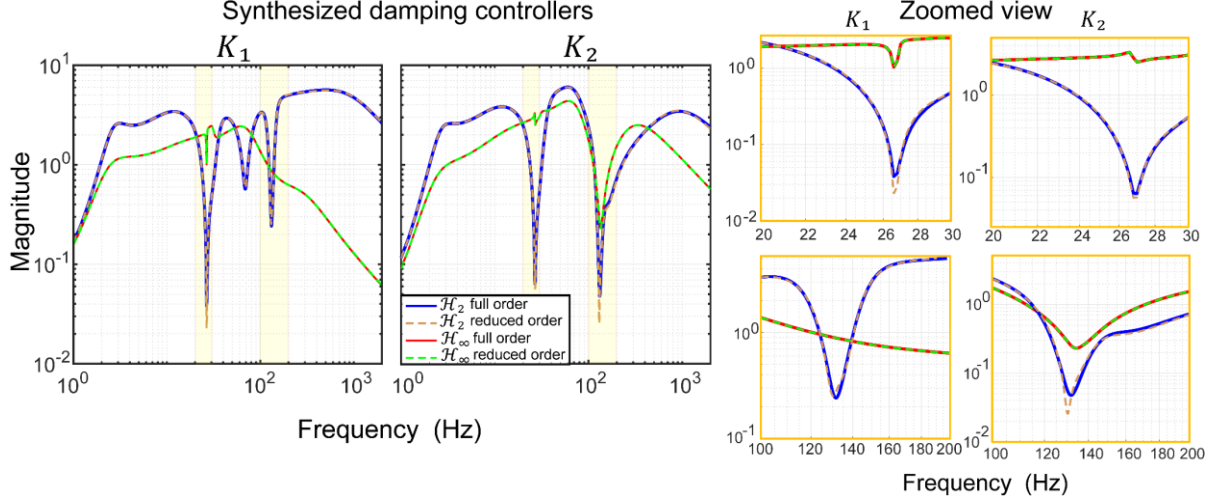


Figure 5.17: Frequency responses of the originally synthesized and reduced-order mixed-sensitivity \mathcal{H}_2 and \mathcal{H}_∞ vibration damping controllers.

As can be seen from the zoomed view of the magnitudes around the natural frequencies in Figure 5.17, there are minor deviations between original and reduced-order controller designs. From observing the synthesized controllers, the attenuation at the first and second natural frequencies are higher in the \mathcal{H}_2 controller than the \mathcal{H}_∞ design. This is due to the fact that an \mathcal{H}_∞ controller minimizes the ∞ -norm (i.e., peak-value) of the disturbance response and an \mathcal{H}_2 controller is designed to minimize the 2-norm (area underneath) of G_{22} .

In order to suppress high-frequency resonances outside the crossover frequency of the feedback controller a filter package was manually added to the damped plant. The notch filters inside the filter package G_{fp} are designed to target the high-frequency resonances at $\omega_{n_1} = 4274$ rad/s (676 Hz), $\zeta_{n_1} = 0.017$, $\zeta_{d_1} = 0.7$, $\omega_{n_2} = 7250$ rad/s (1154 Hz), $\zeta_{n_2} = 0.032$, $\zeta_{d_2} = 0.7$. A low-pass filter is also designed to filter frequencies above 1.2 kHz. The filter pack is stated by.

$$G_{fp}(s) = \prod_{i=1}^2 \left(\frac{s^2 + 2\zeta_{n_i}\omega_{n_i} + \omega_{n_i}^2}{s^2 + 2\zeta_{d_i}\omega_{n_i} + \omega_{n_i}^2} \right) \cdot \frac{\omega_{lpf}}{s + \omega_{lpf}} \quad (5.22)$$

The same filter package was also applied when testing the other two benchmark controllers, P-PI and PPC.

The overall loop transfer function for the mixed-sensitivity \mathcal{H}_2 and \mathcal{H}_∞ controlled plants can be found as $L = G_{fp}(G_{11}K_1 + G_{21}K_2)$. In the above equation K_1 and K_2 are the synthesized damping controllers for the rotational and translational feedback channels. Figure 5.18 shows the frequency responses of the

continuous (s-domain) and discrete time (z-domain) synthesized controllers with the addition of the filter package. The discretization of the controllers was achieved via zero-order hold equivalent method.

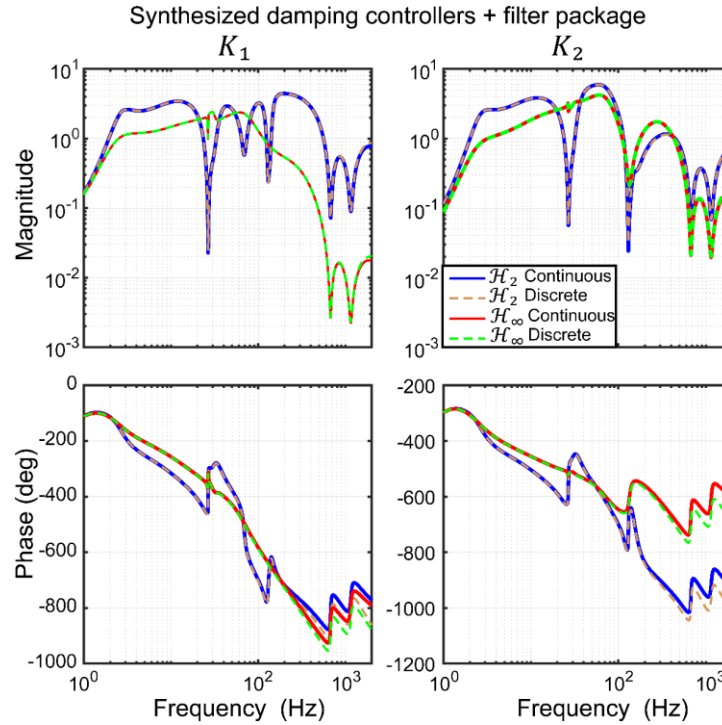


Figure 5.18: Frequency responses of the synthesized mixed-sensitivity \mathcal{H}_2 and \mathcal{H}_∞ damping controllers with the addition of filter package (G_{fp}) in continuous and discrete forms.

5.6.3. Tracking Controller Design

Once the vibration-damping controller is designed, the tracking controller can be constructed based on the actively damped plant. The tracking controller C_f is a simple lead-lag compensator that applies the worktable linear encoder feedback x_2 . The lag compensator increases the control gain and improves error rejection in the low-frequency region, while the lead compensator enhances the phase margin and crossover frequency of the overall system. The lead-lag compensator has the following transfer function.

$$C_f(s) = K_f \left(\frac{T_b s + 1}{T_a s + 1} \right) \cdot \left(\frac{T_d s + 1}{T_f s + 1} \right) \quad (5.23)$$

The frequencies of the zero ($-1/T_b$) and pole ($-1/T_a$) of the lag controller were placed at 10 Hz and 0.05 Hz respectively. In the loop shaping controller design, a phase margin of $PM=35^\circ$ was chosen at the desired crossover frequencies of $\omega_c = 50$ Hz (for the \mathcal{H}_2 damped plant FRF) & $\omega_c = 60$ Hz (\mathcal{H}_∞ damped plant FRF). The required phase lead is found as,

$$\phi_{lead} = -180^\circ + PM - \angle L(j\omega_c) - \phi_{lag} \quad (5.24)$$

Above, $-\angle L(j\omega_c)$ is the phase angle of the damped plant FRF at ω_c . The phase leads were obtained as $\phi_{lead} = 46.21^\circ$ for the \mathcal{H}_2 damped plant FRF and $\phi_{lead} = 44.39^\circ$ for the \mathcal{H}_∞ damped plant FRF. This requires the filters to have a lead ratio of $\gamma = \sqrt{(1 + \sin(\phi_{lead})) / (1 - \sin(\phi_{lead}))} = 2.48$, and 2.38, respectively. The compensator parameters are summarized in Table 5.1.

Table 5.1: Lead-lag compensator parameters.

Parameter	\mathcal{H}_2 controlled plant FRF	\mathcal{H}_∞ controlled plant FRF
$1/T_b$ (rad/s)	$2\pi \times 10$	$2\pi \times 10$
$1/T_a$ (rad/s)	$2\pi \times 0.05$	$2\pi \times 0.05$
$1/T_d$ (rad/s)	$2\pi \times 20.15$	$2\pi \times 25.263$
$1/T_f$ (rad/s)	$2\pi \times 124.42$	$2\pi \times 142.7$
K_f	4028	4658

With the addition of the lead/lag filter, the overall loop transfer function becomes: $L' = K_1 G_1 + K_2' G_2$. Here, the modified translational feedback channel can be expressed as: $K_2' = K_2 + C_f$. The Nyquist plot and sensitivity function $S = 1/(1 + L')$ are used to examine the crossover frequency, phase margins, and peak sensitivity value [25].

In addition to the feedback based tracking controller, feedforward friction and dynamics compensation were added to further improve the tracking performance. In the tracking experiments, the identified Stribeck parameters from Chapter 3 were used in the friction model. To improve the tracking accuracy, inversion of the open-loop rigid body dynamics was achieved, by injecting the velocity and acceleration commands by weighting them with the estimated model inertia and translational damping. A trajectory-prefiltering term was also added to counteract the artefacts in the tracking error which are correlated to the velocity, acceleration, jerk, and snap of the commanded trajectory [130]. The trajectory pre-filter flattens the overall tracking transfer function and bring its phase lag closer to zero. It has the form:

$$P(s) = 1 + K_{vel} G_{lpf} s + K_{acc} G_{lpf}^2 s^2 + K_{jerk} G_{lpf}^3 s^3 + K_{snap} G_{lpf}^4 s^4 \quad (5.25)$$

The coefficients K_{vel} , K_{acc} , K_{jerk} , and K_{snap} are computed using least-squares fitting of the observed error as a function of the low-pass filtered commanded velocity, acceleration, jerk, and snap (4th time derivative of position). The low-pass filter G_{lpf} was chosen to be as 1st order at 80 Hz, to avoid amplifying

numerical round-off errors during discrete differentiation. Hence, the overall control system, which includes the vibration-damping control loop and a tracking controller, is designed according to the structure shown in Figure 5.10.

5.7. Proposed versus Conventional Design for the Sensitivity Weighting Function

In this section, two different approaches for the selection of sensitivity weighting functions are compared in terms of disturbance rejection capabilities. In the first design, the proposed sensitivity shaping function in Eq. (5.17) was used for the damping control synthesis. In the second design, the sensitivity weighting function follows one of my most widely used conventional choices in performing \mathcal{H}_2 or \mathcal{H}_∞ stacked sensitivity optimization: $W_e^{-1}(s) = K_e^{-1} \frac{s+\omega_b\varepsilon}{s/M_s+\omega_b}$. The proposed \mathcal{H}_2 and \mathcal{H}_∞ designs require the selection of four parameters in comparison to seven variables that need to be adjusted in the conventional method. The comparison of the design parameters can be found in Table 5.2 and Table 5.3. In setting the conventional parameters, care was taken to achieve as favorable vibration damping, disturbance rejection, and noise immunity characteristics as possible, by running extensive simulations and carrying out complementary frequency domain analyses, just as done for the proposed method.

Table 5.2: Proposed controller design parameters.

Parameter	\mathcal{H}_2	\mathcal{H}_∞
α_F	0.05	0.005
W_u	0.005	0.002
ω_{W_n} (rad/s)	$2\pi \times 200$	$2\pi \times 200$
k_{W_n}	0.1	0.1

Table 5.3: Conventional controller design parameters.

Parameter	\mathcal{H}_2	\mathcal{H}_∞
ω_b (rad/s)	$2\pi \times 150$	$2\pi \times 150$
ε	1e-3	1e-3
M_s	2	2
K_e	1e-4	1e-5
W_u	0.005	0.001
ω_{W_n} (rad/s)	$2\pi \times 200$	$2\pi \times 200$
k_{W_n}	0.1	0.1

The proposed \mathcal{H}_2 and \mathcal{H}_∞ vibration damping controller designs were compared to those obtained via the conventional method of setting the sensitivity weight. The comparisons were conducted via frequency domain analyses as well as impact hammer testing on the load side of the setup. Figure 5.19 shows the magnitude plots for the proposed versus the conventional sensitivity shaping functions applied in mixed-sensitivity \mathcal{H}_2 and \mathcal{H}_∞ designs. Compared to the conventional practice, the proposed approach directly considers the open-loop load side compliance in shaping the sensitivity function.

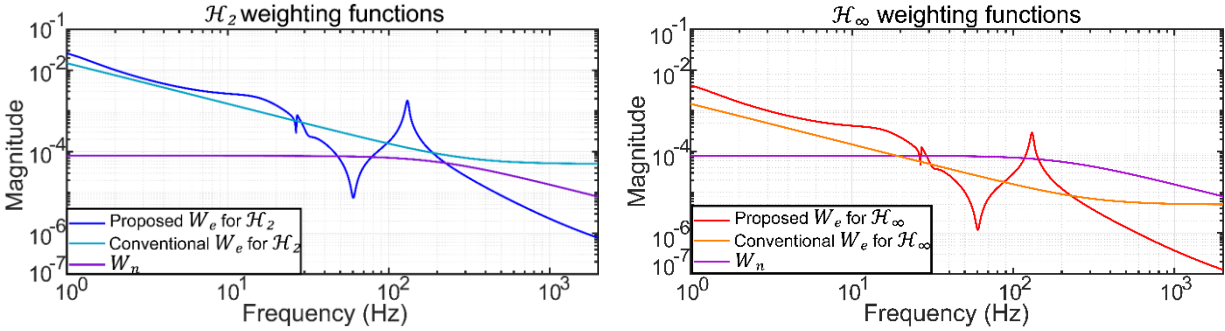


Figure 5.19: Magnitude plots of the proposed and conventional sensitivity shaping function for mixed-sensitivity \mathcal{H}_2 (left) and \mathcal{H}_∞ (right) damping controllers.

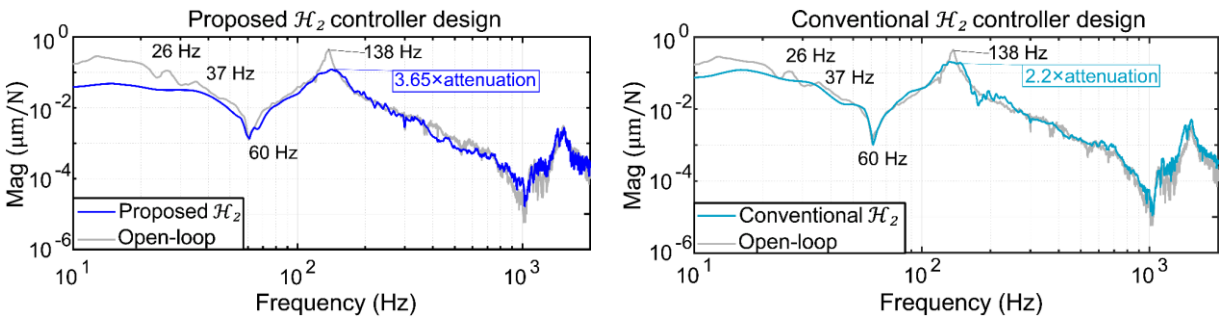


Figure 5.20: Open loop and closed loop load-side disturbance response measurements for the proposed \mathcal{H}_2 (left) and conventional \mathcal{H}_2 (right) mixed-sensitivity vibration damping controllers, measured via impact hammer tests.

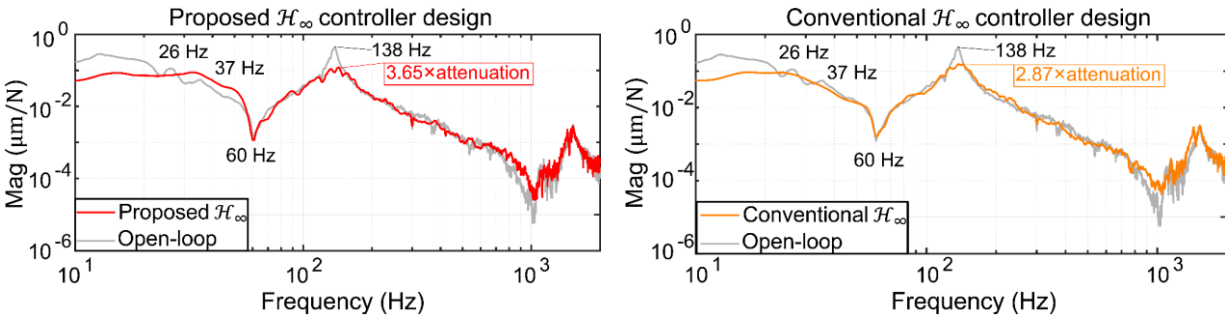


Figure 5.21: Open loop and closed loop load-side disturbance response measurements for the proposed \mathcal{H}_∞ (left) and conventional \mathcal{H}_∞ (right) mixed-sensitivity vibration damping controllers, measured via impact hammer tests.

In the impulse excitation experiments, as the focus is at first on the influence of the weighting function on vibration damping, the additional position tracking loop was not activated. The results, in terms of load side compliance, are shown in Figure 5.20 and Figure 5.21. The table displacements were measured directly using the linear encoder on the load side. In Figure 5.20, which compares the \mathcal{H}_2 designs, it is seen that

compared to the open-loop case (shown with grey), the proposed (i.e., more targeted) approach to setting the sensitivity weighting improves the disturbance over the conventional approach. Indeed, the attenuation of the axial vibration mode at 138 Hz improves from 2.2× to 3.65×. Furthermore, the low frequency part of the compliance is also better suppressed, especially up to and around the resonances at 26 and 37 Hz.

The results for \mathcal{H}_∞ control based damping design are shown Figure 5.21. While similar attenuation of 3.65× is achieved for the axial mode, in the lower frequency part, the conventional weighting seems to yield more favorable suppression this time. However, the latter does not perform as well in attenuating the axial vibration mode, achieving 2.87× improvement. Hence, these results in overall demonstrate that with the proposed approach to setting the sensitivity weighting, even more effective disturbance rejection can be achieved in comparison to the more widely used ‘conventional’ filter-type choice. Thus, the proposed sensitivity weighting method has adopted and used henceforth.

5.8. Experimental Evaluation of the Developed Control Laws

The developed control law, in \mathcal{H}_2 and \mathcal{H}_∞ versions for vibration damping, has been implemented on the ball screw drive and compared in frequency domain analyses, disturbance response tests, and trajectory tracking tests, to the benchmark PPI and PPC designs from Sections 5.3 and 5.4. In the evaluations, both the modeled and measured frequency response functions were considered. To gauge the robustness of the different control laws against frequency response changes due to the feed drive’s axial position (which relates to machine posture), the FRFs were taken at three different points along the travel length, as depicted schematically in Figure 5.22. In the figure, Point B corresponds to the midpoint of travel. Points A and C correspond to -150 and +150 displacements from Point B.

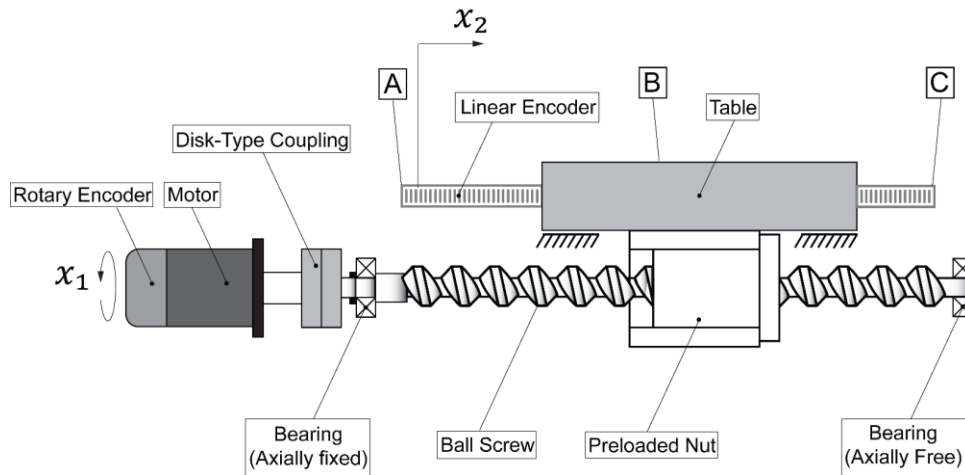


Figure 5.22: Schematic of the feed drive system.

In the measurements, the high-bandwidth linear amplifier in Section 3.6 was used as the source of power. The open-loop frequency response measurements, in response to the motor torque command input, were obtained using the rotary and linear encoders at a sampling rate of 15 kHz. To acquire high quality data, the first set of measurements were conducted using sine-sweep excitation between 10-200 Hz, the results of which are shown in Figure 5.23. As can be observed, depending on the axial location of the table, the frequency and damping ratio of the first axial vibration mode varies between 131 Hz and 140 Hz, and 0.012 to 0.02, respectively. Lower natural frequency and higher damping ratio are obtained when the table is at its furthest location. It is also interesting to note that, especially clearly for points A and B, the main resonance is actually a double mode, as confirmed with the 5th and 6th modes, both describing the axial mode and being very close to each other in frequency (131.1 Hz and 134.1 Hz).

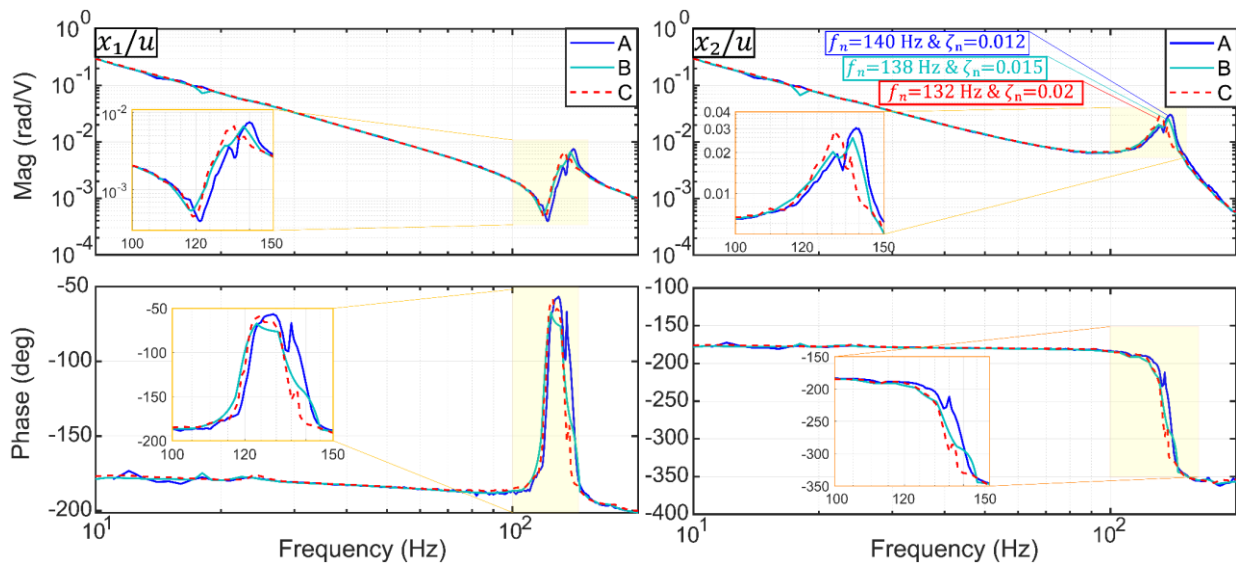


Figure 5.23: Axial vibration mode FRFs at different table locations. Rotary (left) and linear encoder (right) frequency response measurements at motor end (A), middle point (B) and free end (C).

In order to observe the dynamic response over a wider frequency range, rotational and translational position measurements were also conducted by applying chirp-type excitation between 10 Hz and 2 kHz. Figure 5.24 shows the measurement results. It can be seen that while the rotational displacement response is not heavily affected by the table position, after around 300 Hz, greater variation is seen in the table displacement response.

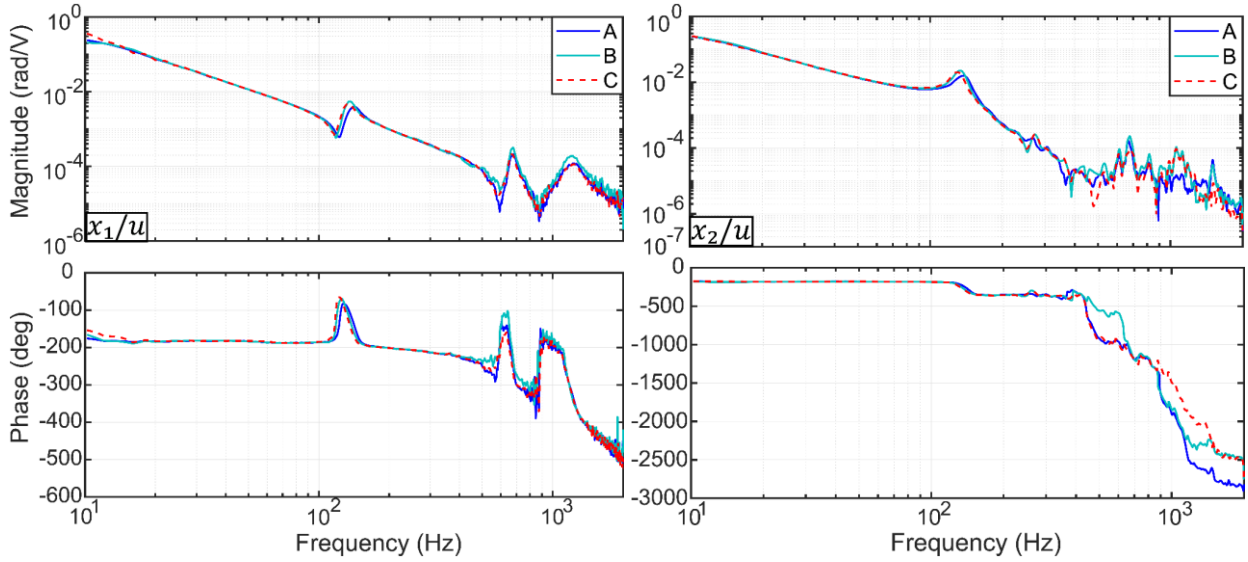


Figure 5.24: Rotary (left) and linear encoder (right) frequency response measurements at motor end (A), middle point (B) and free end (C).

In the following subsections, the following feedback control laws are compared:

- i. \mathcal{H}_2 + LS: \mathcal{H}_2 based vibration damping (with proposed sensitivity weighting) + loop shaping based tracking control
- i) \mathcal{H}_∞ + LS: \mathcal{H}_∞ based vibration damping (with proposed sensitivity weighting) + loop shaping based tracking control
- ii) P-PI: P-PI position-velocity cascade control (Benchmark #1 from Section 5.3)
- iii) PPC: Pole-placement based vibration damping control (Benchmark #2 from Section 5.4)

5.8.1. Frequency-Domain Loop Gain, Stability, and Sensitivity Comparison

In this section, the loop gain crossover frequencies, stability margins, and minimum distances to the ‘-1’ point are inspected from Bode and Nyquist plots of the loop transfer functions for each design.

To allow a fair comparison between the proposed (mixed-sensitivity \mathcal{H}_2 and \mathcal{H}_∞ + loop shaping) and benchmarked designs (P-PI and PPC), the controllers were tuned to possess minimum phase and gain margins of $PM \geq 30^\circ$, $GM \geq 2$, and a maximum sensitivity value of $S \leq S_{max} = 2.25$.

The following figures are based on loop transfer function FRFs which have been calculated using both experimental frequency responses from the setup (designated with ‘exp.’ in the plot legends), and via

frequency response prediction from the plant model used in the controller design (designated with ‘modeled’ or ‘predicted’). The plant model used in \mathcal{H}_2 +LS and \mathcal{H}_∞ +LS controllers is based on the system identification result in Section 5.6.1 for the 10-200 Hz frequency range. In the case of P-PI and PPC controllers, the ball screw dynamics was approximated with a two-inertia model.

The loop transfer function was calculated, as indicated in Section 5.6.3, as $L' = K_1 G_1 + K_2' G_2$, with the feedback path K_2' containing both the vibration damping and tracking loops ($K_2' = K_2 + C_f$).

The loop magnitude plots are shown in Figure 5.25. As can be seen, the proposed controllers have active low frequency ranges up to 36 Hz and also achieve $|L| > 1$ around the axial resonance, up to 139 Hz, indicating expected performance improvement via vibration damping. While the P-PI controller has slightly wider low frequency active range (up to 40 Hz), it does not achieve a second cross-over near the resonance, implying a lesser degree of active vibration damping. The PPC, on the other hand, demonstrates the widest low frequency cross-over (59 Hz), while also having an effective loop gain of $|L| > 1$ around the axial resonance, with a second cross-over at 138 Hz.

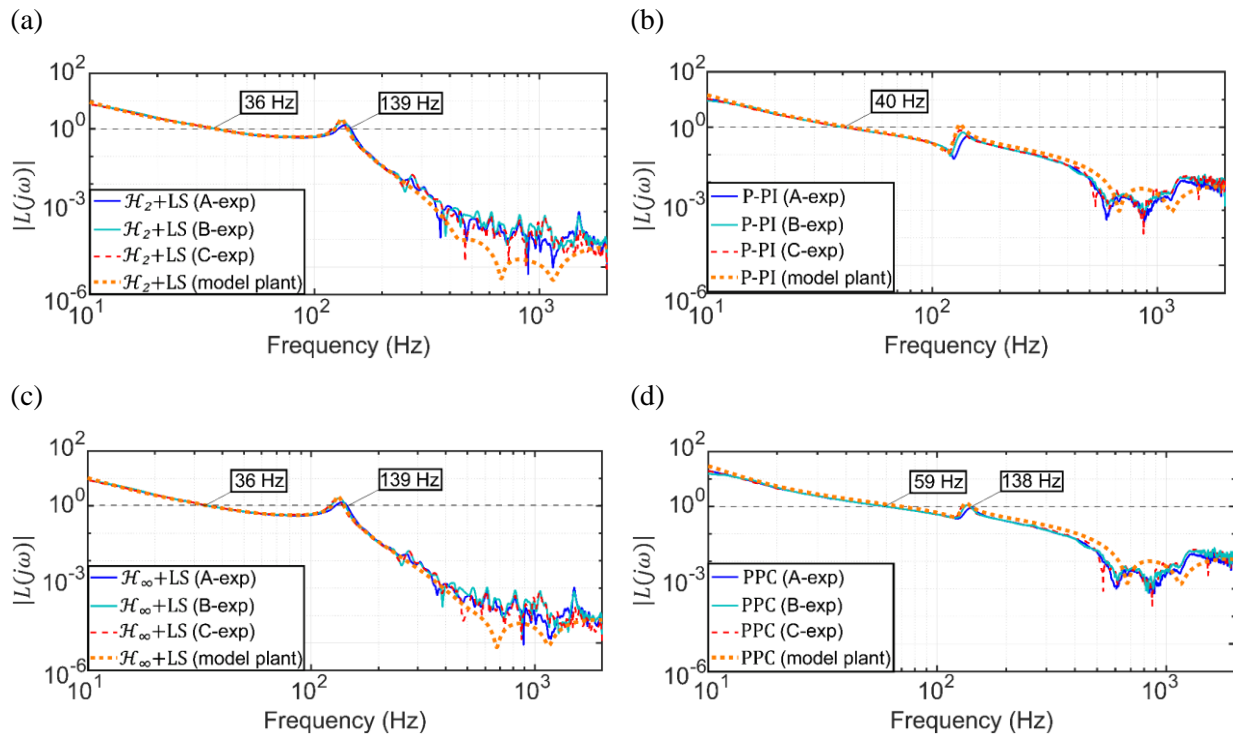


Figure 5.25: Loop transfer function magnitudes for: (a) proposed \mathcal{H}_2 +LS, (b) P-PI Cascade Structure, (c) proposed \mathcal{H}_∞ +LS, and (d) the vibration-damping PPC.

Figure 5.26 shows the Nyquist diagram for the loop transfer function considering the four different controller designs. The plots present frequency response characteristics considering both the applicable

model(s) and experimentally measured FRFs for the plant. As can be verified, all designs have larger than 30° phase margin (PM). In constructing the Nyquist plots and conducting the stability analyses, the locus of $L(\omega)$ was carefully checked to ensure there would be no clockwise encirclements of the ‘-1’ point, in order to guarantee the stability of the closed loop system.

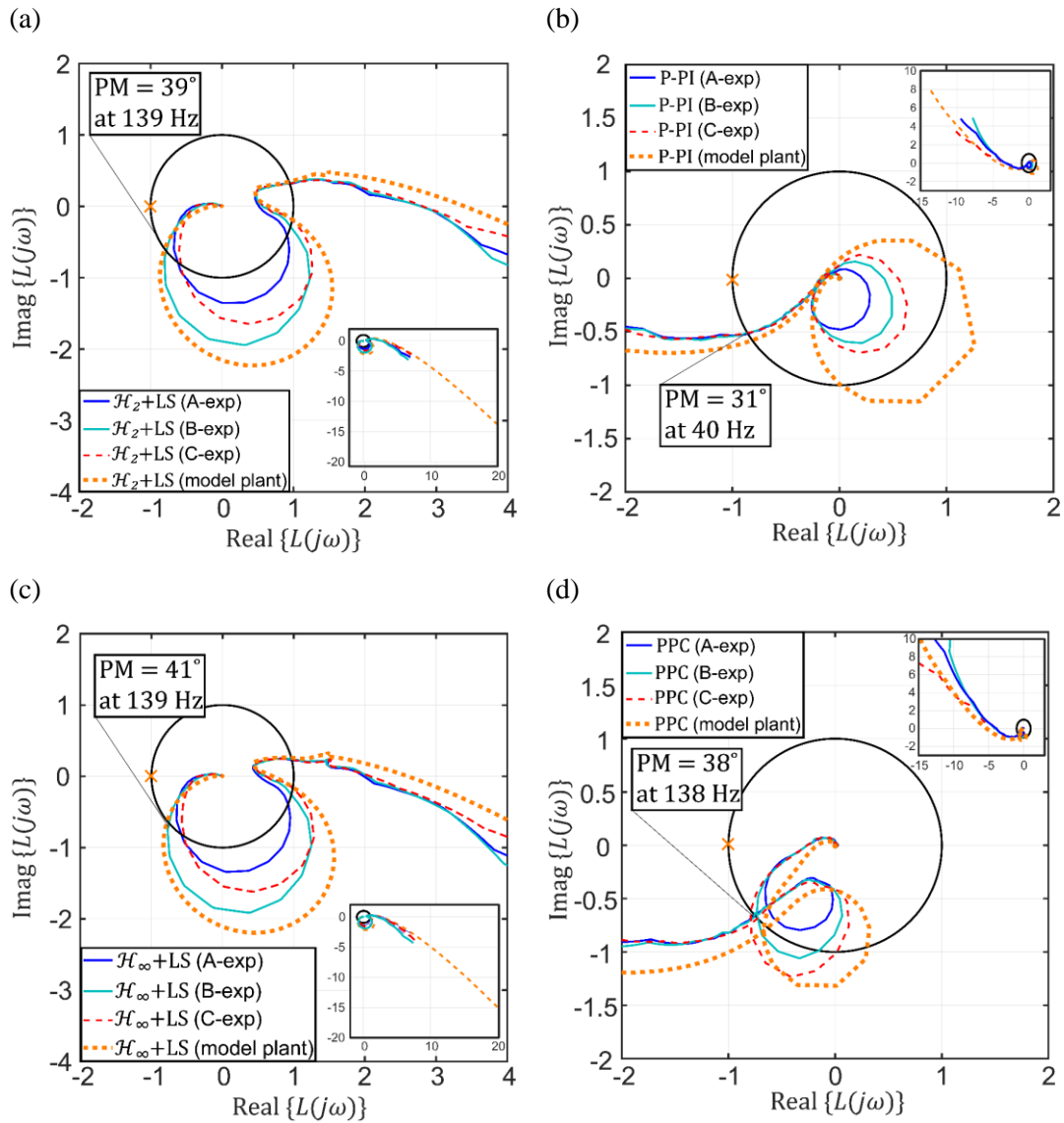


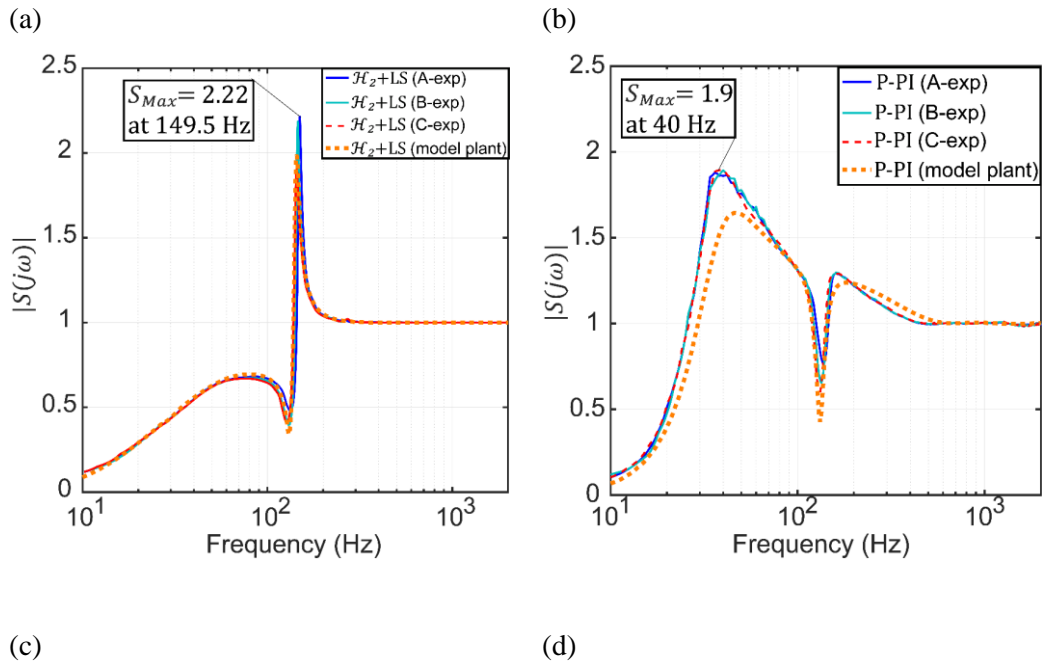
Figure 5.26: Nyquist plots for: (a) proposed \mathcal{H}_2 +LS control, (b) P-PI cascade structure, (c) proposed \mathcal{H}_∞ +LS, (d) vibration-damping PPC.

The sensitivity function can be used to inspect the stability robustness, as its reciprocal is an indication of how closely the Nyquist plot passes to the ‘-1’ point, or in the multivariable case, how closely $\det(I + G(\omega)K(\omega))$ passes to the origin [25]. Considering the reduction of the dual feedback loop structure into a

single loop (Figure 5.15), in this evaluation the sensitivity function has been computed as a SISO equivalent as $S = 1/(1 + L)$.

The magnitude of the computed sensitivity function for the four designs is shown in Figure 5.27. As can be seen, the peak value is limited to 2.22. For P-PI, the critical mode is near 37-40 Hz, implying that the yawing-pitching motion of the table can be easily excited. For the other designs, the peak sensitivity is associated with the axial vibration mode near 140 Hz.

All designs achieve small sensitivity ($|S| < 1$) at low frequencies and show damping improvement around the axial resonance near 136 Hz. The proposed \mathcal{H}_2 +LS and \mathcal{H}_∞ +LS designs seem to achieve even greater suppression of the sensitivity function (i.e., potentially better disturbance rejection) up to the resonance frequency. However, the true sensitivity function is actually a frequency-dependent multivariable matrix: $S(\omega) = (I + G(\omega)K(\omega))^{-1}$, with lower and upper singular values which represent the best-case and worst-case disturbance transmission possibilities, depending on the nature of the open-loop disturbance response transfer function. Thus, the true disturbance rejection achieved with the four controllers is best evaluated through direct physical measurements, as carried out in the next subsection.



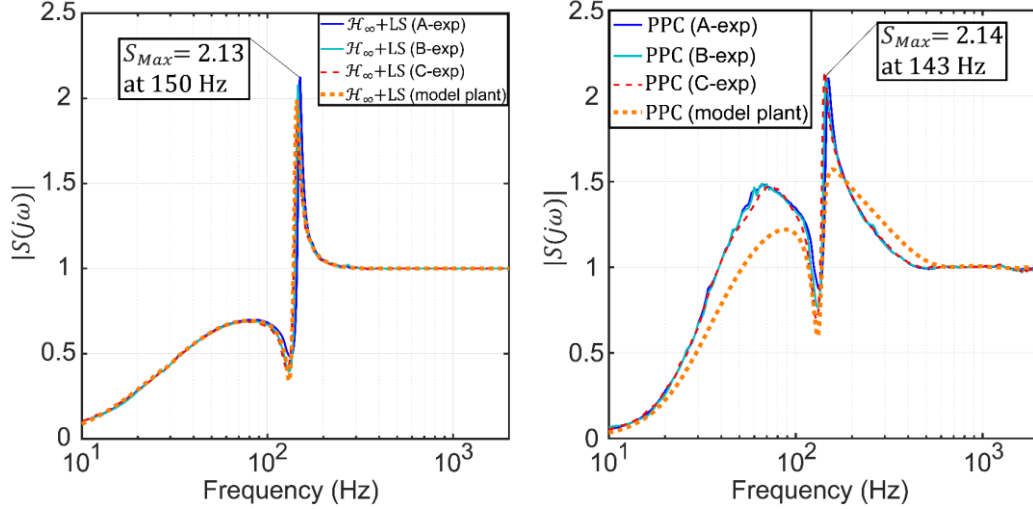


Figure 5.27: Equivalent SISO analysis based sensitivity function gain plots for: (a) proposed \mathcal{H}_2 +LS (a), (b) P-PI cascade structure, (c) proposed \mathcal{H}_∞ +LS, (d) vibration-damping PPC.

5.8.2. Load Side Mechanical Disturbance Rejection

The mechanical disturbance rejection capability achieved with the four controllers has been measured by impact hammer testing on the worktable of the experimental setup. The feed drive's table displacement was measured using the linear encoder. Differing from the intermediate results presented in Section 5.7, which considered mainly the vibration damping capability for different sensitivity weighting functions, for the tests presented here, the position tracking loop (i.e. loop shaping lead/lag filter) was also activated. The measurement results are presented in Figure 5.28 for the individual controllers, and in overlaid combinations in Figure 5.28, which compare the experimental dynamic compliance achieved with the proposed two control designs to their benchmark counterparts.

Considering Figure 5.28, the predicted dynamic compliance FRFs shown with dashed lines are based on the feed drive models used in the controller design (i.e., 12th order model for \mathcal{H}_2 +LS & \mathcal{H}_∞ +LS, versus 4th order lumped mass model for P-PI and PPC). Thus, in describing the open-loop dynamics and in predicting the different control methods' outcomes, better consistency is observed with the proposed modeling and design method, over the benchmarks #1 and #2. This is especially true in the frequency range of 30...140 Hz. In general, the prediction accuracy in the lower frequency range however seems to suffer for all cases, due to the existence of nonlinear friction in the setup.

Comparing the proposed \mathcal{H}_2 +LS with the cascade P-PI controller in both figures, it is seen that around $2.5\times$ better damping of the axial mode is achieved, which can have a dramatic impact on mitigating the permeation of cutting force disturbances to the servo positioning accuracy around this frequency [71]. \mathcal{H}_∞ +

LS also shows better disturbance rejection at low-frequency range and at the vicinity of the axial mode ($\sim 3.85\times$ vs. $\sim 2.3\times$ for P-PI, $\sim 1.86\times$ for PPC).

In the vicinity of the mechanical anti-resonance around 60 Hz, P-PI and PPC designs worsen the disturbance response with the application of closed-loop control. \mathcal{H}_2 + LS, however, is able to take advantage of the ‘natural’ disturbance suppression originating from the damping properties of the mechanical structure (i.e., the motor and rotational inertia of the drive mechanism absorbing the energy for force input from the load side). There is some worsening around the anti-resonance for the \mathcal{H}_∞ + LS controller. This is because \mathcal{H}_∞ design focuses on attenuating the ∞ -norm (i.e., ‘peak value’), whereas \mathcal{H}_2 tries to flatten out the overall compliance response (i.e., ‘area underneath’) by minimizing the 2-norm.

Due to the waterbed effect, deteriorations can be expected at other frequencies outside the target design range. In P-PI and PPC, there is worsening of the dynamic compliance beyond the axial mode at 136 Hz. This is especially visible for PPC at 225 Hz, which seems to correlate to the excitation of the yaw mode of the table, earlier identified at 255 Hz (Section 3.11). Dynamic compliance deterioration can also be seen in P-PI and PPC after 1 kHz. In the proposed designs, however, the deterioration seems to take place near the anti-resonance at 1 kHz, which is already a lower response amplitude region. Thus, its detrimental impact on the disturbance rejection of the feed drive system is diminished.

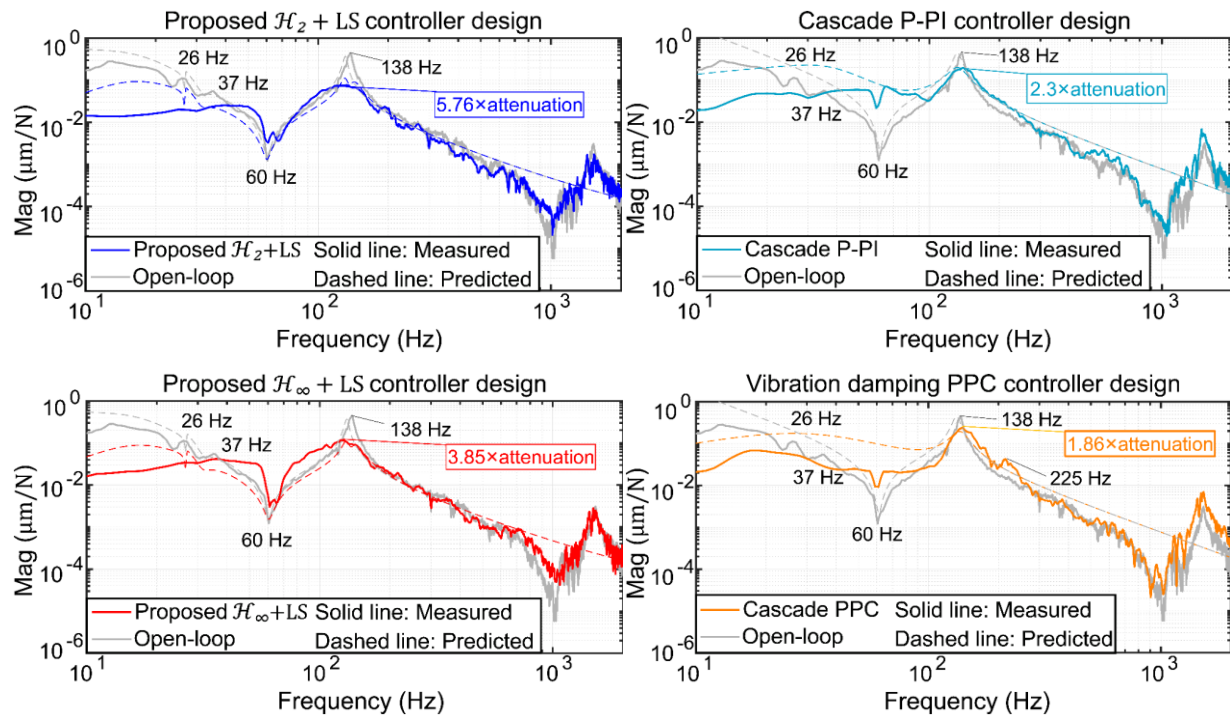


Figure 5.28: Open-loop and closed-loop load-side disturbance response predictions and impact hammer based measurements for: (top-left) proposed \mathcal{H}_2 + LS control, (top-right) P-PI cascade control, (bottom-left) proposed \mathcal{H}_∞ + LS control, and (bottom-right) vibration damping PPC (right).

The overlays in Figure 5.29 show the disturbance rejection improvements accomplished over the two benchmarks for wide frequency ranges by the proposed $\mathcal{H}_2 + LS$ and $\mathcal{H}_\infty + LS$ controller designs. In comparison to P-PI, which is the industrial state-of-the-art, both proposed designs achieve enhanced disturbance rejection nearly for the complete frequency range. In fact, $\mathcal{H}_2 + LS$ achieves 2-3 \times improvement up to 100 Hz, with a small exception near 90...110 Hz. In addition to 2.5 \times better damping of the axial mode at 136 Hz, comparable or even better high-frequency attenuation is also achieved. Compared to PPC, better or at least equivalent disturbance rejection is obtained up to 70...80 Hz, and at some frequencies achieving an improvement almost by 3 \times . However, the improvement is not as consistent across all frequencies as the previous case. The axial resonance damping is enhanced by 3.1 \times , and again similar or more favorable high-frequency characteristics are achieved beyond the axial vibration mode. $\mathcal{H}_\infty + LS$ displays similar trends, but the $\mathcal{H}_2 + LS$ design seems to achieve a better overall performance across the frequency spectrum.

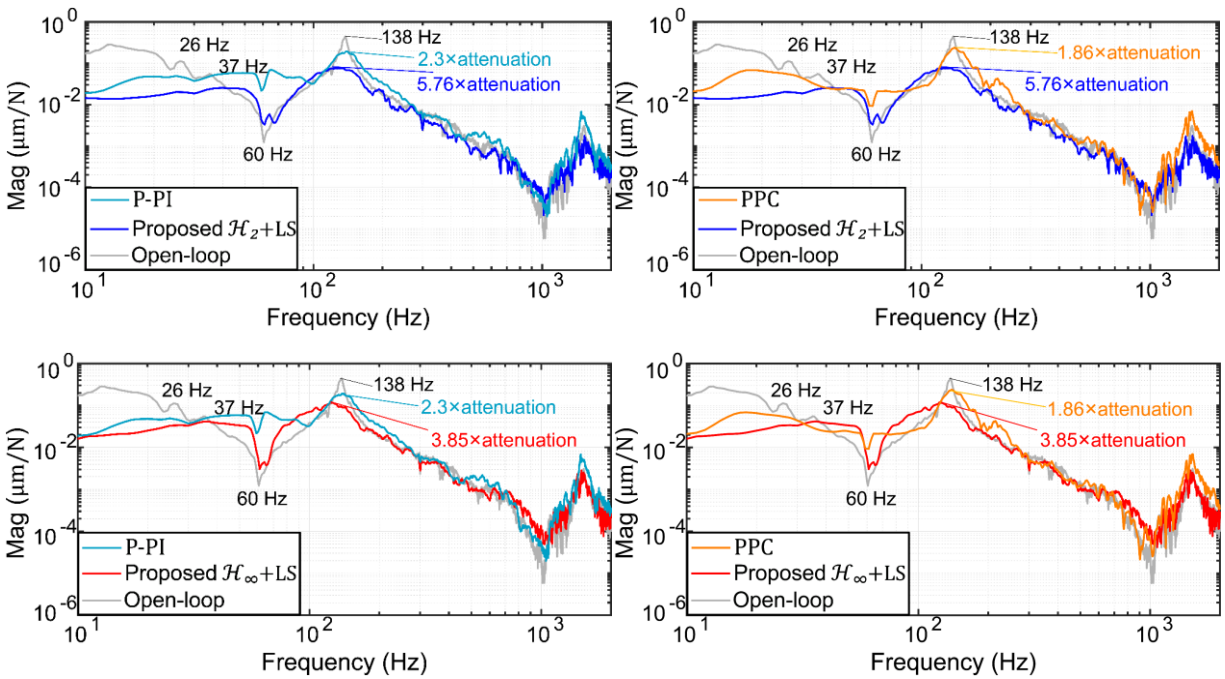


Figure 5.29: Comparison of experimental dynamic compliance characteristics achieved with the proposed controllers versus the other two benchmarks: (top row) $\mathcal{H}_2 + LS$ versus P-PI and PPC, (bottom row)

$\mathcal{H}_\infty + LS$ versus P-PI and PPC.

These experimental results demonstrate and validate one of the most important contributions developed in this thesis, namely superior mechanical disturbance rejection obtained by the proposed high-fidelity model identification and position controller design with multiple vibration mode damping capability.

5.8.3. Tracking Performance Evaluation

In order to evaluate the tracking performance of the proposed controllers, trajectory-tracking experiments were conducted at 420 mm/s velocity, and 1200 mm/s² acceleration. Figure 5.30 shows the jerk-limited commanded trajectory used in the tests. Feedforward velocity and acceleration terms were enabled in the proposed controller designs to further improve the tracking accuracy. In addition to these terms, a trajectory prefilter [130] was tuned experimentally to remove any correlations in the tracking error profile to the reference velocity, acceleration, or jerk. Figure 5.31 and Figure 5.32 illustrate the tracking improvement obtained with the inclusion of the feedforward terms. According to the experimental results, the feedforward terms enable the reduction of the RMS and MAX error values from 3.2 μm & 11.3 μm to 2.4 μm & 8.5 μm for the proposed $\mathcal{H}_2 + LS$ controller. Similarly, for the proposed $\mathcal{H}_\infty + LS$, the RMS and MAX values are reduced from 2.6 μm & 9.6 μm to 2 μm & 6.7 μm , respectively. As mentioned earlier, the harmonic error and control signal components at 20 and 40 Hz are attributed to the ball-screw mechanism and sensor alignment imperfections, which can separately be compensated using the Adaptive Feedforward Control (AFC) method presented in Chapter 6 was kept outside the scope of the feedback controller design developed in this chapter.

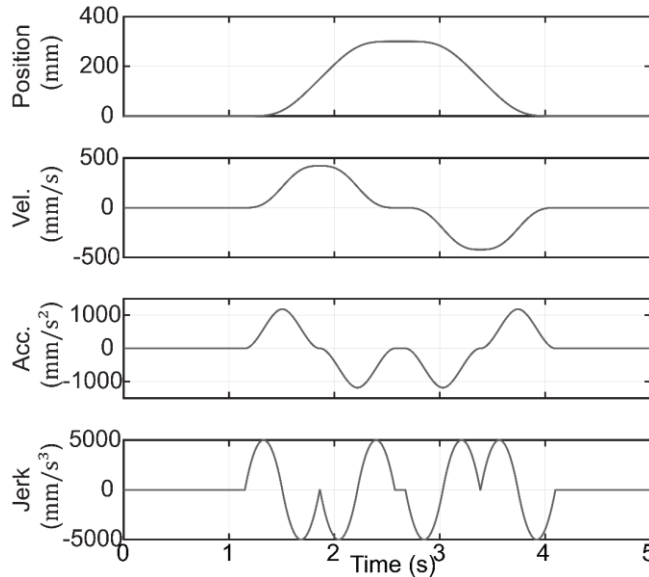


Figure 5.30: Reference trajectory used in the tracking experiments (displacement 300 mm).

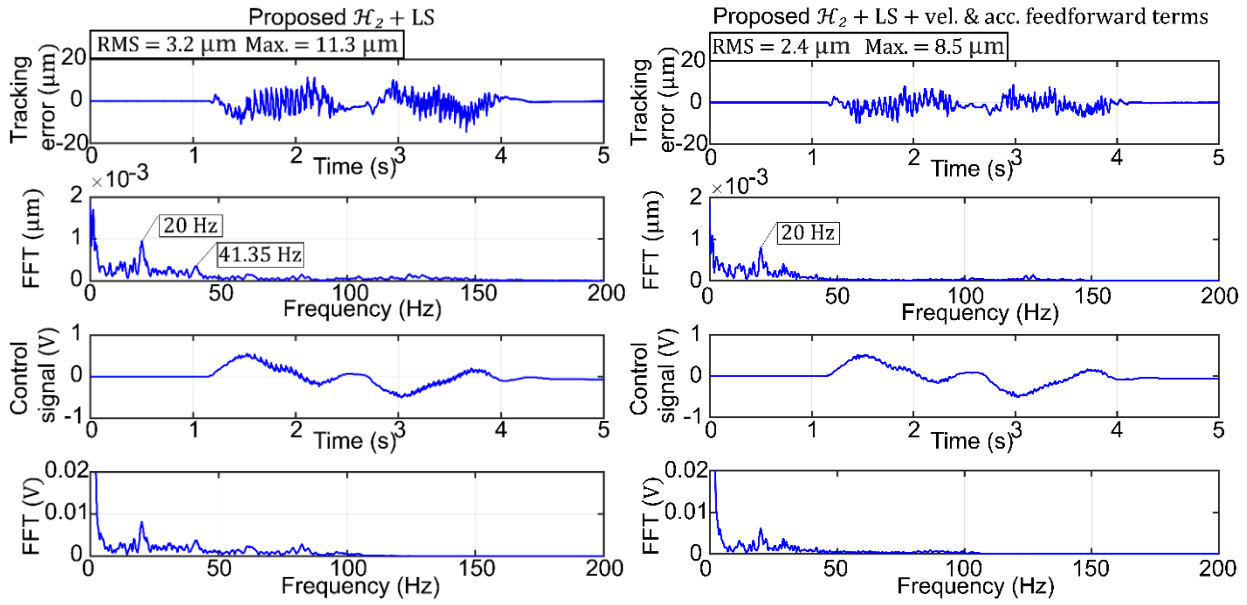


Figure 5.31: Experimentally measured tracking errors and control signals for the proposed $\mathcal{H}_2 + LS$ controller without (left) and with (right) velocity and acceleration feedforward terms.

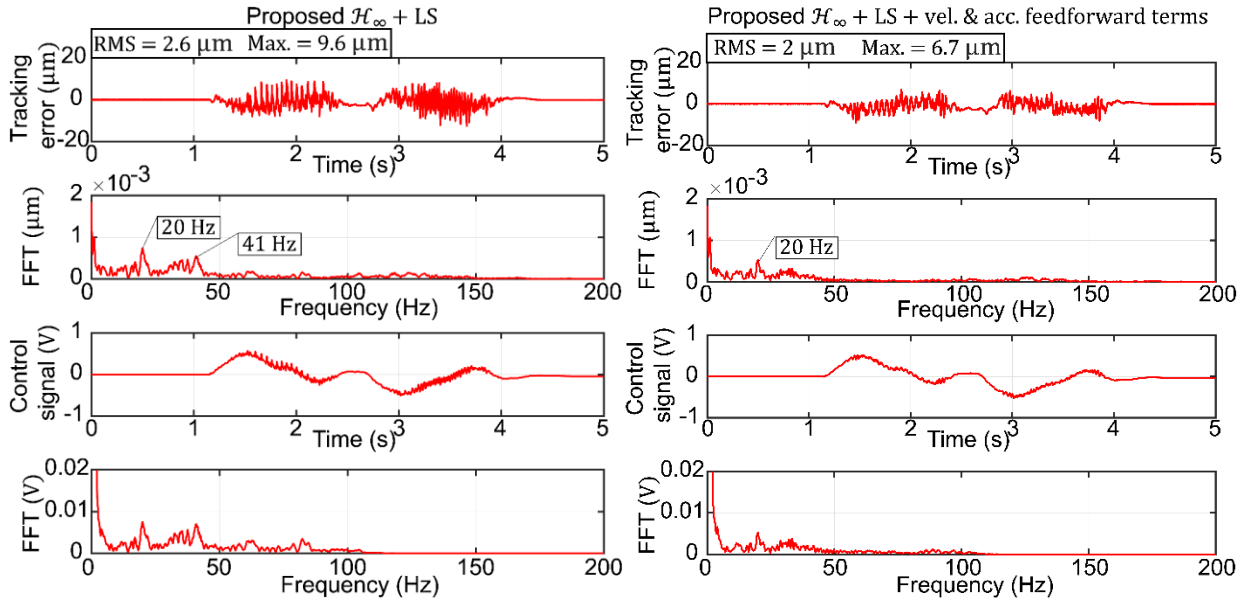
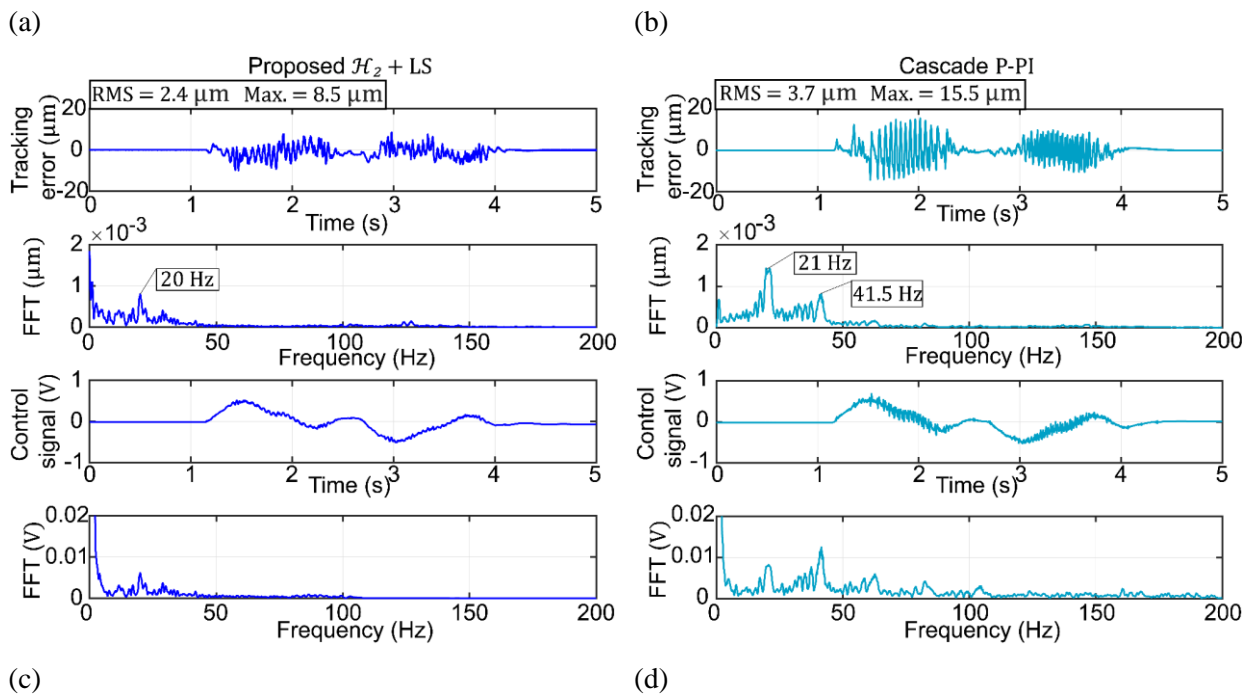


Figure 5.32: Experimentally measured tracking errors and control signals for the proposed $\mathcal{H}_\infty + LS$ controller design without (left) and with (right) velocity and acceleration feedforward terms.

In the proceeding, the proposed controller designs are compared to P-PI and PPC benchmarks in tracking. The trajectory prefilter was tuned individually for each controller, including P-PI and PPC, to improve their dynamic accuracy as much as possible. In implementing the cascade P-PI control, similar velocity and acceleration feedforward terms were used based on the identified inertia and viscous damping

parameters (per Figure 5.4). In PPC, the plant inversion based on the lumped-mass model was used in feedforward per [72] and also a separate state command generator was applied to coordinate the rotational motion commands for the feed drive (i.e., adjusting for expected elastic deformations based on the commanded acceleration). Figure 5.33 illustrates the tracking results obtained by using the four different controllers. As can be seen, the proposed $\mathcal{H}_2 + LS$, and $\mathcal{H}_\infty + LS$ show better tracking performance over the cascade P-PI controller. The tracking error for the vibration-damping PPC is similar to that of the $\mathcal{H}_2 + LS$ controller, and slightly worse than that of the $\mathcal{H}_\infty + LS$ design. It is interesting to note that the proposed controllers also produce less high frequency control activity in comparison to the P-PI and PPC designs, thereby making them also more favorable in terms of energy efficiency.

Overall, the tracking results indicate that in addition to the superior disturbance rejection obtained with the proposed controller designs, high dynamic positioning accuracy can also be simultaneously achieved. This makes the developed control law suitable for application in high precision machine tools.



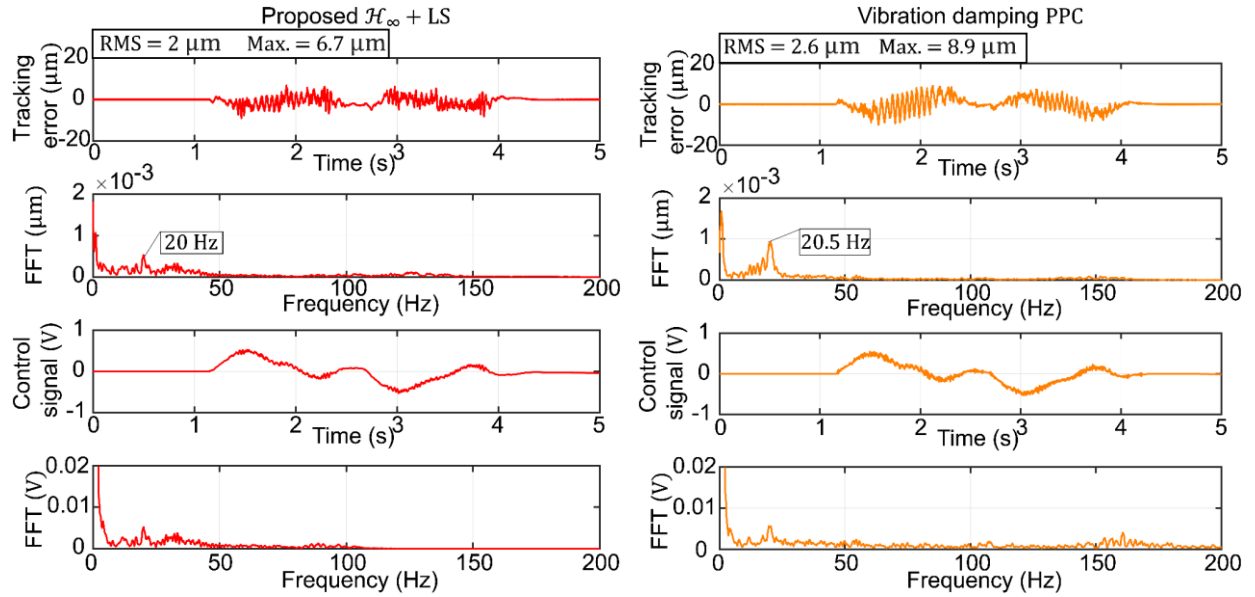


Figure 5.33: Experimentally measured tracking errors and control signals for: (a) proposed $\mathcal{H}_2 + LS$, (b) cascade P-PI, (c) proposed $\mathcal{H}_\infty + LS$, (d) the vibration-damping pole-placement controllers.

5.9. Conclusions

In this chapter, new $\mathcal{H}_2 + LS$ and $\mathcal{H}_\infty + LS$ control schemes have been proposed for enhanced disturbance rejection in machine tool feed drives. To the best of the author's knowledge, multiple vibration mode damping has been developed and experimentally demonstrated for the first time, for a ball-screw drive mechanism. As a result, significant improvement is obtained in the load (table) side dynamic compliance, compared to applying the industry standard P-PI position-velocity cascade control solution, or applying a more advanced model-based vibration-damping controller reported in literature, based on pole-placement.

The controllers were synthesized using the MIMO and high-order feed drive plant identified by the new estimation algorithm developed in Chapter 4. This was key to achieving the reported results. Diverging from the conventional means of setting sensitivity weights in \mathcal{H}_2 and \mathcal{H}_∞ control synthesis, the proposed method sets the sensitivity (i.e., performance) weight to directly minimize the load-side disturbance compliance. In addition to the automated synthesis of vibration damping, loop-shaping principles are used in conjunction to improve the trajectory tracking, along with several feedforward terms.

In disturbance rejection, the proposed designs have achieved 2-3 times improvement over P-PI at nearly all frequencies, and 2.5 times better damping of the most critical axial vibration mode at 136 Hz. Compared to PPC, similar improvements were also observed at different frequency ranges, but not for all frequencies. The proposed designs were also able to exploit the feed drive's natural mechanical damping capability,

around its relatively wide anti-resonance (60 Hz), implying better energy efficiency in responding to cutting forces around this frequency.

In trajectory tracking, the proposed $\mathcal{H}_2 + LS$ and $\mathcal{H}_\infty + LS$ designs have achieved comparable or better accuracy. For example, compared to the industry standard P-PI controller with all feedforward features enabled, the proposed controllers (due to their higher closed-loop bandwidth) have achieved 45-57% reduction in the MAX and 35-46% reduction in the RMS values of the positioning error, while producing control signals which also exhibit less activity in the high frequency range.

It is important to mention that while setting the controller design weights and loop shaping parameters, the loop transfer function Bode and Nyquist plots, the stability and sensitivity margins, and achieved load side compliance FRF need to be iteratively monitored. Thus, while yielding highly promising results, the proposed methodology, at the moment, still requires a noticeable amount of expert input and interaction before it can be applied successfully and reliably in industry. Nevertheless, the results are quite promising and the methodology, in the authors' opinion, can be further developed.

Chapter 6

Suppression of Harmonic Positioning Errors in Ball-Screw Drives using AFC

6.1. Introduction

Harmonic positioning errors can negatively affect the positioning accuracy of the ball-screw drive system. This chapter addresses the problem of harmonic positioning error suppression in ball-screw drives using Adaptive Feedforward Cancellation (AFC). A brief review of the AFC was presented in Section 2.5.1.

In the following, Section 6.2 extends the structure, analysis, and, design to the dual feedback configuration used in ball-screw drives, considering the disturbance and tracking response modification, performance degradation, and robust stability issues. Section 6.3 describes the effect of AFC on rejecting harmonic disturbance sources in closed-loop control of ball-screw drive. The influence of AFC on positioning errors due to command trajectory is investigated in Section 6.4. AFC design in conjunction with two different control schemes for ball-screw drives is presented in Section 6.5.

Section 6.6 demonstrates on-the-fly compensation of position-periodic errors induced by lead imperfections and/or mechanical/sensor misalignments. Sections 6.7 and 6.8 present additional simulation results, comparing the proposed tuning procedure for AFC resonators with the current conventional approach, and also investigating the effectiveness of AFC's harmonic positioning error correction under a variable velocity trajectory. The conclusions for the study are presented in Section 6.9.

6.2. AFC Design for Dual-Feedback Ball-Screw Drive Control System

6.2.1. Basic Structure

The proposed integration of AFC with the dual feedback structure used in ball-screw drives is shown in Figure 6.1. The transfer functions G_1 and G_2 represent the rotational and translational position response of the feed drive. u is the motor current command, which in this study is considered as the control signal. For analysis purposes, the block diagram has been arranged so that the control signal can be written as a combination of the rotational and translational feedback measurements (x_1 and x_2 , respectively) and the modified position command (r^*):

$$u = Rr^* - K_1x_1 - K_2x_2 \quad (6.1)$$

Above, and in Figure 6.1, R , represents the feedforward control dynamics, and K_1 , and K_2 the feedback control dynamics as applied on the rotational and translational measurement channels. Optionally, the control structure may also possess plant inversion and/or trajectory pre-filtering terms, which are designated by I and P , respectively. The positioning error e is calculated by comparing the translational position measurement x_2 (the target feedback) with the original position command r . The AFC block, designated with the transfer function A , generates the harmonic cancellation signal c which offsets the position command to produce the modified position reference r^* . The AFC block can contain one or more resonator, as described earlier in Section 2.5.1. In tuning the phase parameter ϕ_n for each resonator, the phase of the closed loop response from the modified command input to the ball-screw translational response $G_{r^* \rightarrow x_2}$ is considered, as shown in Figure 6.1.

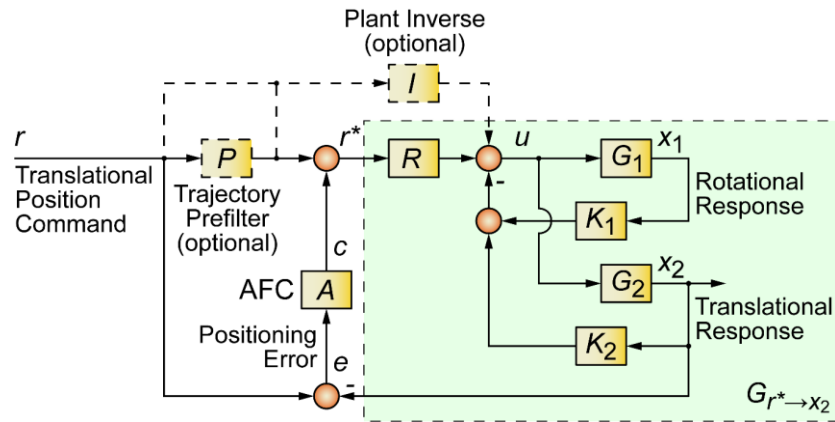


Figure 6.1: AFC integrated inside the dual feedback ball-screw drive control structure.

In the proposed method, the phase selection rule in [107] described in Section 2.5.1, was adopted without modification. It was observed, through extensive simulations, that this rule yields the fastest cancellation when the oscillator gain is kept constant. Here, $G_{r^* \rightarrow x_2}$ can be found by applying the necessary block diagram reduction to Figure 6.2:

$$G_{r^* \rightarrow x_2} = \frac{G_2 R}{1 + K_1 G_1 + K_2 G_2} \quad (6.2)$$

The overall closed-loop response with the inclusion of AFC can be conveniently analyzed by considering the AFC to be an augmentation to the existing translational position feedback filter K_2 , as shown in Figure 6.2. In this case, the new translational position feedback controller becomes:

$$K_2' = K_2 + AR \quad (6.3)$$

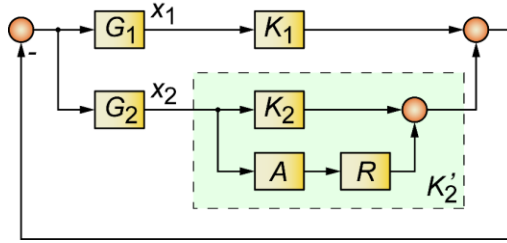


Figure 6.2: Equivalent dynamics in translational position feedback channel, due to inclusion of AFC.

6.3. Influence of AFC on Rejecting Harmonic Disturbances

In ball-screw drive control systems, four main sources of disturbance with harmonic nature are:

- i) Torque ripples in the drive/motor system, which can be considered as input disturbance [142][143][144];
- ii) Alignment errors of the rotary encoder mounted on the ball-screw or motor shaft;
- iii) Ball-screw helix (i.e. lead) errors [8]; and,
- iv) Machining forces that have periodic nature, such as in a manufacturing processes like milling, and thus can be decomposed into harmonic components.

While sensor misalignment on the load side (translational) feedback, originating from the linear scale and reader head, can also lead to harmonic positioning errors, this source of error has been kept outside the scope of this thesis's study. In the experimental setup, all care was taken to properly align the linear encoder head with respect to the measurement scale, and to ensure the necessary parallelism between the scale and the linear motion of the table, as recommended by the encoder manufacturer. In literature, there have been studies examining how machine tool structural vibrations affect linear encoder readings [145][146][147]. However, in this research work, the linear encoder (Heidenhain LIF 101R) is considered as a reference in detecting and compensating for the translational positioning errors caused by the other harmonic error sources listed in factors (i)-(iv). Figure 6.3 illustrates these sources of disturbance in the context of the ball-screw drive control system. In the figure, G_{d1} and G_{d2} represent the motor and load side response to disturbance forces acting on the load (i.e., nut and table) side.

It is important to mention that the true nature of the lead error can be more accurately described as a position dependent gain variation, due to very small changes in the ball-screw gearing ratio, as the table and nut translate via an imperfect helical groove. This, in turn, modifies the manner in which the equivalent

translational inertia is reflected back onto the motor shaft. However, since this fluctuation is extremely small (i.e., in the order of 0.01% for a 20 mm lead ball-screw), it is not easy to directly observe the changes to the system dynamics caused by this subtle nonlinearity. Instead, to simplify the analysis this error source can be reasonably approximated as an output disturbance acting on the translational motion of the ball-screw drive, as shown in Figure 6.3.

The closed loop response of the translational motion x_2 as a function of the disturbance sources can be derived by applying the relevant block diagram algebra, which results in:

$$x_2 = \underbrace{\frac{G_2}{1 + G_1K_1 + G_2K_2}}_{G_{d_1 \rightarrow x_2}} d_1 + \underbrace{\frac{(1 + G_1K_1)G_{d_2} - G_2K_1G_{d_1}}{1 + G_1K_1 + G_2K_2}}_{G_{d_2 \rightarrow x_2}} d_2 + \underbrace{\frac{-G_2K_1}{1 + G_1K_1 + G_2K_2}}_{G_{v_1 \rightarrow x_2}} v_1 + \dots$$

$$+ \underbrace{\frac{1 + G_1K_1}{1 + G_1K_1 + G_2K_2}}_{G_{l_2 \rightarrow x_2}} l_2 \quad (6.4)$$

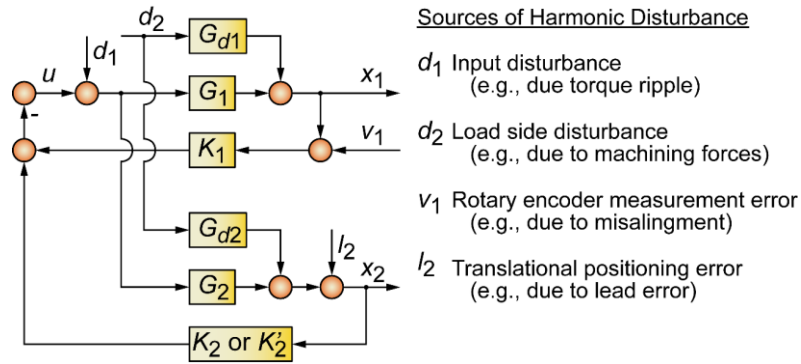


Figure 6.3: Expected harmonic disturbance sources in closed-loop control of a ball-screw drive.

It is interesting to note that the translational feedback K_2 only appears in the denominator of the disturbance transfer functions in Eq. (6.4). When AFC is applied, these transfer functions are modified by the substitution of K'_2 , from Eq. (6.3), in the place of K_2 in Eq. (6.4), leading to:

$$\left. \begin{aligned} G'_{d_1 \rightarrow x_2} &= \frac{G_2}{1 + G_1K_1 + G_2K'_2} , & G'_{d_2 \rightarrow x_2} &= \frac{(1 + G_1K_1)G_{d_2} - G_2K_1G_{d_1}}{1 + G_1K_1 + G_2K'_2} \\ G'_{v_1 \rightarrow x_2} &= \frac{-G_2K_1}{1 + G_1K_1 + G_2K'_2} , & G'_{l_2 \rightarrow x_2} &= \frac{1 + G_1K_1}{1 + G_1K_1 + G_2K'_2} \end{aligned} \right\} \quad (6.5)$$

The disturbance transfer functions in Eqs. (6.4) and (6.5) represent frequency dependent complex gains. For example, in Figure 6.4, the magnitude of the transfer function related to lead errors ($|G_{l_2 \rightarrow x_2}|$) is shown. In this case, the dynamic response of a ball-screw drive coupled with a P-PI position-velocity cascade

controller is taken into account. The control structure is shown in Figure 6.5a. In obtaining the FRF's in Figure 6.4, the open-loop feed drive model and experimental frequency response measurements representing the terms G_1 , G_2 , G_{d1} , and G_{d2} were obtained following the procedure in [72]. The configuration of K_1 and K_2 terms related to P-PI cascade control elements is also discussed in detailed in [72].

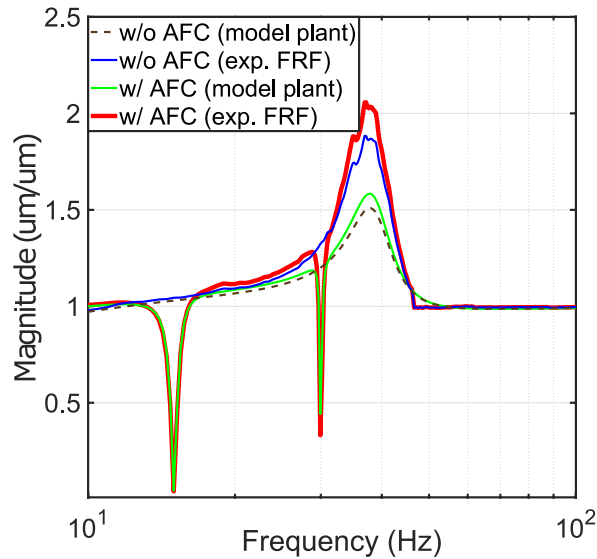
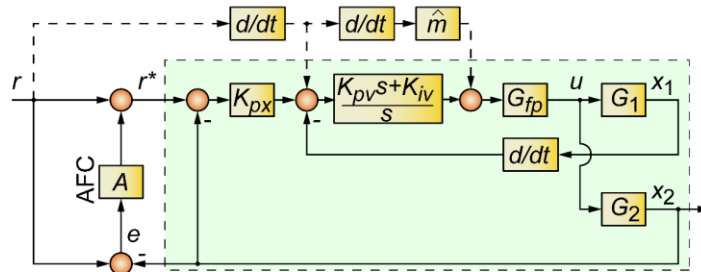


Figure 6.4: Closed-loop response of table position to lead error disturbance, without (w/o) and with (w/) AFC in the translational feedback loop.

(a) Integration of AFC with P-PI Position-Velocity Cascade Control



(b) Integration of AFC with Pole Placement Control

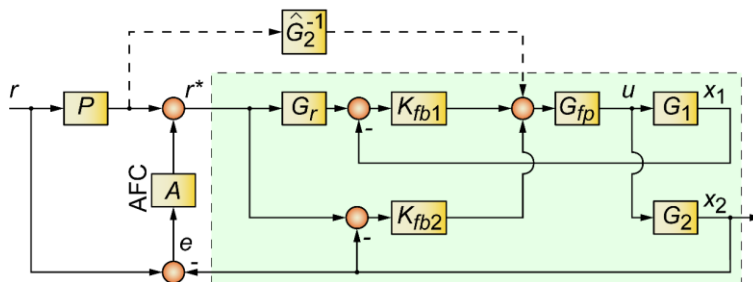


Figure 6.5: Integration of AFC with: (a) P-PI position velocity cascade and, (b) pole-placement control schemes.

In this example, the lead length of the ball-screw (displacement per revolution of the screw shaft) is 20 mm. Hence, when the drive is traveling at 300 mm/s, the principal frequency due to lead error will be 15 Hz and a secondary harmonic at 30 Hz may also exist. Figure 6.4 shows the suppression of $|G_{l_2 \rightarrow x_2}|$ (leading to $|G_{l_2' \rightarrow x_2}'|$) at 15 Hz (i.e., once per screw revolution) and 30 Hz (twice per screw revolution) through AFC design.

The principal function of AFC is to diminish the magnitude of the disturbance response near the expected error harmonic frequencies. However, due to the waterbed effect encountered in linear control systems [25], mitigating the disturbance response at certain target frequencies worsens the performance at others. Since inclusion of the AFC to correct for translational positioning errors only alters the feedback controller K_2 , it can be shown as in the proceeding analysis that the relative change in the four disturbance transfer functions in Eq. (6.4) will be identical.

Comparing the gains of the updated disturbance transfer functions in Eq. (6.5) with their non-AFC counterparts' in Eq. (6.4), it can be seen that a frequency dependent factor (α), defined here as the **response modification factor** via Eq. (6.6), would be sufficient to evaluate the relative improvement (or deterioration) achieved through the inclusion of AFC into the translational feedback loop.

$$\alpha(\omega) = \frac{|G'_{d_1 \rightarrow x_2}(s)|}{|G_{d_1 \rightarrow x_2}(s)|}_{s=j\omega} = \frac{|G'_{d_2 \rightarrow x_2}(s)|}{|G_{d_2 \rightarrow x_2}(s)|}_{s=j\omega} = \frac{|G'_{v_1 \rightarrow x_2}(s)|}{|G_{v_1 \rightarrow x_2}(s)|}_{s=j\omega} = \frac{|G'_{l_2 \rightarrow x_2}(s)|}{|G_{l_2 \rightarrow x_2}(s)|}_{s=j\omega} = \frac{|1 + G_1 K_1 + G_2 K_2|}{|1 + G_1 K_1 + G_2 K_2'|}_{s=j\omega} \quad (6.6)$$

The response modification factor implies that at frequencies where $\alpha < 1$, improvement is achieved over the earlier design excluding AFC. Conversely, at frequencies where $\alpha > 1$, the response is worsened. An advantage of using α is that it applies simultaneously to all concerned disturbance response functions related to the ball-screw drive. Typically, the feedback control law (K_1 and K_2) is first designed by excluding the resonators. The AFC is added afterwards. Thus, it makes sense to use the original disturbance response achieved with the initial design as a baseline for quantifying the AFC's performance gain or loss in the frequency-domain. For example, if no more than 20% deterioration is desirable at frequencies other than the suppressed harmonics, an upper limit on the value of α can be imposed as $\alpha < 1.2$. This rule can be generalized as,

$$\alpha(\omega) \leq \alpha_p \quad (6.7)$$

Above, α_P represents an upper limit on the response modification factor as a *performance* requirement, defined with respect to the nominal feedback design without the AFC. In Eq. (6.4), considering the $1 + G_1K_1 + G_2K_2$ term common to all denominators, application of the Nyquist stability criterion requires the consideration of $L = G_1K_1 + G_2K_2$ (or when AFC is used, $L = G_1K_1 + G_2K'_2$) as the loop-transfer function [25]. This result can also be arrived at by inspecting the parallel forward branches K_1G_1 and K_2G_2 (or K'_2G_2) in Figure 6.3., which join together to form a negative feedback loop at the scalar control signal point u .

In setting a robustness boundary for stability, if the vector margin (i.e., reciprocal of the peak sensitivity value S_{max}) is used, then the robust stability requirement can also be conveniently integrated into the analysis of the response modification factor α . Defining the sensitivity function [25] corresponding to the cases without and with AFC as $S = 1/(1 + L) = 1/(1 + G_1K_1 + G_2K_2)$ and $S' = 1/(1 + L') = 1/(1 + G_1K_1 + G_2K'_2)$, respectively, the response modification factor α can be regarded as the magnitude ratio between these two sensitivity functions:

$$\alpha = \left| \frac{1 + G_1K_1 + G_2K_2}{1 + G_1K_1 + G_2K'_2} \right|_{s=j\omega} = \left| \frac{1}{1 + G_1K_1 + G_2K'_2} \frac{1 + G_1K_1 + G_2K_2}{1} \right|_{s=j\omega} = \left| \frac{S'}{S} \right|_{s=j\omega} \quad (6.8)$$

If the original sensitivity function S is already known, the upper bound on α to achieve such robust stability can be computed, as shown in Eq. (6.8). This ensures that the peak sensitivity of the closed-loop system with AFC remains below S_{max} :

$$|S'(s)|_{s=j\omega} \leq S_{max} \Leftrightarrow \alpha(\omega) \leq \frac{S_{max}}{|S(s)|_{s=j\omega}} = \alpha_{RS}(\omega), \quad \forall \omega \quad (6.9)$$

In the above equation, $\alpha_{RS}(\omega)$ represents the frequency dependent upper limit on α , in order to hold $|S'(\omega)| \leq S_{max}$. The resonator gains g_n are tuned and increased as much as possible, while simultaneously monitoring the frequency dependent profile for $\alpha(\omega)$ to continue satisfying Eq. (6.7) and Eq. (6.9). Thus, a new and practical way to tune the AFC gains is introduced, which keeps in mind both the performance deterioration issue outside the target harmonic frequencies, and also the robust stability requirement for the closed-loop system with the AFC resonator(s).

For example, robust gain selection for two AFC's at 15 and 30 Hz integrated inside the translational feedback channel is shown in Figure 6.6 and Figure 6.7. As mentioned earlier, the AFC's have been designed to block out the first and second harmonic components of the screw's rotation, which can originate from lead errors, torque ripple-type factors, and other potential sources of mechanical or sensor misalignment. Inspection of these figures indicates that successful attenuation is achieved at the target

frequencies while ensuring that performance degradation at other frequencies (due to the two AFC's) does not exceed 20%, and that a desired robust stability margin of $S \leq S_{max} = 2.0$ is also maintained.

To verify the stability in the sense of classical gain and phase margins (GM , PM), and to inspect the achieved loop transfer function crossover frequency (ω_c) as a commonly used measure for control bandwidth ($|L(j\omega_c)| = 1$) [25], the Bode and Nyquist plots for the loop transfer function without and with AFC (L and L') are analyzed, as presented in Figure 6.8 and Figure 6.9. These plots are based on the loop transfer function FRFs which have been calculated both using experimentally recorded frequency response data from the plant (designated with 'exp' in the plot legend), and via frequency response prediction from a model approximation of the feed drive (designated with 'model plant'). The ball screw dynamics was approximated with a two-inertia model, to capture the first axial vibration mode [71][72]. As the controller dynamics is already known, its frequency domain contribution is directly computed analytically.

The fact that the Nyquist plot makes no clockwise encirclement of the '-1' point indicates nominal stability for the closed-loop system. Thus, the peak value of the sensitivity plot in Figure 6.6 can be used to determine stability robustness. It is also noted that the crossover frequency (i.e., 'bandwidth') for the P-PI control without and with AFC is 34 Hz, and local gain amplifications at 15 and 30 Hz help reject the corresponding harmonic disturbances at these frequencies.

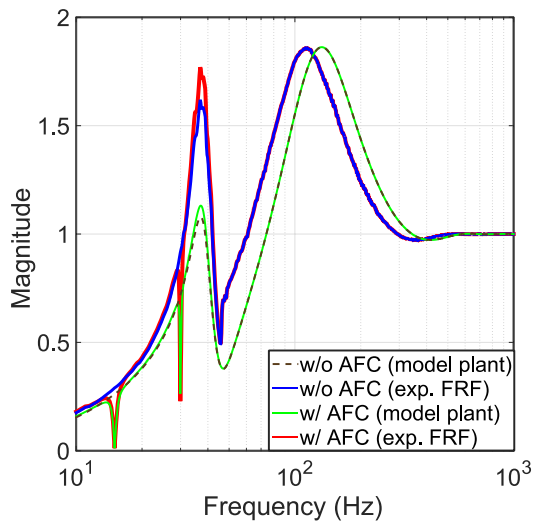


Figure 6.6: Loop sensitivity without and with AFC.

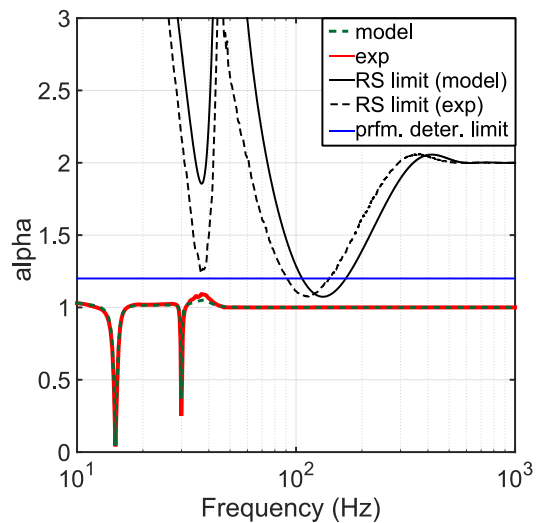


Figure 6.7: Design of AFC through inspection of the response modification factor (α).

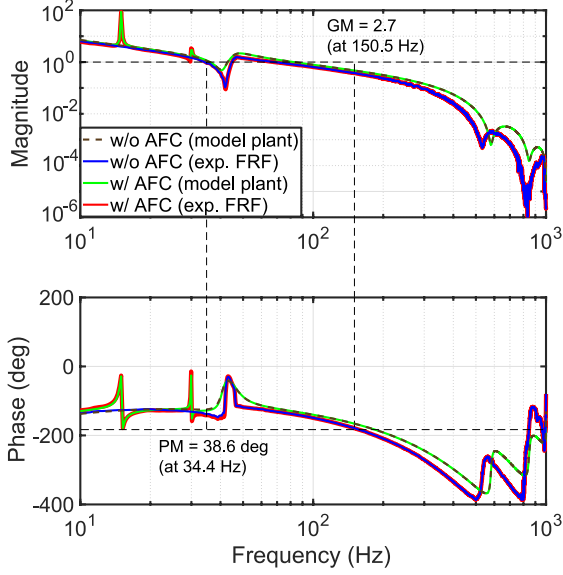


Figure 6.8: Loop transfer function for P-PI controller without and with AFC resonators (target frequencies: 15 Hz, and 30 Hz).

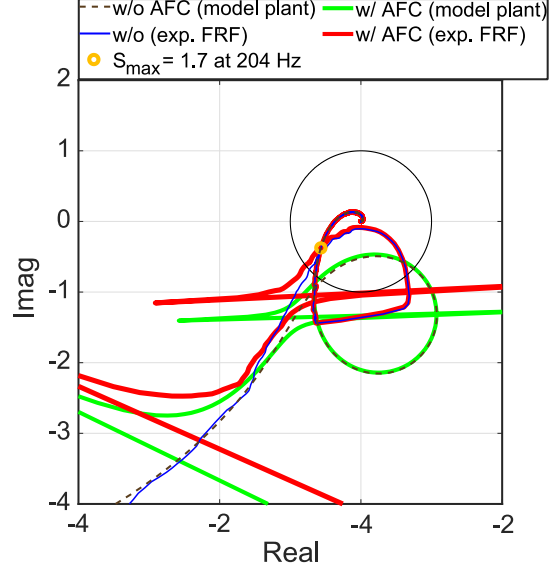


Figure 6.9: Nyquist plot of the loop transfer function for P-PI controller without and with AFC resonators (target frequencies: 15 Hz, and 30 Hz).

6.4. Influence of AFC on Positioning Errors Due to Command Following

Extending the translational response in Eq. (6.4) to consider the effect of the commanded trajectory r , by merging the block diagrams in Figure 6.1 and Figure 6.3, it is possible to obtain the translational response as,

$$\begin{aligned}
 x_2 = & \underbrace{\frac{G_2((I+R)P + RA)}{1 + G_1K_1 + G_2K'_2}}_{G'_{r \rightarrow x_2}} r + \underbrace{\frac{G_2}{1 + G_1K_1 + G_2K'_2}}_{G'_{d_1 \rightarrow x_2}} d_1 + \underbrace{\frac{(1 + G_1K_1)G_{d_2} - G_2K_1G_{d_1}}{1 + G_1K_1 + G_2K'_2}}_{G'_{d_2 \rightarrow x_2}} d_2 + \dots \\
 & + \underbrace{\frac{-G_2K_1}{1 + G_1K_1 + G_2K'_2}}_{G'_{v_1 \rightarrow x_2}} v_1 + \underbrace{\frac{1 + G_1K_1}{1 + G_1K_1 + G_2K'_2}}_{G'_{l_2 \rightarrow x_2}} l_2
 \end{aligned} \tag{6.10}$$

Following Eq. (6.10), the true positioning error can be written as $= r - x_2$, which leads to:

$$\begin{aligned}
e = & \underbrace{\frac{1 + G_1 K_1 + G_2 K_2 - G_2 P(I + R)}{1 + G_1 K_1 + G_2 K_2'}}_{G'_{r \rightarrow e}} r + \underbrace{\frac{-G_2}{1 + G_1 K_1 + G_2 K_2'}}_{G'_{d_1 \rightarrow e}} d_1 + \dots \\
& + \underbrace{\frac{G_2 K_1 G_{d_1} - (1 + G_1 K_1) G_{d_2}}{1 + G_1 K_1 + G_2 K_2'}}_{G'_{d_2 \rightarrow e}} d_2 + \underbrace{\frac{G_2 K_1}{1 + G_1 K_1 + G_2 K_2'}}_{G'_{v_1 \rightarrow e}} v_1 + \dots \\
& + \underbrace{\frac{-(1 + G_1 K_1)}{1 + G_1 K_1 + G_2 K_2'}}_{G'_{l_2 \rightarrow e}} l_2
\end{aligned} \tag{6.11}$$

Focusing on the error response due to the trajectory command ($G_{r \rightarrow e}$), it can be seen that the updated translational feedback term due to AFC ($K_2' = K_2 + AR$) appears, once again, only in the denominator. In the numerator, K_2 represents the translational feedback controller *without* the AFC. Thus, the same observation which was made for α regarding for four disturbance responses in Section 6.3 also applies to the command response:

$$\boxed{
\begin{aligned}
\alpha(\omega) = & \left| \frac{G'_{r \rightarrow e}(s)}{G_{r \rightarrow e}(s)} \right|_{s=j\omega} = \left| \frac{G'_{d_1 \rightarrow e}(s)}{G_{d_1 \rightarrow e}(s)} \right|_{s=j\omega} = \left| \frac{G'_{d_2 \rightarrow e}(s)}{G_{d_2 \rightarrow e}(s)} \right|_{s=j\omega} = \left| \frac{G'_{v_1 \rightarrow e}(s)}{G_{v_1 \rightarrow e}(s)} \right|_{s=j\omega} \\
& = \left| \frac{G'_{l_2 \rightarrow e}(s)}{G_{l_2 \rightarrow e}(s)} \right|_{s=j\omega} = \left| \frac{1 + G_1 K_1 + G_2 K_2}{1 + G_1 K_1 + G_2 K_2'} \right|_{s=j\omega}
\end{aligned}
} \tag{6.12}$$

At a frequency where $\alpha < 1$, the positioning error due to the command input is reduced by α . Conversely, when $\alpha > 1$, the response with AFC deteriorates by α with respect to the baseline (no AFC) design. Thus, AFC can also be used to mitigate harmonics in the tracking error which occur in response to a commanded trajectory. While this property can be exploited in high-speed repetitive trajectory tracking devices, such as fast tool servos [92][93], in the case of machine tool feed drives with ball-screw mechanisms or direct drives, the commanded position is usually made up of ramp, parabola, polynomial, or exponential terms. Thus, distinct harmonic components would typically be lacking in the command signal r , and this renders the mitigation of harmonic error components originating from the commanded trajectory to secondary importance. Nevertheless, the impact of AFC on the command following response with respect to a baseline design can be conveniently analyzed and designed by the help of Eq. (6.11) and (6.12) considering the parameter α , just as done for the disturbance response in Section 6.3.

6.5. AFC in Conjunction with Different Motion Control Laws for Ball-Screw Drives

Figure 6.5 demonstrates the integration of AFC inside two different control structures for ball-screw drives. Figure 6.5a shows the P-PI position-velocity cascade control arrangement, which is widely used in

industry. The PI velocity loop is closed via rotational velocity measurement from the motor side (dx_1/dt), whereas the P position control loop is closed via translational feedback from the load side (x_2). Feedforward compensation, by injecting the expected velocity command (dr/dt) and pre-computed inertial force ($\hat{m} \cdot d^2r/dt^2$) is available, in order to improve the dynamic tracking accuracy. The filter pack G_{fp} contains additional filters, such as notch (for suppressing known structural resonances) and low pass (to facilitate high frequency gain attenuation), in order to achieve a stable loop shape with acceptable stability margins.

Figure 6.5b demonstrates a more advanced scheme based on pole-placement control, which is capable of actively damping the first vibration mode of the ball-screw mechanism, thus accomplishing an even higher active frequency range than P-PI for disturbance rejection and command tracking. Details of the PPC design can be found in [72].

Here, for conciseness only the basic structure is reviewed. The two feedback controllers K_{fb1} and K_{fb2} assume the structure of PD and PID controllers, respectively, and enable the modification of the feed drive's vibratory and rigid body response. G_r is used to coordinate the rotational position commands for the motor side, considering the anticipated elastic deformations of the drive induced by the commanded trajectory. \hat{G}_2^{-1} is an approximation of the feed drive's inverse response (from torque input to translational position output, G_2), and P is a trajectory pre-filter, which is tuned experimentally to remove any artefact in the tracking error correlated to the commanded velocity, acceleration, or jerk profiles.

The feedforward action in both control schemes is essential, in order to yield a tracking error profile which has zero mean (i.e., almost no correlation to the commanded kinematic derivative profiles). This makes it much easier for the AFC to directly target the harmonic error component(s), which need to be suppressed.

6.6. Experimental Implementation: AFC for Rejecting Position Dependent Harmonic Errors

In designing AFC to target errors, which are cyclical with axis position, the AFC resonator frequencies need to be gain-scheduled as a function of velocity. An example of this is the servo error caused by the ball-screw drive's lead imperfection, sometimes referred to as 'run-out'. The lead error profile on our experimental setup was estimated by taking the difference between linear and rotary encoder measurements while jogging the axis forward and backward at low speeds (around 20 mm/s). The ball-screw drive used in the tests is the same one reported in [72]. The feed drive was mounted onto the machine tool to provide actuation along the x-axis. However, the ball-screw mechanism was replaced due to a need for refurbishment. A new ball-screw with the closest external dimensions to the earlier one was procured. The new model is THK BNK 2020-3.6G0 + 1220 LC5-Y. The motor and amplifier were refurbished as well,

with a 3kW Omron R88M-K3K030H servo motor and K3K030T drive. The new mechanism is a double start ball-screw possessing 20 mm diameter and 20 mm lead (i.e., two 10 mm pitch helical grooves). A typical measurement of the lead error profile is shown in Figure 6.10. It is clear that the main component of lead error (l_2) can be approximated with a position dependent sinusoidal function, by considering a spatial frequency of Ω_n ($1/L$) ($=1/0.02 \text{ m}^{-1}$) in the form:

$$l_2(x(t)) = L_2 \sin(\Omega_n x(t) + \Phi_n) \quad (6.13)$$

Above, $x = x(t) = x_2(t)$ designates the drive's translational position, L_2 the lead error magnitude, and Ω_n the phase shift.

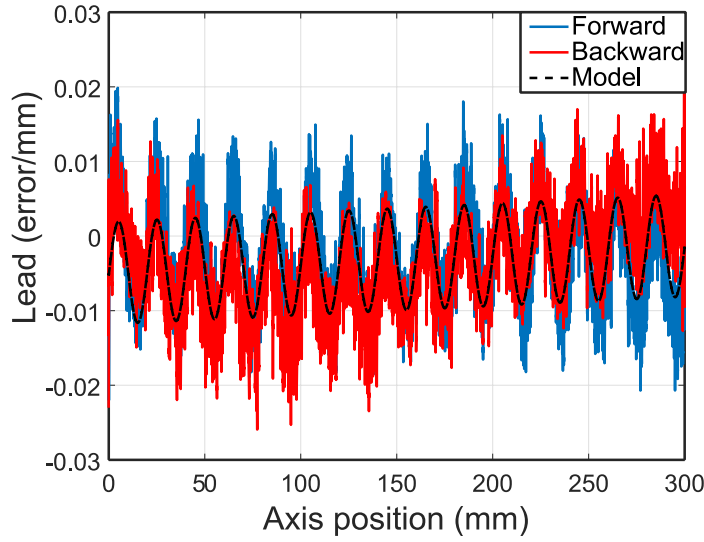


Figure 6.10: Measured and modeled lead error.

During trajectory tracking with velocity $v(t)$, the disturbance source in Eq. (6.13) will contribute to a servo error which has a time dependent form as,

$$e(t) = E \sin(\omega_n t + \phi_n) \quad (6.14)$$

Approximating the instantaneous position $x(t)$ with 1st order Taylor expansion around an earlier state of position and velocity $(x_0, v_0) = (x(t_0), v(t_0))$ corresponding to time t_0 leads to,

$$x(t) \cong x(t_0) + (t - t_0)v(t_0) = x_0 + (t - t_0)v_0 \quad (6.15)$$

Eq. (6.13) can then be re-written as,

$$\begin{aligned}
l_2(x(t)) &\cong L_2 \sin(\Omega_n[x_0 + v(t_0)(t - t_0)] + \Phi_n) = L_2 \sin\left(\frac{\Omega_n v_0 t}{\omega_n} + \frac{\Phi_n + \Omega_n(x_0 - v_0 t_0)}{\Phi'_n}\right) \quad (6.16) \\
&= L_2 \sin(\omega_n t + \Phi'_n)
\end{aligned}$$

Hence, the temporal frequency ω_n contributed by the mechanical lead error becomes the product of the translational velocity v_0 and the lead error's spatial frequency Ω_n . Obviously, this approximation does not consider 2nd or higher order terms, which would account for the influence of nonzero acceleration or jerk values. These effects, for the time being, have been kept outside the scope of this study. Nonetheless, even 1st order approximation is effective in achieving a reduction in the position-dependent harmonic error components through AFC.

Considering Eq. (6.11), the magnitude and phase of the servo error referenced in Eq. (6.14), which are contributed by the disturbance input in Eq. (6.16), can be determined as:

$$E = |G'_{l_2 \rightarrow e}(j\omega_n)|L_2 \quad , \quad \Phi_n = \angle\{G'_{l_2 \rightarrow e}(j\omega_n)\} + \Phi'_n \quad (6.17)$$

In the case that the lead error has multiple harmonics, the same treatment would apply for each harmonic with different spatial frequency. Moreover, if there are other position dependent disturbances originating, for example, from motor or load side torque ripples, or component/sensor (e.g., rotational encoder head) misalignment in the feed drive assembly, their effects would yield similar temporal harmonic components as explained in Eqs. (6.13) - (6.17) through one of the transfer functions ($G'_{d_1 \rightarrow e}$, $G'_{d_2 \rightarrow e}$, $G'_{v_1 \rightarrow e}$, ...) given in Eq. (6.11). In either case, an AFC designed for a particular temporal frequency would be effective in suppressing the error contribution from any one of these sources regardless of origin, as shown in Eq. (6.12).

As the temporal disturbance frequency ω_n to be used in the AFC design varies as a function of the axis velocity, its value and as required the AFC gain and phase parameters need to be updated at every sampling instant in the form $\omega_n(t) = \Omega_n \cdot v_0(t)$. When multiple resonators are used, every set of simultaneous frequencies at which the resonators would operate need to be considered in advance, by sweeping the axis velocity envelope. The resonator phase values can be gain-scheduled in a straight-forward manner, using $\phi_n = \angle G_{r^* \rightarrow x_2}(j\omega_n)$. The concurrently active resonator gains have to be pre-designed for each velocity, considering both performance deterioration and stability robustness specifications.

Considering a 20 (mm/rev) displacement ball-screw with a maximum expected travel velocity of 400 mm/s, designing a gain-scheduled AFC with two resonators to suppress the first and second harmonics

related to the screw's rotation can be accomplished by targeting, for example in 50 mm/s velocity increments, the following frequency pairs shown in Table 6.1.

Table 6.1: Sweep of expected traversal speeds and corresponding 1st and 2nd harmonic frequencies.

50 mm/s \Rightarrow (2.5,5) Hz	100 mm/s \Rightarrow (5,10) Hz	150 mm/s \Rightarrow (7.5,15) Hz	200 mm/s \Rightarrow (10,20) Hz
250 mm/s \Rightarrow (12.5,25) Hz	300 mm/s \Rightarrow (15,30) Hz	350 mm/s \Rightarrow (17.5,35) Hz	400 mm/s \Rightarrow (20,40) Hz

When a P-PI position velocity cascade control structure is considered along with the ball-screw drive's dynamics [72], the resonator gain and phase values which have to be gain-scheduled at each frequency can be obtained as summarized in Table 6.2. The corresponding response modification factor for traveling speeds of 200 mm/s, 300 mm/s, and 400 mm/s are shown in Figure 6.11 and Figure 6.12. The graphs indicate that the robust stability ($S_{max} \leq 2.0$) and performance retention ($\alpha \leq 1.2$) conditions are always respected. Thus, the values in Table 6.2 have been used in real-time gain scheduling, via an interpolation table, during the experiments. The correct parameters for the resonators are updated at each sampling period, based on the instantaneous commanded velocity.

Table 6.2: AFC resonator gains and phase values for different traversal speeds.

Case	Resonator frequencies / Hz	Resonator gains (g_1, g_2)	Phase (ϕ_1, ϕ_2) / rad
1	50 mm/s \Rightarrow (2.5, 5)	5, 1	-0.5734, -0.9237
2	100 mm/s \Rightarrow (5, 10)	5, 2	-0.9237, -1.2914
3	150 mm/s \Rightarrow (7.5, 15)	7.5, 2	-1.1408, -1.5023
4	200 mm/s \Rightarrow (10, 20)	20, 10	-1.3012, -1.7020
5	250 mm/s \Rightarrow (12.5, 25)	20, 22.5	-1.4398, -1.8248
6	300 mm/s \Rightarrow (15, 30)	17.5, 7.5	-1.5228, -2.0769
7	350 mm/s \Rightarrow (17.5, 35)	20, 7.5	-1.6091, -2.6760
8	400 mm/s \Rightarrow (20, 40)	15, 7.5	-1.7020, 2.6934

To evaluate the effectiveness of AFC in counteracting the harmonic positioning errors, the table was commanded in forward and backwards motions using the profile shown in Figure 6.13. In the figure, the trajectory has a peak velocity of 100 mm/s, acceleration of 1000 mm/s², and a jerk of 20,000 mm/s³. Tests were also performed for 200, 300, and 400 mm/s traversal rates.

Figure 6.14 shows the tracking error profile in time and frequency domains. Table 6.3 shows a summary of the tracking performance based on the measurements from Figure 6.14. To ensure repeatability of the results, each test was performance five times. Figure 6.15 shows the RMS value of tracking error registered, without and with AFC, as observed during each sample test.

As can be seen from Figure 6.14 and Table 6.3, after implementation of the AFC the tracking error components, particularly at the target harmonics, are reduced significantly. However, there are still noticeable spikes in the time-domain signal, which occur when the table reverses direction or goes into motion from standstill. These spikes are mainly due to the nonlinear friction, dominant in pre-sliding and hysteresis regimes. These effects cannot be compensated adequately with a simple friction model of static nature, such as a Coulomb-Striebeck type as was used in the tests.

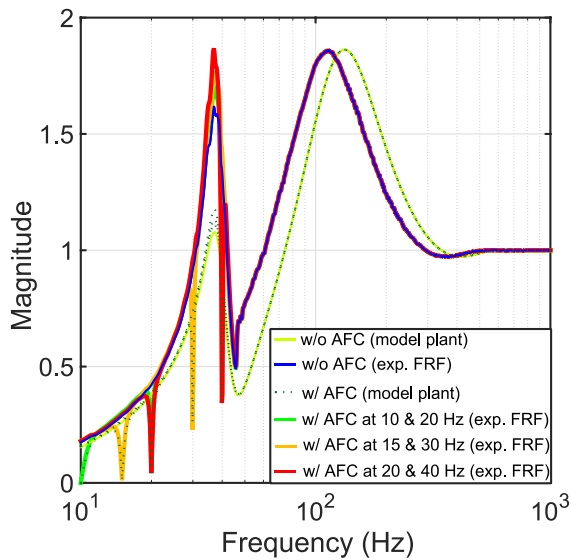


Figure 6.11: Loop sensitivity without and with AFC (target frequencies: 10 Hz & 20 Hz, 15 Hz & 30 Hz, 20 Hz & 40 Hz).

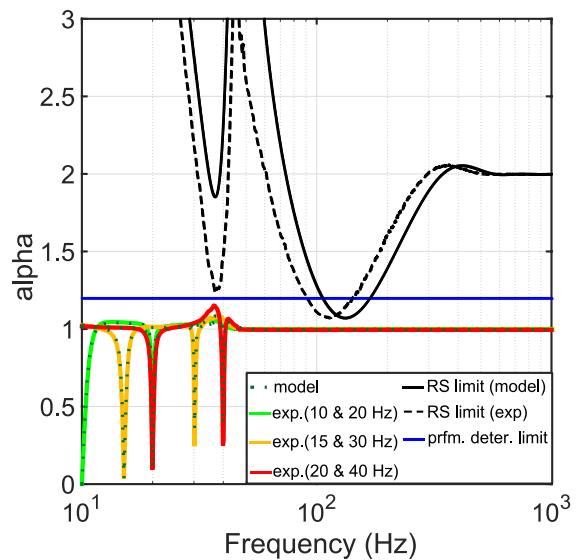


Figure 6.12: Robust design of AFC for 200 mm/s (10 Hz, 20 Hz), 300 mm/s (15 Hz, 30 Hz), 400 mm/s (20 Hz, 40 Hz) through inspection α .

A more elaborate friction model based on the generalized Maxwell-slip (GMS) approach [35] would be more suitable in future research for feedforward compensation, to improve the overall servo accuracy. For example for the case of 100 mm/s velocity, while the harmonic components are successfully quenched, the servo errors due to interaction of the static friction with the feedback loop dynamics tend to be slightly worse (around 3%) than the case with no AFC compensation. More accurate cancellation of friction would ensure that AFC is not misled into producing an erroneous compensation signal, which can deteriorate the servo performance near zero velocity points. Also, while AFC is successful during continuous motion of the feed drive, further investigation is required to ensure that the AFC is smoothly switched off during the stationary (i.e., zero velocity) portions of the commanded trajectory, and smoothly switched on back again during nonzero velocity portions.

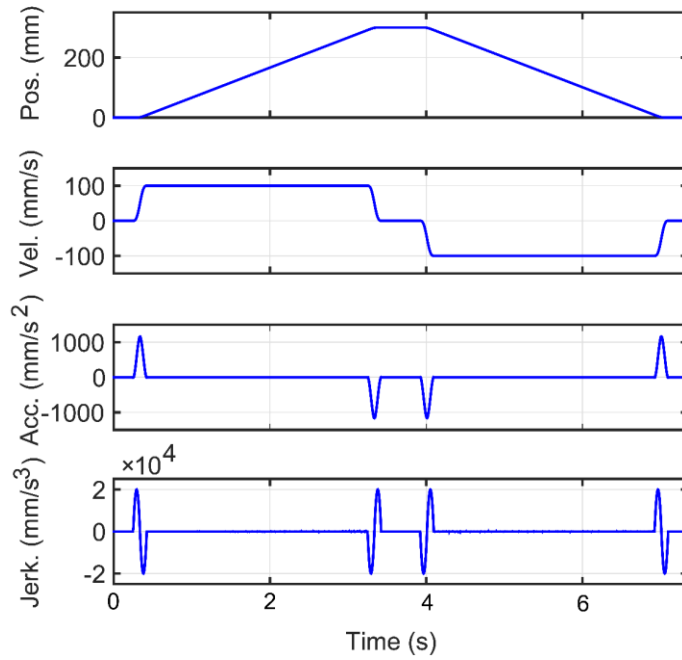


Figure 6.13: Commanded trajectory (displacement: 300 mm).

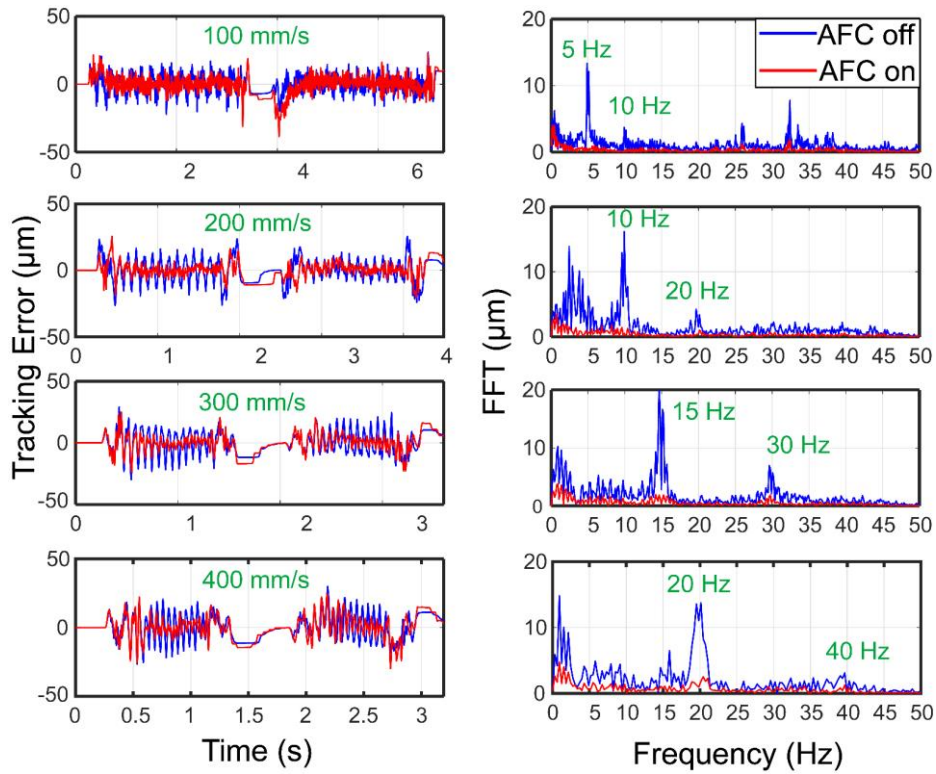


Figure 6.14: Tracking errors at different table speeds in time (left) and frequency-domain components (right).

Table 6.3: Summary of the tracking experiments.

Traveling speed (Principal frequency) (mm/s)	Tracking error (STD) (μm)			Max. tracking error (μm)	
	w/o AFC	w/ AFC	%	w/o AFC	w/ AFC
100 (5 Hz)	6.918	7.116	-2.86	23.6	38.48
200 (10 Hz)	8.652	6.335	26.55	26.31	25.57
300 (15 Hz)	9.231	7.668	16.93	29.81	25.03
400 (20 Hz)	9.307	8.62	7.31	29.97	29.82

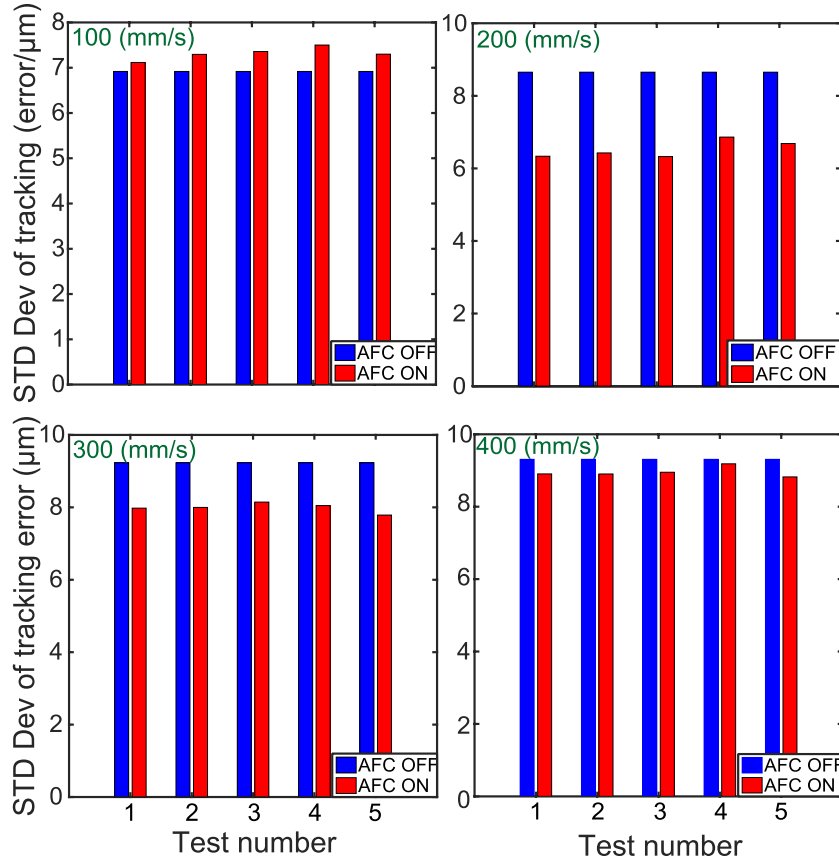


Figure 6.15: RMS value of tracking error without and with AFC, observed over five tests.

Overall, the experimental results validate the effectiveness of AFC in mitigating servo errors of harmonic nature, which exhibit a displacement dependent pattern in ball-screw drives.

6.7. Simulation Results #1: Comparison of the New Tuning Strategy with the Conventional Method

As mentioned earlier, higher resonator gains facilitate faster attenuation of the harmonic error components. However, high resonator gains can also result in performance deterioration at other frequencies, which can adversely affect trajectory tracking or disturbance rejection. In this section, two cases are compared in simulation, to demonstrate the advantage of the proposed tuning over the conventional method [107]. For the plant, a flexible feed drive model is considered with the same dynamics as in Section 4. The lead error is simulated using a model similar to the one in [8]. Considering two significant harmonics (1× and 2× per revolution), corresponding to a ball screw with a double-start thread profile, the below model was used:

$$l_{2,model} = \sum_{i=1}^2 A_i \sin(f_i \theta + \phi_i) \quad (6.18)$$

Above, A_i [V] and ϕ_i [rad] are the amplitude and phase shift for the i th harmonic. f_i is the harmonic frequency ($f_1 = 1$, $f_2 = 2$). θ [rad] is the rotation angle. Additionally, the friction was simulated with Coulomb friction. As the base controller, a P-PI position-velocity cascade controller with 34 Hz crossover, 2.7 gain margin, and 40.8 deg phase margin was designed and used in both AFC implementations. The AFCs were designed to target 10 and 20 Hz (corresponding to 200 mm/s traverse rate), with appropriate phase adjustments as explained in Section 2.5.1.

In implementing the proposed design, the response modification factor α was used to take into account both robust stability and performance requirements, particularly outside the target frequencies. The resonator gains were adjusted to ensure that no more than 5% deterioration occurs throughout the frequency range considered ($\alpha \leq 1.05$). The applied gains correspond to those reported in Table 6.2.

In replicating conventional tuning, the AFC resonators were increased by 2.25×. In this case, the loop phase and gain margins were still preserved, thus complying with the guidelines in [107]. However, the performance retention at other frequencies (α) was not checked.

The loop sensitivity (S), performance retention (α), and Nyquist plots for both designs are compared in Figure 6.16. Both designs successfully attenuate 10 and 20 Hz, with the conventional approach realizing this to a greater extent (Figure 6.16: panels (b) and (d)). While the Nyquist plots (panels (c) and (f)) show that the AFCs in either case does not affect the phase and gain margins, Figure 6.16d indicates further

deterioration of the performance ($\alpha > 1.05$) around 16 and 34 Hz, due to the more ambitious tuning of the resonator gains.

The tracking simulation results and a summary of tracking error values (as standard deviation) are presented in Figure 6.17 and Table 6.4. As can be verified, the proposed tuning, while being a bit less aggressive on the 10 and 20 Hz harmonics, succeeds in retaining a lower RMS value for the tracking error, by limiting the performance degradation at other frequencies. This enables another 14% reduction in the RMS value of the servo error, in comparison to that achieved by the conventional AFC tuning approach.

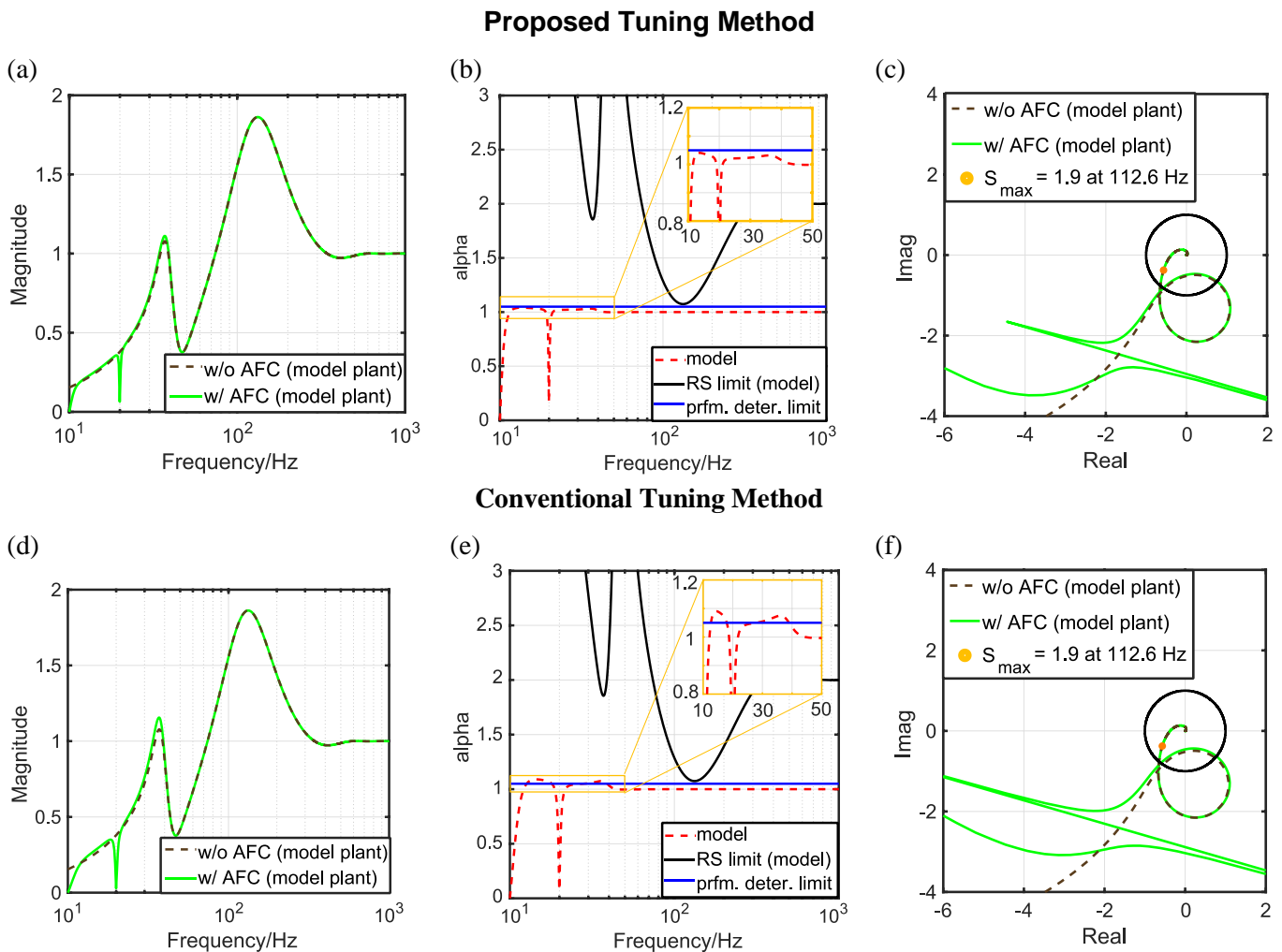


Figure 6.16: Loop sensitivity ((a), (c)), response modification factor ((b), (d)) and Nyquist ((c) and (f)) plots, comparing the proposed AFC tuning method ((a), (b), (c)) with the conventional design ((d), (e), (f)). Target frequencies: 10, 20 Hz.

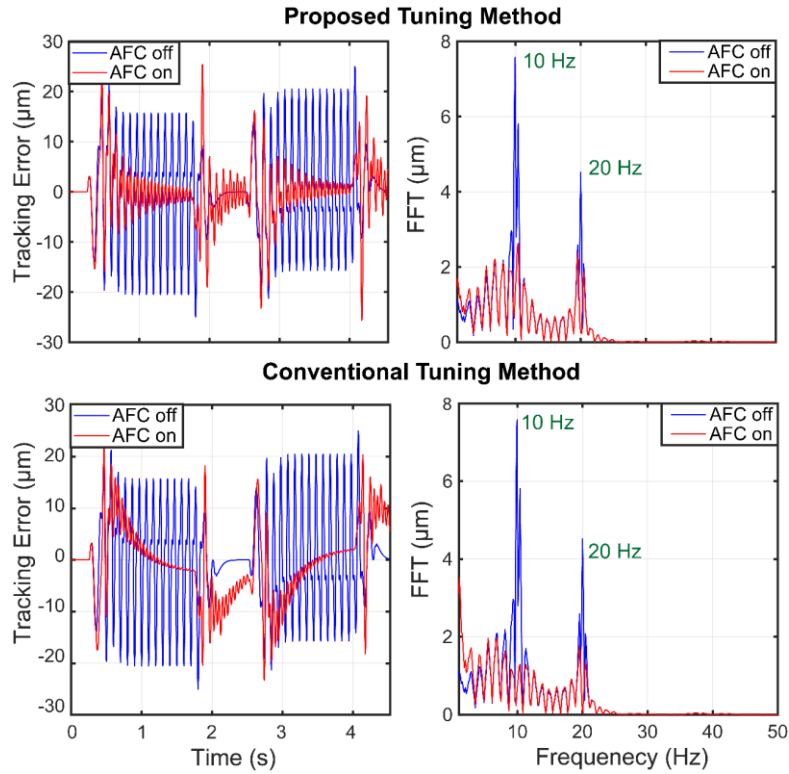


Figure 6.17: Simulated tracking errors at 200 mm/s feed rate using the proposed tuning procedure (top) vs. the conventional tuning procedure (bottom).

Table 6.4: Summary of the tracking simulations.

Tracking error (STD) (μm)			Tracking error (STD) (μm)		
Proposed tuning method			Conventional method		
w/o AFC	w/ AFC	%	w/o AFC	w/ AFC	%
9.43	6.07	35.63	9.43	7.37	21.85

6.8. Simulation Results #2: Rejection of Position Dependent Harmonic Errors During Variable Velocity Motion

In multi-axis manufacturing applications like contour machining, commanded trajectories may often include significant variation in the axis velocity. To evaluate the effectiveness of the position-dependent AFC in handling a variable velocity trajectory, an airfoil path (FX 66-17All-182 airfoil [150]) was considered. Figure 6.18 shows the airfoil profile generated for 1000 mm chord length using cubic spline interpolation. To avoid unwanted feedrate (i.e., tangential velocity) fluctuation during the trajectory generation, 1st order Taylor series based spline interpolation was used [151]. The feedrate, tangential

acceleration, and tangential jerk limits considered were 100 mm/s, 1000 mm/s², and 20 000 mm/s³. In the simulation, the feed drive, lead error (ripple), P-PI axis controller, and AFC model and parameters were the same as those used in Sections 6.5 and 6.7, complying with the corresponding robust stability ($S \leq S_{\max}=2.0$) and performance retention ($\alpha \leq 1.2$) conditions. In evaluating the AFC, the y-axis component of the trajectory was used, as it displays continual velocity variation and sharp acceleration transients in the middle part, when traversing the leading edge of the airfoil shortly after 10 s into the motion.

Figure 6.19 shows the tracking error obtained without and with AFC. The maximum value and standard deviation are summarized in Table 6.5. As can be seen, even when the frequency of the disturbance changes continuously, due to varying velocity, the position-dependent compensation developed in Section 6.5 is still able to achieve significant improvement in the dynamic accuracy. The RMS and MAX error values are reduced by around 58%. Similar to the case of a constant feedrate trajectory (Section 4), there are deteriorations around the friction transition points. Also, as only the first-order term is considered in the compensation per Equations (6.15) and (6.16), AFC naturally loses some of its effectiveness during the high acceleration portion of the trajectory (i.e., tight curvature area).

As described in Section the frequency of the error harmonic disturbance ω_n is approximated as a product of the lead error spatial frequency Ω_n and the traversal speed v_0 . This approximation is effective in implementing the compensation via gain scheduling. It provides suitable instantaneous values for the anticipated error frequency, and the AFC gain and phase values that need to be applied, which would effectively quench the error if the exogenous harmonic input retained the same frequency. However, the transient response of the closed-loop system, under the influence of the AFC, still requires a certain duration to pass before the AFC-targeted error harmonics can be mitigated.

If the rate of change in the harmonic disturbance frequency becomes significant (i.e., during high acceleration movements), a deterioration in the AFC's compensation can be expected, originating mainly from the lag in the transient response governing the AFC's attenuation behavior. In addition, it is clear that gain scheduling of the AFC parameters gain and phase (in a way that satisfies 0th order continuity) may also introduce additional dynamics. These factors would be interesting to study in future research.

Overall, while this simulation example indicates some of the limitations of the position dependent AFC approach, it also highlights that a noticeable improvement can still be achieved in the dynamic accuracy, even in the presence of varying traversal velocity.

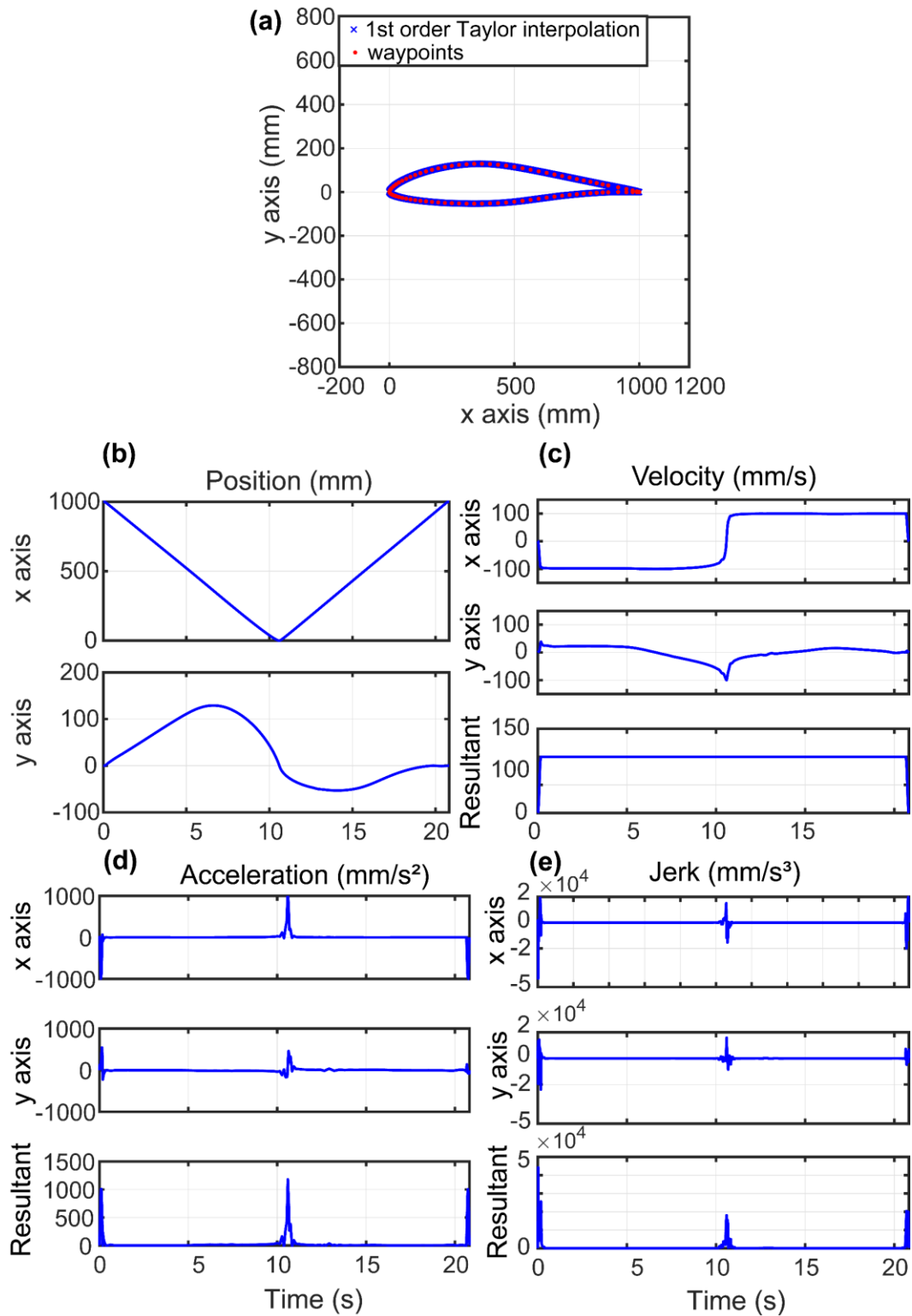


Figure 6.18: Airfoil profile and commanded trajectories for the x- and y-axes.

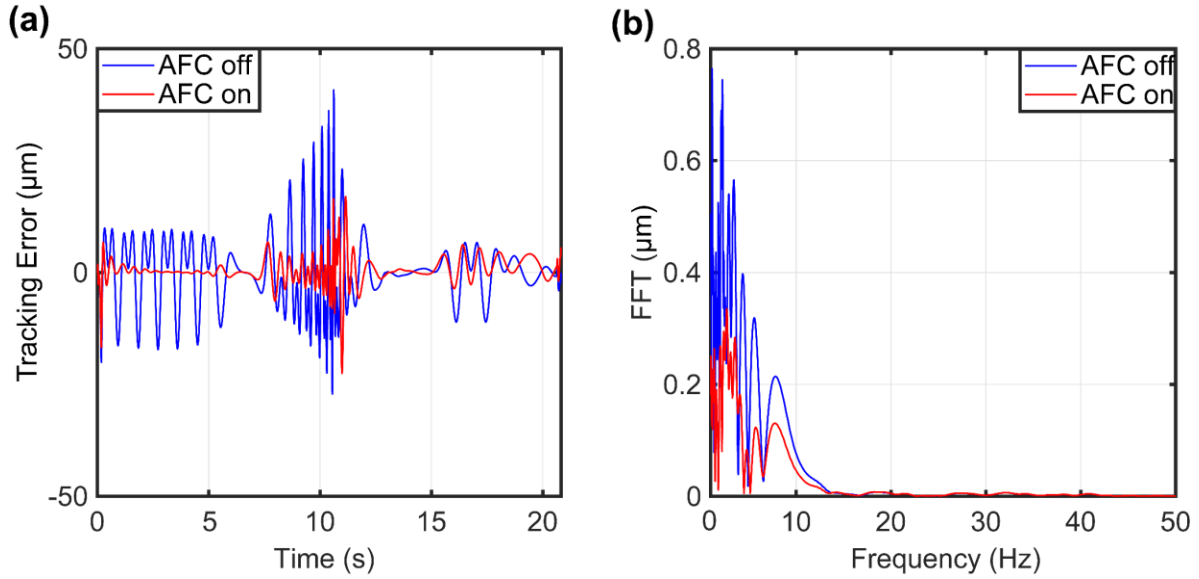


Figure 6.19: Tracking error without (w/o) and with (w/) AFC compensation.

Table 6.5: Summary of the tracking simulation y-axis.

Tracking error (STD) (μm)			Max. tracking error (μm)	
w/o AFC	w/ AFC	%	w/o AFC	w/ AFC
7.6	3.13	58.82	40.8	16.95

6.9. Conclusions

In this chapter, a new methodology for the design of AFC compensators towards reducing harmonic positioning errors in ball-screw drives has been introduced. The AFC has been adapted to suit the dual (i.e., rotational and translational) feedback structure used in machine tool ball-screw drives. The approach takes into account both robust stability and performance retention requirements in the presence of adding AFC resonators into the feedback loop. It is also shown that the reduction of harmonic errors due to different input sources, i.e. the commanded trajectory, motor and load-side disturbances, lead/mechanism errors, and rotational feedback errors, can all be analyzed with respect to a baseline design (before the AFC is added), using a unified parameter named here as the *response modification factor*. The proposed approach enables multiple AFC resonators to be designed and updated simultaneously. The effectiveness of the proposed AFC design has been demonstrated in experimental results involving the mitigation of harmonic servo errors due to position-periodic disturbances, which can originate from the ball-screw mechanism lead and alignment errors.

While in the conducted experiments, actuator saturation did not pose a major problem, future research needs to focus on limiting the output amplitude for each resonator, such that saturation avoidance can be guaranteed. Also, bump-less activation and de-activation of AFC can help make this approach more easily and reliably deployable on industrial ball-screw drives used in machine tools.

Chapter 7

Conclusions and Future Work

7.1. Conclusions

In this thesis, precision modeling, multivariable system identification, and advanced motion control techniques were proposed in order to improve the positioning accuracy and disturbance rejection of machine tool servo systems, with direct implementation results being developed on a ball-screw drive. The main conclusions and contributions of this thesis are summarized as follows:

A new frequency-domain MIMO LTI identification algorithm for accurate model construction of motion control systems was proposed in Chapter 4. The algorithm captures the effect of structural resonances, highly damped complex and real poles, and also enables the inclusion of direct / derivative-like terms (if needed). A key strength of the algorithm is its ability to enforce the commonality of pole locations across all output / input channels. The effectiveness of the algorithm was validated using experimental frequency response measurements obtained from different types of motion control mechanisms (i.e., single axis as well as gantry type ball-screw drives and linear motors). This led to the estimation of MIMO models with output \times input channel sizes of 2×1 , 2×2 , and 4×4 . Furthermore, the proposed method has been benchmarked against two of the most widely used estimation algorithms available in MATLAB software, `tfest` and `modalfit`. The proposed algorithm has demonstrated two order-of-magnitude or better (i.e., 99.55% - 99.67%) improvement over the results obtained with these methods when fitting MIMO models. The developed MIMO model identification algorithm also enabled the second main contribution in this thesis, targeting enhanced disturbance rejection through controller design to actively damp multiple vibration modes.

As the second contribution, presented in Chapter 5, control techniques were proposed for multiple-mode vibration damping and tracking control in feed drive systems using mixed sensitivity $\mathcal{H}_2/\mathcal{H}_\infty$ optimal control in conjunction with loop shaping. The proposed controllers have dual-feedback structure and are synthesized to capture and attenuate not only the principal (axial) vibration mode, but other vibration modes as well, originating from the machine's base frame and interaction of the moving table with the drive's linear guideways. The vibration damping controllers were tuned to minimize the load side disturbance response, by using the corresponding open-loop compliance (i.e. force-to-position response) for the worktable to external (e.g., cutting force) disturbances. Consideration of this transfer function as the inverse sensitivity (i.e., performance) weight enhanced the disturbance rejection over applying a more common filter-type weighting function, that is used typically in mixed sensitivity controller design. This

improvement was verified using experimental impact hammer testing for the proposed and conventional designs.

The performance of the two proposed control laws was compared to the industry-standard P-PI position-velocity cascade controller, and to a vibration damping pole-placement controller (PPC), in terms of disturbance rejection and trajectory tracking. The proposed controllers achieved, on average, 2-3 times better disturbance rejection for wide frequency ranges, and typically 2.5× better damping of the most significant (i.e., axial) vibration mode. The proposed controllers also achieved comparable or better tracking performance in relation to the P-PI and PPC benchmarks, maintaining less than 10 μm of dynamic error during traversals with 420 mm/s velocity and 0.12 g acceleration. While the achievable performance of the proposed designs is impressive, significant amount of expert input was needed to implement these controllers, thus indicating the need for further research and development before they can be effectively and safely used in industry.

As the last contribution, presented in Chapter 6, the analysis and design of adaptive feedforward cancellation (AFC) considering the dual position feedback structure of the ball-screw drives was developed for the suppression of harmonic positioning errors that occur in such mechanisms. A new frequency-dependent parameter, named as the ‘response modification factor α ’ was introduced to allow for quantification of the improvement (or worsening) of the response across all frequencies, after the inclusion of the AFC into an existing feedback control structure. Additionally, a new tuning procedure has been proposed for multi-resonator AFC designs considering robust stability and performance preservation, particularly at frequencies outside those targeted by the AFC resonators. The rejection of position dependent harmonic errors during variable velocity motion was also studied in simulation. Finally, the effectiveness of the proposed design was validated in high-speed tracking experiments, which demonstrated clear improvements in suppressing the expected harmonic components of error. Additional sources of error, especially due to stick-slip friction however, also need to be compensated separately. This can be achieved by following the GMS-based friction compensation, which was demonstrated experimentally in Chapter 3.

7.2. Future Research Directions

The control methods developed in this thesis were proven on a single-axis ball-screw drive. While the LTI designs indicate improvement in disturbance rejection and tracking, the robust control framework can be utilized for defining various uncertainty specifications, both parametric and structural (e.g., unknown dynamics at certain frequency ranges). One of the greatest challenges in the vibration control of structures with very little damping is that small changes in the natural frequency can result in drastic amounts of

relative changes in the plant's gain and phase response, due to the sharpness of these profiles around the resonances. To handle this issue, the suitability of Structured Singular Value (SSV) (μ -) analysis and synthesis methods can be evaluated in the future.

Additionally, multi-degree of freedom motion control systems with mechanical flexibility tend to display different structural properties (i.e., natural frequency, damping, as well as modal stiffness and mass) based on the current posture (i.e., geometric displacements of the axes). Hence, extension of the vibration damping $\mathcal{H}_2 + LS$ and $\mathcal{H}_\infty + LS$ designs to the linear parameter varying (LPV) framework is worth investigating. It is expected that being able to incorporate active damping designs into an LPV framework will enable more aggressive bandwidths and disturbance rejection performance specifications to be achieved, allowing the controllers to be tuned more ambitiously without risking closed-loop destabilization. However, developing LPV based high-order models, with parameters that can be interpolated linearly between different operating points, can be challenging. The controller design would need to consider, for example, stiffness variations in the flexible modes along the screw shaft, based on axis position, or apparent joint level inertia changes felt by actuators as a result of the posture change in different axes, as often encountered in robotics literature. In the time frame of this thesis, the disturbance rejection of the proposed controllers could be tested successfully via impact hammer measurements. However, machining experiments (e.g., via milling) can further validate the effectiveness of the proposed designs over the benchmarked controllers, like P-PI and PPC. A follow-up inspection of the machined part quality, in terms of dimensional accuracy and surface finish, would also provide insight into the benefits that can be gained with the proposed approach.

Another potential study is the design of controllers with different choice of feedback sensors in cases where multiple actuation and measurement points are available, and structural resonances due to the machine tool are prevalent. Some examples include gantry drives, as well as ram- and column-type multiple tool structures. Especially if integrated position, velocity, and acceleration sensors are available within the machine tool, the generalized MIMO model identification and vibration damping methods developed in this thesis can potentially be applied on such systems.

Regarding the positioning accuracy improvement by AFC, actuator saturation as a limiting factor can be studied and included when implementing the multi-resonator design, which targets multiple frequency components. Another idea would be to use a blended approach of model-based (feedforward) and feedback-based (AFC) compensation, with a suitable adaptation or 'learning' algorithm to coordinate the two components. Also, the use of AFC in the context of multiple axes would be interesting to investigate.

Bibliography

- [1] B. Sencer, K. Ishizaki, "Smooth polynomial interpolation for point-to-point trajectories with vibration avoidance", *IECON*, Yokohama, Nov. 9-12, 2015.
- [2] A. Dumanli, B. Sencer, "Robust trajectory generation for multi-axis vibration avoidance", *IEEE/ASME Transactions on Mechatronics*, vol. 14, no. 8, pp. 1-11, 2020.
- [3] G. Ellis, Z. Gao, "Cures for low-frequency mechanical resonance in industrial servo systems", *IEEE Industrial Applications Conference, 36th IAS Annual Meeting*, vol. 1, pp. 252-258, 2001.
- [4] K. Erkorkmaz, Y. Altintas, "High speed CNC system design. Part II: Modeling and identification of feed drives," *International Journal of Machine Tools and Manufacture*, vol. 41, no. 10, pp. 1487-1509, 2001.
- [5] K. Erkorkmaz, W. Wong, "Rapid identification technique for virtual CNC drives", *International Journal of Machine Tools and Manufacture*, vol. 47, pp. 1381-1392, 2007.
- [6] W. Wong, K. Erkorkmaz, "Constrained identification of virtual CNC drives using a genetic algorithm", *International Journal of Advanced Manufacturing Technology*, vol. 50, pp. 275-288, 2010.
- [7] B. Sencer, Y. Altintas, "Identification of 5-axis machine tools feed drive systems for contouring simulation", *Proceedings of 4th CIRP Conference on High Performance Cutting*, 2010.
- [8] A. Kamalzadeh, K. Erkorkmaz, "Compensation of axial vibrations in ball-screw drives," *Annals of the CIRP*, vol. 56, no.1, pp. 373-378, 2007.
- [9] K. Sato, G. J. Maeda, "A practical control method for precision motion: Improvement of NCTF control method for continuous motion control", *Precision Engineering*, vol. 33, no. 2, pp. 175-186, 2009.
- [10] F. Hakoda, Y. Sone, and A. Yamauchi, "Sliding mode control with frequency-shaped hyper-plane for a ball-screw driving stage", *Journal of System Design and Dynamics*, vol. 3, no.1, pp. 25-36, 2009.
- [11] K. Sakata, H. Fujimoto, and K. Saiki, "Positioning of large-scale high-precision stage with vibration suppression PTC", *Proceedings of 17th IFAC World Congress*, Seoul, Korea, pp.3124-3129, 2008.
- [12] L. Dong, W. C. Tang, "Adaptive backstepping sliding mode control of flexible ball-screw drives with time-varying parametric uncertainties and disturbances", *ISA Transactions*, vol. 53, no.1, pp. 110-116, 2014.
- [13] M. H. Richardson, D. L. Formenti, "Parameter estimation from frequency response measurements using rational fraction polynomials", *In Proceedings of the 1st International Modal Analysis Conference*, pp. 167-181, Orlando, USA, 1982.
- [14] M. H. Richardson, D. L. Formenti, "Global curve fitting of frequency response measurements using the rational fraction polynomial method", *In Proceedings of the 3rd International Modal Analysis Conference*, pp. 390-397, Orlando, USA, 1985.

- [15] A. Vicente, R. Hecker, and G. Flores, “Ball-screw drive systems: Evaluation of axial and torsional deformations”, *Asociación Argentina de Mecánica Computacional*, vol. XXVIII, pp. 3265–3277, 2009.
- [16] K. K. Varansani, S. Nayfeh, “The dynamics of lead-screw drives: Low order modelling and experiments”, *Journal of Dynamic System Measurement and Control*, vol. 126, pp. 388-396, 2004.
- [17] R. Whalley, M. Ebrahimi, and A. A. Abdul-Ameer, “Hybrid modelling of machine tool axis drives”, *International Journal of Machine Tools and Manufacture*, vol. 45, no. 14, pp. 1560–1576, 2005.
- [18] S. Frey, A. Dadalau, and A. Verl, “Expedient modeling of ball-screw feed drives”, *Production Engineering*, vol. 6, pp. 205-211, 2012.
- [19] D. A. Vicente, R. L. Hecker, F. J. Villegas, and G. M. Flores, “Modeling and vibration mode analysis of a ball-screw drive”, *International Journal of Machine Tools and Manufacture*, vol. 58, pp. 257–265, 2012.
- [20] L. Dong, W. C. Tan, “Hybrid modeling and analysis of structural dynamic of a ball-screw feed drive system”, *Mechanika*, vol. 19, no. 3, pp. 316-323, 2013.
- [21] M. F. Zaeh, Th. Oertli, J. Milberg, “Finite element modelling of ball-screw feed drive systems,” *CIRP Annals-Manufacturing Technology*, vol. 53, pp. 289-292, 2004.
- [22] C. E. Okwudire, Y. Altintas, “Hybrid modeling of ball-screw drives with coupled axial torsional, and lateral dynamics,” *Journal of Mechanical Design*, vol. 131, no. 7, pp. 071002-1-9, 2009.
- [23] M. Weck, P. Krüger, and C. Brecher, “Limits for controller settings with electric linear direct drives”, *International Journal of Machine Tools and Manufacture*, vol. 41, pp. 65-88, 2001.
- [24] D. J. Ewins *Modal Testing: Theory, Practice and Application*. Baldock, Hertfordshire, England: Research Studies Press, 2000.
- [25] S. Skogestad, I. Postlethwaite, *Multivariable feedback control: analysis and design*. 2nd ed. Wiley; 2005.
- [26] M. H. Turhan, G. W. Tseng, K. Erkorkmaz, B. Fidan, “Dynamic model identification for CNC machine tool feed drives from in-process signals for virtual process planning,” *Mechatronics*, vol. 72, 102445, 2020.
- [27] G. W. G. Tseng, C. Q. G. Chen, K. Erkorkmaz, S. Engin, “Digital shadow identification from feed drive structures for virtual process planning,” *CIRP Journal of Manufacturing Science and Technology*, vol. 24, pp. 55-65, 2019.
- [28] S. Kehne, T. Berners, A. Epple, C. Brecher, “Automatic system identification of forward feed drives in machine tools,” *Advances in Production Research: Proceedings of the 8th Congress of the German Academic Association for Production Technology (WGP)*, pp. 144 – 152, 2019.
- [29] System Identification Toolbox. The MathWorks In., Natick MA.
- [30] A. A. Ozdemir, S. Gumussoy, “ Transfer function estimation in System Identification Toolbox via vector fitting,” *IFAC-PapersOnLine*, vol. 50, no. 1, pp. 6232-6237, July 2017.

- [31] Signal Processing Toolbox. The MathWorks In., Natick MA.
- [32] C. Sanathanan, J. Koerner, “Transfer function synthesis as a ratio of two complex polynomials,” *IEEE Transactions on Automatic Control*, vol. 8, no. 1, pp. 56–58, 1963.
- [33] R. Van Herpen, T. Oomen, M. Steinbuch, “Optimally conditioned instrumental variable approach for frequency-domain system identification,” *Automatica*, vol. 50, no. 9, pp. 2281–2293, 2014.
- [34] L. Ljung, R. Singh, “Version 8 of the System Identification Toolbox,” *Proceedings of the 16th IFAC Symposium on System Identification*, The International Federation of Automatic Control, Brussels, Belgium, July 11-13, 2012.
- [35] F. Al-Bender, V. Lampaert, and J. Swevers, “The generalized Maxwell slip model: A novel model for friction simulation and compensation,” *IEEE Transactions on Automatic Control*, vol. 50, no. 11, pp. 1883–1887, 2005.
- [36] P. Dahl. “A solid friction model”, *Technical Report TOR-0158*, (3107–18)-1, Aerospace Corporation, El Segundo, CA, 1968.
- [37] C. Canudas, H. Olsson, K. J. Åström, and P. Lischinsky, “A new model for control of systems with friction”, *IEEE Transactions on Automatic Control*, vol. 40, no. 3, pp. 419-425, 1995.
- [38] J. Swevers, F. Al-Bender, G. Ganseman, T. Prajogo, “An integrated friction model structure with improved presliding behavior for accurate frictional compensation”, *IEEE Transactions on Automatic Control*, vol. 45, pp. 675–686, 2000.
- [39] V. Lampaert, J. Swevers, and F. Al-Bendar, “Modification of the Leuven integrated friction model structure”, *IEEE Transactions on Automatic Control*, vol. 47, no. 4, 2002.
- [40] Z. Jamaludin, “Disturbance compensation for machine tools with linear motor drives”, Ph.D. thesis, Katholieke Universiteit Leuven, 2008.
- [41] S. Fukada, B. Fang, A. Shigeno, “Experimental analysis and simulation of nonlinear microscopic behavior of ball-screw mechanism for ultra-precision positioning”, *Precision Engineering*, vol. 35, pp. 650-668, 2011.
- [42] X. C. Xi, A. N. Poo, and G. S. Hong, “Tracking error-based static friction compensation for a bi-axial CNC machine”, *Precision Engineering*, vol. 34, pp. 480-488, 2010.
- [43] J. Y. Yoon and D. L. Trumper, “Friction modeling, identification, and compensation based on frictionhysteresis and Dahl resonance,” *Mechatronics*, vol. 24, pp. 734-741, 2014.
- [44] J. Y. Yoon and D. L. Trumper, “Friction micro-dynamics in the time and frequency domains: Tutorial on frictional hysteresis and resonance in precision motion systems,” *Precision Engineering*, vol. 55, pp. 101–109, 2019.
- [45] X. Lu, “Electromagnetically-driven ultra-fast tool servos for diamond turning,” Ph.D. dissertation M.I.T., Cambridge, MA, USA, 2005.
- [46] M. Crudele, T. R. Kurfess, “Implementation of a fast tool servo with repetitive control for diamond turning”, *Mechatronics*, vol. 13, no. 3, pp. 243-257, 2003.

- [47] Y. Mizoshita, S. Hasegawa, and K. Takaishi, "Vibration minimized access control for disk drives", *IEEE Transactions on Magnetics*, vol. 32, no. 3, pp. 1793-1798, 1996.
- [48] S. Nakagawa, T. Yamaguchi, H. Fujimoto, Y. Hori, K. Ito, and Y. Hata, "Multi-rate two-degree-of-freedom control for fast and vibration-less seeking of hard disk drives", *Proceedings of the American Control Conference*, Arlington, VA, June 2001.
- [49] T. Semba, M. T. White, "Seek control to suppress vibrations of hard disk drives using adaptive filtering", *IEEE/ASME Transactions on Mechatronics*, vol. 13, no. 5, pp. 502-509, 2008.
- [50] Z. Mohamed, M.O. Tokhi, "Command shaping techniques for vibration control of a flexible robot manipulator", *Mechatronics*, vol. 14, pp. 69-90, 2004.
- [51] S.K. Tso, T.W. Yang, W. L. Xu, and Z.Q. Sun, "Vibration control for a flexible-link robot arm with deflection feedback", *International Journal of Non-linear Mechanics*, vol. 38, pp. 51-62, 2003.
- [52] E. Omid, S. N. Mahmoodi, "Vibration control of collocated smart structures using H_∞ modified positive position and velocity feedback", *Journal of Vibration and Control*, vol. 22, no. 10, pp. 2434-2442, 2014.
- [53] V. Utkin, "Variable structure systems with sliding modes", *IEEE Transactions on Automatic Control*, vol. 22, no.2, pp. 212-222, 1977.
- [54] D. Dumur, P. Boucher, and G. Ramond, "Direct adaptive generalized predictive control. Application to motor drives with flexible modes", *CIRP Annals Manufacturing Technology*, vol. 49, no. 1, pp. 271-274, 2000.
- [55] M. Cychowski, K. Szabat, and T. O. Kowalska, "Constrained model predictive control of the drive system with mechanical elasticity", *IEEE Transactions on Industrial Electronics*, vol. 56, no. 6, 2009.
- [56] M. Makarov, M. Grossard, P. R. Ayerbe, and D. Dumur, "Active damping strategy for robust control of a flexible-joint lightweight robot", *IEEE International Conference on Control Applications (CCA)*, Oct. 3-5, Dubrovnik, Croatia, 2012.
- [57] C. J. Goh, T. K. Caughey, "On the stability problem caused by finite actuator dynamics in the control of large space structures", *International Journal of Control*, vol. 41, pp.787-802, 1985.
- [58] M. O. T. Cole, T. Wongratanaphisan, "A direct method of adaptive FIR input shaping for motion control with zero residual vibration", *IEEE/ASME Transactions on Mechatronics*, vol. 18, no. 1, pp. 316-327, 2013.
- [59] S. Krzysztof, T. O. Kowalska, "Vibration suppression in a two-mass drive system using PI speed controller and additional feedbacks-comparative study", *IEEE Transactions on Industrial Electronics*, vol. 54, no. 2, pp. 1193-1206, 2007.
- [60] J. Swevers, M. Adams, J. D. Schutter, H. V. Brussel, and H. Thielemans, "Limitations of linear identification and control techniques for flexible robots with nonlinear joint friction", *Proc. 1st Int. Symp. on Experimental Robotics*, June 19-21, 1989, Montreal, Canada.

- [61] Y. Altintas, M. R. Khoshdarregi, “Contour error control of CNC machine tools with vibration avoidance”, *CIRP Annals-Manufacturing Technology*, vol. 61, no. 1, pp. 335–338, 2012.
- [62] X. Beudaert, A. Barrios, K. Erkorkmaz and J. Munoa, “Limiting factors for the active suppression of structural chatter vibrations using the machine's drives”, *XIIth International Conference of High Speed Machining*, Nanjing, China, 2015.
- [63] X. Beudaert, O. Franco, K. Erkorkmaz, M. Zatarain, “Feed drive control tuning considering machine dynamics and chatter”, *CIRP Annals- Manufacturing Technology*, vol. 69, 345-348, 2020.
- [64] J. Slotine, L. Weiping, “Adaptive manipulator control: A case study”, *IEEE Transactions on Automatic Control*, vol. 33, no. 11, pp. 995-1003, 1998.
- [65] Y. Altintas, K. Erkorkmaz, W. H. Zhu, “Sliding mode controller design for high speed feed drives”, *CIRP Annals – Manufacturing Technology*, vol. 49, pp. 265-270, 2000.
- [66] K. Erkorkmaz and A. Kamalzadeh, “High bandwidth control of ball-screw drives,” *CIRP Annals-Manufacturing Technology*, vol. 55, no. 1, pp. 393–398, 2006.
- [67] C. Okwudire, Y. Altintas, “Minimum tracking error control of flexible ball-screw drives using a discrete-time sliding mode controller”, *Journal of Dynamic Systems, Measurement, and Control*, 131:051006, 2009.
- [68] A. H. H. Hosseinabadi, Y. Altintas, “Modeling and active vibration damping of structural vibrations in machine tools”, *CIRP Journal of Manufacturing Science and Technology*, vol. 7, pp. 246-257, 2014.
- [69] K. Aström, B. Wittenmark, “Computer-controlled systems: Theory and design”, *Prentice Hall, Upper Saddle River, NJ, USA*, 1997.
- [70] J. Kautsky, N. K. Nichols, and P. V. Dooren, “Robust pole assignment in linear state feedback”, *International Journal of Control*, vol. 41, no. 5, pp. 1129-1155, 1985.
- [71] K. Erkorkmaz, Y. Hosseinkhani, “Control of ball-screw drives based on disturbance response optimization,” *Annals of CIRP*, vol. 62, no.1, pp. 387–390, 2013.
- [72] D. J. Gordon, K. Erkorkmaz, “Accurate control of ball-screw drives using pole-placement vibration damping and a novel trajectory pre-filter,” *Precision Engineering*, vol. 37, no. 2, pp. 308-322, 2013.
- [73] Y. Hosseinkhani, “Control methods for improving tracking accuracy and disturbance rejection in ball-screw drives”, Ph.D. thesis, University of Waterloo, 2014.
- [74] D. McFarlane, K. Glover, “A loop-shaping design procedure using \mathcal{H}_∞ synthesis”, *IEEE Transactions on Automatic Control*, vol. 37, no. 6, pp. 759-769, 1992.
- [75] Y. Li, F. Marcassa, R. Horowitz, R. Oboe, R. Evans, “Track-following control with active vibration damping of a PZT-actuated suspension dual-stage servo system”, *Proceedings of the 2003 American Control Conference*, vol.3, pp. 2553-2559, 2003.
- [76] B. M. Moghaddam, Robin Chhabra, “On the guidance, navigation and control of in-orbit space robotic missions: A survey and prospective vision”, *Acta Astronautica*, vol. 184, pp. 70-100, 2021.

- [77] L. Chrif, Z. M. Kadda, “Aircraft control system using LQG and LQR controller with optimal estimation-Kalman filter design”, *Procedia Engineering*, vol. 80, no.2, pp. 245-257, 2014.
- [78] S. Jeon, H. J. Ahn, D. C. Han, “Model validation and controller design for vibration suppression of flexible rotor using AMB”, *KSME International Journal*, vol. 16, no. 12, pp. 1583-1593, 2002.
- [79] W. K. Gawronski, *Advanced structural dynamics and control of structures*, Springer New York: Springer-Verlag, 2004.
- [80] B. Sencer, A. Dumanli, “Optimal control of flexible drives with load side feedback”, *CIRP Annals*, vol. 66, pp. 357-360, 2017.
- [81] A. Dumanli, B. Sencer, “Optimal high-bandwidth control of ball-screw drives with acceleration and jerk feedback”, *Precision Engineering*, vol. 54, pp. 254-268, 2018.
- [82] G. Zames, “Feedback and optimal sensitivity: Model reference transformations, multiplicative seminorms, and approximate inverses”, *IEEE Transactions Automation Control*, vol. 26, pp. 301–320, 1981.
- [83] A. A. Stoorvogel, “The \mathcal{H}_∞ Control problem a state space approach”, Ph.D. Dissertation, Technical University Eindhoven, 1990.
- [84] K. Itoh, M. Iwasaki, and N. Matsui, “Robust fast and precise positioning of ball-screw-driven table system on machine stand”, *AMC '04. The 8th IEEE International Workshop on Advanced Motion Control*, 2004.
- [85] N. Wang, W. Lin, “Robust tracking control of AC servo system including a ball-screw”, *Neurocomputing*, vol. 179, pp. 110-117, 2016.
- [86] P. V. D. Braembussche, J. Swevers H. V. Brussel, “Design and experimental validation of robust controllers for machine tool drives with linear motor”, *Mechatronics*, vol. 11, pp. 545-562, 2001.
- [87] L. Dong, W. C. Tang, and D. Bao, “Interpolating gain-scheduled loop shaping design for high speed ball-screw feed drives”, *ISA Transactions*, vol. 55, pp. 219-226, 2015.
- [88] M. Hanifzadegan, R. Nagamune, “Switching gain-scheduled control design for ball-screw drives”, *Journal of Dynamic Systems, Measurement, and Control*, vol. 136, pp. 014503-014503-6, 2014.
- [89] M. Hanifzadegan, R. Nagamune, “Tracking and structural vibration control of flexible ball-screw drives with dynamic variations”, *IEEE/ASME Transactions on Mechatronics*, vol. 20, no. 1, pp. 133-142, 2015.
- [90] J. Q. C. Zeng, “Controller design for active vibration damping with inertial actuators”, M.Sc. thesis, University of Waterloo, 2019.
- [91] J. Hwang, E. S. Chung, “In-process cutter run-out compensation using repetitive learning control,” *International Journal of Precision Engineering and Manufacturing*, vol. 4, no.4, pp. 13-8, 2003.
- [92] S. J. Ludwick, D. A. Chargin, J. A. Calzaretta, D. L. Trumper, “Design of a rotary fast tool servo for ophthalmic lens fabrication,” *Precision Engineering*; vol. 23, no. 4, pp. 253-259, 1999.

- [93] X. D. Lu, D. L. Trumper, "Ultrafast tool servos for diamond turning," *Annals of the CIRP*, vol. 54, no. 1, pp. 383–388, 2005.
- [94] J. H. Kim, S. K. Lee, "Micro-patterning technique using a rotating cutting tool controlled by an electromagnetic actuator," *International Journal of Machine Tools and Manufacture*, vol. 101, pp. 52-64, 2016.
- [95] K. Chew, M. Tomizuka, "Digital control of repetitive errors in disk drive systems," *IEEE Control Systems Magazine*, vol. 10, no. 1, pp. 16-20, 1990.
- [96] Y. Onuki, H. Ishioka, "Compensation for repeatable tracking errors in hard drives using discrete-time repetitive controllers," *IEEE/ASME Transactions on Mechatronics*; vol. 6, no. 2, pp. 132-136, 2001.
- [97] C. Cosner, G. Anwar, M. Tomizuka, "Plug in repetitive control for industrial robotic manipulators," *In: Proceedings of IEEE International Conference on Robotics and Automation 1990, Cincinnati, OH, USA*, vol. 3 pp. 1970-1975, 1990.
- [98] B. A. Francis, W. M. Wonham, "The internal model principle of control theory," *Automatica*, vol. 12, no. 5, pp. 457-465, 1976.
- [99] S. Hara, Y. Yamamoto, T. Omata, M. Nakano, "Repetitive control system: A new type servo system for periodic exogenous signals," *IEEE Transactions on Automatic Control*, vol. 33, no. 7, pp. 659-668, 1988.
- [100] G. Weiss, Repetitive control systems: Old and new ideas. In: *Systems and Control in the 21st Century*, Springer, Boston, MA, USA, pp. 389-404, 1997.
- [101] Z. Jamaludin, "Disturbance compensation for machine tools with linear motor drives," Ph.D. dissertation, Katholieke Universiteit Leuven, Leuven, Belgium, 2008.
- [102] Joseph H. Cattell, "Adaptive feedforward cancellation viewed from an oscillator amplitude control perspective," Master of Science Thesis, Department of Mechanical Engineering, Massachusetts Institute of Technology, Cambridge, MA, 2003.
- [103] C. Kempf, W. Messner, M. Tomizuka, R. Horowitz, "Comparison of four discrete-time repetitive control algorithms," *IEEE Control Systems*, vol. 13, no. 6, pp. 48-54, 1993.
- [104] W. Messner, M. Bodson, "Design of adaptive feedforward algorithms using internal model equivalence," *International Journal of Adaptive Control and Signal Processing*, vol. 9 no. 2, pp. 199-212, 1995.
- [105] M. Bodson, A. Sacks, P. Khosla, "Harmonic generation in adaptive feedforward cancellation schemes," *IEEE Transactions on Automatic Control*, vol. 39, no. 9, pp. 1939-1944, 1994.
- [106] S. J. Ludwick, "A rotary fast tool servo for diamond turning of asymmetric Optics," Ph.D. dissertation, Massachusetts Institute of Technology, Cambridge, MA, 1999.
- [107] M. F. Byl, S. J. Ludwick, D. L. Trumper, "A loop-shaping perspective for tuning controllers with adaptive feedforward cancellation," *Precision Engineering*, vol. 29, no. 1, 27-40, 2005.

- [108] X. Guo, M. Bodson, “Equivalence between adaptive feedforward cancellation and disturbance rejection using the internal model principle,” *International Journal of Adaptive Control and Signal Processing*; vol. 24, no. 3, pp. 211-218, 2010.
- [109] S. Yabui, A. Okuyama, T. Atsumi, M. Odai, “Development of optimized adaptive feed-forward cancellation with damping function for head positioning system in hard disk drives,” *Journal of Advanced Mechanical Design, Systems, and Manufacturing*, vol. 7, no. 1, pp. 39-51, 2013.
- [110] S. Yabui, I. Kajiwara, R. Okita, “Robustness analysis of enhanced adaptive feed-forward cancellation,” *Journal of Advanced Mechanical Design, Systems, and Manufacturing*, vol. 8, no. 1, pp. 1-12, 2014.
- [111] Y. Hosseinkhani, K. Erkorkmaz, “Harmonic disturbance rejection in tracking control of ball-screw drives,” *Proceedings of the 26th ASPE Annual Meeting*. 2011.
- [112] H. K. Shirvani, Y. Hosseinkhani, K. Erkorkmaz, “Suppression of harmonic positioning errors in ball-screw drives using adaptive feedforward cancellation,” *Precision Engineering*, vol. 68, pp. 235-255, 2021.
- [113] J. Schoukens, R. Pintelon, Y. Rolain, and T. Dobrowiecki, “Frequency response function measurements in the presence of nonlinear distortions”, *Automatica*, vol. 37, pp. 939-946, 2001.
- [114] J. Schoukens, J. Swevers, R. Pintelon, and H. V. D. Auweraer, “Excitation design for FRF measurements in the presence of non-linear distortions”, *Mechanical Systems and Signal Processing*, vol. 18, pp. 727-738, 2004.
- [115] T. Riel, R. Saathof, A. Katalenic, S. Ito, G. Schitter, “Noise analysis and efficiency improvement of a pulse-width modulated permanent magnet synchronous motor by dynamic error budgeting”, *Mechatronics*, vol. 50, pp. 225-233, 2018.
- [116] F. Blaschke, “A New method for the structural decoupling of AC induction machines,” *Proceedings of the 2nd Symposium on Multivariable Technical Control Systems (IFAC)*, Dusseldorf, Germany; vol. 1, pp. 1-15, 1971.
- [117] I. Takahashi, and Y. Ohmori, “High-performance direct torque control of an induction motor,” *IEEE Transactions on Industry Applications*, vol. 25, no. 2, pp. 257-264, 1989.
- [118] P. Krause, O. Wasynczuk, S. D. Sudhoff, and S. Pekarek. *Analysis of Electric Machinery and Drive Systems*. Piscataway, NJ: Wiley-IEEE Press, 2013.
- [119] W.A. Gardner, *Introduction to random processes: with applications to signals and systems*. McGraw-Hill Companies, 1990.
- [120] P. D. Welch, “The Use of Fast Fourier Transform for the Estimation of Power Spectra: A Method Based on Time Averaging Over Short, Modified Periodograms”, *IEEE® Transactions on Audio and Electroacoustics*. vol. AU-15, pp. 70–73, 1967.
- [121] R. Pintelon, J. Schoukens, *System identification. A frequency domain approach*. 2nd Ed. Wiley, Hoboken, 2012.

- [122] R.E. Kalman, "A new approach to linear filtering and prediction problems," *Journal of Basic Engineering*; vol. 82, pp. 35-44, 1960.
- [123] B. Peeters, H. V. D. Auweraer, P. Guillaume, and J. Leuridan, "The PolyMAX frequency-domain method: a new standard for modal parameter estimation?," *Shock and Vibration*, vol. 11, pp. 395-409, 2004.
- [124] A. Okyay, K. Erkorkmaz, M. B. Khamesee, "Modal analysis, metrology, and error budgeting of a precision motion stage," *Journal of Manufacturing and Materials Processing*, vol. 2, no.1, 8, 2018.
- [125] Y. Altintas, A. Verl, C. Brecher, L. Uriarte, G. Pritschow, "Machine tool feed drives," *CIRP Annals*, vol. 60, no. 2, pp. 779-796, 2011.
- [126] C. P. Wang, K. Erkorkmaz, J. McPhee, S. Engin, "In-process digital twin estimation for high-performance machine tools with coupled multibody dynamics," *CIRP Annals-Manufacturing Technology*, vol. 69, pp. 321-324, 2020.
- [127] G. F. Franklin, J. D. Powell, A. Emami-Naeini, *Feedback control of dynamic systems*. 5th Ed. Prentice Hall; 2005.
- [128] L. Ljung, *System identification: theory for the user*, 2nd Ed. Prentice-Hall, Englewood Cliffs, 1998.
- [129] Global Optimization Toolbox. The MathWorks In. Natick, MA.
- [130] D. Gordon, K. Erkorkmaz, "Precision control of a T-type gantry using sensor/actuator averaging and active vibration damping," *Precision Engineering*, vol. 36, no. 2, pp. 299-314, 2012.
- [131] P. M. J. Van den Hof, R. J. P. Schrama, "An indirect method for estimation from closed-loop data," *Automatica*, vol. 29, no. 6, pp. 1523-1527, 1993.
- [132] P. Van den Hof, "Closed-loop issues in system identification," *Annual Reviews in Control*, vol. 22, pp. 173-186, 1998.
- [133] K. Erkorkmaz, Y. Altintas, "High speed CNC system design. Part III: high speed tracking and contouring control of feed drives," *International Journal of Machine Tools and Manufacture*, vol. 41, no. 11, pp.1637-1658, 2001.
- [134] P. I. Ro, W. Shim, S. Jeong, "Robust friction compensation for submicrometer positioning and tracking for a ball-screw-driven slide system," *Precision Engineering*, vol. 24, no. 2, pp. 160-173, 2000.
- [135] J. Munoa, I. Mancisidor, N. Loix, L. G. Uriarte, R. Barcena, M. Zatarain, "Chatter suppression in ram type travelling column milling machines using a biaxial inertial actuator," *CIRP Annals*, vol. 62, no. 1, pp. 407-410, 2013.
- [136] G.H. Ellis, *Control system design guide: A practical guide*, Elsevier Academic Press, Boston, MA, USA, 2004.
- [137] K. Glover, and J. C. Doyle, "State-space formulae for all stabilizing controllers that satisfy an H_{∞} norm bound and relations to risk sensitivity," *Systems & Control Letters*, vol. 11, pp. 167-172, 1988.

- [138] J. C. Doyle, K. Glover, P. Khargonekar, and B. Francis, "State-space solutions to standard H₂ and H_∞ control problems," *IEEE Transactions on Automatic Control*, vol. 34, no. 8, pp. 831–847, 1989.
- [139] K. Zhou, J. C. Doyle, and K. Glover, *Robust and optimal control*. Englewood Cliffs, NJ, USA: Prentice-Hall, 1996.
- [140] Robust Control Toolbox. The MathWorks In., Natick MA.
- [141] A. Varga, "Balancing-free square-root algorithm for computing singular perturbation approximations," *Proceedings of the 30th IEEE Conference on Decision and Control*, Brighton, UK, 11-13 December 1991.
- [142] A. Kamalzadeh, K. Erkorkmaz, "Accurate tracking controller design for high speed drives," *International Journal of Machine Tools and Manufacture*, vol. 47, no. 9, pp. 1393–400, 2007.
- [143] N. A. Qamar, C. J. Hatziaioniu, "Cancellation of selected stator harmonics in BLDC by using an adaptive feedforward controller," *Electric Power Systems Research*, vol. 154, pp. 88-94, 2018.
- [144] B. Sencer, E. Shamoto, "Effective torque ripple compensation in feed drive systems based on adaptive sliding mode controller," *IEEE/ASME Transactions on Mechatronics*, vol. 19, no. 6, pp. 1764-1772, 2014.
- [145] X. Yang, D. Lu, J. Zhang, W. Zhao, "Investigation on the displacement fluctuation of the linear feed drive system considering the linear encoder vibration," *International Journal of Machine Tools & Manufacture*, vol. 98, pp. 33-40, 2015.
- [146] I. Alejandre, M. Artés, "Method for the evaluation of optical encoders performance under vibration," *Precision Engineering*, vol. 31, pp. 114–121, 2007.
- [147] J. López, M. Artés, I. Alejandre, "Analysis of optical linear encoder's errors under vibration at different mounting conditions," *Measurement*, vol. 44, pp. 1367–1380, 2011.
- [148] M. Tomizuka, "Zero phase error tracking algorithm for digital control," *ASME Journal of Dynamic Systems, Measurement, and Control*, vol. 109, no. 1, pp. 65-8, 1987.
- [149] J. F. Cuttino, T. A. Dow, B. F. Knight, "Analytical and experimental identification of nonlinearities in a single-nut preloaded ball-screw," *ASME Journal of Mechanical Design*, vol.119, pp. 15-19, 1997.
- [150] Retrieved from <https://m-selig.ae.illinois.edu>
- [151] K. Erkorkmaz, Y. Altintas, "Quintic spline interpolation with minimal feed fluctuation," *ASME Journal of Manufacturing Science & Engineering*, vol. 127, no. 2, pp. 339-349, 2005.

Appendices

Appendix A.1

Summary of the Identified Parameters for the Y-Axis of the T-Type Gantry (MIMO)

Table A.1.1: Summary of identified pole locations for the y-axis gantry before and after nonlinear optimization.

k	Step 5: Linear LS fit (RMS(E) = 0.0015 mm/V)			Step 6: Nonlinear optimization + linear LS (RMS(E) = 0.0010 mm/V)		
	ω_k (Hz)	ζ_k	p_k (Hz)	ω_k (Hz)	ζ_k	p_k (Hz)
1	0.7725	0.0367	0.4122	0.6054	0.0439	1.158
2	0.7958	0.23	-	0.3559	0.5953	-
3	96.0514	0.0463	-	93.4028	0.0370	-
4	105.5881	0.0475	-	97.8552	0.0532	-
5	217.0555	0.0345	-	10.7554	0.0618	-
6	227.2733	0.0059	-	124.4146	0.0067	-
7	303.4766	0.0352	-	328.0024	0.0719	-
8	321.0633	0.0205	-	304.9090	0.0342	-
9	369.7806	0.0529	-	3696.4	0.1124	-
10	373.2661	0.0606	-	375.8603	0.0216	-
11	485.9478	0.0361	-	558.4906	0.0511	-

Table A.1.2: Summary of the identified participation factors after Step 6: Nonlinear optim. + LS fit
($T_{delay} = 1$ ms).

Input/output channels	Input #1 Left-hand actuation					Input #2 Right-hand actuation				
	k	α_k	β_k	γ_k	δ_k	k	α_k	β_k	γ_k	δ_k
	1	-4.2765	-50.433	38.77	-	1	-44.0730	-42.8472	44.97	-
	2	594.8513	11.8146	-	-	2	643.4440	-2.0155	-	-
	3	99.3734	0.2708	-	-	3	-298.3519	-0.1973	-	-
	4	581.7626	-0.2656	-	-	4	-693.4306	0.1310	-	-
Output #1	5	5.2842	0.0273	-	-	5	4.1450	0.0265	-	-
Left-hand	6	-0.0798	-4.4e-04	-	-	6	0.2471	0.0022	-	-
linear	7	320.7744	0.1597	-	-	7	433.4434	0.0565	-	-
encoder	8	76.5300	0.0395	-	-	8	20.8878	0.0021	-	-
	9	1.6418e+05	-16.774	-	-	9	-1.844e+05	132.3665	-	-
	10	234.4709	0.0909	-	-	10	103.8694	0.0695	-	-
	11	-470.4945	0.0206	-	-	11	3.7402e+03	-0.6567	-	-
	k	α_k	β_k	γ_k	δ_k	k	α_k	β_k	γ_k	δ_k
	1	-26.8775	-52.30	40.08	-	1	-13.3100	-40.25	43.17	-
	2	628.3018	12.3646	-	-	2	597.7111	-2.815	-	-
	3	-139.6877	-0.3908	-	-	3	436.1143	0.3343	-	-
	4	-879.0439	0.3407	-	-	4	1.0074e+03	-0.157	-	-
Output #2	5	5.1913	0.0269	-	-	5	4.0760	0.0270	-	-
Right-hand	6	-1.1185	4.79e-4	-	-	6	-2.9589	-0.003	-	-
linear	7	621.0314	0.1644	-	-	7	241.2479	0.151	-	-
encoder	8	36.7284	0.0081	-	-	8	64.4772	0.025	-	-
	9	-2.08e+04	92.9744	-	-	9	2.4686e+04	-52.92	-	-
	10	136.3533	0.1576	-	-	10	85.3106	0.0865	-	-
	11	426.5035	-0.4931	-	-	11	231.2455	0.4425	-	-

Appendix A.2

Summary of the Identified Parameters for the X-Axis of the T-Type Gantry (SISO)

Table A.2.1: Summary of identified pole locations for the x-axis gantry before and after nonlinear optimization.

k	Step 5: Linear LS fit (RMS(E) = 94.57 mm/s ² /V)			Step 6: Nonlinear optimization + linear LS (RMS(E) = 28.13 mm/s ² /V)		
	ω_k (Hz)	ζ_k	p_k (Hz)	ω_k (Hz)	ζ_k	p_k (Hz)
1	15.6373	0.1229	4.5630	96.6626	0.7967	11.6931
2	183.5226	0.0322	674.8170	182.9265	0.0337	896.0423
3	220.5508	0.0058	-	245.0420	0.0471	-
4	234.3168	0.0045	-	284.6926	0.0147	-
5	262.1107	0.0590	-	327.6355	0.0377	-
6	285.9383	0.0078	-	252.3723	0.1173	-
7	330.0826	0.0335	-	358.6669	0.0629	-
8	399.0095	0.0291	-	400.3442	0.0315	-

Table A.2.2: Summary of the identified participation factors after Step 6: Nonlinear optim. + LS fit ($T_{\text{delay}} = 0.5$ ms).

k	α_k	β_k	γ_k	δ_k
1	3.97e+07	7.93e+04	3.1058e+03	-
2	-2.04e+07	3.48e+03	1.0072e+07	-
3	-4.55e+06	-1.7e+04	-	-
4	-2.24e+07	3.02e+03	-	-
5	-9.92e+08	4.23e+04	-	-
6	-8.28e+07	1.94e+04	-	-
7	6.22e+08	-4.6e+04	-	-
8	-1.68e+09	3.48e+05	-	-

Appendix A.3

Summary of the Identified Parameters for the Two-Input Two-Output Ball-Screw Drive System (MIMO)

Table A.3.1: Summary of identified pole locations for the single-axis ball-screw drive after Step 6: Nonlinear optim. + LS fit.

k	ω_k (Hz)	ζ_k	p_k (Hz)
1	0.87 Hz	0.4957	-
2	16.54 Hz	0.4494	-
3	26.8 Hz	0.0094	-
4	30.33 Hz	0.1046	-
5	131.1 Hz	0.0239	-
6	134.1 Hz	0.0455	-

Table A.3.2: Summary of identified pole locations for the single-axis ball-screw drive after Step 6: Nonlinear optim. + LS fit.

Input/output channels	Input #1 Motor					Input #2 Load-side disturbance				
	k	α_k	β_k	γ_k	δ_k	k	α_k	β_k	γ_k	δ_k
Output #1 Rotary encoder	1	1.161e+03	-0.1574	-	-	6	-38.5413	4.3339	-	-
	2	-8.5782	0.0154	-	-	5	346.3009	-5.1795	-	-
	3	-0.3298	-0.0071	-	-	1	0.1887	0.0063	-	-
	4	-2.2730	-0.0716	-	-	2	-35.5480	0.2801	-	-
	5	129.7006	0.0978	-	-	3	-478.0567	0.3467	-	-
	6	101.0017	-0.1505	-	-	4	-109.0282	-0.0822	-	-
Output #2 Linear encoder	k	α_k	β_k	γ_k	δ_k	k	α_k	β_k	γ_k	δ_k
	1	1.168e+03	0.0693	-	-	6	-31.8097	4.2015	-	-
	2	-0.2329	0.0395	-	-	5	387.5805	-4.8010	-	-
	3	-0.2417	-0.0051	-	-	1	10.0583	0.0534	-	-
	4	-1.1139	-0.0478	-	-	2	-53.6894	0.2776	-	-
	5	-370.1848	-0.4534	-	-	3	2.755e+03	-1.1658	-	-
6	-725.4591	0.4203	-	-	4	49.2432	1.0847	-	-	

Appendix A.4

Summary of the Identified Parameters for the X-Axis of the H-Type Gantry (MIMO)

Table A.4.1: Summary of identified pole locations for the H-type gantry after Step 6: Nonlinear optim. + LS fit ($T_{\text{delay}} = 0.05$ ms).

k	ω_k (Hz)	ζ_k	p_k (Hz)
1	0.0007	0.0347	0.3303
2	0.4879	0.1684	3.1947
3	1.3975	0.0179	-
4	25.4048	0.1098	-
5	44.1560	0.0794	-
6	53.2638	0.0226	-

Table A.4.2: Summary of the identified participation factors after Step 6: Nonlinear optim. + LS fit ($T_{\text{delay}} = 0.05$ ms).

Input/output channels	Input #1 Left-hand motor						Input #2 Right-hand motor					
	k	α_k	β_k	γ_k	δ_k		α_k	β_k	γ_k	δ_k		
Output #1 Left-hand rotary encoder	1	-8.903e+7	4.774e+7	-2.868e+7	-		7.30e+8	-4.778e+8	3.11e+8	-		
	2	1.153e+7	-1.94e+7	-3.305e+3	-		9.34e+7	1.696e+8	-2.206e+4	-		
	3	-1.992e+6	3.3044e+5	-	-		-4.99e+6	-2.329e+6	-	-		
	4	129.0452	0.2703	-	-		99.5643	0.2489	-	-		
	5	30.7497	0.0947	-	-		-35.4423	-0.0221	-	-		
	6	4.2600	-0.0040	-	-		-2.9148	0.0139	-	-		
Output #2 Right-hand rotary encoder	1	-1.341e+8	8.881e+7	-5.793e+7	-		-8.235e+8	5.29e+8	-3.417e+8	-		
	2	-1.937e+7	-3.131e+7	4.511e+3	-		-8.416e+7	-1.903e+8	1.86e+4	-		
	3	1.1745e+6	4.256e+5	-	-		3.26e+6	2.68e+6	-	-		
	4	102.5565	0.3196	-	-		72.9962	0.2879	-	-		
	5	-32.1946	-0.0364	-	-		37.7182	0.1093	-	-		
	6	-3.3666	0.0150	-	-		2.5137	-0.0124	-	-		
Output #3 Left-hand linear encoder	1	-1.37e+9	8.7836e+8	-5.67e+8	-		1.368e+8	-9.128e+7	5.956e+7	-		
	2	-1.35e+8	-3.158e+8	3.28e+4	-		2.12e+7	3.217e+7	-4.084e+3	-		
	3	4.7091e+6	4.412e+6	-	-		-1.41e+6	-4.488e+5	-	-		
	4	-100.3431	0.1483	-	-		-96.6583	0.1413	-	-		
	5	-128.8782	-0.2143	-	-		146.4464	0.0134	-	-		
	6	-32.7824	0.0641	-	-		17.6759	-0.0737	-	-		
Output #4 Right-hand linear encoder	1	1.1571e+9	-7.507e+8	4.868e+8	-		-1.316e+9	8.346e+8	-5.365e+8	-		
	2	1.34e+8	2.676e+8	-3.366e+4	-		-1.11e+8	-3.025e+8	2.416e+4	-		
	3	-6.191e+6	-3.67e+6	-	-		2.48e+6	4.32e+6	-	-		
	4	-81.4512	0.3225	-	-		-50.5621	0.1656	-	-		
	5	117.3742	0.1092	-	-		-159.4958	-0.2193	-	-		
	6	8.8338	-0.0538	-	-		-16.8884	0.0249	-	-		

Input/output channels	Input #3 Left-hand disturbance						Input #4 Right-hand disturbance					
	k	α_k	β_k	γ_k	δ_k		α_k	β_k	γ_k	δ_k		
Output #1 Left-hand rotary encoder	1	-5.021e+7	2.166e+7	-1.162e+7	-		-5.754e+7	3.92e+7	-2.583e+7	-		
	2	1.79e+7	-1.024e+7	-4.529e+3	-		-1.0704e+7	-1.355e+7	2.677e+3	-		
	3	-2.426e+6	2.034e+5	-	-		7.682e+5	1.759e+5	-	-		
	4	-15.1635	-0.0398	-	-		5.3706	0.0998	-	-		
	5	-16.8808	-0.2463	-	-		-9.7830	-0.1480	-	-		
	6	0.6880	-0.0071	-	-		-1.6477	-0.0079	-	-		
Output #2 Right-hand rotary encoder	1	8.926e+6	-7.023e+6	4.859e+6	-		9.438e+7	-5.93e+7	3.795e+7	-		
	2	3.73e+6	2.184e+6	-1.14e+3	-		6.627e+6	2.163e+7	-1.286e+3	-		
	3	-3.453e+5	-1.90e+4	-	-		-3.827e+4	-3.13e+5	-	-		
	4	1.1689	-0.0249	-	-		14.1347	0.0676	-	-		
	5	-8.0763	0.1028	-	-		3.4614	0.2255	-	-		
	6	0.2281	0.0147	-	-		2.8129	0.0038	-	-		
Output #3 Left-hand linear encoder	1	-9.376e+8	5.945e+8	-3.825e+8	-		-3.080e+8	1.858e+8	-1.172e+8	-		
	2	-7.847e+7	-2.15e+8	1.978e+4	-		-4.946e+6	-6.961e+7	344.4753	-		
	3	1.618e+6	3.021e+6	-	-		-1.793e+6	1.051e+6	-	-		
	4	26.5918	0.0226	-	-		-16.7023	-0.0179	-	-		
	5	96.8925	0.9283	-	-		103.0617	0.6111	-	-		
	6	1.2255	-0.0021	-	-		16.4800	0.0305	-	-		
Output #4 Right-hand linear encoder	1	-4.954e+8	3.195e+8	-2.068e+8	-		2.152e+9	-1.385e+9	8.956e+8	-		
	2	-5.311e+7	-1.144e+8	1.336e+4	-		2.25e+8	4.963e+8	-5.608e+4	-		
	3	2.172e+6	1.579e+6	-	-		-8.829e+6	-6.873e+6	-	-		
	4	17.4594	0.0015	-	-		-21.0438	0.0486	-	-		
	5	-65.9760	-0.4525	-	-		-34.0001	-0.6371	-	-		
	6	-9.0010	-0.0480	-	-		-11.0223	-0.0201	-	-		

Appendix A.5

Summary of the Identified Parameters for the Y-Axis of the H-Type Gantry (SIMO)

Table A.5.1: Summary of identified pole locations for the H-type gantry y-axis after Step 6: Nonlinear optim. + LS.

k	ω_k (Hz)	ζ_k	p_k (Hz)
1	5.573	0.0389	22.577
2	11.944	0.0364	-
3	16.789	0.0652	-
4	18.812	0.0491	-
5	21.278	0.01672	-
6	22.697	0.01825	-
7	42.229	0.11122	-
8	57.29	0.066	-
9	59.098	0.0097	-
10	62.36	0.0373	-
11	550.787	0.33	-
12	2542.715	0.01	-

Table A.5.2: Summary of the identified participation factors after Step 6: Nonlinear optim. + LS fit ($T_{\text{delay}} = 1.6$ ms).

Input/output channels		Input #1 Motor				
		k	α_k	β_k	γ_k	δ_k
Output #1 Rotary encoder		1	468.7561	4.3683	-6.43	-
		2	17.9430	0.2216	-	-
		3	-22.3687	-0.0432	-	-
		4	120.0595	0.3452	-	-
		5	6.1385	0.0536	-	-
		6	7.0548	0.0923	-	-
		7	5.4764	0.1607	-	-
		8	51.5460	0.0316	-	-
		9	14.0208	-0.0291	-	-
		10	107.1990	0.0371	-	-
		11	-3.9323e+07	7.6907e+03	-	-
		12	8.3996e+08	-3.3000e+05	-	-
		k	α_k	β_k	γ_k	δ_k
Output #2 Linear encoder		1	474.0822	4.6598	-5.14	-
		2	14.2697	0.2125	-	-
		3	-18.9298	-0.0029	-	-
		4	66.1065	0.3635	-	-
		5	1.2997	0.0353	-	-
		6	-1.7462	0.0441	-	-
		7	-12.0812	-0.1446	-	-
		8	-103.5899	0.0157	-	-
		9	-22.2749	0.0549	-	-
		10	-217.3243	-0.0309	-	-
		11	2.0101e+07	-2.9745e+03	-	-
		12	-4.2972e+08	1.4785e+05	-	-

Appendix A.6

Application of the Two-Stage Indirect Method for Open-Loop Frequency Response Estimation of the H-Type Gantry Machine (MIMO)

Having known the stabilizing controller K , the frequency response of the closed-loop system was measured between the input control signal u and disturbance excitation d as shown in Figure A.6.1 a and b for the y (SISO) and x-axis (MIMO) of the gantry machine. Then the estimated open loop plants $H(\omega)$ were derived from the closed-loop frequency responses. The control input for the block diagrams in Figure A.6.1 a and b can be stated by:

$$U(\omega) = D(\omega) + K(\omega)R(\omega) - K(\omega)N(\omega) - K(\omega)H(\omega)U(\omega) \quad (\text{A.6.1})$$

In the above equation, $U(\omega)$, $D(\omega)$, $R(\omega)$, and $N(\omega)$ are the Fourier transformed signals of the control signal $u(t)$, disturbance input $d(t)$, command signal $r(t)$, and measurement noise $n(t)$.

The cross power spectral density between the control input u and excitation signal d ($S_{ud}(\omega) = U(\omega)D^*(\omega)$) can be expressed by:

$$\begin{aligned} S_{ud}(\omega) &= S_{dd}(\omega) + K(\omega)S_{rd}(\omega) - K(\omega)S_{nd}(\omega) - K(\omega)H(\omega)S_{ud}(\omega) \\ S_{ud}(\omega) &= (I + K(\omega)H(\omega))^{-1}S_{dd}(\omega) + \underbrace{K(\omega)(I + K(\omega)H(\omega))^{-1}(S_{rd}(\omega) - S_{nd}(\omega))}_{\text{bias}} \end{aligned} \quad (\text{A.6.2})$$

where, $S_{dd}(\omega) = D(\omega)D^*(\omega)$ is the auto power spectral density of the disturbance signal, $S_{rd}(\omega) = R(\omega)D^*(\omega)$, is the cross power spectral density between the reference command r and disturbance input d , $S_{nd}(\omega) = N(\omega)D^*(\omega)$ is the cross power spectral density between the measurement noise and the disturbance input. The star sign denotes complex conjugate form.

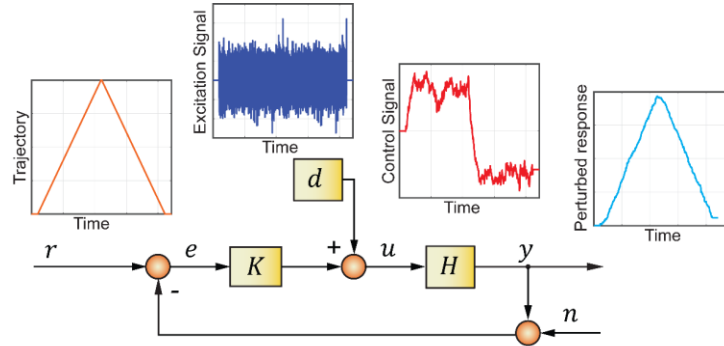
When the reference command r , the disturbance signal d , and the measurement noise n are uncorrelated, the sensitivity is described by the following:

$$S(\omega) = (I + H(\omega)K(\omega))^{-1} \approx S_{ud}(\omega)/S_{dd}(\omega) \quad (\text{A.6.3})$$

Applying a white noise as the excitation signal d , and a constant velocity reference trajectory make $S_{nd}(\omega) = 0$, and $S_{rd}(\omega) = 0$, respectively. This enables an unbiased estimation of the sensitivity function S . Considering the closed-loop system's response to input level disturbances of each axis as $M(\omega) = (I + H(\omega)K(\omega))^{-1}H(\omega)$ where K is the feedback controller the open-loop plant can be obtained as:

$$H(\omega) = M(\omega)(I - K(\omega)M(\omega))^{-1} \quad (\text{A.6.4})$$

(a)



(b)

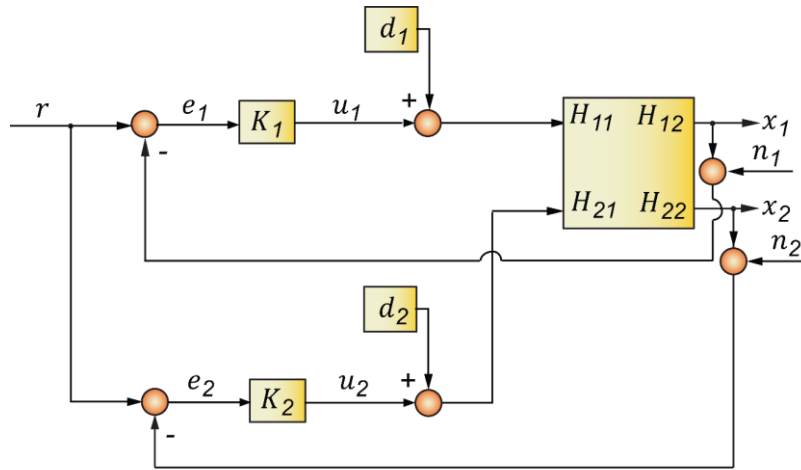


Figure A.6.1: Equivalent SISO (top) and MIMO (bottom) control scheme used in the closed-loop frequency response measurement of the gantry.

For the x-axis of the gantry (MIMO case), the closed-loop measurements, the estimated open-loop frequency responses and the controller can be described by $M = \begin{bmatrix} M_{11} & M_{12} \\ M_{21} & M_{22} \end{bmatrix}$, $H = \begin{bmatrix} H_{11} & H_{12} \\ H_{21} & H_{22} \end{bmatrix}$, and $K = \begin{bmatrix} K_{11} & K_{12} \\ K_{21} & K_{22} \end{bmatrix}$, respectively. In the implementation, the controller cross terms ($K_{12} = K_{21} = 0$) were set to zero to simplify the open-loop extraction of FRFs. To simplify the notation, K_{11} and K_{22} are denoted by K_1 , and K_2 , respectively. The following state the individual SISO transfer functions:

$$M_{\Delta} = M_{11}M_{22} , M_{12} = -M_{21} \quad (\text{A.6.5})$$

$$H_{11} = \frac{K_2 M_{\Delta} - M_{11}}{K_1 M_{11} + K_2 M_{22} - K_1 K_2 M_{\Delta} - 1} \quad (\text{A.6.6})$$

$$H_{21} = \frac{-M_{21}}{K_1 M_{11} + K_2 M_{22} - K_1 K_2 M_{\Delta} - 1} \quad (\text{A.6.7})$$

$$H_{12} = \frac{-M_{12}}{K_1 M_{11} + K_2 M_{22} - K_1 K_2 M_{\Delta} - 1} \quad (\text{A.6.8})$$

$$H_{22} = \frac{K_1 M_{\Delta} - M_{22}}{K_1 M_{11} + K_2 M_{22} - K_1 K_2 M_{\Delta} - 1} \quad (\text{A.6.9})$$

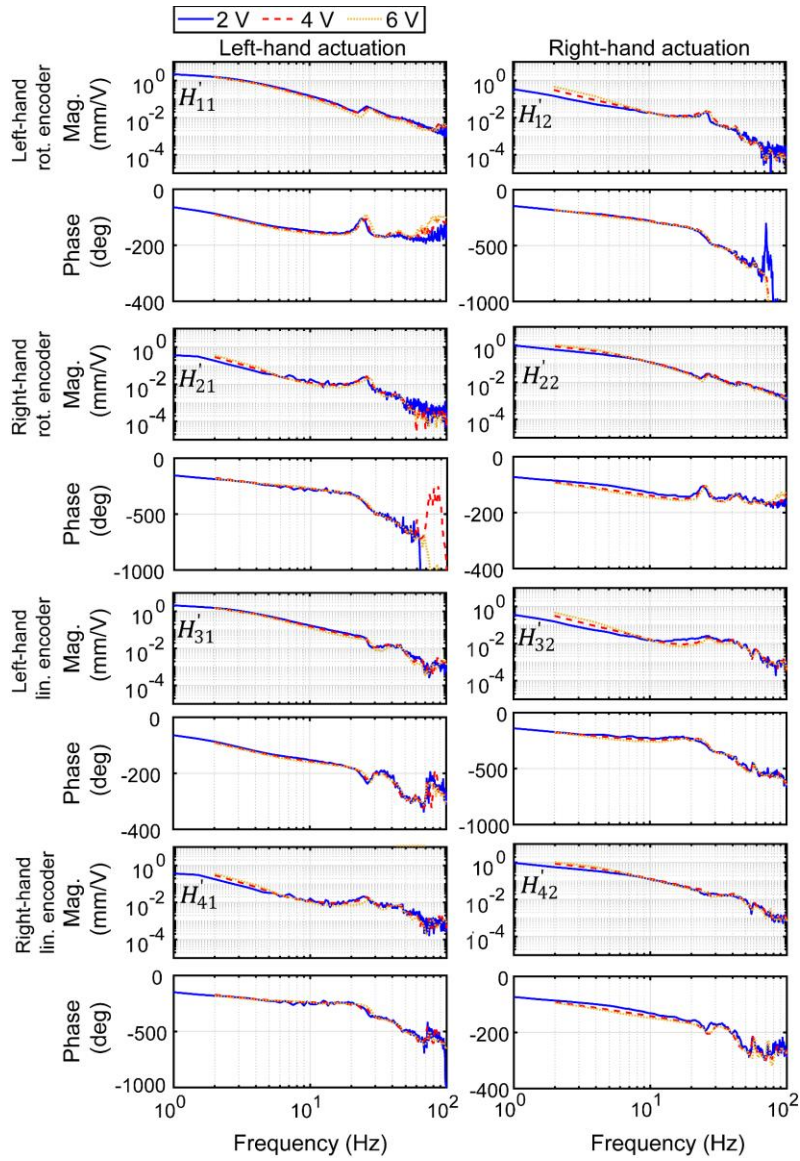


Figure A.6.2: Rotary and linear encoder estimated open-loop frequency responses at different amplitude of excitation.

Appendix A.7

Option Set for MATLAB's `tfest` Function

Note: Regardless of the choice of solver, for the data set used, when the stability bounds were not enforced on the pole locations, the output of the function "`tfest`" converged to the same solution each time.

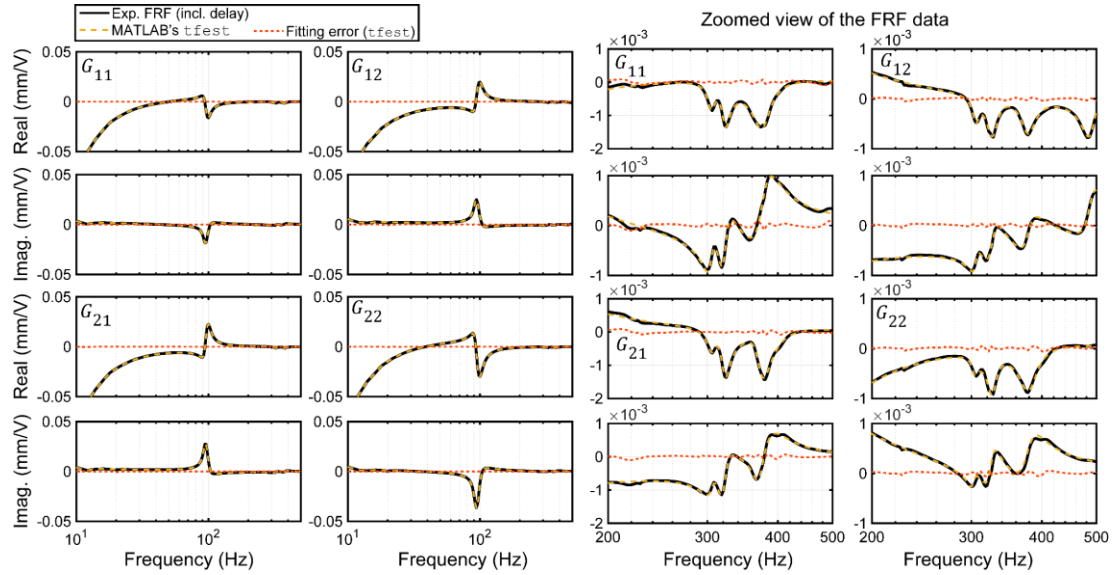


Figure A.7.1: Raw FRF data and fitted models using `tfest` (stability not enforced) function.

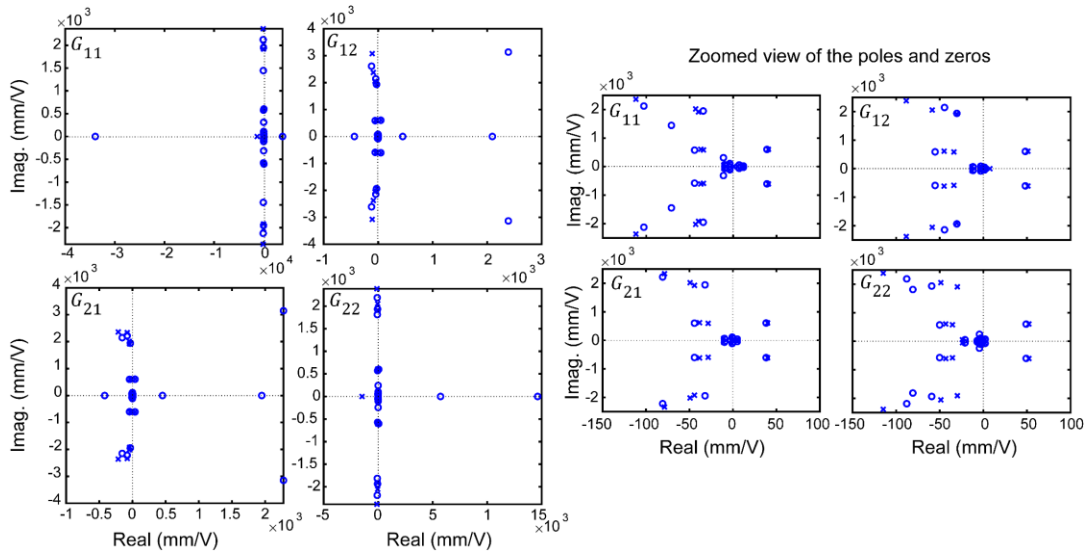


Figure A.7.2: Pole zero map of the identified plant (unstable system) by `tfest`.

Table A.7.1: Application of different `tfest` algorithms (MIMO case).

Fitting algorithm	RMS error (mm)/V	Order
<code>tfest(iv, svf, gpmf, n4sid)</code>	1.4290e-04	23 (2x2)